

The Effective Mean-Free-Path of the Solar Wind

Jesse T. Coburn

Thesis submitted for the degree of
Doctor of Philosophy

Queen Mary University of London

2022

Declaration

I hereby declare that the work presented in this thesis is my own, unless otherwise stated, and resulted from collaborations with Christopher H. K. Chen, Jonathan Squire, Stuart D. Bale, Lynn B. Wilson III, Fan Guo, and Xiangrong Fu.

The results presented in Chapter 5 have been accepted as a letter:

Coburn, J. T., Chen, C. H. K., and Squire J., A Measurement of the Effective Mean Free Path of the Solar Wind Protons, Journal of Plasma Physics (2022).

Jesse T. Coburn
January 15, 2023

Abstract

The high temperature and rarefied ionised gas (plasma) that constitutes the corona of the sun escapes the gravitational bound and flows out into interplanetary space. This plasma is called the solar wind. It is characterised by a long collision mean-free-path (i.e., weakly collisional); it is not in thermodynamic equilibrium. While the plasma is ultimately governed by a kinetic equation, it does appear that the solar wind is described by fluid equations, where it is assumed to be at equilibrium. This is in stark contradiction to the long collision mean-free-path.

The suggestion is that collisionless relaxation processes are playing a strong role in dictating the dynamics of the solar wind. These processes are wave-particle interactions that cause the plasma to relax towards equilibrium, i.e., they are effective collision processes. This thesis takes a novel route to measure the effective mean-free-path of the solar wind, by modelling compressive fluctuations of arbitrary effective mean-free-path, and making a robust comparison to solar wind observations. The effective mean-free-path is measured to be approximately 10^3 times shorter than the collisional mean-free-path. It is shown to be consistent with and justify decades of past solar wind research that use fluid equations.

The theory for the numerical model is derived from first principles and is shown to coincide with previous results, and draw together many concepts about compressive plasma waves. The solar wind dataset used in this thesis was not previously used for scientific analysis, so verification of the data quality is demonstrated.

In addition, data analysis tools are constructed to measure some of the potential effective collision mechanisms. The analysis is tested on simulation data, to verify the accuracy, by measuring key quantities in identifying the relevant role of various effective collision mechanisms. The analysis of the numerical simulation data is shown to be satisfactory and can be employed on spacecraft data.

This measurement resolves a long-standing debate on the utility and accuracy of fluid equations in studying the solar wind. The direct measurement of the effective mean-free-path is important for the field of plasma physics because it dictates the transport and thermodynamics of weakly collisional plasmas.

Acknowledgements

My upmost gratitude goes to Dr. Christopher Chen for unwavering and thorough support over the last few years. This fundamental piece of work is an incredible achievement. I am proud to cite it as J. T. Coburn and C. H. K. Chen. My appreciation also goes to Dr. Jonathan Squire for his collaboration and for always sharing his scientific input. I thank Prof. David Burgess for guidance and creating a charming space to learn space plasma physics.

I thank Prof. Stuart D. Bale for pointing me to the primary dataset of this Thesis and to Dr. Lynn B. Wilson III for helping me to understand the dataset.

I thank Dr. Fan Guo and Dr. Xiangrong Fu for guidance during my two summers working for the Los Alamos National Laboratory.

Contents

1	Introduction	24
1.1	The need for a kinetic theory of plasma	24
1.2	Motivation for thesis	27
2	Plasma physics	32
2.1	Statistical theory of plasmas	33
2.1.1	N-particle density function	33
2.1.2	Bogolyubov, Born and Green, Kirkwood, and Yvon Hierarchy	38
2.1.3	Boltzmann's Equation and Maxwell's Equations	39
2.2	Collisions and transport theory	40
2.2.1	Fokker-Planck	40
2.2.2	Braginskii's work and classical transport theory	44
2.2.3	Bhatnagar-Gross-Krook operator	45
2.3	Kinetic magnetohydrodynamics	45
2.4	Closures	50
2.4.1	Fluid theory	50
2.4.2	Ohm's Law	51
2.4.3	Landau fluid	52
2.5	Plasma waves and instabilities	52
2.5.1	Kinetic theory	53
2.5.2	Fluid theory	57
2.5.3	Branch connections	59
2.6	Quasi-linear theory	59
2.7	Fluid plasma turbulence	63
3	The solar wind	71
3.1	Eugene Parker's solar wind model	71
3.2	Variable generation	74
3.2.1	Composition of interplanetary particles	75
3.3	Magnetic field structure	76

3.3.1	The heliosphere	77
3.4	Heating	78
3.4.1	Collisional heating	79
3.4.2	Wave-particle interactions	80
3.4.3	More sources of heating	81
3.5	Instabilities	81
3.6	Observations of compressive fluctuations	83
3.7	Solar wind turbulence	85
3.7.1	The natural turbulence laboratory	85
3.7.2	Power laws and anisotropy	87
3.7.3	Compressive turbulence	88
3.8	Instruments	89
3.8.1	Top-hat electrostatic analyzer	89
3.8.2	Magnetometer	91
3.8.3	Faraday Cup	92
4	Collisional-kinetic magnetohydrodynamics: dispersion relation	95
4.1	Equations	97
4.2	Normal modes	99
4.2.1	Small-amplitude Fourier analysis	100
4.3	Normalization and eigen-problem	101
4.4	Numerical Methods	104
4.4.1	The plasma dispersion function	105
4.4.2	Root finding	107
4.4.3	Eigen-problem solutions	109
4.5	Numerical Solutions	109
4.5.1	Dispersion relation	110
4.5.2	The ratio of electron to proton temperature	117
4.5.3	The ratio of proton to electron mean-free-path	119
4.6	Method of correlations and amplitudes	121
4.7	Conclusion	126
5	Measuring the effective mean-free-path	130
5.1	Chew-Goldberger-Low correlations	130
5.1.1	Equations of state and the Chew-Goldberger-Low equations	131
5.1.2	The CGL cross-correlations	133
5.2	Breaking the parameter degeneracy	138
5.3	The Wind dataset	141
5.3.1	Comparison with ground moments	141
5.3.2	Comparison with SWE	144

5.3.3	Measured length and time-scales	149
5.3.4	The 3DP 3 second dataset	150
5.4	Comparing the observations and numerical methods	151
5.4.1	Conditioning the observations	151
5.4.2	Measurements of the CGL cross correlations	154
5.4.3	Comparing numerical solutions and observations	155
5.4.4	Measuring the parameters	161
5.4.5	The wavenumber dependence	163
5.4.6	Measuring the transition scale	164
5.5	Conclusion	168
6	Quasi-linear relaxation rate: numerical simulations	172
6.1	The VPIC simulation	172
6.2	The parallel proton cyclotron instability as a case study	173
6.3	The general problem of measuring quasi-linear heating rates	176
6.4	Measuring the pitch-angle gradient	178
6.4.1	Hermite-Laguerre functions	178
6.4.2	Hermite-Laguerre transform	180
6.4.3	Pitch-angle gradients	182
6.4.4	Combining the resonance function with the magnetic field power spectrum	183
6.5	Comparing the time history	186
6.6	Relaxation time	187
6.7	Future work	189
6.7.1	Magnetic field power spectrum	189
6.7.2	Comparison with bi-Maxwellian	190
6.7.3	High-order quasi-linear theory	192
6.8	Conclusion	194
7	Conclusions and future work	196
7.1	Summary	196
7.2	Discussion and future work	197
7.2.1	The fluid nature of plasmas	198
7.2.2	The transport coefficients	198
7.2.3	Compressive turbulence	199
A	Derivation of electromagnetic dielectric tensor	201
A.0.1	The perturbation in the unperturbed orbit frame	203
A.0.2	The unperturbed orbits	204
A.0.3	Fourier Transform	206
A.0.4	Introducing the Bessel functions	212

B Derivation of kinetic magnetohydrodynamics and normal modes	215
B.1 Drift Kinetic Equation	215
B.1.1 Derivation of drift kinetic equation	216
B.1.2 Linearization	222
B.1.3 Fourier analysis	225
B.1.4 Moments of the kinetic equation	227
B.2 Continuity	234
B.2.1 Linearization	234
B.2.2 Fourier Analysis	234
B.3 Single-fluid momentum	235
B.3.1 Linearization	235
B.3.2 Fourier analysis	237
B.4 Induction equation	238
B.4.1 Linearization	239
B.4.2 Fourier analysis	239
B.5 Plasma dispersion function	239
B.6 Useful results on the plasma dispersion relation	243
B.6.1 Density integrals	243
B.6.2 Perpendicular pressure integrals	246
B.6.3 Parallel pressure integrals	247
C The Chew-Goldberger-Low Equations	249
C.1 Derivation	249
C.1.1 Perpendicular pressure equation	250
C.1.2 Parallel pressure equation	253
D Deriving Ohm's Law	256
D.1 Fluid Equations	257
D.1.1 Continuity	257
D.1.2 Momentum Equation	259
D.2 1-Fluid Equations	262
D.2.1 Continuity	264
D.2.2 Combining the momentum equations	265
D.2.3 Ohm's Law	266

List of Figures

1.1	Page 306 of Krall and Trivelpiece [1973]. The timescales are in seconds.	26
1.2	Radial evolution of the solar wind, reproduced from Verscharen et al. [2019]. The horizontal axes are radial distances from the Sun, in units of solar radius (top) and Earth-Sun distance (bottom). The density n_p , n_e and radial magnetic field B_r are empirical models, the proton velocity U_{pr} , is obtained from flux conservation, $n_p U_{pr} / B_r = \text{const}$. The electron and proton temperatures, not shown, connect in situ and remote measurements. The quantities are defined in the text here.	28
1.3	The joint histogram of proton pressure and density measured by the electrostatic analyser on the Wind spacecraft at 1 AU. The dataset is described in Section 5.3. The γ follows from assuming $\log p_p = \gamma \log n_p $, and a linear regression is performed. R^2 is the Pearson correlation coefficient.	29
2.1	Recreated from Dellar [2015]. The left panel represents three particles in \mathcal{N} for one component of space x_0 and velocity v_0 . Each space, denoted by a closed square, is annotated in the top left corner. The dots with tails are their location in phase space at time t . The right panel shows N spaces, where each particle evolves in time in its own space. The left single panel is a cartoon of Eq. 2.1 and the right panels represent Eq. 2.11.	35
2.2	Reproduced from Gary [1993]. The two panels have different electron to proton temperature ratios denoted in the top left corners. The definitions of the quantities and line style choice appears in Section 2.5.1.2. The proton beta doesn't appear in the textbook, but this is explored in later section of this thesis.	55

2.3	Reproduced from Gary [1993]. In the panels the proton temperatures are reported $T_{\parallel i}$, $T_{\perp i}$ where i is used for ion, but in this thesis it corresponds to the proton temperature. The parameters of this system are $v_A/c = 10^{-4}$, $\beta_p = 1$	57
2.4	Reproduced from Howes et al. [2006]. The left panel is the normalized real frequency and the right panel is the normalized damping rate. The horizontal axis is the perpendicular wavenumber times the proton gyroradius (they have used ρ_i). The top left annotation is the proton to electron temperature ratio and the ratio of proton thermal velocity to the speed of light. The line are annotated by the proton plasma beta (here it is β_i) and the line styles can be ignored for this discussion.	58
2.5	Reproduced form Verscharen et al. [2019]. Blue dotted lines are contours of the background distribution function F_s , grey shaded region is the resonant region, black lines are contours of Eq. 2.101, and the blue arrows are the direction of diffusion of the particles.	61
2.6	Reproduced form Yoon [2017]. In the top panels, the evolution of the proton beta are shown for a simulation in solid lines and dashed lines the bi-Maxwellian prediction. The bottom panel shows the magnetic energy with the same line style scheme. The horizontal axis is the time in number of cyclotron periods. Please ignore the “QL” as it is misleading.	62
2.7	The panels on the left show a local and non-local triad interaction. The right hand top panel shows a typical omni-directional magnetic field power spectrum. The bottom right panel shows the k_{\parallel} , k_{\perp} plane where the interactions take place. One would expect enhanced power along lines in this plane. All panels here are cartoons.	66
3.1	Reproduced from Parker [1958]. The vertical axis is velocity and the horizontal axis is the radius normalized by “a” which is the radius at which the corona no longer heats the plasma. The parameters of the model are $a = 10^{11}$ cm and the solar mass. The solutions are shown for a range of temperatures at “a” which are annotated near to the lines.	73

- 3.2 Reproduced from McComas et al. [2003]. Both panels are polar plots where the radius is the solar wind velocity colored by the direction of the magnetic field (labelled on the left panel) measured by Ulysses spacecraft. The background figures are detection of the extreme ultraviolet light, by the Solar and Heliospheric Observatory, which are characteristic of the two different periods indicated in the lower panels. The lower panels show the sunspot number. 74
- 3.3 Reproduced from Fox et al. [2016] which is reproduced from Gloeckler [2010]. The vertical axis is the differential intensity, which is the flux, then divided by the angular coverage of the instrument in steradians and divided by the energy per nucleon. The horizontal axis is the energy per nucleon. Various instrument data products are combined to make this figure. CIR stands for co-rotating interaction region. GCR stands for galactic cosmic ray. ANR stands for anomalous cosmic ray. SEP stands for solar energetic particle. For information on the grey shaded regions, black boxes and annotations at the bottom see Gloeckler [2010]. 76
- 3.4 Reproduced from Owens and Forsyth [2013]. Looking top down at a slice through the ecliptic plane of the sun, magnetic field lines are drawn where the color lines indicate opposite polarity. The black lines that do not exceed the source surface are closed loops. The closed black circle is the source surface where the solar wind expansion dominates the magnetic field forcing it to be only radial, see the annotations. The green dashed spiralled line is the heliospheric current sheet, separating large regions of opposing polarity. 77
- 3.5 Reproduced from Owens and Forsyth [2013]. The global structure of the heliosphere and its boundary with the interstellar medium. The arrows shows direction of plasma (loosely defined here) relative to the sun. In that frame, the heliosphere moves relative to the interstellar medium creating a boundary with multiple shock layers. 78
- 3.6 Reproduced from Smith et al. [2006]. The proton temperature observed by the Voyager 2 spacecraft in circles. The dashed line is adiabatic expansion. The red line is a model that incorporates heating by fluid turbulence and energy injection by pick-up ions. 79

3.7	Reproduced from He et al. [2011]. The top panel is the radial magnetic field measured by the STEREO spacecraft. The middle panel with color is the reduced fluctuating magnetic helicity which has period dependence on the vertical axis and time dependence on the horizontal axis. The bottom panel has been rotated into local magnetic field coordinates so the horizontal axis is the angle between the solar wind velocity direction and magnetic field at that period, centered on that time.	80
3.8	Reproduced from Hellinger et al. [2006]. The joint histogram of the proton temperature anisotropy (vertical axis) and the parallel proton beta (horizontal axis) is indicated with the color bar at the right. The contours drawn here represent the proton cyclotron instability (solid), parallel firehose instability (dashed), mirror instability (dotted), and the oblique firehose instability (dash-dot).	82
3.9	Reproduced from Verscharen et al. [2019]. The green colors are the electron density and the red colors are the magnetic field strength both measured by the Cluster spacecraft. Light grey vertical lines indicate the time scale of the panel that follows below.	84
3.10	Reproduced from Verscharen et al. [2019]. Measurements of the magnetic field power spectral density, see the figure annotations, span more than 7 decades in spacecraft frequency. The color labelled frequencies are the inverse correlation time f_{τ_c} , and the proton inertial length f_{d_p} , the proton gyro-radius f_{ρ_p} , the electron inertial length f_{d_e} , the electron gyro-radius f_{ρ_e} all converted to spacecraft frequency with Taylor's assumption. The black labels indicating power law in frequency, are typical to the solar wind at 1 AU.	86
3.11	Reproduced from Chen [2016] using data from the Wind spacecraft. The top panel is the spectral index of the magnetic field power spectrum conditioned on the local magnetic field direction. The bottom panel is the ratio of the Alfvén time to non-linear time. See Section 2.7.0.3 for definitions.	87
3.12	Reproduced from Chen [2016] using data from the Wind spacecraft. Power spectral density, normalized to be unitless, for the quantities annotated on the plot. Black lines indicate the slope of the power law.	88
3.13	Reproduced from Chen [2016] using data from the Wind spacecraft. The colors are annotated on the top panel. The bottom panel is the ratio. The horizontal axis is the perpendicular wavenumber converted with Taylor's assumption.	89

3.14 Reproduced from Verscharen et al. [2019]. The top-hat design becomes visible from the figure. This is a slice through the instrument, which is symmetric about the \hat{z} direction, through the center of the instrument. The particle of charge $\pm q_j$ will follow the trajectory in blue through the collimator to the detector if it suffices a condition imposed by voltage difference of $2\mathcal{E}$	90
3.15 Reproduced from Verscharen et al. [2019]. The quantities here are the period of the applied field Π , the amplitude of the applied field H_0 , the critical value of the ferromagnet H_c , the applied field $H_d(t)$ (a current is applied to give this field), ΔH_z is the component of the external field to be measured, $B(t)$ is the magnetic field inside the material, B_s is the critical value of $B(t)$ due to H_c , \mathcal{E}_s is the induced voltage in the fluxgate due to $B(t)$, which has amplitude \mathcal{E}_0 . The blue shaded regions indicate when $H(t)$ (defined in text) is saturated at $\pm H_c$ and the pink shaded regions indicate when $B(t)$ will be consequently saturated at B_s	92
3.16 Reproduced from Verscharen et al. [2019]. This diagram aids the explanation of how the current is measured in plasma environments. The quantities are \mathcal{E} the voltage, \mathcal{E}_0 the offset voltage, $\Delta\mathcal{E}$ the peak-to-peak amplitude, t the time, v_z the normal component of the ion velocity, and $v_j^{(c)}$ the cutoff speed due to the voltage. Particle trajectories are shown in blue which enter the wide aperture which are then subjected to a voltage that is applied to middle, shown as vertical dashed lines. Some particles hit the detection plate, shown as a vertical black line, which receives the current.	93
4.1 Starting at the top box labelled “Vlasov-Maxwell” three branches pass to the “Collisional-kinetic MHD” box, identifying the constituents of the set of equations. The two branches leaving the “Collisional-kinetic MHD” box are the linear analysis that produce dispersion relations and perturbations of the plasma parameters. The parameters of the model in order according to the box labelled “Parameters” are the wavenumber, proton beta, propagation angle relative to the background magnetic field, the effective mean-free-path, the proton to electron temperature ratio, and the effective mean-free-path ratio.	96

4.2	The numerical method takes parameters and an analytical estimate of the complex frequency to output the numerical complex frequency and the eigenvalues/vectors of the primary linear system (Eq. 4.23), which are the primary numerical results of the thesis.	104
4.3	The imaginary (right column) and real (left column) parts of the functions shown as the top panels Eq. 4.34, middle panels Eq. B.132, and bottom panels Eq. 4.33. This labelling can be seen as text, directly in the panel. The color bar is log-normal until $\pm 10^{-1}$ and then is linear between $\pm 10^{-1}$	106
4.4	The difference between the expansions (see Eq. 4.37) and the numerical calculation of the dispersion relation function (see Eq. 4.37) for the kinetic expansion (Eq. 4.33) in the top panels and fluid expansion (Eq. 4.34) in the bottom panels.	107
4.5	The real (imaginary) part of the determinant of Eq. 4.23 on the left (right) columns for a span of $\mathcal{I}\{\zeta_s\}$ on the vertical axis and $\mathcal{R}\{\zeta_s\}$ on the horizontal axis. The changed parameters between the rows are the $k_{\parallel} \lambda_{\text{mfp}}^{\text{eff}}$ product.	108
4.6	Dispersion relation of the slow-mode at $\theta_{\mathbf{b},\mathbf{k}} = 80.0^\circ$. The non-magenta curves are produced from the numerical method described in the text. The color corresponds to the proton plasma beta. The legend reports the assumptions behind the analytical functions corresponding to Eqs. 4.45, 4.46, and 4.47. The value of β_p chosen for the analytical curves is the maximum or minimum of the range corresponding to whether the approximation for β_p is \gg or \ll than 1.	112
4.7	Dispersion relation of the slow-mode for $\theta_{\mathbf{b},\mathbf{k}} = 60.0^\circ$. The non-magenta curves are produced from the numerical method described in the text. The color corresponds to the proton plasma beta. The legend reports the assumptions behind the analytical functions corresponding to Eqs. 4.45, 4.46, and 4.47. The value of β_p chosen for the analytical curves is the maximum or minimum of the range corresponding to whether the approximation for β_p is \gg or \ll than 1.	114

4.8	The slow-mode dispersion relations as a function of propagation angle. The non-magenta curves are produced from the numerical method described in the text. The color corresponds to the proton plasma beta. The legend reports the assumptions behind the analytical functions corresponding to Eqs. 4.45, 4.46, and 4.47. The value of β_p chosen for the analytical curves is the maximum or minimum of the range corresponding to whether the approximation for β_p is \gg or \ll than 1. In the bottom left corner of the bottom panel, the parameters $k \lambda_{\text{mfp}}^{\text{eff}} = 50.0$ are reported, corresponding to the collisionless regime.	116
4.9	The slow-mode dispersion relations as a function of propagation angle. The non-magenta curves are produced from the numerical method described in the text. The color corresponds to the proton plasma beta. The legend reports the assumptions behind the analytical functions corresponding to Eqs. 4.45, 4.46, and 4.47. The value of β_p chosen for the analytical curves is the maximum or minimum of the range corresponding to whether the approximation for β_p is \gg or \ll than 1. In the bottom left corner of the bottom panel, the parameters $k \lambda_{\text{mfp}}^{\text{eff}} = 0.2$ are reported.	117
4.10	The slow-mode dispersion relations as a function of plasma beta. The non-magenta curves are produced from the numerical method describe in the text. The color corresponds to the proton plasma beta. The legend reports the assumptions behind the analytical functions corresponding to Eqs. 4.45, 4.46, 4.47, and 4.49. The value of β_p chosen for the analytical curves is the maximum or minimum of the range corresponding to whether the approximation for β_p is \gg or \ll than 1. In the bottom left corner of the bottom panel, the parameters $k \lambda_{\text{mfp}}^{\text{eff}} = 0.5$ are reported, corresponding to the fluid regime.	118
4.11	The slow-mode dispersion relations as a function of temperature ratio. The non-magenta curves are produced from the numerical method describe in the text. The color corresponds to the temperature ratio. The legend reports the assumptions behind the analytical functions corresponding to Eqs. 4.45, 4.46, 4.47, and 4.49. In the upper left corner of the bottom panel, the parameters $k_{\parallel} \lambda_{\text{mfp}}^{\text{eff}} = 15.0$ are reported, corresponding to the collisionless regime.	119

- 4.12 The slow-mode dispersion relations as a function of temperature ratio. The non-magenta curves are produced from the numerical method describe in the text. The color corresponds to the temperature ratio. The legend reports the assumptions behind the analytical functions corresponding to Eqs. 4.45, 4.46, 4.47, and 4.49. In the upper left corner of the bottom panel, the parameters $k_{\parallel} \lambda_{\text{mfp}}^{\text{eff}} = 0.05$ are reported, corresponding to the fluid regime. 120
- 4.13 The slow-mode dispersion relations as a function of the mean-free-path ratio. The non-magenta curves are produced from the numerical method describe in the text. The color corresponds to the mean-free-path ratio. The legend reports the assumptions behind the analytical functions corresponding to Eqs. 4.45, 4.46, 4.47, and 4.49. In the upper left corner of the bottom panel, the parameters $k_{\parallel} \lambda_{\text{mfp}}^{\text{eff}} = 0.05$ are reported, corresponding to the fluid regime. 121
- 4.14 The slow-mode dispersion relations as a function of the mean-free-path ratio. The non-magenta curves are produced from the numerical method describe in the text. The color corresponds to the mean-free-path ratio. The legend reports the assumptions behind the analytical functions corresponding to Eqs. 4.45, 4.46, 4.47, and 4.49. In the upper left corner of the bottom panel, the parameters $k_{\parallel} \lambda_{\text{mfp}}^{\text{eff}} = 0.5$ are reported, corresponding to the intermediate regime. 122
- 4.15 The slow-mode dispersion relations as a function of the mean-free-path ratio. The non-magenta curves are produced from the numerical method describe in the text. The color corresponds to the mean-free-path ratio. The legend reports the assumptions behind the analytical functions corresponding to Eqs. 4.45, 4.46, 4.47, and 4.49. In the upper left corner of the bottom panel, the parameters $k_{\parallel} \lambda_{\text{mfp}}^{\text{eff}} = 2.5$ are reported, corresponding to the collisionless regime. 123
- 4.16 The fluctuations, defined as Eq. 4.54, are plotted as a function of time, displayed on the horizontal axis. The different curves are mapped to the color bar, which is the proton beta. The parameters for these solutions are $\theta_{\hat{b}, \hat{k}} = 80^\circ$ and $k_{\parallel} \lambda_{\text{mfp}}^{\text{eff}} = 0.01$, the fluid regime. 124
- 4.17 The fluctuations, defined as Eq. 4.54, are plotted as a function of time, displayed on the horizontal axis. The different curves are mapped to the color bar, which is the proton beta. The parameters for these solutions are $\theta_{\hat{b}, \hat{k}} = 80^\circ$ and $k_{\parallel} \lambda_{\text{mfp}}^{\text{eff}} = 10$ 125

4.18	The correlations (Eq. 4.55) and amplitudes (Eq. 4.56) are plotted as a function of the plasma beta for different angles. The different curves are mapped to the color bar, which is the propagation angle. The parameters for these solutions are set to $k_{\parallel} \lambda_{\text{mfp}}^{\text{eff}} = 10$.	126
4.19	The correlations (Eq. 4.55) and amplitudes (Eq. 4.56) are plotted as a function of the plasma beta for different angles. The different curves are mapped to the color bar, which is the propagation angle. The parameters for these solutions are set to $k_{\parallel} \lambda_{\text{mfp}}^{\text{eff}} = 0.01$.	127
4.20	The correlations (Eq. 4.55) and amplitudes (Eq. 4.56) are plotted as a function of the plasma beta for different angles. The different curves are mapped to the color bar, which is $k_{\parallel} \lambda_{\text{mfp}}^{\text{eff}}$. The parameters for these solutions are set to $\theta_{\hat{b},\hat{k}} = 75^\circ$.	128
5.1	The correlations and amplitudes (Eqs. 5.8) are plotted as a function of the plasma beta for $k_{\parallel} \lambda_{\text{mfp}}^{\text{eff}}$, seen in the color bar. The obliqueness of the propagation angle $\theta_{\hat{b},\hat{k}}$ increases with k .	134
5.2	The correlations and amplitudes (Eqs. 5.8) are plotted as a function of the plasma beta for $k_{\parallel} \lambda_{\text{mfp}}^{\text{eff}} = 0.06$. a set of angles . The different curves are mapped to the color bar, which is $\theta_{\hat{b},\hat{k}}$.	135
5.3	The dashed line is three different values of the $\lambda_{\text{mfp}}^{\text{eff}}$ and the same $k_{\parallel} \lambda_{\text{mfp}}^{\text{eff}}$. The function in Eq. 5.32 is plotted for a set of parameters, where α is mapped to the color bar and the values for k_{iso} are at 45 degrees where the colored lines meet.	139
5.4	Component 2, see global caption.	142
5.5	Component 1, see global caption.	142
5.6	The blue dots are a scatter plot of the 24 second PLSP x-component of the velocity and 3 second PM x-component of the velocity from level 0, both in the geocentric coordinate system (see text for a description of the coordinate system). The time interval is one day: July 7th, 2007. The linear regression produced the slope (dashed red line) and the Pearson correlation coefficient. The mean can be ignored.	142
5.7	Component 00, see global caption.	143
5.8	Component 11, see global caption.	143
5.9	The blue dots are a scatter plot of the 24 second PLSP 22-component of the pressure tensor and the level zero 3 second PM 22-component of the velocity, both in the geocentric coordinate system. The time interval is one day: July 7th, 2007. The linear regression produced the slope (solid red line) and the Pearson correlation coefficient.	143

5.10 A repeat of the analysis employed by Hellinger et al. [2006]. The black lines are from the paper, corresponding to the mirror (dashed), proton cyclotron (dash-dot), parallel firehose (solid), and oblique firehose (dotted) instability thresholds. This is a joint histogram with logarithmically spaced boxes. The data is taken from years 2005 to 2008 as measured by the Wind 3DP electrostatic analyzer and the Wind MFI.	145
5.11 For the year 2007, the horizontal axis reads day:hour:minute:second. The top panel plots the temperature anisotropy ratio for the two instruments. The interval is nearly 2 days. The second panel from the top indicates when a beam is present by a green line, and the red line can be ignored. The next two panels plot the instability thresholds from Hellinger et al. [2006] where if $-1 + T_{\perp}/T_{\parallel}$ is larger in magnitude than the instabilities (see label), the plasma is unstable to the assumed growth rate.	146
5.12 The joint probability density of the ratio of perpendicular pressures and 3DP density. See global caption for more details.	147
5.13 The joint probability density of the ratio of parallel pressures and 3DP density. See global caption for more details.	147
5.14 The joint probability density of the ratio of pressure anisotropy ratio and 3DP density. The dataset spans all the available data for SWE in 2007 and the nearest time stamp for 3DP. The dashed magenta line is for when the two data products are equal.	147
5.15 The joint probability density of the perpendicular pressures. See global caption for more details.	149
5.16 The joint probability density of the parallel pressures. See global caption for more details.	149
5.17 The joint probability density of the total pressure. The dataset spans all the available data for SWE in 2007 and the nearest time stamp for 3DP. The dotted lines are linear regressions, where the Pearson coefficient and slope are plotted annotated on the figures. 149	
5.18 The FLR ratio (defined as Eq. 5.46) is plotted in blue as a histogram normalized to be the percent of the total data. This dataset here is for year 2007. The open boxes are a cumulative sum. There is %86 of data below 0.3.	152
5.19 The wavenumbers computed via Taylor's hypothesis. The top panel is the probability function for an arbitrary bin number. The bottom panel is three near-to-equal conditioned probability density bins. The red lines are cutoffs, where the probability becomes less than 10^{-3}	153

5.20	The joint probability function of the wavenumber and proton beta. The contours in black are constant values of the joint probability density. The annotated numbers are from the linear regression, seen as the dashed line.	155
5.21	The cross-correlations and amplitudes defined in Section 5.1.2 mapped to a common color bar, that is conditioned on the proton beta. The wavenumber bin is $k_{\text{SW}} = 0.288 \times 10^{-5} \text{ km}^{-1}$. The thin black lines are the 10^{-2} contour. The magenta lines are the beta conditioned mean (dashed), median (solid), and maximum (dotted).	156
5.22	The cross-correlations and amplitudes defined in Section 5.1.2 mapped to a common color bar, that is conditioned on the proton beta. The wavenumber bin is $k_{\text{SW}} = 1.41 \times 10^{-5} \text{ km}^{-1}$. The thin black lines are the 10^{-2} contour. The magenta lines are the beta conditioned mean (dashed), median (solid), and maximum (dotted).	157
5.23	The cross-correlations and amplitudes defined in Section 5.1.2 mapped to a common color bar, that is conditioned on the proton beta. The wavenumber bin is $k_{\text{SW}} = 6.34 \times 10^{-5} \text{ km}^{-1}$. The thin black lines are the 10^{-2} contour. The magenta lines are the beta conditioned mean (dashed), median (solid), and maximum (dotted).	158
5.24	The “Numerical model” and the “Observations” are combined in the blue parallelogram by spanning a large parameter space in $\theta_{\hat{\mathbf{b}}, \hat{\mathbf{k}}}, \lambda_{\text{mfp}}^{\text{eff}}$ and fitting the numerical solution to the observations. This is the data analysis technique implemented in the thesis to make the primary measurements of the thesis.	159
5.25	This figure is for C_{\perp} , $k_{\text{SW}} = 1.41 \times 10^{-5} \text{ km}^{-1}$. The numerical solutions colored by the normalized weight, mapped to the color bar. The black line is the observed beta conditioned median.	160
5.26	The normalized weights, where the weight is calculated from Eq. 5.51. The labelled curves are from Eqs. 5.52. The bin number was chosen arbitrarily.	161
5.27	The integrated weights for C_{\perp} . The quantity of the color bar is defined as Eq. 5.58. The magenta diamonds are the weighted means from Eq. 5.54 and the magenta bars indicate the two sigma confidence interval from Eq. 5.56.	162
5.28	The integrated weights for C_{\parallel} . The quantity of the color bar is defined as Eq. 5.58. The magenta diamonds are the weighted means from Eq. 5.54 and the magenta bars indicate the two sigma confidence interval from Eq. 5.56.	163

5.29	The integrated weights for A_{\perp} . The quantity of the color bar is defined as Eq. 5.58. The magenta diamonds are the weighted means from Eq. 5.54 and the magneta bars indicate the two sigma confidence interval from Eq. 5.56.	164
5.30	The integrated weights for A_{\parallel} . The quantity of the color bar is defined as Eq. 5.58. The magenta diamonds are the weighted means from Eq. 5.54 and the magneta bars indicate the two sigma confidence interval from Eq. 5.56.	165
5.31	This figure is for A_{\perp} , $k_{\text{SW}} = 1.41 \times 10^{-5} \text{ km}^{-1}$. The numerical solutions colored by the normalized weight, mapped to the color bar. The black line is the observed beta conditioned median.	166
5.32	The statistics: weighted geometric mean μ_x (Eq. 5.54), covariance $\hat{\sigma}_{x,y}^2 = \sigma_{x,y}^2 / (\hat{\sigma}_{x,x} \hat{\sigma}_{y,y}^2)$ (Eq. 5.55), and the two sigma confidence interval CI_x (Eq. 5.56) are calculated for the the amplitude ratios and cross-correlations.	167
5.33	The four panels show the β -conditioned mean of cross-correlations and amplitudes for the three median wavenumber bins $k_{\text{SW}} = [0.288, 1.41, 6.34] \times 10^{-5} \text{ km}^{-1}$ as solid (black, blue, magenta) lines respectively. The dashed lines are the numerical solutions corresponding to the maximum \mathcal{W} ; the parameters of the maximum are reported in the panels.	169
6.1	The dispersion relation for the parallel proton cyclotron instability for time 0 Ω_p^{-1} . The top panel is the real part of the complex frequency and bottom panel is the imaginary part. The parameters of the system are annotated on the top panel, in simulation units.	174
6.2	The initial parallel proton beta is 0.5, the initial temperatures are seen in the top panel, they are in simulation units. The bottom panel shows three quantities labelled in the legend, that are all normalized to the value at time = 0 Ω_p^{-1}	175
6.3	The top panel plots the Hermite functions from Eqs. 6.10 and the bottom panel plots the Laguerre functions from Eqs. 6.15. The horizontal axis x is the normalized velocity. The colors correspond to the legend, notice that red is $m = 10$	180

6.4	The top panel shows the distribution function produced by the simulation in parallel velocity coordinates as a dashed orange line and the inverse transform method in blue. The bottom panel is the central difference derivative of the distribution function and the blue line is the derivative produced from the recursion relations.	182
6.5	The 1-dimensional spectral coefficients (Eq. 6.24) are computed for simulation distribution function for multiple times, labelled in the legend. The order of the Hermite polynomial is on the horizontal axis.	183
6.6	The pitch-angle gradient for time $t = 20\Omega_p^{-1}$ for a resonants wave frequency calculated with two methods. In the top panel is the Hermite-Laguerre method described in the text. The bottom panel is 2D central differences scheme. The color bars are the pitch-angle gradients. There is a slight difference in the range of the two color bars.	184
6.7	Various quantities plotted for $t = 15\Omega_p^{-1}$, plotted as a function of the parallel wavenumber times the proton inertial length. The horizontal axis is symmetrical logarithm, so that at $\pm 10^{-1}$ the scale becomes linear to pass from < 0 to > 0 . The colors of the lines correspond to the legend at the very top, which is the order of the resonance, n , where only pink and blue lines contribute to the bottom panels, denoting -1, 1, respectively.	185
6.8	The top panel are the heating rates which are labelled in the legend. The bottom two panels are the VPIC simulation temperatures and the Hermite-Laguerre method (HL) (see Eq. 6.26) temperatures. The time unit is in inverse proton cyclotron frequency.	187
6.9	The rates calculated in a few different ways. The dotted line is defined as Eq. 6.27 and the magenta line is defined as Eq. 6.28. The blue and red lines are discussed in Section 6.5. The horizontal axis is the time in units of inverse proton cyclotron frequency.	188
6.10	This is a repeat of Fig. 6.7, plotted for $t = 40\Omega_p^{-1}$. The third panel down shows the magnetic field power spectrum, where the windowed power spectrum is the dashed orange line.	190
6.11	This is a repeat of Fig. 6.8 for the windowed power spectrum.	191
6.12	This is a repeat of Fig. 6.11 compared with the bi-Maxwellian (Bi-M) time evolution.	192

- 6.13 This is a repeat of Fig. 6.11 for varying maximum Hermite-Laguerre polynomial order, which is indicated in the legend. The horizontal axis has been shifted so the variation in time-evolution of the temperatures can be seen. 193
- 6.14 The Hermite-Laguerre coefficients, defined in Section 6.4.1 for times $0 \Omega_p^{-1}$ (top left), $15 \Omega_p^{-1}$ (top right), $30 \Omega_p^{-1}$ (bottom left), and $45 \Omega_p^{-1}$ (bottom right). The vertical axes are the Laguerre indices, where the tick label is below the box. The horizontal axes are the Hermite indices, where the tick label is to the left of the box. The color bar is normalized to the c_{00} box, which is nearly constant throughout the time evolution. 194
- 7.1 A schematic of the anisotropy of compressive and Alfvénic fluctuations in the inertial range, up to the kinetic ranges. The vertical axis is the logarithm of the perpendicular wavenumber and the horizontal axis is the parallel wavenumber. The coloured lines are labelled, corresponding to contours of maximum power in wavenumber space. The colour then corresponds to the kinetic waves associated with the inertial range (fluid) waves. The black lines are indicated where the wavenumber becomes comparable to important length scales. Notice that the $k_{\parallel} \lambda_{\text{mfp}}^{\text{eff}} \sim k_{\perp} \rho_p$ for the compressive and Alfvénic fluctuations. 200

List of Tables

4.1	List of input parameters to solve the system of Eq. 4.23.	109
5.1	The combined statistics: weighted geometric mean μ_x (Eq. 5.54), covariance $\hat{\sigma}_{x,y}^2$ (Eq. 5.55), and the two sigma confidence interval CI_x (Eq. 5.56).	168

Chapter 1

Introduction

Plasma is the name given to high temperature ionized gas. Nearly all luminous matter in the Universe is in the plasma state. The essential description is to separate the short and long -range electromagnetic fields to determine the particle's statistical properties. The long-range field determines collective properties and therefore involves many particles interacting simultaneously. The short range behaviour is then the classic collision, involving only a few particles, at a very short range. Many plasmas do not experience enough collisions for their statistical properties to be described by the equilibrium distribution function, and therefore much of plasma physics requires consideration of non-equilibrium situations.

1.1 The need for a kinetic theory of plasma

The need for a kinetic theory of plasmas was pointed out by [Vlasov \[1968\]](#), motivated by earlier studies of waves and vibrations in charged gases. His insight led him to develop the Vlasov equation, where a 1-particle distribution function (a probability function in 3 spatial dimensions and 3 momentum dimensions for a single particle) interacts with the collective electromagnetic fields, coupled to Maxwell's equations. These equations support longitudinal and transverse waves, those discovered experimentally by [Tonks and Langmuir \[1929\]](#), and so the kinetic theory of plasma was born. In particular, Anatoly Vlasov was able to derive the dispersion relation for the Langmuir wave, which for length scales larger than the Debye length (to be discussed shortly), an electron-proton plasma vibrates naturally at the plasma frequency,

$$\omega_{p,e} = \sqrt{\frac{4\pi n q_e^2}{m_e}}, \quad (1.1)$$

where the electron density is n , the elementary charge is $-q_e$, and the electron mass is m_e .

The physical process separating short and long range forces was first described in Debye and Hückel [1923]. The basic consideration is to recognise that the electrostatic potential of a charged particle will be altered by the presence of nearby particles, shielding its influence, so that the electrostatic potential is,

$$\phi(r) = \frac{q_s}{r} \exp\{-r/\lambda_D\} \quad (1.2)$$

where q_s is the species “s” charge, r is the radial distance (in a spherical geometry) from the point where q_s is located, and the exponential term is the modification of the surrounding particles which is parameterised by the Debye length,

$$\lambda_D = \sqrt{\frac{k_B T}{4\pi n q_e^2}} \quad (1.3)$$

where k_B is Boltzmann’s constant. This is the Debye length for a proton-electron plasma, equal in temperature and density, where the former equality is not necessary and the final is the quasi-neutral assumption invoked throughout this Thesis. It is related to the plasma frequency by the thermal speed $v_e = \sqrt{2}\lambda_D\omega_{p,e}$. The length scale can be produced from considering an electrostatic plasma at equilibrium. This length scale dictates the sphere of influence of a particle, defining the short and long -range action of charged particles.

When the Debye sphere $4\pi\lambda_D^3/3$ contains many particles, they are governed by the collective field, and when it does not contain many particles, the individual particles will interact with each other i.e., they collide. This defines the plasma parameter,

$$g = \frac{1}{n\lambda_D^3} \propto \frac{n^{1/2}}{T^{3/2}} \quad (1.4)$$

as the inverse number of particles in the Debye sphere. It is the appropriate expansion parameter used to derive the kinetic equation for a plasma, shown in Chapter 2. It essentially governs the influence of collisions, as it is proportional to the collision frequency, as shown in Section 2.2. This point is not to be confused; g governs how many particles need to be considered, is it a two, three -body problem? The collision frequency can be large, only incorporating two-body collisions.

Figure 1.1 contains a table reproduced from the textbook Krall and Trivelpiece [1973] displaying these characteristic quantities of well-studied plasmas. The number of particles in the Debye sphere is in general large, validating the

Table 6.4.1 APPROXIMATE MAGNITUDES FOR SOME TYPICAL HYDROGEN PLASMAS*

Plasma	Number density n_0 , cm $^{-3}$	Tempera- ture T , °K	Plasma frequency $\left(\frac{4\pi n_0 e^2}{m}\right)^{1/2}$, s $^{-1}$	Debye length $L_D = \left(\frac{kT}{8\pi n_0 e^2}\right)^{1/2}$, cm	Particles in a Debye sphere $n_0 L_D^3$	$\ln \Lambda$	Deflection time for electrons τ_D	Deflection time for protons τ_D
Interstellar gas	1	10^4	6×10^4	5×10^2	10^8	22	3×10^2	3×10^5
Gaseous nebula	10^3	10^4	2×10^6	15	3×10^6	20	3	3×10^2
Solar corona	10^6	10^6	6×10^7	5	10^8	22	3	3×10^2
Solar wind	10	10^5	2×10^5	5×10^2	10^9	25	10^6	10^8
Solar atmosphere	10^{12}	10^4	6×10^{10}	5×10^{-4}	10^2	9	10^{-8}	10^{-6}
Gas discharge	10^{14}	10^4	6×10^{11}	5×10^{-5}	12	7	10^{-10}	10^{-8}
Hot plasma	10^{14}	10^5	6×10^{11}	1.5×10^{-4}	3×10^2	9	2×10^{-9}	2×10^{-7}
		10^6	6×10^{11}	5×10^{-4}	10^4	13	5×10^{-8}	5×10^{-6}
Diffuse hot plasma	10^{12}	10^6	6×10^{10}	5×10^{-3}	10^3	15	5×10^{-6}	5×10^{-4}
Dense hot plasma	10^{16}	10^6	6×10^{12}	5×10^{-5}	10^3	11	6×10^{-10}	6×10^{-8}
Thermonuclear plasma	10^{16}	10^8	6×10^{12}	5×10^{-4}	10^6	18	4×10^{-7}	4×10^{-5}

* The numbers are chosen only to illustrate orders of magnitude, and the nomenclature is somewhat arbitrary.
 SOURCE: Table 6.4.1 is from D. C. Montgomery and D. A. Tidman, "Plasma Kinetic Theory," p. 31, McGraw-Hill, New York, 1964.

Figure 1.1: Page 306 of Krall and Trivelpiece [1973]. The timescales are in seconds.

kinetic approach, and the collision frequency between ions and electrons ν_{ei} is smaller than the plasma frequency ω_{pe} implying that collisions are not a dominate process, or that the mean-free-path of electron-ion collisions $\lambda_{\text{mfp}}^{ie} = v_e / \nu_{ei}$ is very long compared with other length scales.

The definition and difference of the kinetic and fluid descriptions will now be made clear. When the collisions frequency is small relative to the other plasma frequencies or the mean-free-path is long relative to other plasma length scales, the plasma distribution function (e.g., the 1-particle distribution function) evolves via electromagnetic field. This is the kinetic regime when the full distribution function needs to be described. Some examples, in the linear and quasi-linear phases, are the wave-particle resonance where free energy is swapped between the two populations, and particle trapping of ions (electrons) in the wells (crests) of the electric potential. These processes and all kinetic processes are marked by the departure of the distribution function from the equilibrium. Throughout the thesis the kinetic regime will also be called the collisionless regime.

The fluid picture evolves moments of the distribution function via the electromagnetic field and is valid when frequencies (e.g. wave frequency) are small relative to the collision frequency and the length scales are large relative to the mean-free-path. Examples include sound waves that propagate in an elastic manner through undulations of magnetic and thermal pressure, or Alfvén waves that propagate freely due to the tension of the magnetic field. The processes are marked by no departure from the equilibrium distribution function because collisions restore the system to equilibrium faster than these processes operate. There is no damping or growth through resonance nor velocity dependent effects.

One of the immediate issues with fluid theory is how to close the equations,

and for the purpose of this thesis, the fluid picture can be confined to when the system is closed with an assumption about the pressure (e.g., adiabatic or isothermal equation of states). Any extensions (e.g. heat flux) are considered an attempt to incorporate kinetic effects into the fluid description. A classic discussion of this appears at the end of Section 3.3.2 of Krall and Trivelpiece [1973] and also see Section 8.18 of Krall and Trivelpiece [1973] for an extended and consistent discussion.

A more modern interpretation can be found in Schekochihin et al. [2016] where the moments are considered as a series, governed by dynamic equations, which are dictated by collisionless and collisional processes. This thesis explores the plausibility of collisionless processes truncating the moment chain i.e., collisionless processes act to restore the plasma distribution function to equilibrium so the fluid description is valid.

1.2 Motivation for thesis

The wide separation in scales, e.g., the ratio of time scales in Fig. 1.1, is why plasmas are called multi-scale systems. Focussing on the solar wind, Fig. 1.2 demonstrates plasma time and length scales as a function of radial distance from the Sun.

The additional length scales here are the inertial length $d_s = \omega_{ps}/c$ where the speed of light is c , the gyroradius $\rho_s = v_s/\Omega_s$ where the cyclotron frequency is $\Omega_s = q_s B/m_s c$. The electron inertial length is the characteristic length of exponential decay of a light wave propagating at a frequency less than the plasma frequency. The proton inertial length governs the scale at which protons and electrons will decouple from each other. The gyroradius, is the radius at which the particle gyrates around the static magnetic field. The bottom panel plots timescales defined as $\Pi_\alpha = 2\pi/\alpha$, where ν_c here is the proton-proton collision frequency. The definition $\tau = 1\text{AU}/U_{pr}$ is the expansion time.

The middle panel shows the proton-proton mean-free-path in blue (note that the vertical axis is on the right hand side of the middle panel) where it can be seen how much larger it is than the other scales. The bottom panel shows the same idea, but represented as the time scales. This is the basic argument for a collisionless description of the solar wind.

Focussing on the scale dependence of this argument, working in frequency space, when $\omega \ll \nu_{\text{coll}}$, where ω is a temporal frequency of a plasma fluctuations (e.g., the density) and ν_{coll} is the largest collision frequency of the system, the plasma will be near to equilibrium. This regime of the plasma $\omega \ll \nu_{\text{coll}}$ is the true fluid regime. The opposite case $\omega \gg \nu_{\text{coll}}$ is the collisionless regime.

Most plasmas display brilliant multi-scale dynamics, where the frequency

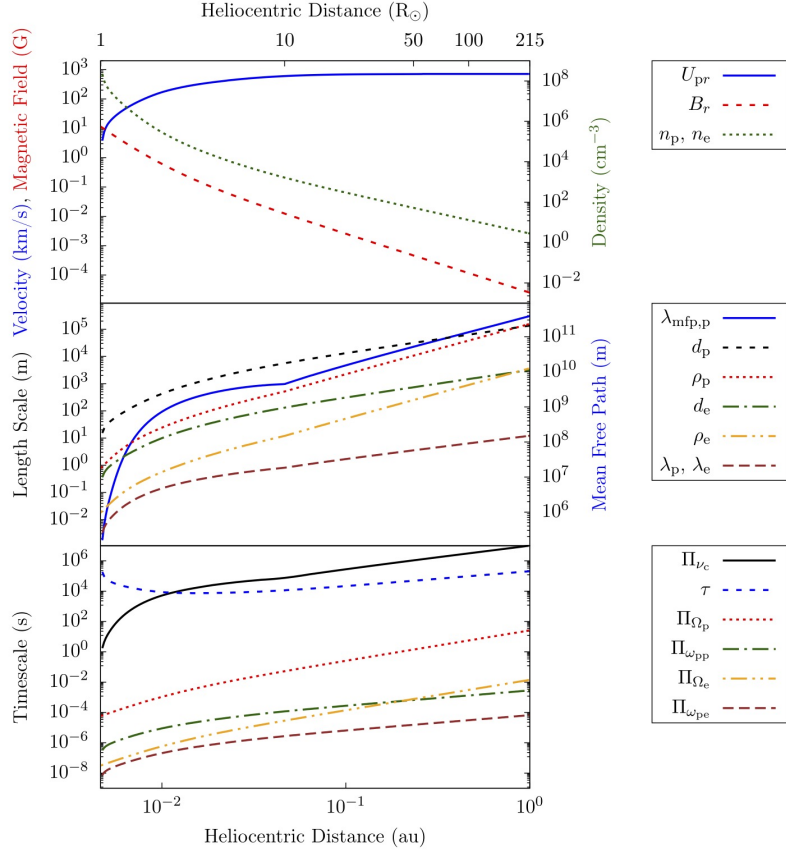


Figure 1.2: Radial evolution of the solar wind, reproduced from Verscharen et al. [2019]. The horizontal axes are radial distances from the Sun, in units of solar radius (top) and Earth-Sun distance (bottom). The density n_p , n_e and radial magnetic field B_r are empirical models, the proton velocity U_{pr} , is obtained from flux conservation, $n_p U_{pr} / B_r = \text{const}$. The electron and proton temperatures, not shown, connect in situ and remote measurements. The quantities are defined in the text here.

range of fluctuations in plasma properties (e.g., the magnetic field) overrun the range between the collision frequency and electron gyroscale where there is a transition scale where ($\omega \simeq \nu_{\text{coll}}$) which separates the fluid and collisionless regime regimes. This is the true separation in scale between the fluid and collisionless regimes.

What are these timescales for the solar wind? At 1 AU, the proton-proton collision frequency is approximately 4×10^{-7} Hz, measured in Section 5.3.3. To convert this to the spacecraft frame frequency Taylor's assumption is used, where the temporal dynamics are neglected when the medium is being advected relatively quicker (covered in Section 5.3.4). This leads to $f_{\nu_{\text{coll}}} = U_{pr} \nu_{\text{coll}} / 2\pi v_p = 8 \times 10^{-7}$ Hz. This frequency is orders of magnitude smaller than all other time

scales, including the inverse magnetic field correlation time [Bruno and Carbone, 2013], implying all the magnetic field fluctuations are governed by collisionless plasma equations.

For decades, fluid equations, in particular the magnetohydrodynamic equations, have been successfully used to study solar wind behaviour [Bruno and Carbone, 2013]. The power spectral density shape can be predicted from fluid equations [Tu and Marsch, 1995, Matthaeus and Goldstein, 1982, Goldreich and Sridhar, 1995], transport of magnetic fluctuations (e.g. radial transport) [Zank et al., 1996], and heating by the energy cascade [Stawarz et al., 2009]. This is due in part to the presence of Alfvén waves, or Alfvénic fluctuations, that do not perturb the distribution function at scales larger than the proton gyroradius [Schekochihin et al., 2009]. Linearly, the Alfvén wave is incompressible until the frequency of the wave becomes comparable to the proton gyrofrequency when the wave gains a compressive component, where it is identified to be the kinetic Alfvén wave. To not be ignorant to the complexity of the situation, when the small-amplitude assumption is abandoned (the solar wind is turbulent), the Alfvénic fluctuation gains a compressive component [Barnes and Hollweg, 1974]. Therefore, the total fluctuation would perturb the distribution function, except for in the perpendicular limit of the wavenumber (often called reduced) [Schekochihin et al., 2009]. Fortunately, this complication can be set aside since there is a non-negligible fraction of compressive fluctuations in the solar wind, which provide exemplary evidence of fluid behaviour.

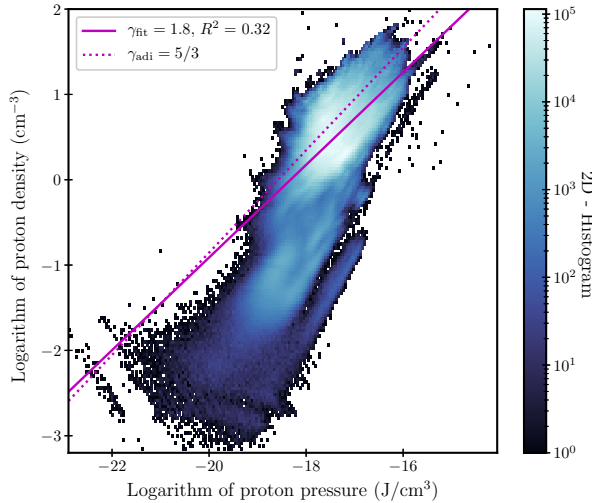


Figure 1.3: The joint histogram of proton pressure and density measured by the electrostatic analyser on the Wind spacecraft at 1 AU. The dataset is described in Section 5.3. The γ follows from assuming $\log|p_p| = \gamma \log|n_p|$, and a linear regression is performed. R^2 is the Pearson correlation coefficient.

Spacecrafts make *in situ* measurements of the proton (and other species) pressure and density making it possible to study aspects of compressive plasma waves. Figure 1.3 displays the joint histogram of the solar wind proton pressure and density measured by the Wind spacecraft measured over 11 years spanning 2005 - 2015. While the Pearson correlation coefficient (see the legend) is not excellent, the correlation between the density and pressure is clear. This correlation indicates the equation of state invoked is a fluid closure of the moment chain as described at the end of Section 1.1. Considering the relation of the pressure and density to be given by the polytropic equation of state, where γ is the ratio of specific heats, is nearly adiabatic. This is remarkable, given the long mean-free-path and magnetised properties of the solar wind.

This Thesis studies the compressive fluctuations to better understand the equation of state of the solar wind. In fact, this has a long history in fluids. Before the development of thermodynamics, Isaac Newton pointed out that the speed of sound in air should depend on the square root of the elastic force directly and on the square root of the density inversely [Newton, 1687]. Isaac Newton also measured the speed of sound and found a disagreement between the experimental and theoretical values. Many developments occurred in the years after, attracting attention from many scientists, including Leonhard Euler, Daniel Bernoulli, Joseph-Louis Lagrange, and eventually Pierre-Simon Laplace who pointed to the correct thermodynamic characterisation: adiabatic process Finn [1964].

What could be maintaining the fluid behaviour of the solar wind? Collisionless plasmas react to perturbations secularly in the linear phase, and then in the non-linear phases, begin to resist and settle. These processes are generally called collisionless relaxation processes. They include instabilities where the electromagnetic wave interacts with particles altering their pitch-angle, effectively diffusing particles in velocity space. Micro-scale instabilities are of the most well studied and beautiful properties of plasmas. Another way this can happen is the plasma wave echo, which is a non-linear process in plasmas that inhibits free energy from moving to finer scales in velocity space [Meyrand et al., 2019]. All of these processes inhibit fine-scale structure from forming in the velocity distribution function. In a weakly collisional and turbulent plasma, these processes happen at much faster rates than particle collisions.

Fundamentally, these processes cause the plasma to behave more fluid-like since the higher-order moments are not activated (e.g., heat flux) so that a closure can be made and then the fluid equations can be used. Physically, the mean-free-path of the particles is shortened to what is called the *effective* mean-free-path. The analogy from wave-particle interactions works quite well, that the pitch-angle is scattered, interrupting the free streaming of the particles.

This thesis describes the measurement of the effective mean-free-path of the protons at 1 AU. The method is to model collisionless relaxation processes on to kinetic equation then generate compressive fluctuations (e.g., the density and pressure). These fluctuations are parameterised by the effective mean-free-path; physically, for a short mean-free-path they respond like an adiabatic equation of state, and for a long-mean-free path, the equation of state requires higher-order moments. These predictions are compared with solar wind observations to measure the effective mean-free-path. The measurement justifies the long use of fluid theory to describe the solar wind and demonstrates that effective collision processes can drastically alter the transport and thermodynamics of weakly collisional plasmas.

Chapter 2

Plasma physics

The Introduction (Chapter 1) presents examples of ionized gases in the Universe and made the basic justifications of the mathematical theory of plasmas. Examples of the characteristic quantities of plasmas appear in Fig. 1.1 which provides important time and length scales. The second column of the table in Fig. 1.1 displays the diverse range of number density, starting with less dense plasmas which have been detected remotely (e.g., Gaseous nebula), and some that are detected directly (e.g., the solar wind). Further down the column, increasing number density, to human made plasmas such as thermonuclear plasmas. The increase in number density is accompanied by an increase in the temperature (third column of the table on Fig. 1.1) as the plasma parameter (see Eq. 1.4) must be small, which is the inverse of the “particles in a Debye sphere” which appears as column six of the table.

Further complexity is provided by the yet to be mentioned magnetic field, as the strength, relative to the thermal pressure further dictates many plasma properties. For example, in the solar wind the thermal and magnetic pressure are nearly equal on average, and in the interstellar medium and galactic clusters (higher temperature and smaller number density than the interstellar medium [[Schekochihin and Cowley, 2006](#)]), have very weak magnetic fields relative to the thermal pressure.

In this Chapter, the plasma description is formulated rigorously to present the full N-particle description and follow the classic route to Boltzmann’s equation for a plasma which are coupled to Maxwell’s equations. These equations are then considered in more detail: waves, instabilities, and closures of the equations. Finally, a short section on fluid turbulence where the theory of compressible turbulence is reviewed.

2.1 Statistical theory of plasmas

The kinetic gas description is formally derived from the N-particle density function. The procedure relates the ensemble average of the N-particle density function to the reduced N-particle probability function. This procedure introduces the statistical nature of the description and a closure problem that needs to be truncated. The final set of equations are the Boltzmann-Maxwell equations. Almost all plasma models are derived from these equations.

2.1.1 N-particle density function

These sections closely follow Section 7 of Krall and Trivelpiece [1973] and Dellar [2015]. The N-particle system is fully described by the function,

$$\mathcal{N}(t, x_i, v_i) = \sum_{\alpha=1}^N \delta[x_i - x_i^\alpha(t)] \delta[v_i - v_i^\alpha(t)], \quad (2.1)$$

where α identifies the particle, giving the type (e.g., protons), t is the time coordinate, x_i is canonical spatial vector, and v_i is the canonical velocity vector (we are dealing with non-relativistic particles). Index notation is used where they are kept in the lower position since the indices do not become overly complicated. On the right hand side the sum is over each particle indicated with α up to N particles. Equation 2.1 is the N-particle density, so that each particles spatial location x_i^α and velocity v_i^α can be identified by the delta function, such the number of particles as a function of time is given by,

$$\int d^3x \int d^3v \mathcal{N}(t, x_i, v_i) = N(t). \quad (2.2)$$

These coordinates evolve in time by the equations of motion,

$$\frac{d}{dt} x_i^\alpha = v_i^\alpha, \quad \frac{d}{dt} v_i^\alpha = \frac{q_\alpha}{m_\alpha} \left(E_i^{N'} + \frac{1}{c} \epsilon_{ijk} v_j^\alpha b_k^{N'} \right), \quad (2.3)$$

where q_α is the charge, m_α is the mass, and c is the speed of light. The electric and magnetic fields $E_i^{N'}$, $b_k^{N'}$, respectively, are given by all of the particles except for itself, denoted by N' . They are the self-consistent electric and magnetic fields due to all the particles. To anticipate later assumptions, these fields contain short and long range contributions. The fields are further described by

Maxwell's equations,

$$\frac{\partial}{\partial x_i} E_i^N = 4\pi \int d^3v q'_\alpha \mathcal{N}, \quad (2.4)$$

$$\epsilon_{ijk} \frac{\partial}{\partial x_j} b_k^N = \frac{1}{c} \frac{\partial}{\partial t} E_i^N + \frac{4\pi}{c} \int d^3v q'_\alpha v_i \mathcal{N}, \quad (2.5)$$

$$\epsilon_{ijk} \frac{\partial}{\partial x_j} E_i^N = -\frac{1}{c} \frac{\partial}{\partial t} b_i^N, \quad (2.6)$$

$$\frac{\partial}{\partial x_i} b_i^N = 0. \quad (2.7)$$

Each particle contributes to the fields, where $E_i^N = E_i^N(t, x_i^\alpha)$, $b_i^N = b_i^N(t, x_i^\alpha)$. The use of q'_α indicates the charge of the particles in \mathcal{N} . This anticipates the fact that eventually the particles are assumed to be indistinguishable, so the charge and mass are chosen. This notation massively simplifies the mathematical details. Using chain rule and properties of the Dirac delta functions, the conservation equation can be written,

$$\left[\frac{\partial}{\partial t} + v_i \frac{\partial}{\partial x_i} + a_i \frac{\partial}{\partial v_i} \right] \mathcal{N} = 0, \quad (2.8)$$

known as the Klimontovich-Dupree equation. Notably, the variables are of x_i not x_i^α . The acceleration is defined,

$$a_i = \frac{q'_\alpha}{m'_\alpha} \left(E_i^N + \frac{1}{c} \epsilon_{ijk} v_j b_k^N \right) \quad (2.9)$$

All of the particles with coordinates $(x_i^1, v_i^1), \dots, (x_i^N, v_i^N)$ are in x_i, v_i space where the motions are given by Eq. 2.3 which couples to Eqs. 2.4. This picture is clarified with Fig. 2.1, where the left most panel represents \mathcal{N} .

2.1.1.1 N-particle distribution function

The Klimontovich-Dupree equation (Eq. 2.8), while exact, is difficult to extract information from because each particle depends on the others deterministically, and not statistically. A more complicated function is introduced, but it is more simple to reduce for a statistical theory. Start by introducing the phase-space variable,

$$\mathcal{V}_i^\alpha = (x_i^\alpha, v_i^\alpha), \quad d^3\mathcal{V}^\alpha = d^3x^\alpha d^3v^\alpha. \quad (2.10)$$

The N-particle probability distribution function is defined as,

$$\mathcal{F}(t, \mathcal{V}_i^1, \dots, \mathcal{V}_i^N) = \Pi_\alpha^N g(\mathcal{V}_i^\alpha - \mathcal{V}_i^\alpha(t)), \quad (2.11)$$

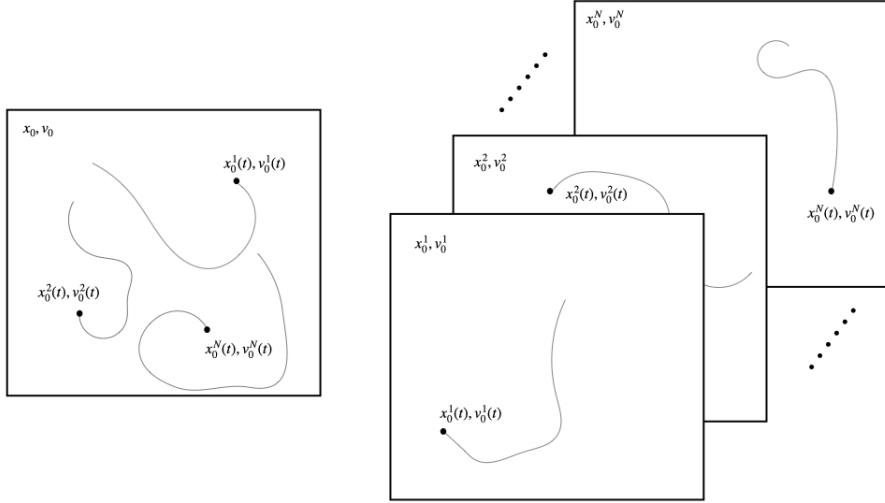


Figure 2.1: Recreated from Dellar [2015]. The left panel represents three particles in \mathcal{N} for one component of space x_0 and velocity v_0 . Each space, denoted by a closed square, is annotated in the top left corner. The dots with tails are their location in phase space at time t . The right panel shows N spaces, where each particle evolves in time in its own space. The left single panel is a cartoon of Eq. 2.1 and the right panels represent Eq. 2.11.

where Π_α is the product operator. Here, $g(\mathcal{V}_i^\alpha - \mathcal{V}_i^\alpha(t))$ is a probability distribution in \mathcal{V}_i^α . This is clarified by Fig. 2.1, where it is seen that each particle lives in its own space and is endowed with a probability function.

It should be understood that each particle α has a charge and mass identified by α . This function $\mathcal{F}(t', \mathcal{V}_i^1, \dots, \mathcal{V}_i^N)$ is interpreted as the probability that the phase coordinates of the particles at t' given by $\mathcal{V}_i^1(t'), \dots, \mathcal{V}_i^N(t')$ are in $d\mathcal{V}_i^1, \dots, d\mathcal{V}_i^N$. Integration leads to the normalization,

$$\int \Pi_\alpha^N d^3\mathcal{V}^\alpha \mathcal{F}(t, \mathcal{V}_i^1, \dots, \mathcal{V}_i^N) = 1. \quad (2.12)$$

The probability distribution function also satisfies,

$$\frac{\partial}{\partial t} \mathcal{F} + \sum_{\alpha} \left[\frac{dx_i^\alpha}{dt} \frac{\partial}{\partial x_i^\alpha} + \frac{dv_i^\alpha}{dt} \frac{\partial}{\partial v_i^\alpha} \right] \mathcal{F} = 0, \quad (2.13)$$

which is the Liouville theorem: conservation of probability. Averages are then

defined as,

$$\langle \mathcal{G}(t, \mathcal{V}_i^1, \dots) \rangle_N = \int \Pi_\alpha^N d^3\mathcal{V}^\alpha \mathcal{F}(t, \mathcal{V}_i^1, \dots, \mathcal{V}_i^N) \mathcal{G}(t, \mathcal{V}_i^1, \dots) \quad (2.14)$$

where \mathcal{G} is often something simple, like the proton peculiar velocity v_i^p . The subscript of the average “N” is to indicate the N-particle average. The n -particle probability distribution functions follow from Eq. 2.11,

$$f_n(t, \mathcal{V}_i^1, \dots, \mathcal{V}_i^n) = \frac{N!}{(N-n)!} \int d^3\mathcal{V}_i^{n+1}, \dots, d^3\mathcal{V}_i^N \mathcal{F}(t, \mathcal{V}_i^1, \dots, \mathcal{V}_i^N), \quad (2.15)$$

where if $n = 1$ the dependence of $f(\dots)$ is just on t, \mathcal{V}_i^1 and the integral is just $d\mathcal{V}_i^2 \dots d\mathcal{V}_i^N$. The factor $N!/(N-n)!$ out front stems from the fact that the particles are indistinguishable. There are N ways \mathcal{F} can be integrated that give f_1 , and $N(N-1)$ ways that give f_2 , and so on.

The connection between the density function \mathcal{N} , defined as Eq. 2.1, and the n -particle probability distribution function (f_n) is seen by taking the N-particle average of the density function,

$$\langle \mathcal{N}(t, x_i, v_i) \rangle_N = \int \Pi_\alpha^N d^3\mathcal{V}^\alpha \mathcal{F}(t, \mathcal{V}_i^1, \dots, \mathcal{V}_i^N) \mathcal{N}(t, x_i, v_i). \quad (2.16)$$

It simplifies easily since the sum in \mathcal{N} gives a factor of N out front if the particles are indistinguishable,

$$\langle \mathcal{N}(t, x_i, v_i) \rangle_N = N \int \Pi_\alpha^N d^3\mathcal{V}^\alpha \mathcal{F}(t, \mathcal{V}_i^1, \dots, \mathcal{V}_i^N) \delta(\mathcal{V}_i - \mathcal{V}_i^1(t)), \quad (2.17)$$

so the integral $d^3\mathcal{V}^1$ yields,

$$\langle \mathcal{N}(t, x_i, v_i) \rangle_N = N \int d^3\mathcal{V}^2, \dots, d^3\mathcal{V}^N \mathcal{F}(t, \mathcal{V}_i, \dots, \mathcal{V}_i^N), \quad (2.18)$$

where the right hand side is now the 1-particle probability distribution function of \mathcal{V}_i ,

$$\langle \mathcal{N}(t, x_i, v_i) \rangle_N = f_1(t, \mathcal{V}_i). \quad (2.19)$$

This makes clear the statistical approach of $f_1(t, \mathcal{V}_i)$ due to the $\langle \dots \rangle_N$. Now a time-evolution equation can be written by taking the N -average of the Klimontovich-

Dupree equation, defined as Eq. 2.8

$$\begin{aligned} & \left\langle \left[\frac{\partial}{\partial t} + v_i \frac{\partial}{\partial x_i} + a_i \frac{\partial}{\partial v_i} \right] \mathcal{N} \right\rangle_N \\ &= \frac{\partial}{\partial t} f_1(t, \mathcal{V}_i) + v_i \frac{\partial}{\partial x_i} f_1(t, \mathcal{V}_i) + \left\langle a_i \frac{\partial}{\partial v_i} \mathcal{N} \right\rangle_N. \end{aligned} \quad (2.20)$$

The average is over x_i^1, v_i^1 not x_i, v_i , so the first two terms are simple. The final term presents almost all of the difficulty of plasma physics because the equation of motion, defined as Eq. 2.3, depends on all of the other particles,

$$a_i = \frac{q'_\alpha}{m'_\alpha} \left(E_i^N + \frac{1}{c} \epsilon_{ijk} v_j b_k^N \right), \quad (2.21)$$

since E_i^N, b_i^N depend on all the particles, seen in Eq. 2.4. Now, average Maxwell's Equations from Eqs. 2.4,

$$\frac{\partial}{\partial x_i} E_i = 4\pi \sum_s q_s \int d^3v f_s(t, \mathcal{V}_i), \quad (2.22)$$

$$\epsilon_{ijk} \frac{\partial}{\partial x_j} b_k = \frac{1}{c} \frac{\partial}{\partial t} E_i + \frac{4\pi}{c} \sum_s q_s \int d^3v v_i f_s(t, \mathcal{V}_i), \quad (2.23)$$

$$\epsilon_{ijk} \frac{\partial}{\partial x_j} E_i = -\frac{1}{c} \frac{\partial}{\partial t} b_i, \quad (2.24)$$

$$\frac{\partial}{\partial x_i} b_i = 0. \quad (2.25)$$

where,

$$\langle E_i^N \rangle_N = E_i, \langle b_i^N \rangle_N = b_i. \quad (2.26)$$

The exact fields E_i^N, b_i^N are determined by all the particles, and averaged fields E_i, b_i are determined by the 1-particle probability distribution function. The new notation of subscript s

$$f_1(t, \mathcal{V}_i) \rightarrow f_s(t, \mathcal{V}_i) \quad (2.27)$$

makes the notation consistent and massively simplified the notation of the derivation. Averaging the acceleration,

$$\langle a_i \rangle_N = \frac{q_s}{m_s} \left(E_i + \frac{1}{c} \epsilon_{ijk} v_j b_k \right). \quad (2.28)$$

Returning to Eq. 2.20 and manipulating the equation,

$$\begin{aligned} \frac{\partial}{\partial t} f_s(t, \mathcal{V}_i) + v_i \frac{\partial}{\partial x_i} f_s(t, \mathcal{V}_i) + \frac{q_s}{m_s} \left(E_i + \frac{1}{c} \epsilon_{ijk} v_j b_k \right) \frac{\partial}{\partial v_i} f_s(t, \mathcal{V}_i) \\ = - \left\langle \frac{q_\alpha}{m_\alpha} \left(E_i^N + \frac{1}{c} \epsilon_{ijk} v_j b_k^N \right) \frac{\partial}{\partial v_i} \mathcal{N} \right\rangle_N \\ + \frac{q_s}{m_s} \left(E_i + \frac{1}{c} \epsilon_{ijk} v_j b_k \right) \frac{\partial}{\partial v_i} f_s(t, \mathcal{V}_i). \end{aligned} \quad (2.29)$$

The left hand side is the time-evolution of the 1-particle species s probability distribution function via the N -particle average fields, which couple to Maxwell's equations. The right hand side contains all of the particle-particle physics with the contribution of the 1-particle probability distribution function, evolved by the N -particle average field, subtracted off.

2.1.2 Bogolyubov, Born and Green, Kirkwood, and Yvon Hierarchy

The Bogolyubov, Born and Green, Kirkwood, and Yvon (BBGKY) hierarchy is the closure to Eq. 2.29. The idea will only be sketched in this section. Solutions for the fields due to each particle from Eqs. 2.4 will look like,

$$E_i^N \propto 4\pi\ell \int d^3v q'_\alpha \mathcal{N}, \quad (2.30)$$

$$b_i^N \propto 4\pi c\tau \int d^3v q'_\alpha \mathcal{N}, \quad (2.31)$$

both proportional to \mathcal{N} , where ℓ, τ are arbitrary length and timescales to keep the units correct. Returning to Eq. 2.29 the right hand side has two significant terms, the first with the above arguments will be proportional to,

$$-\left\langle \frac{q_\alpha}{m_\alpha} \left(E_i^N + \frac{1}{c} \epsilon_{ijk} v_j b_k^N \right) \frac{\partial}{\partial v_i} \mathcal{N} \right\rangle_N \propto \left\langle \mathcal{N} \mathcal{N} \right\rangle_N. \quad (2.32)$$

The second term on the right hand side from Eq. 2.29,

$$\frac{q_s}{m_s} \left(E_i + \frac{1}{c} \epsilon_{ijk} v_j b_k \right) \frac{\partial}{\partial v_i} f_s(t, \mathcal{V}_i) \propto \left\langle \mathcal{N} \right\rangle_N \left\langle \mathcal{N} \right\rangle_N. \quad (2.33)$$

Both of these terms can be related to products of f_1 and terms proportional to f_2 , which are the 1-particle and 2-particle probability distribution functions (see Eq. 2.15), respectively. Regarding collisions, f_2 is the joint probability that two particles are in respective phase-space locations at a given time.

A time evolution equation for the 2-particle probability distribution function

(f_2) must be introduced to close these equations. That leads to an equation for the 3-particle probability distribution function, which persists as an infinite chain, developing into a classic closure problem. The BBGKY hierarchy is this infinite chain, and the closure procedure is to introduce a small parameter,

$$g = \frac{1}{n\lambda_D^3} \ll 1, \quad (2.34)$$

the plasma parameter which was introduced as Eq. 1.4. Recalling the Debye length,

$$\lambda_D = \sqrt{\frac{k_B T}{4\pi n q_e^2}} \quad (2.35)$$

where the temperature T is the total temperature and n is the plasma density. The expansion is then made as,

$$f_n \propto \mathcal{O}\{g^{n-1}\}. \quad (2.36)$$

The typical closure is to order out $n + 1$ terms and close the equations for the n terms.

The plasma parameter is the inverse number of particles in the Debye sphere. When there are many particles in the Debye sphere, the 1-particle distribution function (f_1) interaction with the average fields (E_i, b_i) is more significant than the interaction of any two particles, communicated by f_2 . The intuition is a bit easier to understand when considering the reverse situation. When there are only a few particles in the Debye sphere, individual two-particle interactions will dominate the dynamics. Figure 1.1 has been provided to give some examples of observed plasmas, where the 5th column is the number of particles in the Debye sphere. This leads naturally to the definition of collisions in plasma physics: short-range interaction of two or more particles.

2.1.3 Boltzmann's Equation and Maxwell's Equations

With the BBGKY hierarchy established the Boltzmann Equation can be written from Eq. 2.29 as,

$$\begin{aligned} \frac{\partial}{\partial t} f_s(t, x_i, v_i) + v_i \frac{\partial}{\partial x_i} f_s(t, x_i, v_i) + \frac{q_s}{m_s} \left(E_i + \frac{1}{c} \epsilon_{ijk} v_j b_k \right) \frac{\partial}{\partial v_i} f_s(t, x_i, v_i) \\ = \mathcal{C}[f_s(t, x_i, v_i), f_{s'}(t, x_i, v_i)], \end{aligned} \quad (2.37)$$

The right hand side has been rewritten with $\mathcal{C}[\dots]$ representing the collision operator truncated at order 1. The electric and magnetic fields are averaged

over all the particles $\langle \dots \rangle_N$ and couple to Maxwell's Eqs.,

$$\frac{\partial}{\partial x_i} E_i = 4\pi \sum_s q_s \int dv_i f_s(t, x_i, v_i), \quad (2.38)$$

$$\epsilon_{ijk} \frac{\partial}{\partial x_j} b_k = \frac{1}{c} \frac{\partial}{\partial t} E_i + \frac{4\pi}{c} \sum_s q_s \int dv_i v_i f_s(t, x_i, v_i), \quad (2.39)$$

$$\epsilon_{ijk} \frac{\partial}{\partial x_j} E_i = -\frac{1}{c} \frac{\partial}{\partial t} b_i, \quad (2.40)$$

$$\frac{\partial}{\partial x_i} b_i = 0. \quad (2.41)$$

Employing a closure technique for the collision operator, these equations are a self-consistent description of a non-relativistic plasma.

2.2 Collisions and transport theory

A collision operator is derived in this section and some properties of collision operators and timescales are shown. The classic Spitzer-Härm problem is described and the solution is sketched followed by a discussion of Braginskii's contribution to collisional transport theory. Last, the Bhatnagar-Gross-Krook operator is introduced.

2.2.1 Fokker-Planck

Instead of working with the right hand side of Eq. 2.29, the more common Fokker-Planck collision operator is used, which can be derived from the Chapman-Kolmogorov equation. Considering a probabilistic evolution of the distribution function,

$$f_s(t + \Delta t, x_i, v_i) = \int d^3 \Delta v P_{\Delta t}(\Delta v_i, v_i - \Delta v_i) f(t, x_i, v_i - \Delta v_i), \quad (2.42)$$

where $P_{\Delta t}$ gives the probability density at v_i and $t + \Delta t$ was previously $\Delta v_i - v_i$ at t . This is the Kolmogorov-Chapman Equation for the case of spatial homogeneity. Rewriting the time derivative,

$$f_s(t, x_i, v_i) + \Delta t \frac{\partial}{\partial t} f(t, x_i, v_i) = \int d^3 \Delta v P_{\Delta t}(\Delta v_i, v_i - \Delta v_i) f(t, x_i, v_i - \Delta v_i), \quad (2.43)$$

and now assuming that Δv_i is small (i.e., $\Delta v_i \ll$ thermal velocity) expanding to second order,

$$\begin{aligned} f_s(t, x_i, v_i) + \Delta t \frac{\partial}{\partial t} f_s(t, x_i, v_i) \\ = \int d^3 \Delta v \left[P_{\Delta t}(\Delta v_i, v_i) f_s(t, x_i, v_i) \right. \\ - \Delta v_i \frac{\partial}{\partial v_i} P_{\Delta t}(\Delta v_i, v_i) f_s(t, x_i, v_i) \\ \left. + \Delta v_i \Delta v_j \frac{\partial}{\partial v_i} \frac{\partial}{\partial v_j} P_{\Delta t}(\Delta v_i, v_i) f_s(t, x_i, v_i) + \dots \right], \quad (2.44) \end{aligned}$$

The first terms on the left and right hand sides cancel since the probability integrates $P_{\Delta t}$ to unity, and now write this in the classic Fokker-Planck form,

$$\frac{\partial}{\partial t} \Big|_{\text{coll}} f_s(t, x_i, v_i) = \left[- \frac{\partial}{\partial v_i} A_i + \frac{\partial}{\partial v_i} \frac{\partial}{\partial v_j} D_{ij} \right] f_s(t, x_i, v_i), \quad (2.45)$$

$$A_i = \left\langle \frac{\Delta v_i}{\Delta t} \right\rangle_P, \quad (2.46)$$

$$D_{ij} = \frac{1}{2} \left\langle \frac{\Delta v_i}{\Delta t} \frac{\Delta v_j}{\Delta t} \right\rangle_P. \quad (2.47)$$

where $\langle \dots \rangle_P$ is the weighted integral over $d^3 \Delta v$. Rewriting the time derivative requires the contribution from higher-order derivatives to be small, putting a constraint on Δt . The expansion in Δv_i is inherent in the use of the $P_{\Delta t}(\Delta v_i, v_i)$, i.e., large jumps in Δv_i are less probable, so it is easy to justify.

The coefficients A_i , D_{ij} are drag and diffusion, respectively. Both are in velocity space, so drag effects the particle momentum and diffusion effects the particle energy or macroscopic thermal temperature.

2.2.1.1 Coulomb Collisions

To determine the drag and diffusion tensors from Eq. 2.45 the Δv_i are found from considering the deflection of one particle colliding with another via the classic scattering cross section technique of Rutherford.

The technique is outlined as follows, replace the average $\langle \dots \rangle_P$ with an integral over the number of scatters, which can be rewritten by introducing the cross section. It is the product of the density of particles (probability distribution function integrated over the velocity), infinitesimal cross-section, and distance the relative velocity travels in Δt . Then Δv_i needs to be calculated from the geometry of the scatter. The procedure follows until a divergent integral arises,

where the Coulomb logarithm is introduced,

$$\ln |\Lambda| = \ln \left(\frac{3}{2} \frac{T^{3/2}}{\sqrt{\pi n} Z_a Z_b q_p^2} \right), \quad (2.48)$$

where T is the total plasma temperature, n is the plasma density, and Z_s is the unit species charge number. The Coulomb logarithm assumes the potential around a particle is the average field (from Eq. 2.4) i.e., the plasma approach. It turns out, that the value of Λ is the number of particles in the Debye sphere, so it is large. Figure 1.1 shows some values of the Coulomb logarithm.

The deflection in velocity calculated from the kinematic equations are averaged over the particle distribution function to provide the coefficients A_i , D_{ij} of the Fokker-Planck Eq. 2.45. Various times scales can be calculated from Eq. 2.45 by considering a beam of test particles e.g., a Dirac delta function, interacting with a distribution of ions and electrons. For example,

$$\tau_D = \left(\int d^3v v_i^2 F_{\text{test}} \right) \left(\frac{\partial}{\partial t} \Big|_{\text{coll}} \int d^3v v_i^2 F_{\text{test}} \right)^{-1} \quad (2.49)$$

where F_{test} is the test distribution function, and time derivative is that of the equation 2.45. This is the time it takes for a beam of test particles to diffuse towards isotropy by collisions. Clearly the choice of test particle species, energy, and plasma constituents (e.g., bi-Maxwellian proton) deserve a full treatment, but the last two columns of the table in Fig. 1.1 provide these timescales for suprathermal particles scattering off a Maxwellian plasma. For low density plasma, these times scales are very long.

The final form of the collision operator from Eq. 2.37, won't be written here since it is not used in the thesis, and is usually simplified. However, the properties will be written here,

$$\text{Conservation of Particles: } \int d^3v \int d^3x \mathcal{C}[f_s(t, x_i, v_i)] = 0, \quad (2.50)$$

$$\text{Conservation of Momentum: } \int d^3v m_s v_i \mathcal{C}[f_s(t, x_i, v_i)] = 0, \quad (2.51)$$

$$\text{Conservation of Energy: } \int d^3v \frac{m_s}{2} v_i^2 \mathcal{C}[f_s(t, x_i, v_i)] = 0, \quad (2.52)$$

$$\text{H-Theorem: } - \frac{d}{dt} \Big|_{\text{coll}} \int d^3v f_s(t, x_i, v_i) \ln |f_s(t, x_i, v_i)| \geq 0. \quad (2.53)$$

The integrand in the final line here is the entropy. Collisions are the sole mechanism behind entropy production. The equal sign in this equation is the result for Maxwell's distribution function.

These conservation properties give some reassurance to the use of $P_{\Delta t}$ to de-

scribe a collisional process, and is a necessary step to produce the final property here. Two particles are uncorrelated before they interact, perfectly correlated after the interaction, and then become uncorrelated after a few interactions with other particles. This time asymmetry due to the stochastic nature of collisions was pointed out by Ludwig Boltzmann and is called the “Stossahlansatz”. The correlation function is asymmetric in time, therefore giving the system an irreversible property. When passing from Klimontovich-Dupree equation to the probabilistic description here, the irreversible nature is introduced.

2.2.1.2 Spitzer-Härm

The next task is to use the collision operator to compute transport coefficients. In literature this is called the *Spitzer-Härm problem*, which is to compute the conductivity σ and thermal conductivity α ,

$$j_i = \sigma E_i + \alpha \frac{\partial}{\partial x_i} T_e \quad (2.54)$$

where j_i is the current, from the kinetic equation via the Chapman-Enskog expansion [Spitzer and Härm, 1953]. In this relation many terms have been dropped. Returning to the Boltzmann equation for electrons,

$$\frac{\partial}{\partial t} f_e + v_i \frac{\partial}{\partial x_i} f_e + \frac{q_e}{m_e} \left(E_i + \frac{1}{c} \epsilon_{ijk} v_j b_k \right) \frac{\partial}{\partial v_i} f_e = \mathcal{C}[f_e], \quad (2.55)$$

where the implicit dependence has been dropped. It is then reduced to

$$\frac{q_e}{m_e} E_i \frac{\partial}{\partial v_i} f_e = \mathcal{C}[f_e], \quad (2.56)$$

where the temporal term is ignored due to transport phenomena being longer than collisional time scale, the spatial term is ignored due to previous spatial homogeneity of collisions, and finally consider the unmagnetised case. Continuing, to compute the electric field from the above equation the electron distribution function must be known. This is difficult so the Chapman-Enskog expansion is considered,

$$f_e = f_e^{(0)} + \chi f_e^{(1)} + \chi^2 f_e^{(2)} + \dots \quad (2.57)$$

where $\chi = \omega_{p,e}/\nu_e$. The expansion comes from normalizing the electric field $|\bar{E}_i| = m_e v_e \omega_{p,e}/q_e$ and taking the right hand side of Eq. 2.56 to be proportional

to $\propto \nu_e f_e$. Then matching order 0 and 1 gives,

$$\mathcal{C}[f_e^{(0)}] = 0 \quad (2.58)$$

$$\mathcal{C}[f_e^{(1)}] = \frac{q_e}{m_e} E_i \frac{\partial}{\partial v_i} f_e^{(0)}, \quad (2.59)$$

The first equation is the result for a Maxwellian plasma. The second equation is the problem at hand, and for demonstration purposes, the idea is to invert the collision operator,

$$f_e^{(1)} = \mathcal{C}^{-1} \left[\frac{q_e}{m_e} E_i \frac{\partial}{\partial v_i} f_e^{(0)} \right]. \quad (2.60)$$

The calculation is in general very difficult due to complexity of the collision operator. The important part of the procedure is to introduce an expansion of the first order distribution function in the Legendre polynomials. With a solution for f_e^1 and for protons, the current and temperature can be solved for, and the conductivities from Eq. 2.54 are computed. Spitzer and Härm found,

$$\sigma^{\text{SH}} = \frac{32}{3\pi} \frac{q_e^2 n_e}{m_e \nu_{ei}}, \quad \alpha^{\text{SH}} = \frac{16}{\pi} \frac{q_e n_e}{m_e \nu_{ei}}, \quad (2.61)$$

where the ion-electron collision frequency ν_{ei} is the dominant frequency in the collision operator [Spitzer and Härm \[1953\]](#). At this point, it is often pointed out that the parametric dependence can be found from a fluid theory (i.e., the momentum equation), and the transport theory provides the coefficients, which are not trivial and can be significant. This limitation stems from necessity of the Maxwellian as the 0th order distribution function and an expansion in $\omega_{pe}/\nu_e \ll 1$.

2.2.2 Braginskii's work and classical transport theory

The general procedure of expanding the distribution function and relating higher-orders back through the expansion to calculate transport coefficients became known as classical transport theory. A massive contribution to the theory was made by [Braginskii \[1957\]](#). His theory incorporates ions and electrons, collisions between them, and magnetization of the plasma. The final piece is done by transforming into the gyro-center frame and ordering out the non-gyrotropic terms with expansion in $\rho_s/L \ll 1$ where ρ_s is the gyroradius of species “s” and L is the length scale of variation, say of the temperature $T_e/|\partial T_e/\partial x_i|$. A subsidiary expansion is done in $\rho_s/\lambda_{\text{mfp}}^s$, so that particles gyrate quicker than the collision frequency. This has strong implications on the dynamics, most notably the constants in Eqs. 2.61, which become tensors oriented with respect to the

magnetic field. Particles can stream along the magnetic field easier than across the field, due to the Lorentz force, so that perpendicular coefficients are smaller.

For the purpose of this thesis, which explores the weakly collisional regime of plasmas, the methods of classical transport are insufficient to bridge the entire gap between the collisional and collisionless regimes. The low-order moment nature is built directly into the expansion, so collisionless effects can not be incorporated. This is shown with numerical methods in Section 4.5.1.

2.2.3 Bhatnagar-Gross-Krook operator

The Bhatnagar-Gross-Krook (BGK) operator was introduced as a mathematical simplification for the full Boltzmann collision operator (cf., Gross and Krook [1956] and Bhatnagar et al. [1954]). The line of thinking for the BGK operator is to construct an operator that maintains absorption and emission of “particles” so as to also conserve total particle number, momentum and energy [Bhatnagar et al., 1954]. Following Gross and Krook [1956], the Boltzmann collision operator is replaced with,

$$\left(\frac{\partial f_s}{\partial t} \right)_{\text{coll}} = \sum_{s'} \nu_{s,s'} (F_{s,s'}(v_i, n_s, T_s) - f_s). \quad (2.62)$$

The term containing the distribution function f_s is the absorption term and $F_{s,s'}$ is the emission term. Meaning, when there is a deficit in the difference $F_{s,s'} - f_s < 0$ over some $d\mathbf{v}$ there is absorption at a rate of $\nu_{s,s'}$. The opposite case for emission follows the same idea. The interpretation can also be phrased as $\nu_{s,s'}$ playing the role of a relaxation of f_s to $F_{s,s'}$.

This thesis uses the BGK operator to model any processes that restore equilibrium (see Sec. 2.6). The final point is that due to dependence on the density and temperature of the equilibrium distribution function $F_{s,s'}(v_i, n_s, T_s)$, the use of the BGK operator is similar to the local thermodynamic equilibrium approach.

2.3 Kinetic magnetohydrodynamics

The kinetic magnetohydrodynamic (KMHD) equations were derived to incorporate micro-scale effects into the stability analysis of plasmas [Rosenbluth and Rostoker, 1959, Kruskal and Oberman, 1958, Kulsrud, 1983]. The equations are appropriate to a non-relativistic, gyrotropic, and collisionless plasma. The equations permit a variety of closure schemes which have been explored in exhaustive detail in both Hunana et al. [2019b] and Snyder et al. [1997] so that small amplitude perturbations can be calculated. The microscopic effects that

are most necessary to incorporate are Landau damping [Landau, 1965] and Barnes damping [Barnes, 1966] or transit-time damping.

There are two approaches to derive the linear kinetic equations. The first is to transform into the guiding center frame of the Vlasov equation and take the gyro-radius to be small [Kulsrud, 1983]. The second is to perturb the full system of Vlasov-Maxwell equations and take the gyrotropic limit. The compatibility of these two approaches was pointed out by Hunana et al. [2019b] where the negligence of the gyrotropic terms is made more clear. The approach of Kulsrud [1983] is used to derive the drift kinetic equation in Appendix B but with some necessary detail to the assumptions imposed on the equations.

The important modification is to add the BGK collisional operator (see Section 2.2.3). The equilibrium distribution function will be taken to be the Maxwellian distribution $F_s = F_{s,M}$, defined as,

$$F_{s,M} = n_s \left(\frac{m_s}{2\pi k_B T_s} \right)^{3/2} \exp \left\{ - \frac{m_s}{2k_B T_s} (v - u_{\parallel}^s)^2 \right\}, \quad (2.63)$$

where n_s is the number density, m_s is the mass, k_B is Boltzmann's constant, T_s is the temperature, v is the magnitude of the peculiar velocity and u_{\parallel}^s is the parallel bulk velocity. It should be clear that $\mathcal{C}[f_s; n_s, u_{\parallel}^s, T_s]$ (the BGK operator) depends on the coordinates t, x_i, v_i through $f_s = f_s(t, x_i, v_i)$ and $F_{s,M} = F_{s,M}(v_i; n_s, u_{\parallel}^s, T_s)$ where $n_s = n_s(t, x_i)$ etc. From here on the Maxwellian $F_{s,M}$ is the BGK equilibrium choice.

Writing the kinetic equation,

$$\frac{\partial}{\partial t} f_s + v_i \frac{\partial}{\partial x_i} f_s + \frac{q_s}{m_s} \left(E_i + \frac{1}{c} \epsilon_{ijk} v_j b_k \right) \frac{\partial}{\partial v_i} f_s = -\nu_s (f_s - F_s), \quad (2.64)$$

where q_s is the charge, m_s is the mass, E_i is the electric field, b_i is the magnetic field. The ordering can be done in the $\varepsilon = m_s/q_s$ ratio, where f_s, E_i, b_i all follow the ordering,

$$\chi = \varepsilon^0 \chi^0 + \varepsilon^1 \chi^1 + \dots \quad (2.65)$$

so to lowest order (ε^0),

$$\left(E_i^0 + \frac{1}{c} \epsilon_{ijk} v_j b_k^0 \right) \frac{\partial}{\partial v_i} f_s^0 = 0. \quad (2.66)$$

Regarding collisions, the assumption is that the effective collision frequency is larger than the gyrofrequency which takes the form $\nu_s \sim \varepsilon^0$ for the expansion. In reality, it is not, and this is an open avenue for incorporating parallel electric fields into the system. Transforming to the guiding center $w_i = v_i - u_i^s$ where

the guiding center is $u_i^s(x_i, t) = u_i^s = (c/|b_l|^2)\epsilon_{ijk}E_j b_k$ gives,

$$\begin{aligned} & \left(E_i^0 + \frac{1}{c}\epsilon_{ijk}v_j b_k^0 \right) \frac{\partial}{\partial v_i} f_s^0 \\ & \rightarrow \left[E_i^0 + \frac{1}{c}\epsilon_{ijk}w_j b_k^0 + \frac{b_k^0}{|b_l|^2}(E_k^0 b_i^0 - E_i^0 b_k^0) \right] \frac{\partial}{\partial w_i} f_s^0, \end{aligned} \quad (2.67)$$

using $\epsilon_{ikj}\epsilon_{klm} = \delta_{im}\delta_{jl} - \delta_{il}\delta_{jm}$ and now notice that the magnetic field geometry,

$$E_{\parallel} = \hat{b}_i E_i, \quad (E_{\perp})_i = E_i - E_{\parallel} \hat{b}_i \quad (2.68)$$

where $\hat{b}_i = b_i/|b_l|$, shows that,

$$\frac{b_k^0}{|b_l|^2}(E_k^0 b_i^0 - E_i^0 b_k^0) = -E_i^0 + E_{\parallel}^0 \hat{b}_i^0. \quad (2.69)$$

This permits,

$$\begin{aligned} & \left[E_i^0 + \frac{1}{c}\epsilon_{ijk}w_j b_k^0 + \frac{b_k^0}{|b_l|^2}(E_k^0 b_i^0 - E_i^0 b_k^0) \right] \frac{\partial}{\partial w_i} f_s^0 \\ & = \left(E_{\parallel}^0 \hat{b}_i^0 + \frac{1}{c}\epsilon_{ijk}w_j b_k^0 \right) \frac{\partial}{\partial w_i} f_s^0 = 0. \end{aligned} \quad (2.70)$$

Now putting both the remaining cross product and velocity gradient into cylindrical coordinates,

$$w_i = \begin{pmatrix} w_{\perp} \cos(w_{\phi}) \\ w_{\perp} \sin(w_{\phi}) \\ w_{\parallel} \end{pmatrix}, \quad \frac{\partial}{\partial w_i} = \begin{pmatrix} \cos(w_{\phi}) \frac{\partial}{\partial w_{\perp}} - \frac{\sin(w_{\phi})}{w_{\perp}} \frac{\partial}{\partial w_{\phi}} \\ \sin(w_{\phi}) \frac{\partial}{\partial w_{\perp}} + \frac{\cos(w_{\phi})}{w_{\perp}} \frac{\partial}{\partial w_{\phi}} \\ \frac{\partial}{\partial w_{\parallel}} \end{pmatrix} \quad (2.71)$$

where the perpendicular velocity component is $w_{\perp} = |w_i - w_{\parallel} \hat{b}_i|$, the parallel component is $w_{\parallel} = \hat{b}_i w_i$ and the azimuthal component $w_{\phi} = \arctan(w_y/w_x)$. The result,

$$\left(E_{\parallel}^0 \frac{\partial}{\partial w_{\parallel}} + \frac{|b_l|}{c} \frac{\partial}{\partial w_{\phi}} \right) f_s^0 = 0. \quad (2.72)$$

Now, with the argument of Kulsrud [1983], the solution for f_s^0 is a helix extending from negative to positive infinity in velocity space, and therefore unphysical, so that $E_{\parallel}^0 = 0$ gives a gyrotropic (independent of w_{ϕ}) solution to f_s^0 . The next

order (ε^1) of Eq. 2.64, before the transformations,

$$\begin{aligned} \frac{\partial}{\partial t} f_s^0 + v_i \frac{\partial}{\partial x_i} f_s^0 + \frac{q_s}{m_s} \left(E_i^0 + \frac{1}{c} \epsilon_{ijk} v_j b_k^0 \right) \frac{\partial}{\partial v_i} f_s^1 \\ + \frac{q_s}{m_s} \left(E_i^1 + \frac{1}{c} \epsilon_{ijk} v_j b_k^1 \right) \frac{\partial}{\partial v_i} f_s^0 = -\nu_s (f_s^0 - F_s^0), \end{aligned} \quad (2.73)$$

now transform to cylindrical coordinates (see Eqs. 2.71) and the guiding center (see Eq. 2.67),

$$\begin{aligned} \frac{\partial}{\partial t} f_s^0 + v_i \frac{\partial}{\partial x_i} f_s^0 + \frac{q_s}{m_s} \left(E_i^0 + \frac{1}{c} \epsilon_{ijk} v_j b_k^0 \right) \frac{\partial}{\partial v_i} f_s^1 \\ + \frac{q_s}{m_s} \left(E_i^1 + \frac{1}{c} \epsilon_{ijk} v_j b_k^1 \right) \frac{\partial}{\partial v_i} f_s^0 = -\nu_s (f_s^0 - F_{s,M}^0), \end{aligned} \quad (2.74)$$

$$\begin{aligned} \rightarrow \left(\frac{\partial}{\partial t} f_s^0 + v_i \frac{\partial}{\partial x_i} f_s^0 \right)_{\text{reg}} + \frac{q_s}{m_s} \frac{|b_l|}{c} \frac{\partial}{\partial w_\phi} f_s^1 \\ + \frac{q_s}{m_s} \left(E_{\parallel}^1 \frac{\partial}{\partial w_\parallel} + \frac{1}{c} \epsilon_{ijk} w_j b_k^1 \frac{\partial}{\partial w_i} \right) f_s^0 = -\nu_s (f_s^0 - F_s^0), \end{aligned} \quad (2.75)$$

where the $E_{\parallel}^0 = 0$ was used and the subscript ‘‘reg’’ contains terms where the transformation hasn’t been completed for brevity. This procedure is lengthy and carried out in Appendix B.1. Rearranging for the order f_s^1 ,

$$\begin{aligned} \frac{q_s}{m_s} \frac{|b_l|}{c} \frac{\partial}{\partial v_\phi} f_s^1 = -\nu_s (f_s^0 - F_{s,M}^0) - \left(\frac{\partial}{\partial t} f_s^0 + v_i \frac{\partial}{\partial x_i} f_s^0 \right)_{\text{cyl}} \\ + \frac{q_s}{m_s} \left(E_{\parallel}^1 \frac{\partial}{\partial w_\parallel} + \frac{1}{c} \epsilon_{ijk} w_j b_k^1 \frac{\partial}{\partial w_i} \right) f_s^0. \end{aligned} \quad (2.76)$$

Integrating over v_ϕ provides a solution for f_s^1 . Following Kulsrud [1983], he suggests setting 2.76 to zero and solving the right hand side. This is equivalent to ignoring all first order non-gyrotropic effects [Hunana et al., 2019b]. The resulting equation is known as the drift kinetic equation, a point that will be made clear soon. This equation is used by many authors (e.g., [Snyder et al., 1997]) to derive the Landau fluid models. A few points need to be made about the drift kinetic equation, but can be seen from Eq. 2.76:

1. The ordering in m_s/q_s follows the same for $\rho_s \ll 1$ where $\rho_s = m_s v_\perp c / q_s |b_l|$ is the gyroradius Rosenbluth and Rostoker [1959]. This normalization was not chosen here but can be seen in Eq. 2.76 if v_i is normalized.
2. The moment closure of the linear equation happens at 2nd order (for the pressure) Rosenbluth and Rostoker [1959]. This does not mean there are no perturbations of higher order moments (e.g., heat flux). This is the primary reason the drift equation is studied.

3. It has been shown by Kruskal and Oberman [1958] that collisions, while denying the constants of motion, do not destroy stability, i.e., it is sensible to consider an equilibrium problem.
4. Here, the collision operator has been reduced to the difference with a static Maxwellian which is not desirable since it is likely a more formal operator.
5. Any perturbation following from Eq. 2.76 will be subsidiary.

The last two points motivated the approach that appears in Appendix B.1. The approach follows,

1. Change to the gyro-center frame.
2. Integrate over the gyro-angle assuming the entire distribution function is gyrotropic.
3. Perturb about a static background where the background parallel electric field is zero with Kulsrud's condition (Eq. 2.72).

This allows the use of the Maxwellian (Eq. 2.63) as the BGK equilibrium and there will be no subsidiary issue in perturbing the kinetic equation. This gives the same kinetic equation employed by Snyder et al. [1997], Kulsrud [1983] with the BGK operator in its non-perturbed form, where the assumption that $\nu_s \gg \Omega_s (= q_s |b_i| / m_s c)$ still holds.

Regarding the use of the BGK operator with a kinetic equation, Snyder et al. [1997] perturbs the Maxwellian, defined in Eq. 2.63, to approximately recover the Braginskii transport coefficients and Sharma et al. [2003] does as well to recover adiabatic pressure equations in the collisional limit. Additionally, the equations recover the collisionless (gyrotropic) regime which the Braginskii and Landau Fluid equations do not.

Now return to equations of motion to demonstrate physical aspects of the equations. Following Section 4.2 of Hunana et al. [2019b] the equations of motion are,

$$\mu = \frac{m_s w_\perp^2}{2|b_i|}, \quad \Rightarrow \quad \frac{d}{dt} \left(\frac{w_\perp^2}{|b_i|} \right) = 0, \quad \Rightarrow \quad \frac{dw_\perp}{dt} = \frac{w_\perp}{2|b_i|} \frac{d|b_i|}{dt}, \quad (2.77)$$

and the parallel equation of motion,

$$m_s \frac{dw_\parallel}{dt} = -m_s \frac{du_i^s}{dt} + q_s E_\parallel - \mu \hat{b}_i \frac{\partial}{\partial x_i} |b_j|, \quad (2.78)$$

where the definition,

$$\frac{d}{dt} = \frac{\partial}{\partial t} + (w_\parallel \hat{b}_i + u_i^s) \frac{\partial}{\partial x_i}, \quad (2.79)$$

meaning the Lagrange derivative in the guiding-center frame. The perpendicular equation of motion (Eq. 2.77) acts to conserve the magnetic moment μ in the guiding-centre frame.

The parallel equation of motion (Eq. 2.78) contains the important kinetic aspects which should be retained in the model. The first term on the right hand side is the non-inertial forces due to transforming into the gyro-center frame. The second term is the force responsible for Landau damping [Landau, 1967] which is the interaction of the parallel electric field with particles streaming with similar parallel phase velocity (cf., Jackson [1960] for a physical explanation). The second term is the magnetic mirror force which is responsible for transit-time damping. Stix [1992] introduces various aspects of transit-time damping in Section 11-4, where the same mechanism described by Jackson [1960] applies, which is made clear in Section 11-8, clarifying the fact that Landau damping and transit-time damping are 0th order resonant interactions. These two effects are why compressive waves are severely damped in collisionless proton-electron plasmas [Barnes, 1966].

The work of Barnes [1966] is of direct interest to this thesis. The key insight of this thesis was to add the BGK operator to equations similar to that of Barnes [1966] to model equilibrium restoring effects. The role of the BGK operator is to restore the perturbations back to equilibrium. The KMHD-BGK equation is explored numerically in Chapter 4.

2.4 Closures

In this section a brief overview of closures is provided to give a comparison of the various plasma models discussed in previous sections. In a general sense, taking moments of Boltzmann's Equation (seen in Section 2.1.3) produces a chain, where the density is coupled to the velocity, velocity to the pressure etc. In the collisionless case, the moment chain is infinite, as high-order deformations (high-order moments) of the distribution function will be present. Truncating this chain is the closure.

2.4.1 Fluid theory

Physically, collisions truncate this chain, since collisions push the distribution function towards the Maxwellian distribution function, which has no high-order moments (e.g., the heat flux is zero). At equilibrium, the closure is provided by the equation of state. In the non-equilibrium or collisionless case, the equation of state derives from truncation and closure of the moment equations. The fluid description is built upon taking moments of the kinetic equations which will

couple to higher and lower moments.

The density couples to Gauss' Law (first of Eqs. 2.38) and the velocity couples to Ampere's Law (second of Eqs. 2.38). These two couplings also couple different species together. This is treated in the next section (Section 2.4.2).

The chain of moments is effectively truncated by collisions. This formal approach is that of Spitzer-Härm, to allow higher-order moments to effect the lower moments through transport coefficients, which was introduced in Section 2.2. This introduces viscosity and thermal diffusion. More complicated closures can be incorporated, going to higher moments in the chain, giving more transport coefficients, provided that higher moments are smaller than previous moments.

2.4.2 Ohm's Law

Ohm's Law is introduced to simplify the coupling of the momentum equation to the electric and magnetic field. The electric field is often thrown out with the single-fluid assumption by adding the momentum equations for different species and then using the quasi-neutral assumption. The magnetic term couples to Maxwell's equations and then back to the electric field, where Ohm's law is traditionally implemented to simplify the equations with valid approximations.

The entire derivation of Ohm's law is provided in Appendix D. In Section D.2.2 the momentum equations for the electrons and protons are combined to write an equation for the current. This does require single-fluid approximations which appear in Section D.2. In Section D.2.3 the time-evolution equation for the current is written subject to the single-fluid approximations. Next, Ampere's law and Faraday's law are combined to write a time evolution equation for the current to simplify. Next, the equation is normalized according to Section D.2.3.1 so that further simplifications can be made. Equation D.106 is rewritten here,

$$\begin{aligned} & -\frac{1}{\mu m_p} \left[\left(\frac{\Omega_p}{\omega_{p,p}} \right)^2 \frac{\partial^2}{\partial t^2} E_j - \frac{\partial}{\partial x_l} \frac{\partial}{\partial x_l} E_j \right] + \frac{1}{\mu m_p} \frac{\partial}{\partial x_i} \left(u_j j_i + j_j u_i - j_j j_i \right) \\ & = \frac{1}{\mu m_p} \frac{\partial}{\partial x_i} \left(P_{ij}^e - P_{ij}^p \right) + E_j + \epsilon_{jlm} u_l B_m - \frac{1}{\mu m_e} \epsilon_{jlm} j_l B_m \end{aligned} \quad (2.80)$$

where $\mu = 1/m_p + 1/m_e$, the proton cyclotron frequency is Ω_p , the plasma frequency is $\omega_{p,p} = 4\pi n q_p^2 / m_p$, the current is $j_i = q_p n_p u_i^p - q_p n_p u_i^p$ and the rest have been previously defined. Next, the mass ratio $1/\mu m_p \approx m_e/m_p$ is taken to be small, and the Hall term $\propto \epsilon_{jlm} B_m$ is neglected, to write the ideal Ohm's

Law,

$$E_j = -\epsilon_{jlm} u_l B_m \quad (2.81)$$

This equation is used to rewrite the induction equation as a function of only the magnetic field and velocity, closing the equations. The ideal Ohm's law is valid at scales much larger than the proton inertial length. One piece neglected here is the effect of collisions on the Ohm's Law, which can be typically neglected when the resistivity is small.

2.4.3 Landau fluid

Before describing the Landau fluid equations, some clarity needs to be given to the nomenclature of various plasma models. Since any fluid model is derived from Boltzmann-Maxwell equation, the attempt to incorporate collisionless or kinetic effects into fluid equations blurs the line between what is kinetic and what is fluid. For example, high-order fluid moments begin to incorporate collisionless effects. In general, the fluid equations are a low-order fluid model (no heat flux) with a simple Ohm's Law. Often non-ideal Ohm's law terms are incorporated, when the scales of the plasma become comparable to the ion inertial length, and these are called kinetic effects. Non-Maxwellian features, simply just the temperature anisotropy, is often called a kinetic effect. In general, any effect from the collisionless equation that is incorporated into fluid equations is called a kinetic effect.

The kinetic effects that are desirable for this thesis are the 0th order wave-particle resonances, called Landau and Barnes damping. These effects can be built into fluid equations, using a similar method to [Braginskii \[1957\]](#), which lead to the Landau fluid equations [[Hammett and Perkins, 1990](#)]. They are low-order moment and ideal Ohm's Law closed equations, where the coefficients for resistivity, thermal transport etc. are determined from an expansion, where the small-amplitude fluctuations are provided by linearizing the drift kinetic equation and taking moments. They approximate Landau and Barnes damping very accurately, yet have the desirable properties of closed fluid equations, and are therefore called the Landau fluid equations.

2.5 Plasma waves and instabilities

The various models for plasma can be studied with a normal mode analysis to produce waves, incorporating a range of effects that hold some of the beautiful properties of plasmas. The classic plasma wave has an electromagnetic part, e.g.,

δb_\perp – fluctuation of the perpendicular magnetic field, and an acoustic response, e.g., δn_e fluctuations of the electron density.

A key part of this thesis is to bridge the gap between collisionless and fluid waves, a formidable task, so these sections are dedicated to detailing some literature on wave properties, so the context of the results can be made more clear.

2.5.1 Kinetic theory

The kinetic theory of plasma waves is usually studied by assuming $\omega_r \gg \nu_s$ where ω_r is the real part of the frequency, i.e., setting the collision frequency to zero in Boltmann's Eqs. 2.37. Kinetic theory has a few notable features, first that the waves can be damped by resonance phenomena, as pointed out by Lev Landau [Landau, 1965], to ensure a causal relationship between the plasma variables [Stix, 1992]. Next, the waves are highly susceptible to growth or instability, due to the non-equilibrium nature of the system. Together, these effects lead to reversible energy exchange between the particles and electromagnetic waves i.e., not just the wave action of an undamped acoustic wave.

2.5.1.1 Electromagnetic dielectric tensor

The spatially homogeneous electromagnetic dielectric tensor is derived in Appendix A. The dielectric tensor, Eq. A.51, is rewritten here,

$$\frac{c^2}{\omega(k_i)^2} (k_i k_j \hat{E}_j - k_j^2 \hat{E}_i) + \hat{E}_i = -\frac{4\pi i}{\omega(k_i)} \sum_s q_s \int d^3v v_i \hat{f}_s \quad (2.82)$$

The perturbed distribution function \hat{f}_s appears as Eq. A.73 and is rewritten here,

$$\begin{aligned} \hat{f}_s = & -\frac{q_s}{m_s} \sum_{n,m=-\infty}^{\infty} \frac{J_m(\lambda_s) \exp\{i(m-n)v_\phi\}}{i[k_\parallel v_\parallel - \omega(k_i) + n\Omega_s]} \\ & \times \left[\hat{E}_x \frac{n}{\lambda_s} J_n(\lambda_s) \frac{\partial}{\partial \alpha_+} + i \hat{E}_y \frac{\partial}{\partial \lambda_s} J_n(\lambda_s) \frac{\partial}{\partial \alpha_+} + \hat{E}_z J_n(\lambda_s) \left(\frac{\partial}{\partial v_\parallel} + \frac{n}{\lambda_s} \frac{\partial}{\partial \beta_+} \right) \right] F_s. \end{aligned} \quad (2.83)$$

where the Bessel function of the first kind are $J_n(\lambda_s)$, the argument is $\lambda_s = k_\perp v_\perp / \Omega_s$, and the Fourier transformed electric field is \hat{E}_i . The right hand side involves derivatives of the background distribution function F_s which must be prescribed. The angular component of the velocity in cylindrical coordinates is v_ϕ , the complex frequency is $\omega(k_i)$, and the species "s" gyrofrequency is Ω_s .

The derivatives are,

$$\frac{\partial}{\partial \alpha_{\pm}} = \frac{\partial}{\partial v_{\perp}} \pm \omega(\pm k)^{-1} k_{\parallel} \left(v_{\perp} \frac{\partial}{\partial v_{\parallel}} - v_{\parallel} \frac{\partial}{\partial v_{\perp}} \right) \quad (2.84)$$

$$\frac{\partial}{\partial \beta_{\pm}} = \pm \omega(\pm k)^{-1} k_{\perp} \left(v_{\parallel} \frac{\partial}{\partial v_{\perp}} - v_{\perp} \frac{\partial}{\partial v_{\parallel}} \right). \quad (2.85)$$

This version of the Fourier transform (see Section A.0.3) is appropriate to the asymptotic solutions of the perturbed Vlasov Equation. This approach ignores the ballistic response [Krall and Trivelpiece, 1973].

From this dielectric tensor, all collisionless and homogeneous waves are derived. The basic ingredients are the background distribution function, the species concentration, the propagation angle (relative to the background magnetic field), and finally the magnetic field, which can be considered static for electrostatic case, or often the quasi-parallel or perpendicular case, for the wavenumber relative to the magnetic field direction.

2.5.1.2 Kinetic waves

Various kinetic waves and instabilities will be discussed in this coming section. Almost all of the figures will be reproduced from Gary [1993] and so a brief explanation of the notation and figure line style is necessary. The real frequency and imaginary part ω_r, γ are $\mathcal{R}\{\omega\}, \mathcal{I}\{\omega\}$, respectively. The ion plasma frequency is ω_i and k_i is the ion Debye wavenumber, which is $(2\pi/\lambda_{D,p})$ in this notation, with $\lambda_{D,p} = \sqrt{k_B T_p / 4\pi n_p q_p^2}$. The real frequency is plotted as a solid line unless it is critically damped ($\gamma < -|\omega_r|/2\pi$), then the line is continued as a dashed line. The damping rate is always plotted as a dotted line.

The polarization is defined in the standard Stix [1992] and Gary [1993] formalism where the right and left hand is defined by looking in the direction of the background magnetic field at a fixed spatial location for positive real frequency. Therefore handedness changes with the sign of the wavenumber (propagation direction).

2.5.1.2.1 Ion acoustic wave The ion acoustic wave was found by the famous experiments of Tonks and Langmuir [1929]. It is of particular interest to this thesis since it is the collisionless limit of the model constructed in Chapter 4. The ion acoustic wave propagates in an electrostatic proton-electron plasma. Returning to Section 2.5.1.1, this is accomplished by taking k_{\perp} to be zero (no background magnetic field) so that only $n, m = 0$ Bessel functions survive. This provides the electrostatic dielectric function. The next step is to choose a background distribution function, which for this Section is a Maxwellian.

The restoring force of the ion acoustic wave is the electron response to charge separation caused by perturbed protons. This view is supported by Figure 2.2 where the damping rate is small for large electron temperature (right panel) and small wavenumber.

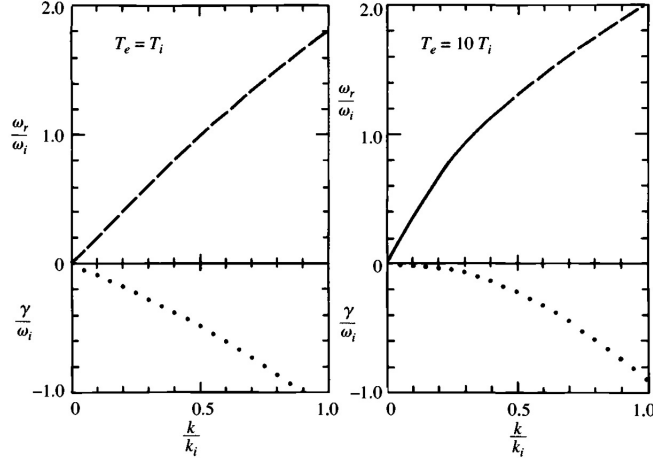


Figure 2.2: Reproduced from Gary [1993]. The two panels have different electron to proton temperature ratios denoted in the top left corners. The definitions of the quantities and line style choice appears in Section 2.5.1.2. The proton beta doesn't appear in the textbook, but this is explored in later section of this thesis.

Using asymptotic expansions on the plasma dispersion function and taking the long wavelength limit, the phase speed reduces to,

$$c_s = \sqrt{\frac{T_e + 3T_p}{m_p}}, \quad (2.86)$$

defined as the ion acoustic speed. The denominator is $\sqrt{m_p}$ proving the inertial role of the protons. The wave action is along the propagation direction i.e., longitudinal waves.

The role of a static background magnetic field modifies the dispersion relation in a simple way,

$$\omega_r = k_{\parallel} c_s, \quad (2.87)$$

so that a cosine term appears. The wave does not propagate across the field, since the electrons can not neutralize due to their gyro-motion about the magnetic field.

Moving on to the electromagnetic theory of the ion acoustic wave for a Maxwellian proton-electron plasma. In the low frequency limit, the ion acous-

tic wave, for the full electromagnetic description, gains only a small magnetic field fluctuation, so the electrostatic dispersion relation remains a good description. This small magnetic fluctuation does however have a component along the background magnetic field direction which leads to Barnes damping [Barnes, 1966]. This wave is explored in Chapter 4 since it is one of the waves studied numerically in this thesis.

2.5.1.2.2 Proton cyclotron wave The most simple form of the proton cyclotron wave is the electrostatic case of the dielectric tensor in Section 2.5.1.1 with a static background magnetic field for an electron-proton plasma. The character of the wave is heavily affected by the background distribution function and ion species present in the plasma. Therefore, the name of the waves and their properties deserves some clarification. In the magnetospheric community the wave is called the electromagnetic ion-cyclotron wave since the effects of multiple ion species must be considered, in plasma textbooks it is often called the proton or ion cyclotron wave, and in the solar wind turbulence community it is called the Alfvén / ion cyclotron wave because it connects to the Alfvén wave in the low frequency limit for parallel propagation.

In general, the wave has left circular polarization where the direction of propagation (fluctuations are transverse) and is non-dispersive (proportional to the Alfvén speed) until it nears a cyclotron resonance. The wave is cyclotron resonant which occurs at $\omega_r = k_{\parallel}v_{\parallel} - m\Omega_s$, where v_{\parallel} is the parallel velocity, m is the order of the resonance and Ω_s is the species “s” cyclotron frequency. When the phase velocity of the wave, or an integer harmonic Ω_s/k_{\parallel} , the wave energy converts to particle free energy, and this is called wave damping.

The wave can be generated by proton temperature anisotropy. This phenomena in plasma physics is treated as wave growth, where free energy in the plasma distribution function is converted into wave energy. Formally, a portion of the particle distribution function has a negative absorption coefficient (or positive emission) Melrose [1986].

Returning to Section 2.5.1.1 and using a bi-Maxwellian distribution function provides the kinetic description of the temperature anisotropic proton cyclotron instability. Figure 2.3 displays the wave properties for three values of the temperature anisotropy (see caption). As the perpendicular temperature becomes larger relative to the parallel temperature, the imaginary part of the complex frequency, defined as γ , transitions from negative to positive, indicating wave growth.

The next important feature is in the phase velocity. At small wavenumbers, the group velocity is the Alfvén speed, at larger wavenumber the phase velocity levels off and becomes heavily damped, this is due to the cyclotron resonance

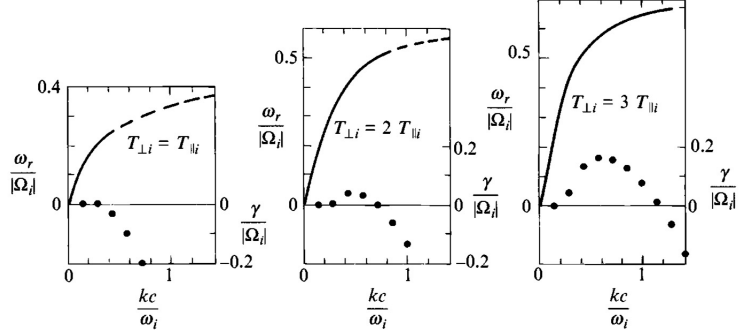


Figure 2.3: Reproduced from Gary [1993]. In the panels the proton temperatures are reported $T_{\parallel i}$, $T_{\perp i}$ where i is used for ion, but in this thesis it corresponds to the proton temperature. The parameters of this system are $v_A/c = 10^{-4}$, $\beta_p = 1$.

at first order $\omega_r/|\Omega_p| \approx 1$. This resonance is then affected by the abundance of other ions in the plasma, as their masses give different resonances.

Finally, the proton cyclotron wave is connected to the Alfvén wave in the quasi-parallel limit. This has implications in turbulence theory, to be addressed in Section 2.7.

2.5.1.2.3 Kinetic Alfvén wave The kinetic Alfvén wave [KAW] is the short wavelength extension of the Alfvén wave in the perpendicular limit. It is a right-hand elliptically polarised electromagnetic wave. The interesting features can be seen at the gyro-scale, where the wave is compressive, opposed to the long wavelength limit.

Figure 2.4 shows the dispersion relation for the KAW in an equal temperature proton-electron plasma. Near to the $k_{\perp}\rho_p \simeq 1$ scale, the phase speed of the wave increases dramatically from its short wavelength value, and becomes heavily damped. Additionally, the wave gains a compressive component. The wave-particle interaction is through the 0th order resonance of Landau damping, where the plasma beta comes into play. For low beta plasma, the protons are preferentially heated and at high beta, the electrons are preferentially heated.

2.5.2 Fluid theory

In this section fluid waves will be addressed. The key physics not described by fluid theory is the wave-particle resonance. In the fluid theories, the macro fluid variables (e.g., density, momentum) are coupled to the fields. At the most basic level, this is accomplished through the induction equation and Ohm's law. The closure of the equations is provided by an equation of state. This gives

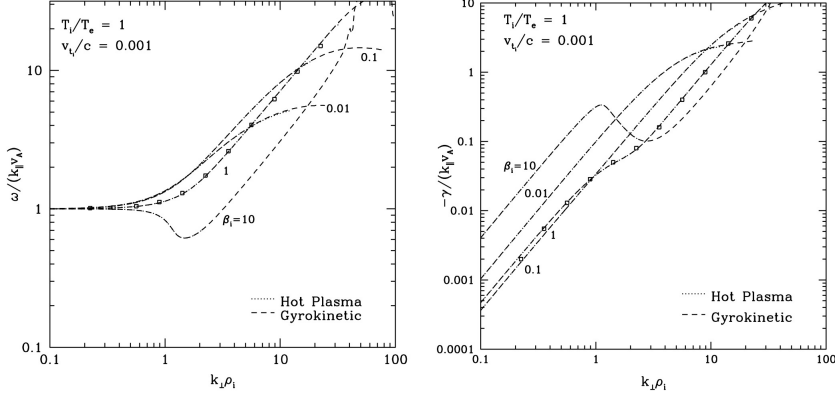


Figure 2.4: Reproduced from Howes et al. [2006]. The left panel is the normalized real frequency and the right panel is the normalized damping rate. The horizontal axis is the perpendicular wavenumber times the proton gyroradius (they have used ρ_i). The top left annotation is the proton to electron temperature ratio and the ratio of proton thermal velocity to the speed of light. The line are annotated by the proton plasma beta (here it is β_i) and the line styles can be ignored for this discussion.

quite a lot of variety in the equations and resulting waves that can be produced. To keep this section brief, the four classic waves produced by MHD theory are presented in the anisotropic limit $k_{\parallel} \ll k_{\perp}$.

The first wave is the Alfvén wave which has a dispersion relation,

$$\omega = \pm k_{\parallel} v_A. \quad (2.88)$$

The wave is transverse and carries no compressive fluctuation. The restoring force of the wave is the tension of the magnetic field. The wave was theorized by Hannes Alfvén along with magnetohydrodynamics [Alfvén, 1942]. Two compressive waves result from the study of magnetohydrodynamic equations. The first,

$$\omega \simeq \frac{k_{\parallel} v_A}{\sqrt{1 + v_A/c_s}}, \quad (2.89)$$

$$(2.90)$$

is the slow-mode, where c_s is the sound speed, but typically the electron pressure is ignored in magnetohydrodynamics, so it simplifies to a numerical multiple of the thermal velocity. This wave is compressional with the magnetic pressure and thermal pressure anti-correlated, the unique identifier of this wave. The cosine factor restricts propagation across the magnetic field. Next is the fast

mode,

$$\omega \simeq \pm k_{\perp} \sqrt{c_s^2 + v_A^2}. \quad (2.91)$$

This compressive wave's restoring force is the magnetic pressure and thermal pressure in phase. The final mode discussed here is the entropy mode,

$$\omega = 0. \quad (2.92)$$

The mode is non-propagating and produced by linearising the equation of state.

2.5.3 Branch connections

The waves discussed in the kinetic theory Section 2.5.1.2 and the fluid (or low frequency waves) discussed in Section 2.5.2 are extensions of each other in various limits.

Beginning with the Alfvén wave, there are two names given to its small scale extension: the proton cyclotron wave in the parallel limit ($k_{\parallel} \gg k_{\perp}$) and the kinetic Alfvén wave in the perpendicular limit ($k_{\perp} \gg k_{\parallel}$).

The MHD slow-mode is connected to ion-acoustic mode and another kinetic mode called the kinetic non-propagating mode [Foote and Kulsrud, 1979]. These modes and their plasma beta, collision frequency, and propagation angle dependence are well-explored in Chapter 4.

The fast-mode is connected to the whistler mode, a mode that wasn't explained in the Section 2.5.1.2. They are not the focus of this thesis, but do have plenty of application in laboratory and magnetospheric/ionospheric plasmas.

This entropy mode is not connected to a kinetic wave, as it depends on the definition of entropy. However, it is related to pressure balance of the magnetic and thermal pressure, which also leads to a non-propagating mode in the kinetic regime [Howes et al., 2006].

2.6 Quasi-linear theory

Quasi-linear theory provides a way to understand how waves interact with the plasma distribution function. The derivation is outlined in Stix [1992], Yoon [2017] in great detail. The idea can be sketched from Eq. A.13 in Appendix A,

$$\left[\frac{\partial}{\partial t} + \frac{q_s}{m_s} \left(c^{-1} \epsilon_{ijk} v_j B_k \right) \frac{\partial}{\partial v_i} \right] F_s = - \left\langle \left[\frac{q_s}{m_s} \left(E_i + c^{-1} \epsilon_{ijk} v_j b_k \right) \frac{\partial}{\partial v_i} \right] f_s \right\rangle. \quad (2.93)$$

The background magnetic field is B_k and the fluctuation is b_k , the electric field fluctuation is E_i , the averaged distribution function is F_s , and the perturbed distribution function is f_s . The magnetic term on the left hand side can be ignored for a gyrotrropic distribution function. The right hand side is second-order in the perturbation. Linear perturbations are found for the right hand side (shown in Appendix A) and inserted i.e., the quadratic nonlinearity is assumed to be the product of the linear perturbations. This requires assuming the wave growth / damping is small compared to the real frequency, the averaged distribution function evolves on a slow time scale, the wave spectrum is homogeneous and there are no wave-wave interactions. This final assumption is often quoted as to why quasi-linear theory is incompatible with turbulence.

The final set of equations describe the time evolution of an averaged distribution function with a set of plasma waves. The time evolution equation for the averaged distribution function,

$$\frac{\partial}{\partial t} F_s = \int_{-\infty}^{\infty} \frac{d^3 k}{(2\pi)^3} \hat{B}(k_i) \frac{1}{v_\perp} \frac{\partial}{\partial \alpha} v_\perp \nu_s^{\text{scatt}}(k_i; v_\parallel, v_\perp) \frac{\partial}{\partial \alpha} F_s \quad (2.94)$$

where the normalized magnetic field power spectrum is,

$$\hat{B}(k_i) = \frac{8\pi}{B_0^2} \left(\frac{k_\parallel}{|k_i|} \right)^2 \frac{|\hat{b}_i(k_i)|^2}{1 - |\hat{k}_i e_i|^2}, \quad (2.95)$$

where $e_i = \delta_{ix}e_x + \delta_{iy}e_y + \delta_{iz}e_z$ is the polarization vector. The pitch-angle gradient is,

$$\frac{\partial}{\partial \alpha} = v_\perp \frac{\partial}{\partial v_\parallel} + \left(\frac{\omega_r(k_i)}{k_\parallel} - v_\parallel \right) \frac{\partial}{\partial v_\perp}, \quad (2.96)$$

where ω_r is the real part of the wave frequency. The relaxation or scattering rate,

$$\nu_s^{\text{scatt}}(k_i; v_\parallel, v_\perp) = \pi \frac{\Omega_s^2}{k_\parallel} \sum_{n=-\infty}^{\infty} \delta(v_{\text{res}} - v_\parallel) |\Psi_n|^2. \quad (2.97)$$

The resonant velocity is defined,

$$v_{\text{res}} = \frac{\omega_r - n\Omega_s}{k_\parallel}, \quad (2.98)$$

where Ω_s is the species cyclotron frequency. Additionally,

$$\Psi_n = \frac{1}{\sqrt{2}} \left[e_r J_{n+1}(\lambda_s) + e_l J_{n-1}(\lambda_s) \right] + \frac{v_\parallel}{v_\perp} e_z J_n(\lambda_s), \quad (2.99)$$

is defined where $\lambda_s = k_\perp v_\perp / \Omega_s$ is the argument of the Bessel functions J_n and the right/left handed polarization vectors,

$$e_r = \frac{e_x - ie_y}{\sqrt{2}}, \quad e_l = \frac{e_x + ie_y}{\sqrt{2}}. \quad (2.100)$$

These equations describe the plasma in the quasi-linear phase.

When an electromagnetic wave's phase speed matches a harmonic of the resonant velocity, the energy transfer between the two will occur if the pitch-angle gradient is non-zero. The evolution has two interesting view points: macro and micro. Beginning with the micro-evolution, particles interacting with waves will follow contours of,

$$\left(v_\parallel - \frac{\omega_r}{k_\parallel} \right)^2 + v_\perp^2 = \text{const.}, \quad (2.101)$$

in v_\perp, v_\parallel - space. Figure 2.5 shows contours of the distribution function F_s

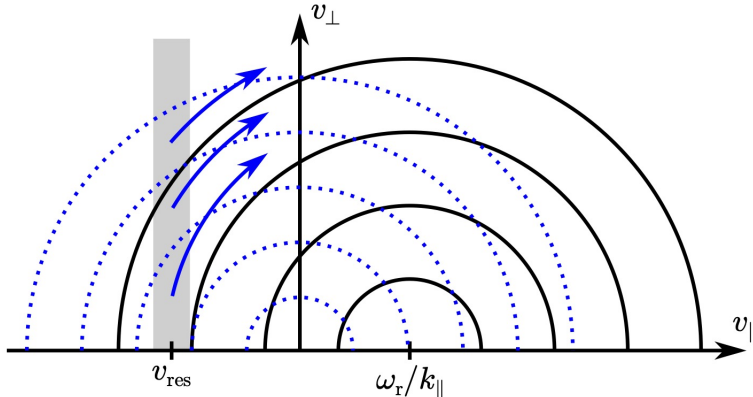


Figure 2.5: Reproduced from Verscharen et al. [2019]. Blue dotted lines are contours of the background distribution function F_s , grey shaded region is the resonant region, black lines are contours of Eq. 2.101, and the blue arrows are the direction of diffusion of the particles.

in blue dotted lines, of which particles in the resonant region (in grey) evolve on contours of the circle given by Eq. 2.101. The direction depends on the slope of F_s at that point, as the particles will diffuse to lower F_s . The process is properly called diffusion due to the form of the time evolution equation of the distribution function (Eq. 2.94). In this case, the particles are diffusing to a region of higher $v_\perp^2 + v_\parallel^2$ so they gain energy at the expense of the wave energy. Qualitatively, Fig. 2.5 also shows that particles in the resonant region with small v_\perp will gain more v_\perp than v_\parallel due to the shape of the contours from Eq. 2.101. The anisotropy in energization v_\perp, v_\parallel leads well in the macroscopic

picture: anisotropic heating.

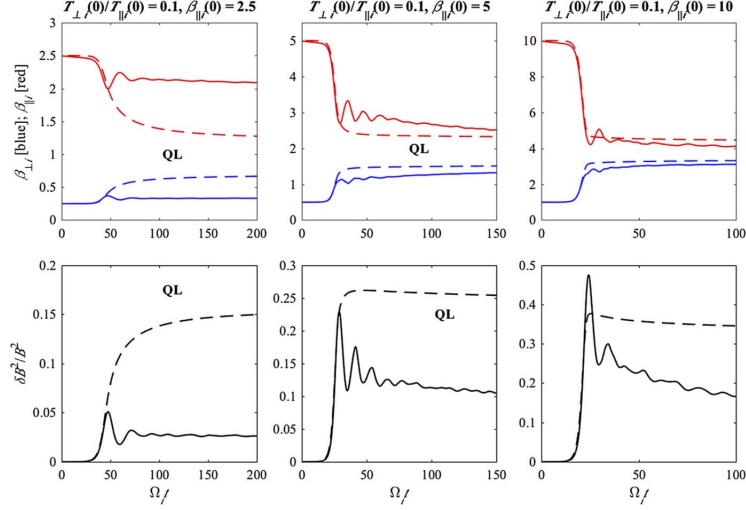


Figure 2.6: Reproduced from Yoon [2017]. In the top panels, the evolution of the proton beta are shown for a simulation in solid lines and dashed lines the bi-Maxwellian prediction. The bottom panel shows the magnetic energy with the same line style scheme. The horizontal axis is the time in number of cyclotron periods. Please ignore the “QL” as it is misleading.

The macroscopic variables can be produced by taking appropriate moments of Eq. 2.94 for the evolutions of the momentum or temperature [Yoon, 2017]. The moment appropriate to the temperature $\partial T_s / \partial t$ is the definition of heating in the quasilinear picture; it is reversible. Figure 2.6 compares a simulation of a plasma to the bi-Maxwellian prediction. The simulation solves the Vlasov equation for the protons kinetically with the Particle-In-Cell (PIC) approach and the electrons are assumed to be fluid. The particular instability that is considered is the parallel firehose instability.

The instability forms when there is a kink in the magnetic field that cannot be stabilized by the particle motions. This happens because the parallel motion (i.e., parallel temperature) contributes to a centrifugal force on the arc of the kink. Therefore, the instability occurs when $T_{\parallel}/T_{\perp} > 1$.

The bi-Maxwellian assumption for F_s in Eq. 2.94 simplifies the system dramatically. After taking moments for the temperature in Eq. 2.94, the bi-Maxwellian system is then just related to the wave energy, and a simple differential equation can be solved for the time evolution of the temperatures, assuming they are bi-Maxwellian throughout the time evolution. While basic, it does provide some insight into the nature of the quasi-linear approach, and appears as the solid lines in Fig. 2.6.

Starting with the right most panels of Fig. 2.6, the the bi-Maxwellian case

and the simulation evolve similarly for the perpendicular and parallel β . The magnetic energy in the bottom panel is significantly different after the initial phase, but this can be described better for the middle panels. In the middle panels, the evolution for small times are again similar but then depart drastically. There is a decaying oscillation in the quantities, which are indeed out of phase, this is the nonlinear stage called particle trapping. Here it does appear to affect the asymptotic state of the magnetic energy and temperatures.

Moving towards the left most panels of Fig. 2.6, it can be seen that the simulation and bi-Maxwellian assumption do not match well. What is happening here, is that the evolution departs from the bi-Maxwellian state quickly after the instability begins. Returning to the microscopic picture from Fig. 2.5 and looking at the width of the grey region, here it is slender. This will cause a deformation of the particle distribution function that is not bi-Maxwellian. Returning to Fig. 2.6, the resonant region at high beta (most right panels) have a large resonant region, relative to the distribution function, and that decreases moving left.

This ends the discussion of quasi-linear theory. The quasi-linear approach has been outlined and some of the equations have been shown. While the quasi-linear theory breaks the equations, it provides a description of how waves will interact with the particle distribution function. The macroscopic picture was also visited, to show the importance of the resonances and demonstrate how measurable quantities (e.g., temperature) are affected by quasilinear mechanisms.

Clearly for the quasi-linear evolution, the full particle distribution function and wave character must be known to understand what is happening. This is the endpoint of this Section and the beginning of Chapter 6.

2.7 Fluid plasma turbulence

To describe any physical process of the solar wind it is necessary to understand how it fits in with its turbulent nature. This section has been written to cover turbulence concepts with a focus on how to describe the density and pressure fluctuations (compressive fluctuations). A key piece of this thesis is the measurement of the scale dependent anisotropy of compressive fluctuations and the scale at which kinetic processes will decay their power. This scale is extremely important because it is relevant to plasma heating and its prediction and comparison to previous observations is a basic check of the equations. This section shows aspects of fluid plasma turbulence so that the final measurements can be put into a more complete picture of the solar wind.

Fluid plasma turbulence, and not the kinetic theory, which will not be cov-

ered here, is concerned with the classic problem of turbulence: how is energy reshuffled in wavenumber space by non-linear mechanisms. Fluid plasma turbulence is concerned primarily with two additional problems, the effect of magnetic fields and since most plasmas are collisionless, how this energy is transported to scales where kinetic effects become dominant.

To demonstrate the general problem more clearly some ideas will be presented by studying the resistive incompressible MHD equations. They can be written in the Elsasser variable form,

$$\frac{\partial}{\partial t} z_i^\pm \mp A_j \frac{\partial}{\partial x_j} z_i^\pm + z_j^\mp \frac{\partial}{\partial x_j} z_i^\pm = -\frac{\partial}{\partial x_i} p_{\text{tot}} + \eta \frac{\partial^2}{\partial x_j^2} z_i^\pm, \quad (2.102)$$

$$\frac{\partial}{\partial x_i} z_i^\pm = 0 \quad (2.103)$$

where $z_i^\pm = u_i \pm b_i / \sqrt{4\pi m_p n_p}$. The sum of the magnetic and thermal pressures is p_{tot} . The magnetic field b_i is normalized to be the Alfvén velocity, so the equations can be written in the above form [Elsasser, 1950]. For demonstration, the background Alfvén velocity is A_i which will be local, so it is a function of x_i, t . This breaks the Reynold's decomposition and is formally treated with a filter, but it helps to demonstrate important points about MHD turbulence. The background velocity field is zero since that frame can be chosen. Equations 2.102 show that $z_j^\mp z_i^\pm$ are responsible for non-linear phenomena and the $A_j z_i^\pm$ is responsible for advection.

The spatial Fourier transform of the fields,

$$z_i^\pm(t, x_i) = \int d^3k \hat{z}_i^\pm(t, k_i) \exp\{ik_i x_i\}, \quad (2.104)$$

$$\hat{z}_i^\pm(t, k_i) = (2\pi)^{-3} \int d^3x z_i^\pm(t, x_i) \exp\{-ik_i x_i\}, \quad (2.105)$$

where k_i is a wavenumber. The bounds on these integrals are not important for the demonstration. Taking the Fourier transform of the incompressible MHD equations,

$$\frac{\partial}{\partial t} \hat{z}_i^\pm + i \int d^3x \exp\{-iq_i x_i\} k_j (z_j^\mp \mp A_j^\pm) z_i^\pm = -ik_i \hat{p}_{\text{tot}} - \eta k_j^2 \hat{z}_i^\pm, \quad (2.106)$$

$$k_i \hat{z}_i^\pm = 0, \quad (2.107)$$

where the wavenumbers will be implicit when they are in the integral to keep track of everything. Notice that the incompressibility condition does not apply

to inner products such $k_i \hat{z}_i(p_i)$, therefore $k_i \hat{z}_i(p_i) \neq 0$. The non-linear term,

$$\begin{aligned} \int d^3x \exp\{-iq_i x_i\} k_j z_i^\pm (z_j^\mp \mp A_j^\pm) = \\ i \int d^3x \int d^3k \int d^3p k_j \hat{z}_i^\mp(k_i) [\hat{z}_j^\mp(p_i) \mp \hat{A}_j^\pm(p_i)] \exp\{ix_i(k_i + p_i - q_i)\}, \end{aligned} \quad (2.108)$$

where the integral over x_i gives the Dirac delta function $\delta^3(k_i + p_i - q_i)$ and then the integral over p_i gives,

$$\begin{aligned} \int d^3 \exp\{-iq_i x_i\} k_j z_i^\pm (z_j^\mp \mp A_j^\pm) = \\ i \int d^3k k_j \hat{z}_i^\pm(k_i) [\hat{z}_j^\mp(p_i - k_i) \mp \hat{A}_j^\pm(p_i - k_i)], \end{aligned} \quad (2.109)$$

and with the incompressibility condition $k_i z_i^\pm(k_i) = 0$, a term can be added to recover,

$$\begin{aligned} \int d^3 \exp\{-iq_i x_i\} k_j z_i^\pm (z_j^\mp \mp A_j^\pm) = \\ ik_j \int d^3k \hat{z}_i^\pm(k_i) [\hat{z}_j^\mp(p_i - k_i) \mp \hat{A}_j^\pm(p_i - k_i)]. \end{aligned} \quad (2.110)$$

The pressure can be dealt with by taking the divergence of the incompressible MHD equation,

$$\left(z_j^\mp \mp \frac{\partial}{\partial x_i} A_j \right) \left(\frac{\partial}{\partial x_j} z_i^\pm \right) = -\frac{\partial^2}{\partial x_i^2} p_{\text{tot}}, \quad (2.111)$$

the Fourier transform and a similar procedure to the non-linear term produces,

$$\hat{p}_{\text{tot}}(k_i) = -\frac{k_i k_j}{k_l^2} \int d^3p \hat{z}_i^\pm(p_i) [\hat{z}_j^\mp(k_i - p_i) \mp \hat{A}_j(k_i - p_i)] \quad (2.112)$$

Inserting Eqs. 2.110, 2.112 into Eq. 2.106,

$$\begin{aligned} \frac{\partial}{\partial t} \hat{z}_i^\pm + \eta k_l^2 \hat{z}_i^\pm \\ = ik_l \left(\delta_{ij} - \frac{k_i k_j}{k_n^2} \right) \left(\int d^3p \hat{z}_j^\pm(p_i) [\hat{z}_l^\mp(k_i - p_i) \mp A_l(k_i - p_i)] \right). \end{aligned} \quad (2.113)$$

Now some important results from MHD turbulence theory can be made. The final equation here possesses an integral in the convolution form. This is the defining character of non-linearity in turbulence, that each wavenumber of the fields, interacts with all other wavenumber. Taking a look at Eq. 2.108, the integral in d^3x resulted in the Dirac delta function $\delta(k_i + p_i - q_i)$ which shows

that three wavenumbers mediate the interactions. Looking at Fig. 2.7, the panels on the left show local interactions, where all the wavenumbers are the same, and non-local, where k_i is different in magnitude than the other two. Thinking to the convolution integral present in the equation, it can be seen that local interactions will dominate, since similar wavenumbers will have similar energy and shape (e.g., a harmonic will have similar shape, but not energy, so the interaction is not dominant). This interaction, of successive interactions in wavenumber space, which inevitably carry energy from one scale to another is the energy cascade. A cartoon of this can be seen in the top right panel of Fig. 2.113 where the outer scale and dissipation range are widely separated. The inertial range is where the energy cascade is responsible for energy transfer in scale, connecting the two ranges.

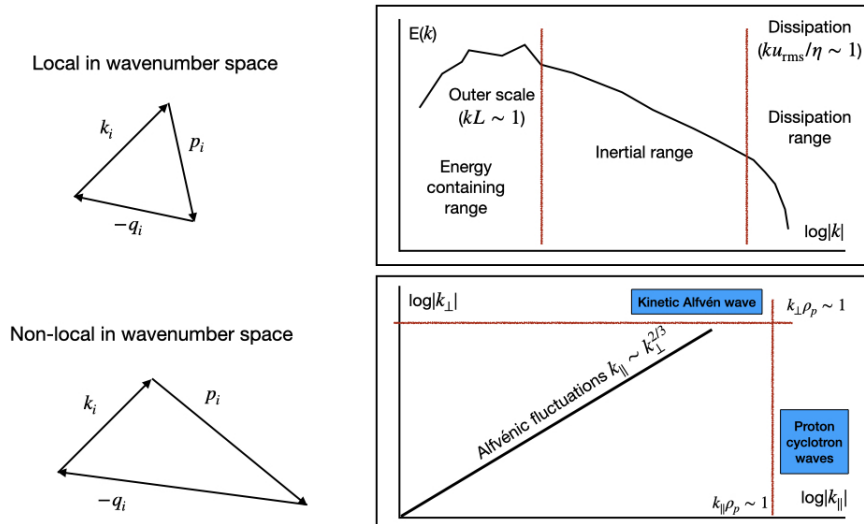


Figure 2.7: The panels on the left show a local and non-local triad interaction. The right hand top panel shows a typical omni-directional magnetic field power spectrum. The bottom right panel shows the k_{\parallel} , k_{\perp} plane where the interactions take place. One would expect enhanced power along lines in this plane. All panels here are cartoons.

Returning to Eq. 2.113, notice that $A_l(k_i - p_i)$ is the local Alfvén velocity direction. The wavenumber given by this interaction is always along the magnetic field direction k_{\parallel} . This has a drastic effect on the energy cascade giving a local anisotropy to the background magnetic field direction.

In a weakly collisional plasma, the fate of the energy is not that of resistive heating, but damping by other mechanisms. One of the popular mechanisms is

that of the wave-particle interaction. This is sketched in the bottom right panel of Fig. 2.7, focussing on the anisotropy in wavenumber space. Energy at small scales will follow the critical balance curve, distribution of power in parallel and perpendicular wavenumber space, to the gyro-scale, where the Alfvén wave is more properly called the kinetic Alfvén wave and can be damped. If the energy were to be stronger in the parallel direction, then the proton cyclotron mechanism would be responsible for damping of the wave energy.

2.7.0.1 Kolmogorov's index

In 1941 Andrei Kolmogorov produced three papers on turbulence theory [Kolmogorov, 1941a,b,c] which culminate in the prediction of the shape of the power spectrum of the velocity field for a set of conditions. The prediction is derived from the incompressible Navier-Stokes equations. The conditions are statistical homogeneity, infinite Reynold's number, time-stationarity, isotropy, and scale independence. The final point is the key insight of Kolmogorov. A sketch of the key insight will follow for later discussions. Based on all the conditions except for scale independence,

$$\epsilon \approx \frac{\langle \delta u^3 \rangle}{l} \quad (2.114)$$

where ϵ is the mean energy dissipation rate from the energy budget equation, $\delta u = u(x + l) - u(x)$ is the velocity increment over l , and the angled brackets are an ensemble average or over space by the ergodic theorem. Vectors have been dropped due to the assumptions of statistical homogeneity and isotropy. No viscosity is present, which led to Kolmogorov's suggestion that the predicted form would be universal. Clearly, the mean energy dissipation rate is constant, so upon assuming,

$$\mathcal{S} = \frac{\langle \delta u^3 \rangle}{\langle \delta u^2 \rangle^{3/2}} = \text{const.} \Rightarrow \langle \delta u^2 \rangle \approx \epsilon^{2/3} l^{2/3}. \quad (2.115)$$

This is the assumption of scale independence, that $\mathcal{S} = \text{const.}$ The statistical function $\langle \delta u^2 \rangle$ is the second-order structure function which is related to the correlation function $\langle u(x+l)u(x) \rangle$, simply $\delta u^2 = u(x+l)^2 + u(x)^2 - 2u(x+l)u(x)$ and the correlation function is the Fourier pair of the energy spectrum $E(k)$. The connection between the energy spectrum and the second-order structure function is,

$$\langle \delta u^2 \rangle \approx r^p \Rightarrow E(k) \approx k^{-p-1}. \quad (2.116)$$

This leads to the famous $-5/3$ scaling often observed in turbulent fluids. A final point is that the constancy of skewness (\mathcal{S}) is not observed. This led to a 1962 paper by Kolmogorov which used the underlying distribution of the mean energy dissipation rate to write a set of scaling exponents for the orders of the structure functions. This is called intermittency.

2.7.0.2 Kraichnan & Iroshnikov

[Kraichnan, 1965] and [Iroshnikov, 1964] independently theorized the spectrum from the magnetohydrodynamics equations. The essential insight is that the background Alfvén velocity present in Eq. 2.102 slows the rate of energy transfer and modifies the energy spectrum. The mean energy dissipation rate is proportional to the Alfvén time l/v_A and depends only on the spectrum, so that dimensionally,

$$\epsilon \approx \frac{l}{v_A} \frac{\delta u^4}{l^2}, \quad (2.117)$$

where the second term can be produced by dimensional analysis, using only the quantities related to the spectrum. This leads to the $-3/2$ prediction for the energy spectrum. The use of δu here is for normalized cross-helicity of 0, so $\delta u = \delta b / \sqrt{4\pi n_p m_p}$. Additionally, the spectrum produced is isotropic.

2.7.0.3 Goldreich & Sridhar

One of the essential modifications from analyzing the incompressible MHD equations that the magnetic field provides is anisotropy in k-space. This was the essential contribution of Goldreich and Sridhar [1995]. First, a simplifying point can be made that is helpful in producing scaling laws, which is to assess the nonlinear time,

$$\epsilon = \frac{\delta u^2}{\tau_{NL}}. \quad (2.118)$$

The nonlinear times for Kolmogorov's prediction (τ_{NL}^{Kol}) and Iroshnikov-Kraichnan prediction (τ_{NL}^{IK}) are then,

$$\tau_{NL}^{Kol} = \frac{l}{\delta u}, \quad (2.119)$$

$$\tau_{NL}^{IK} = \frac{v_A l}{\delta u^2} \quad (2.120)$$

which are the rate at which energy is transferred from one scale to another. They then consider the transverse nature of the Alfvén wave to connect the

perpendicular length scale l_{\perp} to the parallel scale l_{\parallel} through critical balance,

$$\frac{l_{\perp}}{\delta u} = \frac{l_{\parallel}}{v_A}. \quad (2.121)$$

Physically, it is a balance between the linear Alfvén time and nonlinear time. This leads to a prediction of the scaling of the energy spectrum in the parallel and perpendicular directions. The prediction is that the perpendicular wavenumber energy spectrum is $E(k_{\perp}) \propto k_{\perp}^{-5/3}$ and the parallel wavenumber energy spectrum is $E(k_{\parallel}) \propto k_{\perp}^{-2}$. This modification only happens locally, as pointed out in time evolution of the spectral energy equations derived earlier.

2.7.0.4 Compressive fluctuations

Since this thesis is focussed on compressible fluctuations, the focus will point in that direction. For clarity, compressible means a density n_p or pressure p_p that has spatiotemporal dependence. The extension of the incompressible MHD equations to that of the compressible, is largely complicated because a relations like Eq. 2.114 includes many more terms on the right hand side, so a simple scale independent assumption will not directly predict a scaling law with l for the energy spectrum. Instead, expansion in a small parameter about the incompressible MHD equations can be assumed to produce a spectrum of density fluctuations. This was considered by [Montgomery et al. \[1987\]](#) by relating the density fluctuations through the equation of state to the magnetic field energy spectrum with a relation like Eq. 2.112. This gives an energy spectrum for the density scaling like $k^{-5/3}$.

In [Goldreich and Sridhar \[1995\]](#) the pressure perturbations to leading order are parallel to the magnetic field, therefore Alfvénic fluctuations (transverse to the background magnetic field direction) would not perturb the pressure, so the compressive mode must be considered. This was considered by [Lithwick and Goldreich \[2001\]](#) who suggested that compressible modes are passive to the Alfvénic perturbation, so they will follow the same scaling as the magnetic field, as produced by the Alfvénic perturbation. Additionally, they recognised the severe damping of the compressive fluctuations, due to collisionless processes [[Barnes, 1966](#)], depends directly on the parallel wavenumber. They also recognise that the cutoff for dissipative range is probably not simply the mean-free-path based on discussions in [Foote and Kulsrud \[1979\]](#).

The damping of the slow-mode is important to discuss a bit more. An additional point, is that due to the obliqueness of the Alfvénic perturbations, which the slow-mode is assumed to follow passively, the parallel wavenumber will be very small (i.e., Barnes and Landau damping can not occur) [[Schekochihin et al.](#),

[2009](#)]. Another idea, is that processes that restore the system to equilibrium, such as collisionless relaxation, could inhibit the severe damping of the slow-mode. This idea is supported by this thesis, and the scale that modulates the wavenumber dependence on the damping, is the effective mean-free-path. The physics behind the effective mean-free-path is complicated.

Chapter 3

The solar wind

The solar wind is an ionized gas in the plasma state, that is accelerated in the corona, streaming away from the Sun into interplanetary space. It carries the magnetic field generated by the Sun, defining the heliosphere. The plasma is detectable by spacecrafts, e.g., the particles and electromagnetic fields, therefore it presents a grand opportunity to develop a better understanding of plasma physics.

In this Chapter an overview of the solar wind is presented, beginning with Eugene Parker's prediction of its existence. Then some "big picture" sections follow relying on famous spacecraft missions. Next, a more detailed look at plasma heating, instabilities, and turbulence, with a focus on the compressive nature of the plasma. Finally, there is a section describing spacecraft instruments.

3.1 Eugene Parker's solar wind model

The solar wind, as it is known today, was first theorized by Eugene Parker in his famous article [Parker \[1958\]](#). Observations of comet tails seemed to require a gas pressure, not just photon, to describe the dynamics and the double tail, one of which is redirected due to ionized material coupling to the magnetic field. These conclusions led him to consider the coronal temperature to be the source of an out flowing gas which then couples to the magnetic field, both of which constitute the interplanetary medium.

Parker used equations for a gas to show that if the corona is thermally conducting, then a hydrostatic equilibrium is unphysical, as the pressure is non-vanishing with increasing radial distance. The basic prescription for the solar wind is to take the fluid equations for a gas in stationary spherical expansion. This leads to a differential equation where boundary conditions of the corona lead to the prediction of an escaping plasma, the solar wind. Briefly, a gas with

spherical symmetry and at static equilibrium,

$$\frac{\partial}{\partial r} p(r) = -\frac{GM_S m_p}{2} \frac{p(r)}{T(r)r^2}, \quad (3.1)$$

where r is the radial direction, p is the gas pressure, G is the gravitational constant, M_S is the solar mass, m_p is the proton mass, and T is the gas temperature (in units of energy). The solution is,

$$p(r) = p(a) + \exp \left\{ -\frac{GM_S m_p}{2} \int_a^r dr \frac{1}{T(r)r^2} \right\}, \quad (3.2)$$

where a is the radius where the heat source ceases. It can be seen that as r increases, $T(r)$ must decrease faster than $T \propto r^{-2}$ for the pressure to vanish. The steady-state heat flow equation for hydrogen, calculated from transport theory, gives $r^{-3/2}$, so the static equilibrium is denied. Allowing for stationary expansion of the gas gives,

$$m_p n(r) u(r) \frac{\partial}{\partial r} u(r) + \frac{\partial}{\partial r} p(r) = -\frac{GM_S m_p}{2} \frac{p(r)}{T(r)r^2}, \quad (3.3)$$

$$\frac{\partial}{\partial r} m_p n(r) u(r) r^2 = 0 \quad (3.4)$$

where the second equation is the stationary continuity equation in spherical geometry. This gives,

$$\frac{1}{u(r)} \frac{\partial u(r)}{\partial r} \left(u^2(r) - \frac{2T(r)}{m_p} \right) = \frac{4T(r)}{m_p r} - \frac{GM_S}{r^2}. \quad (3.5)$$

The right hand side is zero at $r = r_c$,

$$r_c = \frac{GM_S m_p}{4T(r_c)}. \quad (3.6)$$

Now, for $r < r_c$, a coronal temperature of 3×10^6 K [Parker, 1958], the right hand side is less than zero. Physically, $u(r)$ is small $< \sqrt{2T(r_c)/m_p}$ at the coronal base (denying two of the solutions to the equations), and so that demands $\partial u(r)/\partial r > 0$ when $r < r_c$. Now consider what happens at the critical radius. If $\partial u(r)/\partial r > 0$ at the critical radius, then the term in the large parentheses gives $u(r_c) = \sqrt{2T(r_c)/m_p}$. Slightly larger than the critical radius the term in the parentheses is positive and so the sign of $\partial u(r)/\partial r > 0$ is positive as well, since the right hand side becomes positive at the critical radius. The other solution, where $\partial u(r)/\partial r = 0$ at the critical radius, would then demand $u(r) \rightarrow 0$ which is unphysical [Parker, 1958]. This is the basic arguments behind an outflowing gas, that is faster than the sound speed $\sqrt{2T/m_p}$.

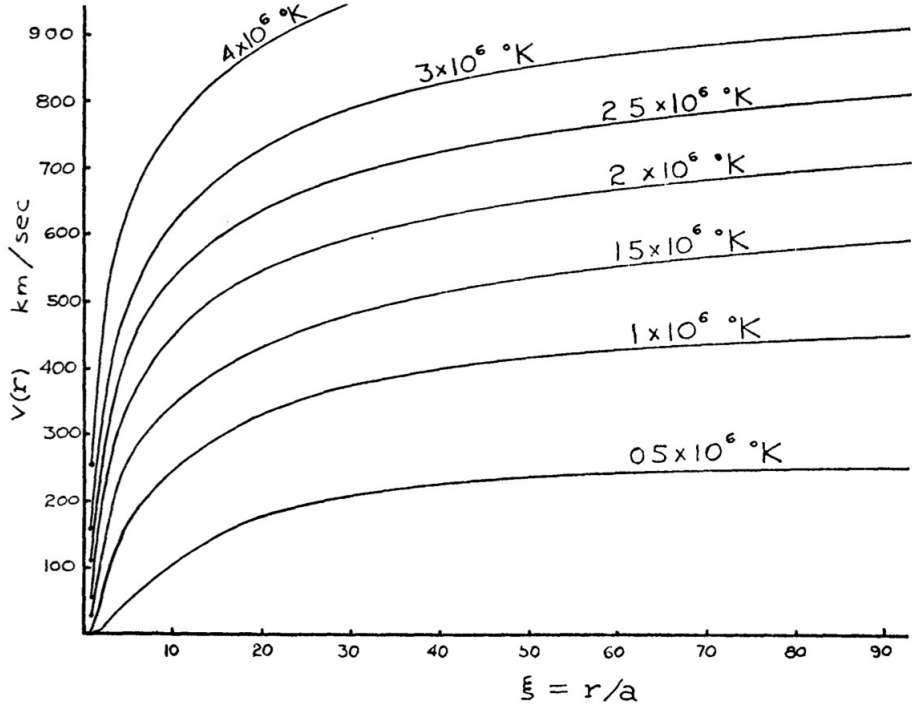


Figure 3.1: Reproduced from Parker [1958]. The vertical axis is velocity and the horizontal axis is the radius normalized by “ a ” which is the radius at which the corona no longer heats the plasma. The parameters of the model are $a = 10^{11}$ cm and the solar mass. The solutions are shown for a range of temperatures at “ a ” which are annotated near to the lines.

Figure 3.1 shows the solutions found by Eugene Parker for the solar wind speed. The solar wind, during expansion, accelerates to speeds above the acoustic and Alfvén speed of the medium. Next, he supposed that the solar wind will be tied to the magnetic field. Considering spherical expansion of the solar wind, the saddle condition on the magnetic field, and solar rotation permits a description of the interplanetary magnetic field. It follows an Archimedes spiral.

In 1959 the Luna 1 spacecraft made in situ observation of the solar wind plasma along with subsequent spacecraft observations, confirmed Parker’s model. Since the solar wind’s detection, it has been continuously monitored by spacecrafts which have provided a wealth of knowledge into plasma physics [Bruno and Carbone, 2013].

3.2 Variable generation

Eugene Park's model considered the solar acceleration to be secondary to the heating of the corona. The heating and acceleration mechanisms are still not well understood and they're called the coronal heating problem, in particular the faster wind [Marsch, 2006]. The Ulysses spacecraft unveiled classic features of the solar wind and insight into the generation mechanism, that is highly variable in speed McComas et al. [2003]. The solar wind has two nominal velocities: slow which is near to 300 km/s and fast which is 600 km/s with overlapping spread about the two modes.

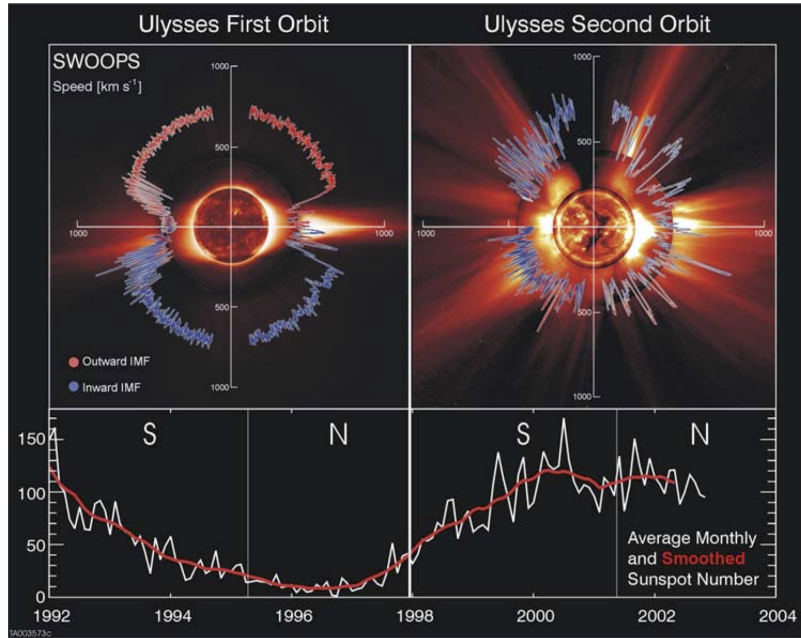


Figure 3.2: Reproduced from McComas et al. [2003]. Both panels are polar plots where the radius is the solar wind velocity colored by the direction of the magnetic field (labelled on the left panel) measured by Ulysses spacecraft. The background figures are detection of the extreme ultraviolet light, by the Solar and Heliospheric Observatory, which are characteristic of the two different periods indicated in the lower panels. The lower panels show the sunspot number.

Figure 3.2 is a composite image that shows the variability of the solar wind. The bottom panel on the left hand side shows the sunspot number over the years 1992-1998, which when compared to the right hand side is smaller in abundance. This is indicative of the solar minimum period. The top left panel shows characteristics of that period. The coordinates of the polar plot are as follows, the radial coordinate is the velocity of the solar wind measured by spacecraft, and the angle is the latitudinal coordinate of the spacecraft at

the time of the measurement. Additionally, the direction of the interplanetary magnetic field (IMF) is outward for red and inward for blue. The solar wind in the solar minimum period is then characterized by a uniform wind (and relatively fast) outside of the ecliptic, where the magnetic field is very near to a dipole. In the ecliptic plane there is structure accompanied by the streamer belt.

Comparing these features to the right hand side, starting in the bottom panel, where sunspot number is larger, indicates the solar maximum period. The top panel shows a less structured solar wind outflow that has great variability in the wind speed and magnetic field structure. The background white light image also reveals more activity. These two periods comprise a 11 year cycle which the sun behaves in two different manners.

3.2.1 Composition of interplanetary particles

The primary particles that compose the solar wind are hydrogen (often just called protons) and electrons with minor populations of heavier ions. These heavier ions often have much larger energy/nucleon so are a seed population for solar energetic particles [Gloeckler \[2010\]](#). The Advanced Composition Explorer (ACE) is a L1 sitting spacecraft designed to study composition, with a set of instruments that can detect and discern charge state, energy and mass of most interplanetary particles.

Figure 3.3 displays the differential intensity (see caption) versus the energy per nucleon. Starting at low energy per nucleon, the bulk solar wind (solid thin black line) is indicated in the upper left hand corner. As the energy per nucleon increases, the differential intensity decreases by multiple orders of magnitude. The suprathermal proton tail is indicated with an arrow and the pickup hydrogen bump by a dotted line. These are neutrals that have been ionized by collisions or photoelectrically and then begin to interact with the solar wind, being "picked up", relative to the solar wind they have a higher energy. Many other heavier ions are observed in the solar wind, besides oxygen (considering Fig. 3.3), but are not as continuously observed.

Going to higher energy per nucleon more non-solar born particles can be seen, such as galactic cosmic rays (see caption for labelling). The remaining particles at high energy per nucleon all interact with the solar wind and make up the composition of the interplanetary medium. The solar energetic particles of oxygen are solar born particles accelerated during solar flare sights or shock fronts of coronal mass ejections.

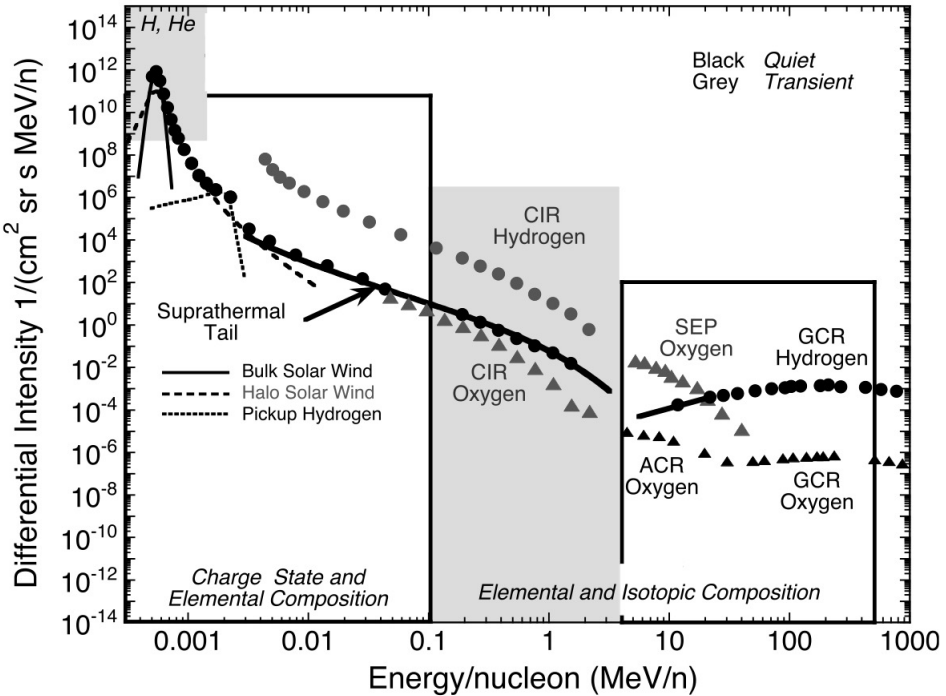


Figure 3.3: Reproduced from [Fox et al. \[2016\]](#) which is reproduced from [Gloeckler \[2010\]](#). The vertical axis is the differential intensity, which is the flux, then divided by the angular coverage of the instrument in steradians and divided by the energy per nucleon. The horizontal axis is the energy per nucleon. Various instrument data products are combined to make this figure. CIR stands for co-rotating interaction region. GCR stands for galactic cosmic ray. ANR stands for anomalous cosmic ray. SEP stands for solar energetic particle. For information on the grey shaded regions, black boxes and annotations at the bottom see [Gloeckler \[2010\]](#).

3.3 Magnetic field structure

Eugene Parker described the interplanetary magnetic field structure [[Parker, 1958](#)], where a pressure driven solar wind through the scale heights of the corona balances the pressure of the magnetic field, carrying it out into interplanetary space. The structure is dynamic over a set of time scales, for example returning to Fig. 3.2, the solar boundary conditions have drastic differences over the solar cycle. Over the years since detection by the Mariner spacecraft in the early 1960s to now, when the Voyager spacecrafsts have entered interstellar space, the picture that Parker gave of the steady-state magnetic field continues to provide an excellent description of the interplanetary magnetic field on the largest scales.

Figure 3.4 displays the steady-state solar magnetic field in the ecliptic plane. In the region close to the sun the magnetic field dominates the dynamics and is

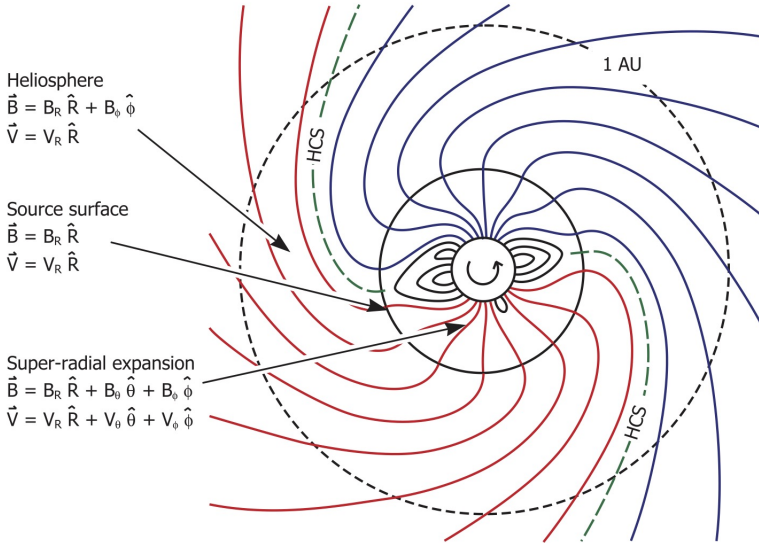


Figure 3.4: Reproduced from Owens and Forsyth [2013]. Looking top down at a slice through the ecliptic plane of the sun, magnetic field lines are drawn where the color lines indicate opposite polarity. The black lines that do not exceed the source surface are closed loops. The closed black circle is the source surface where the solar wind expansion dominates the magnetic field forcing it to be only radial, see the annotations. The green dashed spiralled line is the heliospheric current sheet, separating large regions of opposing polarity.

very non-radial. At a few solar radii, the expansion of the solar wind begins to dominate turning the magnetic field to be radial, which then acts as a boundary condition for the Archimedian spiral into the heliosphere. The annotations on the figure provide the necessary coordinate system to describe the field in the different regions.

Taking the solar wind to have a constant speed in the heliosphere, magnetic flux conservation leads to the radial magnetic field being proportional to the inverse square of the radial distance (on the figure it is $B_R \propto R^{-2}$). Then using the geometry of the rotating system, the azimuthal component is found to be proportional to the inverse radial distance (on the figure $B_\phi \propto R^{-1}$), but the field overall is more azimuthal with increasing radial distance.

3.3.1 The heliosphere

The interplanetary magnetic field extends out defining the heliosphere. At the boundary, the heliosphere interacts with the local interstellar medium. Figure 3.5 displays the global structure. The solar wind and interplanetary magnetic field expand out until the pressure, which is supported largely by pick-up ions, balances the pressure of the local interstellar medium [Kallenrode, 2004]. As it

passes from super- to sub- Alfvénic, a standing termination shock forms, and the Parker spiral description is no longer applicable. The heliosheath is further compressed and hotter plasma, interacting with interstellar plasma.

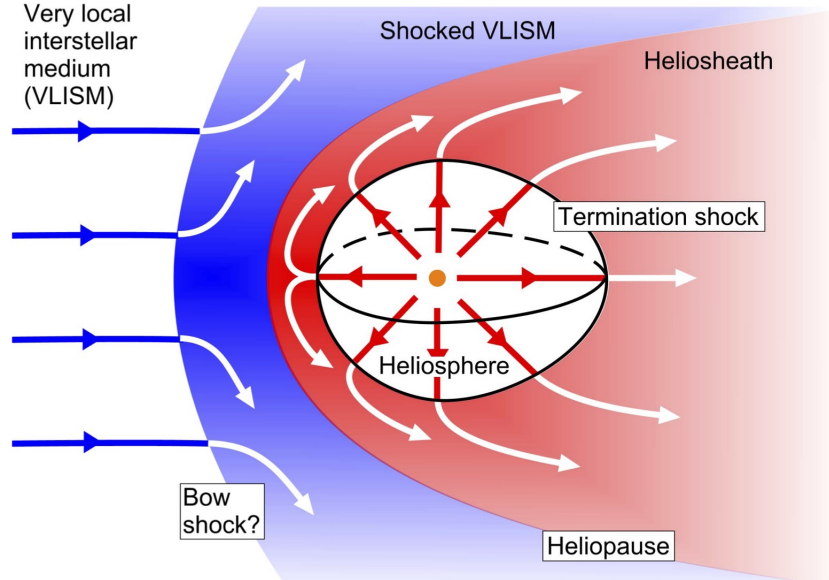


Figure 3.5: Reproduced from Owens and Forsyth [2013]. The global structure of the heliosphere and its boundary with the interstellar medium. The arrows shows direction of plasma (loosely defined here) relative to the sun. In that frame, the heliosphere moves relative to the interstellar medium creating a boundary with multiple shock layers.

Further out, there is the heliopause, where the pressure of the heliosheath and interstellar medium balance each other. Still further out, is potentially the bow shock. This will form if the local interstellar medium is super-sonic and becomes sub-sonic due to balancing the pressure of the heliosheath.

3.4 Heating

Parker's model is based on transport of heat up into the corona sourced by the heating that happens at the base of the corona. While considering the entire problem is one of the big goals of space plasma physics, called the coronal heating problem, the solar wind is heated in situ, as it expands into interplanetary space.

Figure 3.6 shows the temperature of protons as a function radial distance measured by the Voyager spacecraft. The difference between adiabatic expansion (dashed line) and the proton temperature (circles) can be described by turbulence heating models up to radial distances of about 20 AU [Smith et al.,

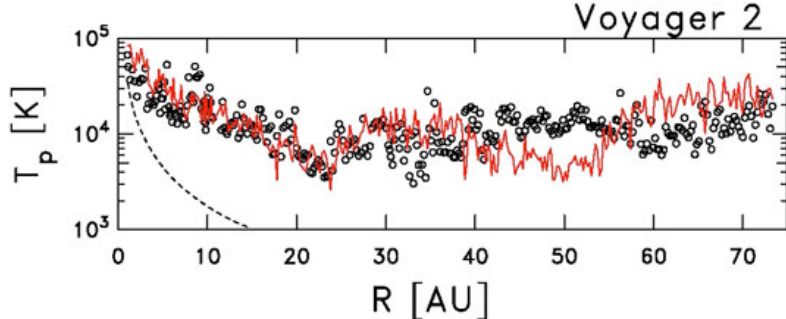


Figure 3.6: Reproduced from [Smith et al. \[2006\]](#). The proton temperature observed by the Voyager 2 spacecraft in circles. The dashed line is adiabatic expansion. The red line is a model that incorporates heating by fluid turbulence and energy injection by pick-up ions.

[2006](#)]. After distances of 20 AU, the effect of pick-up ions must be taken into account to explain the radial temperature dependence.

The heating of the solar wind plasma is not well understood and is a major goal of space plasma physics. The essential idea is that large-scale gradients in the solar wind (e.g., magnetic field, velocity) are broken up and cascade by non-linear mechanism, called the energy cascade (see Section 2.7), to small scales where the energy can be converted to particle energy [[Bruno and Carbone, 2013](#)].

3.4.1 Collisional heating

Collisions are the sole mechanism that can increase entropy in a gas, therefore will be responsible for irreversible processes. Section 2.2.1.1 discusses Coulomb collisions in the plasmas and Fig. 1.1 displays some collision times. The deflection time for solar wind protons is 10^8 seconds and electrons is 10^6 seconds. These time scales are much larger than all other time scales in the solar wind.

While the variation in density and temperature (the quantities that determine Coulomb collision frequency) in the solar wind is large, these numbers suit the general conclusion, that the solar wind is collisionless after a few solar radii from the Sun [[Marsch, 2006](#)]. A classic study of collisions in the solar wind by [Marsch and Goldstein \[1983\]](#) show that for only low temperature and high density (not a common state of the solar wind), when the classical collision frequency is large, there is evidence for collisions dictating the observed distribution functions.

It is pretty well accepted that the solar wind at 1 AU must have experienced non-collisional heating to be in the state observed [[Hartle and Sturrock, 1968](#), [Cranmer, 2014](#)]. This is an important reason the primary study of this thesis was necessary.

3.4.2 Wave-particle interactions

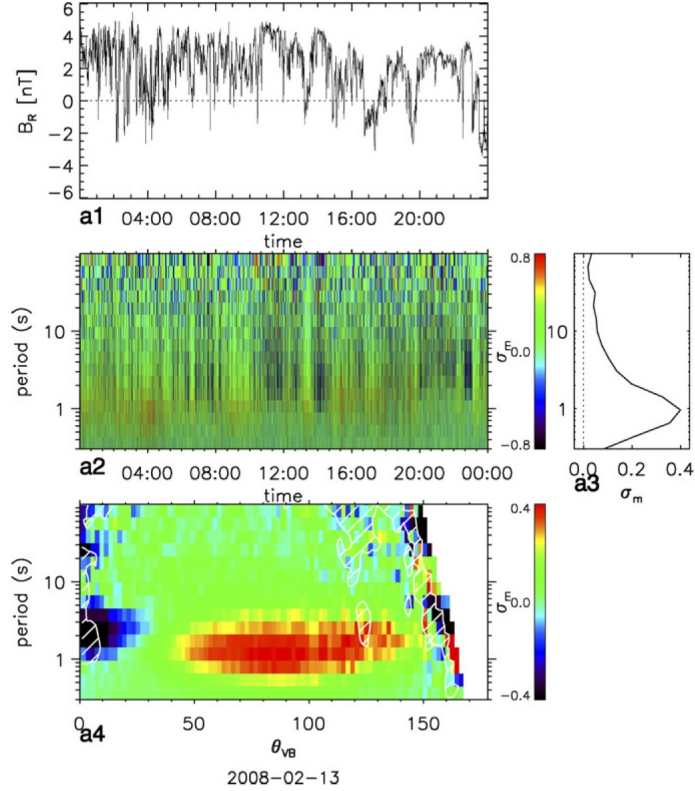


Figure 3.7: Reproduced from He et al. [2011]. The top panel is the radial magnetic field measured by the STEREO spacecraft. The middle panel with color is the reduced fluctuating magnetic helicity which has period dependence on the vertical axis and time dependence on the horizontal axis. The bottom panel has been rotated into local magnetic field coordinates so the horizontal axis is the angle between the solar wind velocity direction and magnetic field at that period, centered on that time.

Observational support for heating by plasma waves is displayed in Fig. 3.7. In Section 2.5.1.2 the proton cyclotron and kinetic Alfvén wave were discussed, while the proton cyclotron was discussed in the context of growth, this wave experiences Landau damping as well. The magnetic helicity signature (not discussed here, see He et al. [2011]) is consistent with the dark blue area for the parallel proton cyclotron wave and red for the oblique kinetic Alfvén wave. This observation shows that the waves are present and probably participate in the increase of temperature. This is not irreversible heating, but a plasma process that can increase the temperature.

3.4.3 More sources of heating

To not be ignorant about solar wind heating, here are some more ways that plasma can be heated, applicable to the solar wind. At low plasma beta particles will scatter stochastically off structures on the scale size of the gyro-radius, for which turbulence can provide through the energy cascade, heating the plasma [Chandran et al., 2010].

The structure of the magnetic field fluctuations, when turbulent, can create the setting for reconnection in current sheets intermittently spaced throughout some plasma volume, whereby reconnection is an efficient heating process [Osman et al., 2011]

Additionally, instabilities (treated in a broader context in Section 3.5), are wave-particle interactions that will heat and cool the plasma, in particular anisotropic to the magnetic field. Their role in heating is not well established.

3.5 Instabilities

Instabilities play a significant role in plasma physics (see Section 2.5) due to the abundance of free energy when the system is not at equilibrium. They lead to conversion of energy between the particles and fields (see Section 2.6). They are a central theme in understanding weakly collisional plasmas and the literature on them is extensive [Melrose, 1986, Gary, 1993].

In the solar wind, the role of instabilities, for protons, is well summarized in Hellinger et al. [2006]. The temperature anisotropic proton cyclotron instability was considered in the text surrounding Fig. 2.3. The basic prescription for this class of instabilities is to study the electromagnetic dielectric tensor with a bi-Maxwellian distribution function and keep the electrons Maxwellian. Then the instability growth rate is well-parameterised by the two parameters $T_{\perp}^p/T_{\parallel}^p$, β_{\parallel}^p . In particular, well enough to fit contours of maximum γ/Ω_{pc} , where γ is the growth rate, and Ω_{pc} is the proton cyclotron frequency.

Figure 3.8 displays measurements made by the Faraday cup on the Wind spacecraft over the years 1995-2001 for solar wind speed < 600 km /s. The contours of the growth rates constrain the observations. It can be understood in this way, that once the thresholds are crossed, the plasma is unstable. The linear stage growth stage is secular so it quickly becomes unphysical; the quasi-linear stage takes over (described in Section 2.6) where the particle energy is converted into waves causing heating/cooling and relaxation of the plasma (i.e., decrease of temperature anisotropy). This stage of the instability has less evidence, and has only been supposed by looking at the details of the distribution function for hints of quasi-linear heating [Marsch, 2006]. This will be treated again in

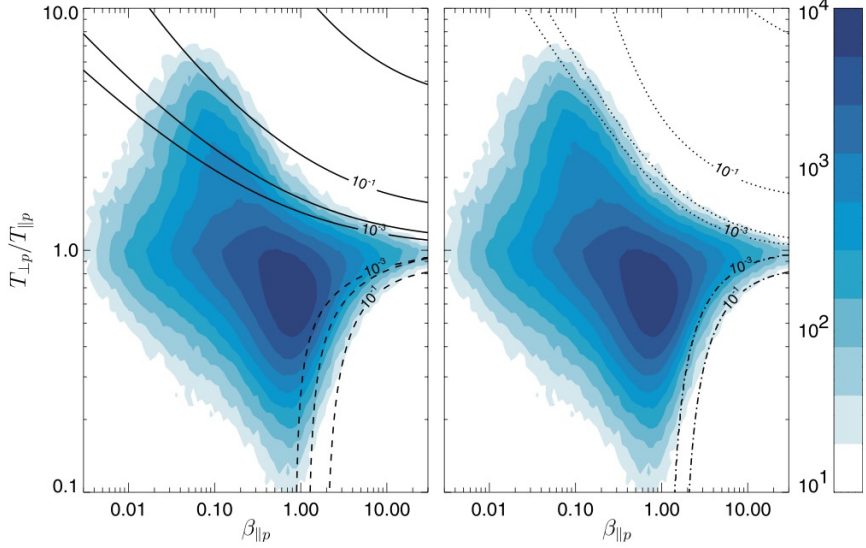


Figure 3.8: Reproduced from Hellinger et al. [2006]. The joint histogram of the proton temperature anisotropy (vertical axis) and the parallel proton beta (horizontal axis) is indicated with the color bar at the right. The contours drawn here represent the proton cyclotron instability (solid), parallel firehose instability (dashed), mirror instability (dotted), and the oblique firehose instability (dash-dot).

Chapter 6. A major effect of the instabilities, in the quasi-linear stage, is to restore the system towards an equilibrium state (see Section 2.6).

To speak a bit more about instabilities in the solar wind, the discussion will steer away from measurements at 1 AU. Matteini et al. [2007] repeated the analysis of Hellinger et al. [2006] with observations by the Helios spacecrafts at radial distances closer to the sun to show that the expansion of the solar wind causes the instabilities to play a role. The solar wind, just after acceleration near to the sun, is at low beta, and as it expands the magnetic field strength decreases according to the Parker spiral, and the density drops due to expansion, which decreases the proton temperature anisotropy and increases the parallel proton beta. This effect has been explored for other species and other effects like collisions have been included to explain features of the solar wind at 1 AU in great detail by Yoon [2017]. Other mechanisms have been proposed for instigating instabilities, such as large-amplitude compressive waves [Verscharen et al., 2016], and Alfvén waves [Squire et al., 2017a], and turbulence [Servidio et al., 2015].

3.6 Observations of compressive fluctuations

In Section 3.6 the anisotropic limit of the MHD dispersion relations were shown where two compressive waves, the Alfvén wave and the entropy wave were briefly introduced. The Alfvén wave is the dominant wave mode observed in the solar wind dating back to the famous study by [Belcher and Davis \[1971\]](#). These waves are not compressive until the wave frequency matches the gyrofrequency, then called the kinetic Alfvén wave, which was discussed in Fig. 2.4.

One of the first studies conducted on compressive fluctuations by [Burlaga and Ogilvie \[1970\]](#) using Explorer 34 data found that at large scales ~ 2 day averages, the thermal (only protons) and the magnetic field were correlated, which is indicative of stream structure interactions. The accelerated solar wind is patchy at its source, so streams will interact creating compressions of the fields. This picture is also confirmed by [McComas et al. \[1995\]](#) who used Ulysses data to study helio-latitudinal effects, where the solar source region is different i.e., the size of the patches is different. The finding is a different scale separating the correlated and anti-correlated pressures. Both studies found that at smaller scales the thermal and magnetic pressure are anti-correlated. An example of what a spacecraft detection of the smaller scale structure looks like appears as Fig. 3.9.

Much of the literature on compressive waves in the solar wind has been guided by the theoretical study of [Barnes \[1966\]](#) who found that all compressive wave modes are severely damped in a collisionless plasma. This led [Burlaga and Ogilvie \[1970\]](#) to consider these measurements as structure, not waves. This then led many studies on compressive fluctuations, where the anti-correlated magnetic and kinetic pressure, was thought to indicate the perpendicular limit of the slow-mode since its propagation speed and damping factor go to zero, but continue to call them pressure balance structures [[Tu and Marsch, 1995, 1994](#)].

Single-spacecraft measurements of plasma quantities give a reduced picture of the solar wind. It is difficult to procure wave properties, e.g., propagation direction and speed. First, the polarization and magnetic helicity need to be well-measured, which is difficult since the polarization depends on two directions of the electric field, a notoriously difficult measurement to make. Next, the measurement is affected by the flow direction. Typically the propagation angle is the angle between the magnetic field and the direction of propagation of the wave. The flow direction of the solar wind then dictates the observed direction relative to the magnetic field, therefore the wave must be propagating in this direction.

This forces researchers to rely on a set of diagnostics that are simply cross-correlations of variables (e.g., cross-correlation of the temperature and magnetic

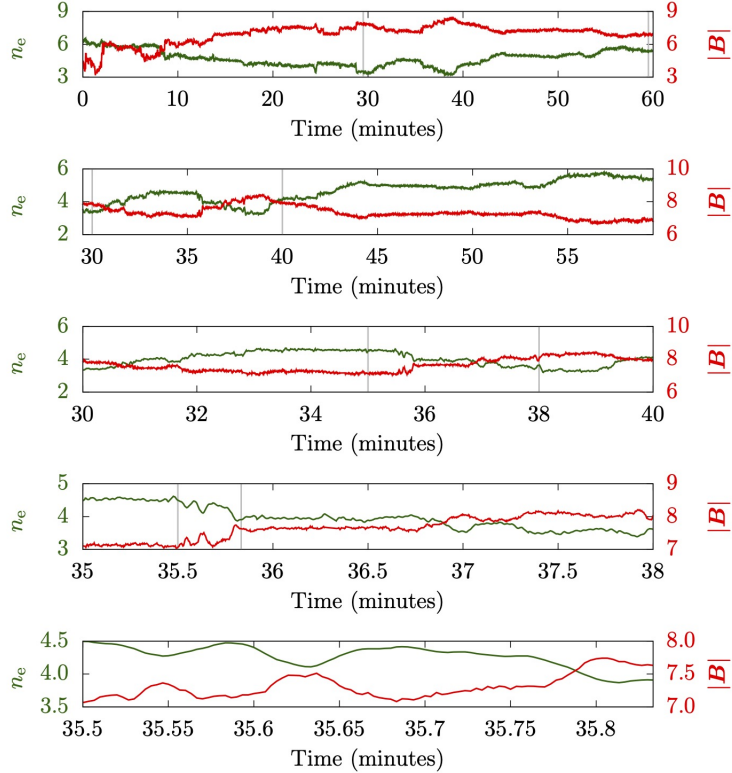


Figure 3.9: Reproduced from Verscharen et al. [2019]. The green colors are the electron density and the red colors are the magnetic field strength both measured by the Cluster spacecraft. Light grey vertical lines indicate the time scale of the panel that follows below.

field pressure) generated from linear theory [Gary, 1993]. While it is readily implemented, it is significantly less direct than measuring the polarization and does not give any information about propagation direction. The characteristic cross-correlation used to identify the slow-mode is between the thermal pressure and magnetic pressure. Due to the typical closure of fluid equations, being the polytropic equation of state, the pressure and density are coupled in a simple manner, so the density is used as well.

The electron density and magnetic pressure were found to be anti-correlated across a broadband of frequencies [Kellogg and Horbury, 2005]. The same diagnostic was then used to show the fraction of fast-mode to slow-mode has to be nearly zero [Howes et al., 2011] to explain the solar wind compressive fluctuations. This diagnostic was combined with cross-helicity and the flow angle to show that the compressive fluctuations are consistent with oblique slow-modes [Yao et al., 2013]. The general consensus of the community is that compressive fluctuations in the solar wind are indeed slow-modes [Verscharen et al., 2017].

At scales between the proton and electron plasma frequencies the ion acoustic wave has been directly observed by Gurnett and Frank [1978] with some follow up studies. It appears that the wave is generated by the local electron heat flux. While this is an interesting body of research, the focus of the thesis is on larger scale compressive fluctuations because they probe the equation of state of the solar wind.

The general idea is that they are produced by stream interactions [Tu and Marsch, 1995] or expansion and cascaded to smaller scales (to be discussed in Section 3.7), and produced by the parametric decay instability [Derby, 1978, Bowen et al., 2018], which is a non-linear process. More on compressible fluctuations and their role in turbulence is discussed in Section 3.7.3.

3.7 Solar wind turbulence

The theory of fluid plasma turbulence was treated in Section 2.7 where predictions for the magnetic field energy spectrum were presented. Section 3.4 discussed a heating scenario where turbulence transports energy in scale to where it can be efficiently converted to thermal energy. In this brief section, a short history of observations that pertain to predictions and some fundamental results will be shown.

3.7.1 The natural turbulence laboratory

Coleman [1968] presented the power spectral density of the magnetic field measured by the Mariner 2 spacecraft near to 1 AU. He showed for a large span in frequency that the power spectral density follows a power law consistent with the prediction of Kraichnan -3/2 (see Section 2.7), the power in the fluctuations is anisotropic and the inferred heating rate is sufficient to describe the measured proton temperature near 1 AU. This birthed the field of solar wind turbulence.

It did take a while before the solar physics community was convinced that the solar wind is indeed turbulent. It was not until the Voyager spacecrafts measured magnetic field power, to around 10 AU, that it became clear that only turbulent transport models could describe the radial scaling of the magnetic field fluctuations Zank et al. [1996].

The reason it is called a natural laboratory, coined by Bruno and Carbone [2013], is due foremost to the fact that the plasma and electromagnetic fields are directly measurable and the solar wind is turbulent. In addition, the flow speed is large enough to apply Taylor's assumption and the whole steradian of magnetic field geometries are measurable. Taylor's assumption is that when the flow speed V_{sw} is much faster than the temporal frequency (e.g. wave

frequency) the time cadence Δt of the measurement can be used to convert to a spatial wavenumber $k \approx 1/\Delta t V_{\text{SW}}$ [Bruno and Carbone, 2013]. The magnetic field geometry allows measurements with respect to the magnetic field, and together with Taylor’s assumption, the wavenumber parallel and perpendicular to the magnetic field can be measured. Finally, the solar wind plasma spans a wide range in the plasma beta (protons and electrons) and presents a variety of large-scale structure which drives the turbulence.

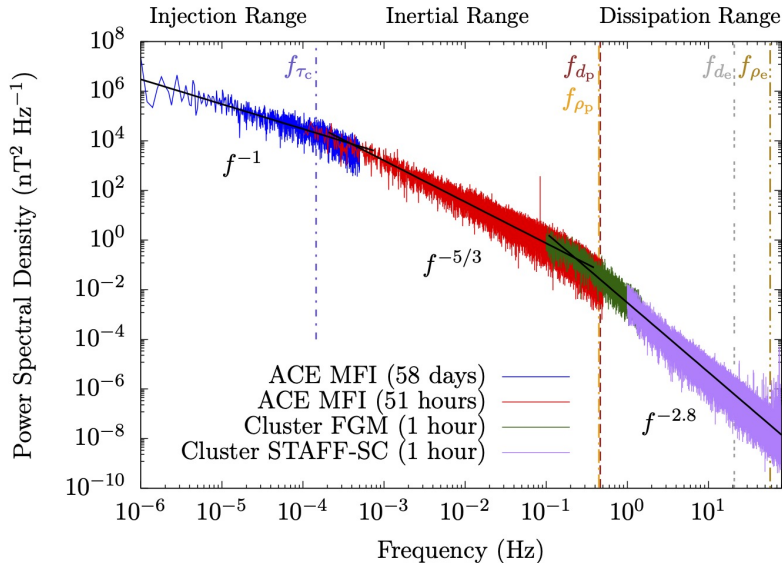


Figure 3.10: Reproduced from Verscharen et al. [2019]. Measurements of the magnetic field power spectral density, see the figure annotations, span more than 7 decades in spacecraft frequency. The color labelled frequencies are the inverse correlation time f_{τ_c} , and the proton inertial length f_{d_p} , the proton gyro-radius f_{ρ_p} , the electron inertial length f_{d_e} , the electron gyro-radius f_{ρ_e} all converted to spacecraft frequency with Taylor’s assumption. The black labels indicating power law in frequency, are typical to the solar wind at 1 AU.

The modern picture of the magnetic field power spectrum at 1 AU can be seen in Fig. 3.10. The ranges characterized by different power laws in frequency are present. First, the f^{-1} range where it is thought that fluctuations at this scale break-up and then the energy is cascaded through the inertial range. The inertial range scales as $f^{-5/3}$ for the majority of the solar wind measurements until frequencies near 10^{-1} Hz, which roughly coincide with the proton gyroradius and proton inertial length. It is not emphasized in this figure, but near to 10^{-1} Hz there is the so called transition region, before the dissipation range, which is characterized by the $f^{-2.8}$ power law. In these ranges, it is thought that the electromagnetic energy is then able to interact strongly with particles and energize or heat the plasma.

3.7.2 Power laws and anisotropy

The anisotropy of the magnetic field power spectrum was suggested by [Coleman \[1968\]](#) and for decades after various models were proposed to explain the anisotropy [[Bruno and Carbone, 2013](#)], as it is relevant to the heating mechanisms (see Section 3.4.2). [Horbury et al. \[2008\]](#) demonstrated that using the local magnetic field frame provided the scaling laws consistent with the critical balance model by [Goldreich and Sridhar \[1995\]](#).

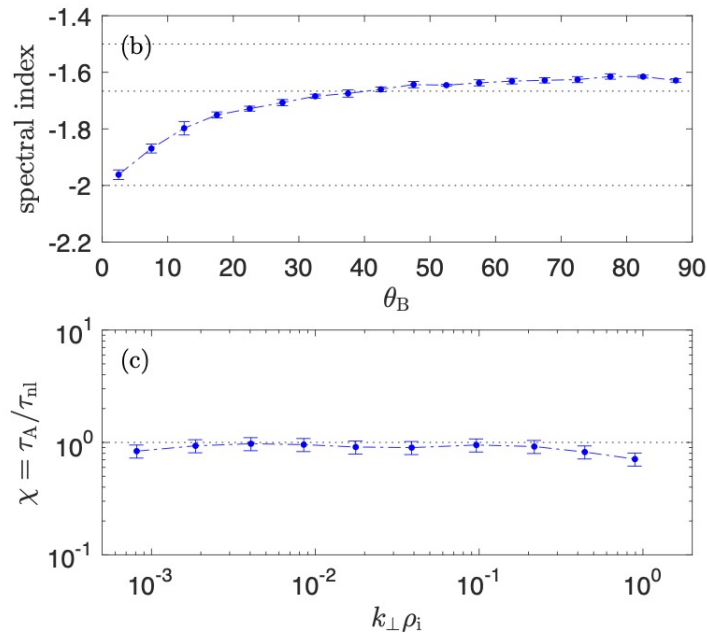


Figure 3.11: Reproduced from [Chen \[2016\]](#) using data from the Wind spacecraft. The top panel is the spectral index of the magnetic field power spectrum conditioned on the local magnetic field direction. The bottom panel is the ratio of the Alfvén time to non-linear time. See Section 2.7.0.3 for definitions.

Figure 3.11 shows the exemplary evidence for critical balance from solar wind measurements. In the top panel, the spectral index is conditioned on the angle between the flow and local magnetic field direction, hence the anisotropy of the wavenumber. Parallel to the field, the spectral index is near to -2, and perpendicular it follows a -5/3 spectrum. The bottom panel shows the ratio of the Alfvén time to non-linear time is consistently ~ 1 throughout the inertial range. The horizontal axis of Fig. 3.11 is converted from spacecraft frequency to wavenumber with Taylor's assumption.

3.7.3 Compressive turbulence

Almost all theories of turbulence stem from incompressible MHD and compressive turbulence is considered in the aftermath. This in part is due to the fact that %90 of the fluctuations measured in the solar wind are non-compressive [Chen, 2016]. For a long time, this was considered consistent with Barnes [1966], but as stressed in Section 3.6, there is a compressive component. Some theories of compressive turbulence were reviewed in Section 2.7.0.4.

Turning towards observations, Fig. 3.12 displays measurements of the power spectrum of the density and magnetic field strength alongside the magnetic field. Seen here, both power laws are very similar to that of the magnetic field providing evidence that they are passive to the magnetic field fluctuations discussed in Section 2.7.0.4. Additionally, the power in these fluctuations is much reduced.

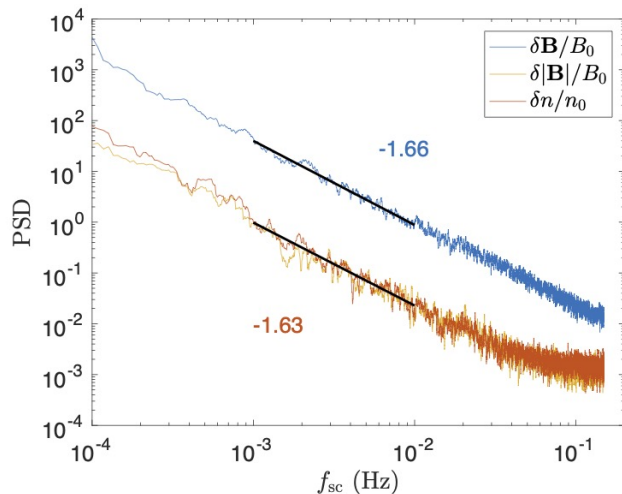


Figure 3.12: Reproduced from Chen [2016] using data from the Wind spacecraft. Power spectral density, normalized to be unitless, for the quantities annotated on the plot. Black lines indicate the slope of the power law.

The anisotropy of the compressive fluctuations was addressed in Chen [2016] as well, reproduced as Fig. 3.13. Here it seen that the compressive fluctuations are more anisotropic than the Alfvénic fluctuations.

While it seems that there is evidence for a passive view of the compressible fluctuation, seen in Fig. 3.12, there is also opposing evidence, seen in Fig. 3.13, but present studies and theory do not have the clarity necessary to make a definitive statement about the role of compressive fluctuations in plasma turbulence. For example, the lack of Alfvénic fluctuations is accompanied by more compressible fluctuations [Bavassano and Bruno, 1989], and there is evidence

for the interplay of compressible slow-modes and Alfvén modes located at temperature enhancements in the solar wind [He et al., 2015a].

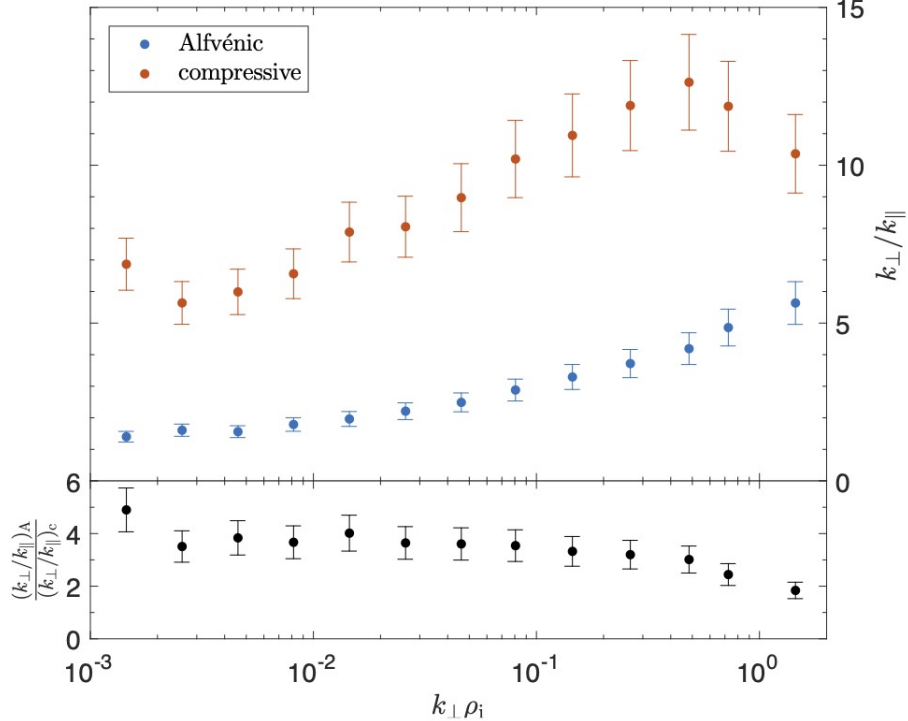


Figure 3.13: Reproduced from Chen [2016] using data from the Wind spacecraft. The colors are annotated on the top panel. The bottom panel is the ratio. The horizontal axis is the perpendicular wavenumber converted with Taylor’s assumption.

3.8 Instruments

The instruments onboard spacecrafts will be briefly introduced for the purpose of discussion. The instruments are the electrostatic analyzer and the fluxgate magnetometer.

3.8.1 Top-hat electrostatic analyzer

The electrostatic analyzer is employed to study the fine structure of the distribution function due to the ability to resolve the particle energy to high precision. Figure 3.14 shows a particle entering the collimator and hitting the detector. As seen on the bottom part of the figure, a voltage difference of $2\mathcal{E}$ across the two shells. The resulting electric field will deflect the entering particle, if the kinetic

energy to charge ratio of the particle is within the right range, the particle will follow through the collimator into the detector. The voltage difference can be swept through a set of values to resolve a range of energy.

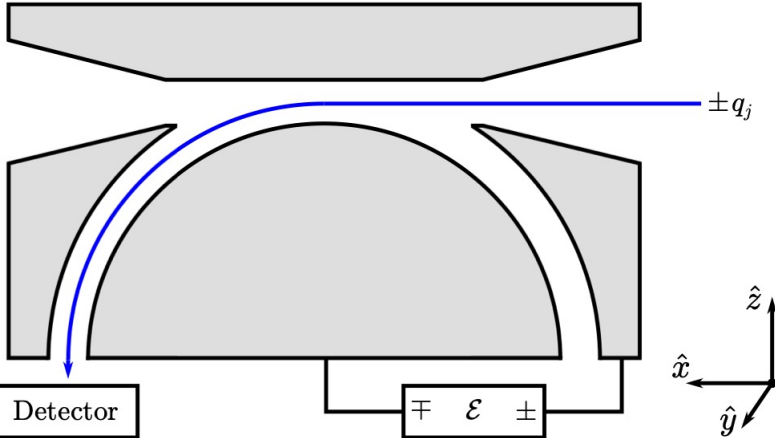


Figure 3.14: Reproduced from [Verscharen et al. \[2019\]](#). The top-hat design becomes visible from the figure. This is a slice through the instrument, which is symmetric about the \hat{z} direction, through the center of the instrument. The particle of charge $\pm q_j$ will follow the trajectory in blue through the collimator to the detector if it suffices a condition imposed by voltage difference of 2ϵ .

The detection is typically done by electron multipliers. This is done by constructing a plate with an electrostatic potential, so that when a charged particle strikes it, a cascade of electrons occurs. In a simple sense, the detection is amplified and a current is produced which can be counted by a detector. After the detection, there is a dead time, when the plate has not charged to its detection state.

Returning to Fig. 3.14, looking at where the particle is entering the collimator, there is a field of view that the particles must also suffice to be detected. Typically, the spacecraft relies on the spin of the spacecraft to capture the full view, say rotating around \hat{y} . Due to the top-hat design, the particle can enter from all directions in the \hat{x} , \hat{y} -plane. This provides the number of particles with two angular coordinates and energy per charge. The number of particles collected in a time interval is then the collection volume times the density. Then it can be related to the particle distribution function used in plasma physics theory.

This distribution function can then be rotated or transformed into a cartesian coordinate system. Moments of this distribution function are often reported, such as the density or pressure. This is done in a simple manner, considering the energy and angle coordinate system and then making the appropriate moment.

3.8.1.1 Wind electrostatic analyzer

The ESAs on Wind are described in Lin et al. [1995a] where details on energy and angular resolution can be found. The name of the suite of instruments is called 3DP which consists of two electron and two proton electrostatic analysers, and then two additional solid state telescopes that detect electrons and protons to very high energies. The PESA-L electrostatic analyser measures solar wind protons, where ‘‘L’’ corresponds to the lower sensitivity which covers the energy range of the protons 3 eV to 30 keV. Throughout out the thesis PESA-L and 3DP refer to the electrostatic analyser. The data products are off loaded at different time cadences and quality. A couple capabilities of Wind worth mentioning, is that there are two positive ion ESAs, one for the lower energies and another for the higher energies, making the accuracy on the core consistently good. Second, the instruments have dedicated microprocessors that compute the moments of the distribution function.

3.8.2 Magnetometer

Measurements of the magnetic field are typically made by a fluxgate magnetometer for low frequency < 10 Hz or a search coil magnetometer for > 10 Hz. In this section a brief description of the fluxgate magnetometer is given since it is the instrument on the Wind spacecraft that provides the magnetic field database used for this thesis. The instrument is called the magnetic field instrument (MFI) [Lepping et al., 1995].

The description is based on Figure 3.15 from Verscharen et al. [2019]. The basic idea is a ferromagnet wrapped by two coils, one that is the drive coil and the other is the sense coil. Starting with the top left panel, the black line $H_d(t)$ is an applied triangle wave in time, to the drive coil. If there is an external field ΔH_z , which is to be measured, the resulting field is $H(t) = \Delta H_z + H_d(t)$. It is offset. The ferromagnet is chosen so its property H_c , the saturated field (the maximum internal field due to the applied field) is below the maximum of the driven field. It is chosen so that it saturates for positive and negative values of H . This can be seen in the center left panel, where the horizontal axis is H . The internal field, which experiences the saturation, is B on the vertical axis. On this panel, the time dependence cannot be seen; the blue shaded regions are when the field is saturated, corresponding to measurable saturation in $B(t)$ shaded in pink (center right panel). Notice how the offset effects the signal. The waveform of the internal magnetic field induces a voltage via the time dependent magnetic flux, which can be measured by the sense coil seen in the bottom right panel.

Clearly, the offset provides the differences between the skinny and wide pink

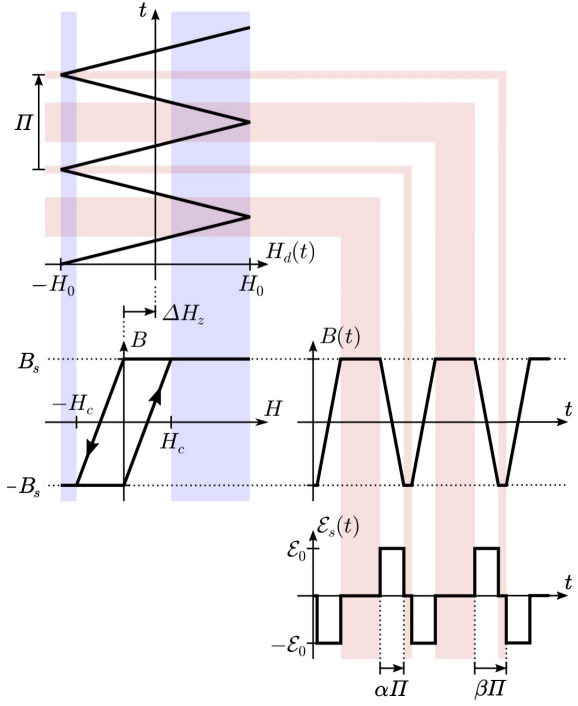


Figure 3.15: Reproduced from Verscharen et al. [2019]. The quantities here are the period of the applied field Π , the amplitude of the applied field H_0 , the critical value of the ferromagnet H_c , the applied field $H_d(t)$ (a current is applied to give this field), ΔH_z is the component of the external field to be measured, $B(t)$ is the magnetic field inside the material, B_s is the critical value of $B(t)$ due to H_c , \mathcal{E}_s is the induced voltage in the fluxgate due to $B(t)$, which has amplitude \mathcal{E}_0 . The blue shaded regions indicate when $H(t)$ (defined in text) is saturated at $\pm H_c$ and the pink shaded regions indicate when $B(t)$ will be consequently saturated at B_s .

shaded regions. A Fourier expansion of the signal then provides a measurement of the offset and the external magnetic field. When there is no offset, the signal is even, so the odd order of the expansion permit a measurement.

3.8.3 Faraday Cup

The Faraday cup makes measurements of ions by imposing a voltage barrier and measuring the current that passes the barrier. They have long been used on spacecrafts to detect ion velocity and temperature. For the purposes of this thesis, comparison between the temperature measurement by the electrostatic analyzer and Faraday cup are made, so the premise of the Faraday cup is briefly explained.

Figure 3.16 displays the basic idea of the instrument, see the caption for

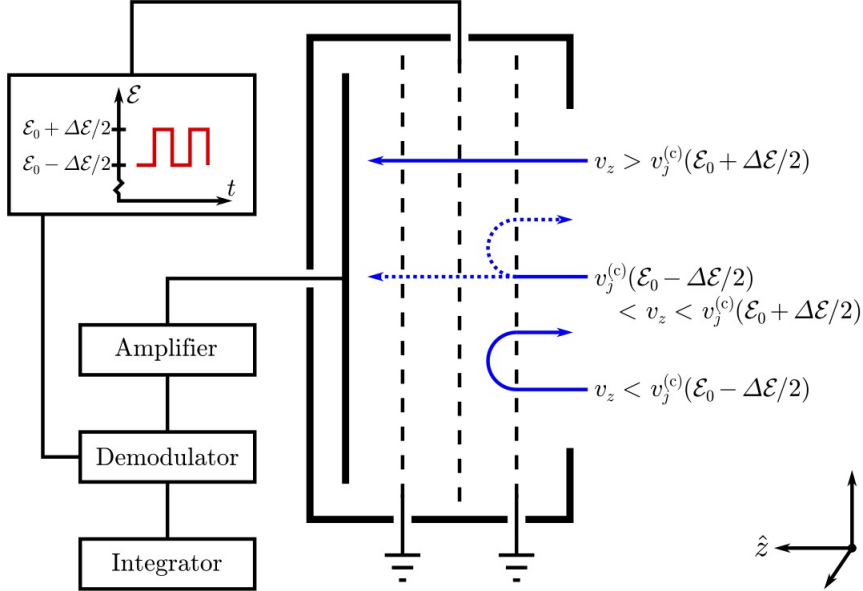


Figure 3.16: Reproduced from Verscharen et al. [2019]. This diagram aids the explanation of how the current is measured in plasma environments. The quantities are \mathcal{E} the voltage, \mathcal{E}_0 the offset voltage, $\Delta\mathcal{E}$ the peak-to-peak amplitude, t the time, v_z the normal component of the ion velocity, and $v_j^{(c)}$ the cutoff speed due to the voltage. Particle trajectories are shown in blue which enter the wide aperture which are then subjected to a voltage that is applied to middle, shown as vertical dashed lines. Some particles hit the detection plate, shown as a vertical black line, which receives the current.

the definition of the quantities and the various lines that compose the cartoon. Particles, shown as blue trajectories, will enter the aperture, and react to the voltage (\mathcal{E}) applied to the middle grid (middle vertical dashed line). The particle will pass through if the normal component of the incoming particle's velocity is greater than the cutoff velocity, and be deflected if not. The voltage is varied between two states $\mathcal{E} = \mathcal{E}_0 \pm \Delta\mathcal{E}/2$, which is represented with a graph in the top left of the figure. The measured current is then differenced between these two states. This primary measurement is then used to infer the particles energy distribution. Additional reasons that the current is varied in time is to deflect particles of opposite charge e.g., photoelectrons, as the difference has little to no effect on these particles.

A set of voltages and voltage steps then define the resolution and range of energy the Faraday cup will detect. The detection of differential current is then related to the charge, aperture area, normal velocity and the particle distribution function. To infer information about the particle distribution function, a few methods exist, and for the Faraday cup, either the particle distribution function

is inferred through the differential current to calculate moments (e.g., density, velocity, etc.) or model distributions can be fit.

The Wind Faraday cup instrument is explained in [Ogilvie et al. \[1995\]](#). The two Faraday cups provide measurements of the density, velocity and temperature of the solar wind ions. The temperature anisotropy to the background magnetic field, is used in this thesis to better understand the data products that are measured by the electrostatic analyzer. For further information on how the temperature anisotropy is calculated, see [\[Kasper et al., 2006\]](#).

Chapter 4

Collisional-kinetic magnetohydrodynamics: dispersion relation

In this thesis the kinetic magnetohydrodynamic equations (KMHD) are studied numerically to form a basis for the understanding of compressive fluctuations in the solar wind. The essential attributes retained in this description is the collisionless damping of hydromagnetic waves. The essential insight of the thesis is that effective collision processes act to lessen the role of collisionless damping and alter the density, pressure and magnetic field fluctuations in a physically identifiable manner. This leads to a measurement of the effective collision frequency. This effective collision processes is modelled in the kinetic equation i.e., the KMHD equations. The final set of equations are linearised and a numerical model is built to study the properties of the waves which are compared with solar wind measurements in Chapter 5.

The history and utility of the KMHD have been explored in Section 2.3. In Section 2.2.3, the Bhatnagar-Gross-Krook operator (BGK) was introduced, which plays the role of the effective collision operator in this thesis. The combined system of equations, now called the KMHD-BGK, includes the physical effects of transit-time damping, Landau damping, and effective collisionality. The effective collisionality modulates the kinetic effects permitting the exploration of numerical solutions between the fluid and kinetic regime.

A flow chart of the KMHD-BGK or collisional-kinetic magnetohydrodynamic equations has been provided as Fig. 4.1 to show the derivation of the final equations. To be clear about the approximations and regions of applicability of these equations, they are appropriate to a non-relativistic plasma $v_A/c \ll 1$, where v_A is the Alfvén speed and c is the speed of light, so rest masses can be used and

no displacement currents arise. The system is assumed to be gyrotropic, the so-called magnetized plasma approximation, where the gyroradii ρ_s are much smaller than the characteristic length scales ($\rho_s \ll L$), e.g., an acoustic wavelength. Formally, this permits both the gyrotropic assumption and the ignorance of the 0th order (background) electric field (see Section 2.3). Last, the proton inertial length d_p is taken to be much smaller than the characteristic length scales ($d_p \ll L$) so that the ideal Ohm's Law can be used. These assumptions can be checked with measurements and can be ensured through a normalization when constructing a numerical code.

The added assumption here, due to collision operator, is that the effective collision frequency, ν_s , is much smaller than the gyrofrequency $\nu_s \ll \Omega_s$. This is necessary when working through the ordering of Kulsrud [1983] which provides the formal arguments that set the background electric field to zero, enforcing a gyrotropic distribution function.

Collisional-kinetic magnetohydrodynamic equations

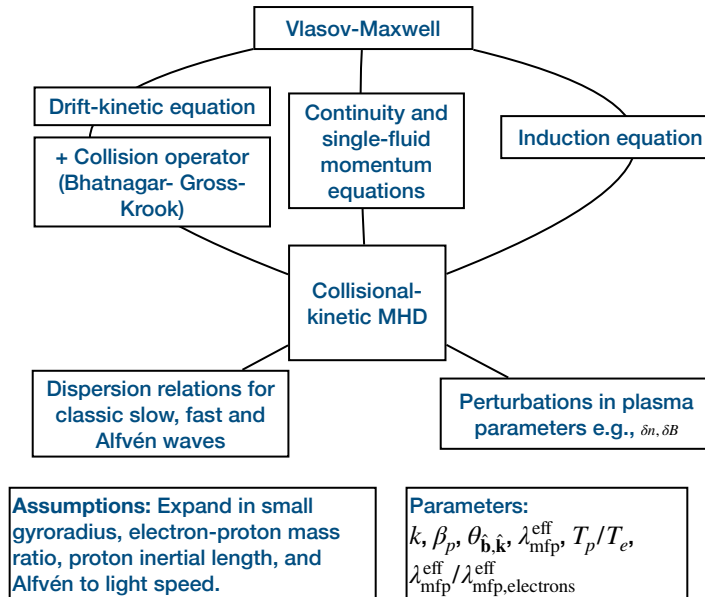


Figure 4.1: Starting at the top box labelled “Vlasov-Maxwell” three branches pass to the “Collisional-kinetic MHD” box, identifying the constituents of the set of equations. The two branches leaving the “Collisional-kinetic MHD” box are the linear analysis that produce dispersion relations and perturbations of the plasma parameters. The parameters of the model in order according to the box labelled “Parameters” are the wavenumber, proton beta, propagation angle relative to the background magnetic field, the effective mean-free-path, the proton to electron temperature ratio, and the effective mean-free-path ratio.

The system of equations, in particular the assumptions, are valid for low frequency / large wavelength scales of the solar wind (Chapter 3). The normal modes of this system contain the compressive slow-mode (Section 3.6) which is the dominant mode observed in the solar wind. Compressive fluctuations perturb quantities like the pressure and density, which are sensitive to the equation of state, and the effective mean-free-path. Therefore, a model of the slow-mode wave is useful to measure the effective mean-free-path (Chapter 5).

This Chapter introduces the system of equations in Section 4.1 where most of the derivations appear in the appendices. The normal modes of the system of equations are computed in Section 4.2. Then they are normalized and the eigenvalue problem is constructed in Section 4.3. The numerical methods used to solve the system of equations appear in Section 4.4. In Section 4.5 the numerical solutions are presented where the dispersion relation for various parameter regimes is shown. Finally, the method of correlations and amplitude ratios of the fluctuating plasma quantities is shown in Section 4.6.

4.1 Equations

The drift kinetic equation,

$$\begin{aligned} & \left\{ \frac{\partial}{\partial t} + (\hat{b}_i w_{\parallel} + u_i^s) \frac{\partial}{\partial x_i} + \frac{w_{\perp}^2}{2} \frac{\partial \hat{b}_i}{\partial x_i} \frac{\partial}{\partial w_{\parallel}} \right. \\ & + \left[\frac{q_s}{m_s} E_{\parallel} - \hat{b}_i \left(\frac{\partial u_i^s}{\partial t} + u_j^s \frac{\partial u_i^s}{\partial x_j} \right) \right] \left(\frac{\partial}{\partial w_{\parallel}} + \frac{w_{\parallel}}{w} \frac{\partial}{\partial w} \right) \\ & - \frac{w_{\perp}^2}{2w} \frac{\partial u_i^s}{\partial x_i} \frac{\partial}{\partial w} + \hat{b}_i \hat{b}_j \frac{\partial u_i^s}{\partial x_j} \left[\left(\frac{w_{\perp}^2}{2} - w_{\parallel}^2 \right) \frac{1}{w} \frac{\partial}{\partial w} - w_{\parallel} \frac{\partial}{\partial w_{\parallel}} \right] \left. \right\} f_s \\ & = -\nu_s [f_s - F_s] \end{aligned} \quad (4.1)$$

is derived in Appendix B.1. The quantities relevant to a particle species are given a sub/superscript “*s*” denoting “*e*” for electrons and “*p*” for protons. The quantities are the unit magnetic field vector $\hat{b}_i = b_i/|b_j|$, the parallel (perpendicular) peculiar velocity w_{\parallel} (w_{\perp}), the guiding-center velocity $u_i^s = u_i^s(t, x_i)$, the parallel electric field E_{\parallel} , $f_s = f_s(t, x_i, v_i)$ is the single-particle distribution function, and ν_s is the effective collision frequency. The equilibrium distribution function $F_s = F_s(v_i; n_s, T_s)$ has space and time dependence through the density $n_s = n_s(t, x_i)$ and the temperature $T_s = T_s(t, x_i)$.

The derivation in Appendix B.1 transforms into the guiding center so that the peculiar velocity vector is $w_i = v_i - u_i^s$ where v_i is in the laboratory frame and u_i^s is the guiding center frame. This is the essential idea behind the drift kinetic approach is to choose u_i^s to be the $E \times B$ drift velocity because this

frame, to 0th order is gyrotropic, so one of components of the peculiar velocity can be neglected. Non-gyrotropic terms constitute an immense difficulty so this simplification is powerful [Hunana et al., 2019b].

Moments of the kinetic equation are necessary for the density, velocity and pressures. It is easier to take moments of the Vlasov equation, with the BGK operator as the collision operator, and then apply the assumptions, rather than taking moments of the drift kinetic equation (Eq. 4.1). The drift kinetic equation is useful for breaking the moment-chain linearly at 2nd order, a more complex task. The 0th order moment gives the continuity equation,

$$\frac{\partial}{\partial t} n_s + \frac{\partial}{\partial x_i} n_s u_i^s = 0, \quad (4.2)$$

where the right hand side is zero since the BGK operator conserves particle number (see Section 2.2.3). The 1st order moment gives the momentum equation,

$$m_s \left(\frac{\partial}{\partial t} n_s u_i^s + \frac{\partial}{\partial x_j} n_s u_i^s u_j^s \right) = - \frac{\partial}{\partial x_j} p_{ij}^s + q_s n_s \left(E_i + c^{-1} \epsilon_{ijk} u_j^s b_k \right), \quad (4.3)$$

where the total pressure tensor is p_{ij}^s , which due to the assumption of gyrotropy, will be reduced. There is no collisional term because the BGK operator conserves momentum. The typical approach is to add the proton momentum equation to the electron momentum equation to eliminate the electric field with the quasi-neutral assumption $n_p = n_e$. Then use the mass ratio $m_p \gg m_e$ to ignore the electron inertia, giving the single-fluid momentum equation,

$$\begin{aligned} m_p \left(\frac{\partial}{\partial t} n_p u_i^p + \frac{\partial}{\partial x_j} n_p u_i^p u_j^p \right) \\ = - \frac{\partial}{\partial x_j} (p_{ij}^p + p_{ij}^e) + c^{-1} \epsilon_{ijk} b_k (u_j^p q_p n_p + u_j^e q_e n_e). \end{aligned} \quad (4.4)$$

The final term here is the current $j_i = (u_j^p q_p n_p + u_j^e q_e n_e)$. The current is prescribed from Ampere's Law (Eqs. 2.38) by using the non-relativistic approximation $v_A/c \ll 1$ to neglect the displacement current,

$$j_i = \frac{c}{4\pi} \epsilon_{ijk} \frac{\partial}{\partial x_j} b_k. \quad (4.5)$$

The total momentum equation is then,

$$\begin{aligned} m_p \left(\frac{\partial}{\partial t} n_p u_i^p + \frac{\partial}{\partial x_j} n_p u_i^p u_j^p \right) \\ = - \frac{\partial}{\partial x_j} (p_{ij}^p + p_{ij}^e) + \frac{1}{4\pi} b_k \left(\frac{\partial}{\partial x_k} b_i - \frac{\partial}{\partial x_i} b_k \right). \end{aligned} \quad (4.6)$$

Next, a time-evolution equation for the magnetic field is derived from Faraday's Law (Eqs. 2.38) by deriving an Ohm's Law for electric field. The procedure is to multiply the proton and electron momentum equations by their respective charges q_s and add them, then using Ampere's and Faraday's Laws to rewrite the equation. Next, the equation is reduced by using the smallness of the mass ratio m_e/m_p , the proton inertial length d_p and the non-relativistic approximation $v_A/c \ll 1$. Neglecting the Hall current gives,

$$E_i = -\epsilon_{ijk} u_j^p b_k. \quad (4.7)$$

Inserting this into Faraday's Law gives,

$$\frac{\partial}{\partial t} b_i = \epsilon_{ijk} \frac{\partial}{\partial x_j} \epsilon_{klm} u_l^p b_m = \frac{\partial}{\partial x_j} u_i^p b_j - \frac{\partial}{\partial x_j} u_j^p b_i. \quad (4.8)$$

The Eqs. D.26, 4.6, and 4.8 are closed by an equation for the pressure, which comes from the drift-kinetic equation. In this Chapter we are interested with normal modes in the linear analysis.

4.2 Normal modes

The system of equations has been assembled in Section 4.1 and now Eqs. 4.1, D.26, 4.6, and 4.8 will be linearized. The perturbations are,

$$\begin{aligned} b_i &= b'_i + b_0 \hat{b}_i, \\ E_{\parallel} &= E'_{\parallel}, \\ u_i^s &= u_i^{s'}, \\ f_s &= f'_s + F_s^0, \\ F_s^0 &= n_{s,0} \left(\frac{m_s}{2\pi k_B T_{s,0}} \right)^{3/2} \exp \left\{ -\frac{m_s}{2k_B T_{s,0}} v^2 \right\}, \\ n_s &= n_{0,s} + n'_s \rightarrow n^s + n'^s, \\ p_{\perp} &= p_{\perp,0}^s + p_{\perp}^{s'} \rightarrow p_{\perp}^s + p_{\perp}^{s'}, \\ p_{\parallel} &= p_{\parallel,0}^s + p_{\parallel}^{s'} \rightarrow p_{\parallel}^s + p_{\parallel}^{s'}, \end{aligned} \quad (4.9)$$

where the primed variables are the fluctuations about the unprimed variables (static background). First, since the guiding center frame is used, the background velocity field is zero. The background electric field is ignored, typically this is argued to be zero [Kulsrud, 1983], but this requires a reduced description, which is inconsistent with the equilibrium distribution function used in the BGK operator. Formally, both need to be assumed for a non-reduced description. This detail is discussed at length in Section 2.3. The distribution function f_s is perturbed about a static Maxwellian F_s^0 and the equilibrium distribution function used in the BGK operator F_s is the local Maxwellian, so n_s , T_s are perturbed as well.

The linearization of these equations with the above perturbations are kept to the appendices. The linearization of the drift kinetic equation (Eq. 4.1) appears in Appendix B.1.2, the continuity equation (Eq. D.26) in Appendix B.2, the single-fluid momentum equation (Eq. 4.6) in Appendix B.3, and the induction equation (Eq. 4.8) in Appendix B.4.

4.2.1 Small-amplitude Fourier analysis

The temporal Fourier transform of the system of equations, treats only the asymptotic solutions since it ignores the ballistic response, see Section 8.5 of Krall and Trivelpiece [1973]. The Fourier transform of the variables appears as,

$$\begin{aligned}
f'_s(x_\perp, x_\parallel, w_\parallel, w, t) &= \tilde{f}_s(w_\parallel, w) \exp\{i(k_\perp x_\perp + k_\parallel x_\parallel - \omega t)\}, \\
b'_i(x_\perp, x_\parallel, t) &= \tilde{b}_i \exp\{i(k_\perp x_\perp + k_\parallel x_\parallel - \omega t)\}, \\
u'_i(x_\perp, x_\parallel, t) &= \tilde{u}_i \exp\{i(k_\perp x_\perp + k_\parallel x_\parallel - \omega t)\}, \\
E'_\parallel(x_\perp, x_\parallel, t) &= \tilde{E}_\parallel \exp\{i(k_\perp x_\perp + k_\parallel x_\parallel - \omega t)\}, \\
\tilde{n}_s(x_\perp, x_\parallel, t) &= \int d^3w \tilde{f}_s(w_\parallel, w, t) \\
&= n'_s(x_\perp, x_\parallel, t) \exp\{i(-k_\perp x_\perp - k_\parallel x_\parallel + \omega t)\}, \\
\tilde{p}_\perp^s(x_\perp, x_\parallel, t) &= \frac{m_s}{2} \int d^3w w_\perp^2 \tilde{f}_s(w_\parallel, w, t) \\
&= p_\perp^{s,\prime}(x_\perp, x_\parallel, t) \exp\{i(-k_\perp x_\perp - k_\parallel x_\parallel + \omega t)\}, \\
\tilde{p}_\parallel^s(x_\perp, x_\parallel, t) &= m_s \int d^3w w_\parallel^2 \tilde{f}_s(w_\parallel, w, t) \\
&= p_\parallel^{s,\prime}(x_\perp, x_\parallel, t) \exp\{i(-k_\perp x_\perp - k_\parallel x_\parallel + \omega t)\}. \tag{4.10}
\end{aligned}$$

These can inserted directly into the linearized equations so that wave properties can be studied. The Fourier analysis is kept to the Appendices. The Fourier transform of the perturbed distribution function is shown in Appendix B.1.3, and then moments are taken, beginning in Appendix B.1.4, for the macroscopic

variables. Appendix B.1.4 introduces the plasma dispersion function and various results on the plasma dispersion function.

The density moment, the perpendicular pressure, the parallel pressure are Fourier analyzed and then they are simplified in Appendix B.1.4.4. Next, the Fourier analysis of the continuity equation is in Appendix B.2.2, the single-fluid momentum in Appendix B.3.2, and the induction equation in Appendix B.4.2.

4.3 Normalization and eigen-problem

The following normalizations are introduced,

$$\begin{aligned} \nu &\rightarrow \nu \omega_p, & \tilde{n}_s &\rightarrow \tilde{n}_s n_p, & \tilde{u}_\alpha^p &\rightarrow \tilde{u}_\alpha v_s, & \omega &\rightarrow \omega \omega_p, \\ \tilde{b}_\alpha &\rightarrow \tilde{b}_\alpha B, & \tilde{p}_\alpha^s &\rightarrow \tilde{p}_\alpha^s p_B, & k_\alpha &\rightarrow k_\alpha v_s^{-1} \omega_p \end{aligned} \quad (4.11)$$

where $\alpha = \perp, \parallel$ and where the plasma frequency $\omega_p = (4\pi n_p q_s^2 / m_p)^{1/2}$, the Alfvén speed $v_A = B/(4\pi n_p m_p)^{1/2}$, the thermal speed $v_s = (2k_B T_s / m_s)^{1/2}$ and the magnetic pressure $p_B = B^2/8\pi$. The temperature is defined $T_s = p_s / n_s k_B$. The proton plasma beta $\beta^p = v_p^2/v_A^2 = p^p/p_B = 8\pi n_p k_B T_p / B^2$ where, $p^s = (2p_\perp^s + p_\parallel^s)/3$ is the background total pressure. The linear Fourier analyzed equations after normalization,

$$\omega \tilde{n} - (k_\parallel \tilde{u}_\parallel + k_\perp \tilde{u}_\perp) = 0, \quad (4.12)$$

$$\omega \tilde{u}_\perp + \frac{1}{\beta_p} (-k_\perp \tilde{b}_\parallel + k_\parallel \tilde{b}_\perp) - \frac{k_\perp}{2\beta_p} (\tilde{p}_\perp^p + \tilde{p}_\perp^e) = 0, \quad (4.13)$$

$$\omega \tilde{u}_\parallel - \frac{k_\parallel}{2\beta_p} \tilde{p}_\parallel = 0, \quad (4.14)$$

$$\omega \tilde{b}_\perp + k_\parallel \tilde{u}_\perp = 0, \quad (4.15)$$

$$\omega \tilde{b}_\parallel - k_\perp \tilde{u}_\perp = 0, \quad (4.16)$$

appearing in order as continuity from Eq. B.95, perpendicular momentum Eq. B.114, parallel momentum Eq. B.111, perpendicular induction Eq. B.122, and parallel induction Eq. B.121. The argument of the plasma dispersion functions $Z(\zeta_s)$ is redefined,

$$\zeta_s = \zeta_s^\omega + \zeta_s^\nu, \quad (4.17)$$

$$\zeta_p^\nu = \frac{i\nu_s}{v_s |k_\parallel|}, \quad \zeta_s^\omega = \frac{\omega}{v_s |k_\parallel|} \quad (4.18)$$

and then for protons and electrons the normalization,

$$\zeta_p^\omega = \frac{\omega + i\nu_p}{v_p |k_\parallel|} \rightarrow \frac{\omega + i\nu_p}{|k_\parallel|}, \quad (4.19)$$

$$\zeta_e^\omega = \frac{\omega + i\nu_e}{v_e |k_\parallel|} \rightarrow \frac{\omega + i\nu_e}{|k_\parallel|} \sqrt{\frac{T_p m_e}{T_e m_p}}. \quad (4.20)$$

The normalized Eq. B.90 and Eq. B.85 become,

$$\begin{aligned} \tilde{n}_s [1 + 2\zeta_s^2 R(\zeta_s)] - \frac{\tilde{p}_\parallel}{\beta_s} R(\zeta_s) &= \zeta_s^\omega \tilde{b}_\parallel [2\zeta_s R(\zeta_s) - Z(\zeta_s)] \\ &+ \frac{3}{2} \zeta_s^\nu \tilde{n}_s [2\zeta_s R(\zeta_s) - Z(\zeta_s)] + \frac{\zeta_s^\nu}{2} \left(\frac{2}{3} \frac{\tilde{p}_\perp^s}{\beta_s} + \frac{1}{3} \frac{\tilde{p}_\parallel^s}{\beta_s} \right) [Z(\zeta_s) - 2\zeta_s R(\zeta_s)], \end{aligned} \quad (4.21)$$

$$\tilde{n}_s \left(1 + \zeta_s^\nu Z(\zeta_s) \right) - \frac{\tilde{p}_\perp^s}{\beta_s} \left(1 + \frac{2}{3} \zeta_s^\nu Z(\zeta_s) \right) - \zeta_s^\omega \tilde{b}_\parallel Z(\zeta_s) - \frac{1}{3} \zeta_s^\nu \frac{\tilde{p}_\parallel^s}{\beta_s} Z(\zeta_s) = 0, \quad (4.22)$$

where $R(\zeta_s) = 1 + \zeta_s Z(\zeta_s)$ is used for brevity. The derivations for these are well covered in Appendix B.1.4.4. These equations are the linearized KMHD-BGK equation of state. Equations 4.21, 4.22 have been studied by Sharma et al. [2003] who investigated subsidiary expansions $\zeta_s^\omega / \zeta_s^\nu \ll 1$ on these equations to show the linearized adiabatic equation of state can be recovered. This is essential; the adiabatic equation of state is included in the KMHD-BGK description.

Now the linear system of equations can be written,

$$\begin{bmatrix}
\omega & 0 & k_{\parallel}/\beta_p & -k_{\perp}/\beta_p & 0 & -k_{\perp}/2\beta_p \\
0 & \omega & 0 & 0 & 0 & 0 \\
k_{\parallel} & 0 & \omega & 0 & 0 & 0 \\
-k_{\perp} & 0 & 0 & \omega & 0 & 0 \\
-k_{\perp} & -k_{\parallel} & 0 & 0 & \omega & 0 \\
0 & 0 & 0 & \mathcal{A}_{64}^p & \mathcal{A}_{65}^p & \mathcal{A}_{66}^p \\
0 & 0 & 0 & \mathcal{A}_{74}^p & \mathcal{A}_{75}^p & \mathcal{A}_{67}^p \\
0 & 0 & 0 & \mathcal{A}_{64}^e & \mathcal{A}_{65}^e & 0 \\
0 & 0 & 0 & \mathcal{A}_{74}^e & \mathcal{A}_{75}^e & 0
\end{bmatrix}
\begin{bmatrix}
0 & -k_{\perp}/2\beta_p & 0 & \tilde{u}_{\perp} & 0 \\
-k_{\parallel}/2\beta_p & 0 & -k_{\parallel}/2\beta_p & \tilde{u}_{\parallel} & 0 \\
0 & 0 & 0 & \tilde{b}_{\perp} & 0 \\
0 & 0 & 0 & \tilde{b}_{\parallel} & 0 \\
0 & 0 & 0 & \tilde{n} & 0 \\
\mathcal{A}_{67}^p & 0 & 0 & \tilde{p}_{\perp}^p & 0 \\
\mathcal{A}_{77}^p & 0 & 0 & \tilde{p}_{\parallel}^p & 0 \\
0 & \mathcal{A}_{66}^e & \mathcal{A}_{67}^e & \tilde{p}_{\perp}^e & 0 \\
0 & \mathcal{A}_{76}^e & \mathcal{A}_{77}^e & \tilde{p}_{\parallel}^e & 0
\end{bmatrix} = \begin{bmatrix} 0 \\ 0 \\ 0 \\ 0 \\ 0 \\ 0 \\ 0 \\ 0 \end{bmatrix}, \quad (4.23)$$

with the definitions,

$$\mathcal{A}_{64}^s = -\zeta_{\omega} Z(\zeta_s), \quad (4.24)$$

$$\mathcal{A}_{65}^s = 1 + \zeta_{\nu}^s Z(\zeta_s), \quad (4.25)$$

$$\mathcal{A}_{66}^s = -\frac{1}{\beta^s} \left[1 + \frac{2}{3} \zeta_{\nu}^s Z(\zeta_s) \right], \quad (4.26)$$

$$\mathcal{A}_{67}^s = -\frac{\zeta_{\nu}^s Z(\zeta_s)}{3\beta^s}, \quad (4.27)$$

$$\mathcal{A}_{74}^s = -1 - 2(\zeta^s)^2 R(\zeta_s) + R(\zeta_s) - \zeta_{\nu}^s [Z(\zeta_s) - 2\zeta^s R(\zeta_s)], \quad (4.28)$$

$$\mathcal{A}_{75}^s = 1 + 2(\zeta^s)^2 R(\zeta_s) + \frac{3}{2} \zeta_{\nu}^s [Z(\zeta_s) - 2\zeta^s R(\zeta_s)], \quad (4.29)$$

$$\mathcal{A}_{76}^s = -\frac{1}{3\beta^s} \zeta_{\nu}^s [Z(\zeta_s) - 2\zeta^s R(\zeta_s)], \quad (4.30)$$

$$\mathcal{A}_{77}^s = -\frac{1}{\beta^s} \left\{ R(\zeta_s) + \frac{1}{6} \zeta_{\nu}^s [Z(\zeta_s) - 2\zeta^s R(\zeta_s)] \right\}. \quad (4.31)$$

This system of equations can be solved with a numerical recipe for the plasma dispersion relation and a numerical root finder.

4.4 Numerical Methods

The numerical methods include a numerical method for the integral form for the plasma dispersion relation function, a root finding algorithm, and an eigenvalue decomposition. A flow chart of the numerical method is presented as Fig. 4.2.

Numerical Method

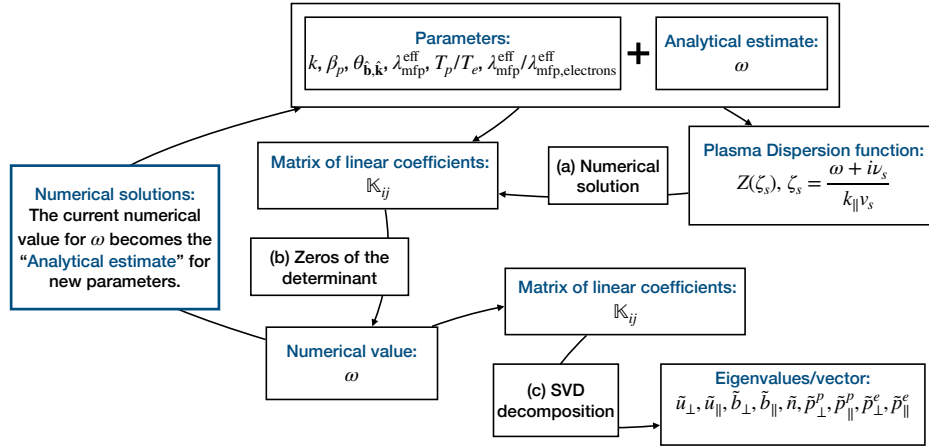


Figure 4.2: The numerical method takes parameters and an analytical estimate of the complex frequency to output the numerical complex frequency and the eigenvalues/vectors of the primary linear system (Eq. 4.23), which are the primary numerical results of the thesis.

Starting at the top box, the parameters are set and the analytical estimate are inserted into the matrix of linear coefficients defined in Eq. 4.38 and the plasma dispersion function. The technique outlined in Sec. 4.4.1 is used to generate a numerical solution for the plasma dispersion function, which is inserted into the matrix of linear coefficients, labelled (a). Using the numerical technique outlined in Sec. 4.4.2 a zero of the determinant is found, this is labelled (b). The numerical value of the complex frequency can then be used to produce the eigenvalues and eigenvectors with the method discussed in Sec. 4.4.3, labelled (c) in the flow chart. The numerical value for the complex frequency can then be inserted back into the top box as the analytical estimate. This produces the traditional dispersion relation, if k is altered, or trends with parameters such as β , to compare with measurements.

4.4.1 The plasma dispersion function

The plasma dispersion function is central to linear kinetic theory and is the primary modification of the plasma equations when studying warm plasmas. Some useful results appear in Appendix B.5. The function,

$$Z(\zeta_s) = \frac{1}{\sqrt{\pi}} \int_{C_L} du \frac{\exp\{-u^2\}}{u - \zeta_s}, \quad (4.32)$$

where the argument ζ_s has been defined. It can be seen that ζ_s is the location of poles in complex space, to which the integral path C_L is modified to encircle and use the residue theorem to give the complex frequencies of the wave modes. More on the plasma dispersion function can be found in Appendix B.5. The plasma dispersion function can be expanded in terms of its argument, often used for analytical treatment,

$$Z(\zeta_s) \approx i\sqrt{\pi} \exp\{-\zeta_s^2\} - 2\zeta_s \left(1 - 2\frac{\zeta_s^2}{3} + 4\frac{\zeta_s^4}{15} + \dots\right), \quad |\zeta_s| \ll 1, \quad (4.33)$$

$$Z_{\text{kin}}(\zeta_s) = i\sqrt{\pi} \exp\{-\zeta_s^2\} - 2\zeta_s \left(1 - 2\frac{\zeta_s^2}{3} + 4\frac{\zeta_s^4}{15}\right), \quad (4.33)$$

$$Z(\zeta_s) \approx i\sigma\sqrt{\pi} \exp\{-\zeta_s^2\} - \frac{1}{\zeta_s} \left(1 + \frac{1}{2\zeta_s^2} + \frac{3}{4\zeta_s^4} + \dots\right), \quad |\zeta_s| \gg 1, \quad (4.34)$$

$$Z_{\text{fluid}}(\zeta_s) = i\sigma\sqrt{\pi} \exp\{-\zeta_s^2\} - \frac{1}{\zeta_s} \left(1 + \frac{1}{2\zeta_s^2} + \frac{3}{4\zeta_s^4}\right), \quad (4.34)$$

where,

$$\begin{aligned} \sigma = 0, \quad & \mathcal{I}\{\zeta_s\} > 0, \\ \sigma = 1, \quad & \mathcal{I}\{\zeta_s\} = 0, \\ \sigma = 2, \quad & \mathcal{I}\{\zeta_s\} < 0. \end{aligned} \quad (4.35)$$

The definitions “fluid” and “kinetic” are clear when recalling the argument,

$$\zeta_s = \frac{\omega}{v_s |k_\parallel|} + \frac{i\nu_s}{v_s |k_\parallel|}, \quad (4.36)$$

so that for small k_\parallel and large ν_s the fluid case $|\zeta_s| \gg 1$ and for large k_\parallel and $\nu_s = 0$, the kinetic case $|\zeta_s| \ll 1$ is consistent. To get a sense of the plasma dispersion function Figure 4.3 is provided. The left column of panels plot the real parts and the right column plots the imaginary parts. The top panels are the fluid approximation (Eq. 4.34) of the numerical solutions of Eq. B.132 which are displayed as the middle panels. The bottom panels are the real (left) and imaginary (right) kinetic approximation (Eq. 4.33). The presence of

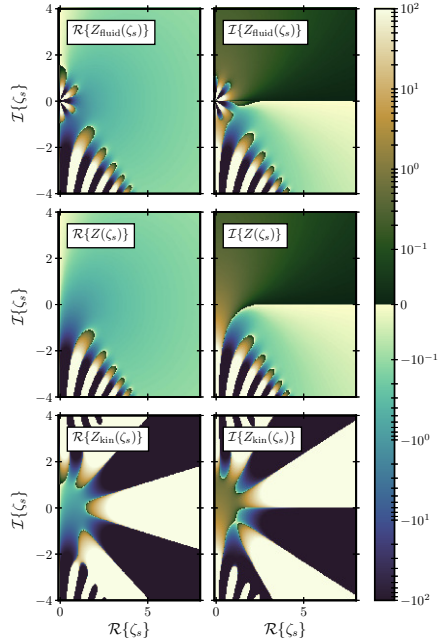


Figure 4.3: The imaginary (right column) and real (left column) parts of the functions shown as the top panels Eq. 4.34, middle panels Eq. B.132, and bottom panels Eq. 4.33. This labelling can be seen as text, directly in the panel. The color bar is log-normal until $\pm 10^{-1}$ and then is linear between $\pm 10^{-1}$.

the collision frequency in the argument shown as Eq. 4.36 increases the total imaginary part. The imaginary part of ω requires a complicated solution to Eq. 4.23, but in general the imaginary part of Eq. 4.36 will be positive, so it is important to resolve the plasma dispersion function there.

To show the accuracy of the expansions, Figure 4.4 is provided. The norm of the difference between the functions is shown, the upper right hand corner of the panels is to be understood as,

$$\Delta \mathcal{X}(\zeta_s) = \mathcal{X}(\zeta_s) - Z(\zeta_s), \quad (4.37)$$

where $Z(\zeta_s)$ is Eq. B.132 and \mathcal{X} is one of the expansions. The regions of applicability, where the color is white, are consistent with approximations written in Eq. 4.34 and Eq. 4.33. Comparing the two regions where the approximations hold well, it is apparent that the actual function (Eq. B.132) will need to be evaluated. The main point here is that for large imaginary part $I\{\zeta_s\}$ neither approximation holds well, so the full numerical solution for the plasma dispersion relation must always be considered.

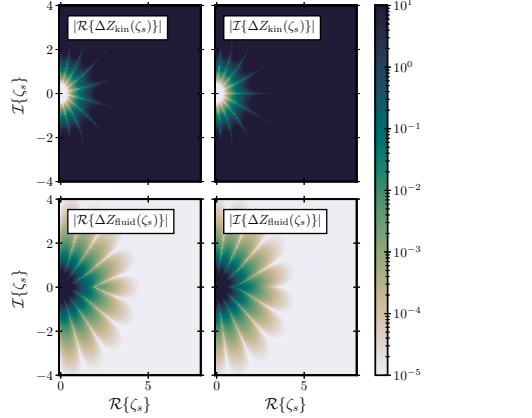


Figure 4.4: The difference between the expansions (see Eq. 4.37) and the numerical calculation of the dispersion relation function (see Eq. 4.37) for the kinetic expansion (Eq. 4.33) in the top panels and fluid expansion (Eq. 4.34) in the bottom panels.

4.4.2 Root finding

The root finding algorithm is the ‘hybrid’ technique from More et al. [1980], the infamous “MINPACK”, which is the basis for all modern least-square techniques. The general method was proposed by Powell [1964] to efficiently find minimums of several variables without taking derivatives. The technique is called the conjugate-gradient method which involves a series of steepest-descent steps with intermediate orthonormalisation (or conjugacy) to decrease the number of steps necessary, therefore increasing the efficiency. The method does require the input of an initial guess that does need to be near the minimum of the function, but that turns out to be an excellent property for the plasma dispersion functions since it contains an infinite number of zeros. The physically relevant solution is the one that is least damped and this can be found easily, rather than finding the infinite set of least damped solutions.

Fig. 4.5 has been provided to get a sense of what the functions, which will be minimized, look like. It is convenient to redefine Eq. 4.23,

$$\mathbb{K}_{ij}\mathbb{V}_j = \delta_{i'i}, \quad (4.38)$$

where \mathbb{K}_{ij} is the matrix containing all the coefficients from 4.23 (not rewritten

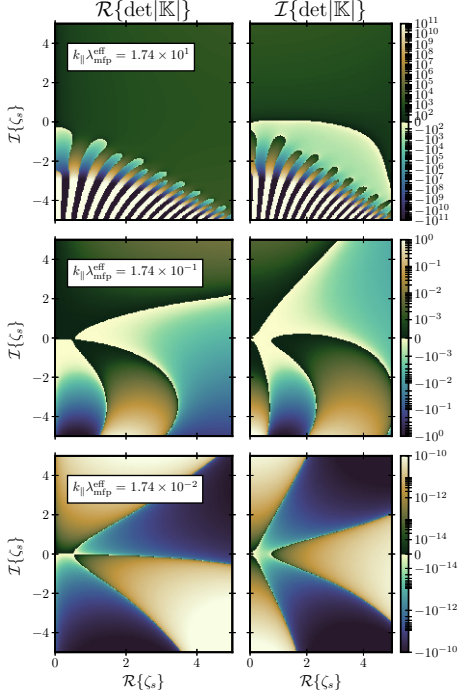


Figure 4.5: The real (imaginary) part of the determinant of Eq. 4.23 on the left (right) columns for a span of $\mathcal{I}\{\zeta_s\}$ on the vertical axis and $\mathcal{R}\{\zeta_s\}$ on the horizontal axis. The changed parameters between the rows are the $k_{\parallel}\lambda_{\text{mfp}}^{\text{eff}}$ product.

here) and then the two definitions,

$$\mathbb{V}_j = \begin{bmatrix} \tilde{u}_{\perp} \\ \tilde{u}_{\parallel} \\ \tilde{b}_{\perp} \\ \tilde{b}_{\parallel} \\ \tilde{n} \\ \tilde{p}_{\perp}^p \\ \tilde{p}_{\parallel}^p \\ \tilde{p}_{\perp}^e \\ \tilde{p}_{\parallel}^e \end{bmatrix}, \quad \delta_{i'i} = \begin{bmatrix} 0 \\ 0 \\ 0 \\ 0 \\ 0 \\ 0 \\ 0 \\ 0 \\ 0 \end{bmatrix}, \quad (4.39)$$

where $\delta_{i'i}$ is defined so that $i' \neq i$. Comparing the left and right columns from 4.5 there are overlapping contours of zero (where the light blue turns to dark green), where the location of the root will be. The rows plot the determinant for different values of $k_{\parallel}\lambda_{\text{mfp}}^{\text{eff}}$. This choice of parameters will be explained in 4.4.3, but for now $\lambda_{\text{mfp}}^{\text{eff}} = v_p/\nu_p$. Looking at the top two panels, it can be seen that

there are many zeros, but with increasingly negative $\mathcal{I}\{\zeta_s\}$. The point here is that when using the conjugate-gradient method on a function with infinite roots a *good* initial guess (near to the least damped solution) must be performed to obtain the least damped solution, in particular for the top panels of Fig. 4.5.

4.4.3 Eigen-problem solutions

The numerical method to solve Eq. 4.23 once a solution for ω has been found is the eigen-decomposition method called singular value decomposition (SVD). SVD is a highlight of linear algebra, but for the purposes of this thesis, this section is simplified to the essential information. The modern numerical implementation of SVD appears in the “LAPACK” software library [Anderson et al., 1999]. SVD is a numerically efficient way to find the nullspace of a matrix, such as the problem in Eq. 4.23.

The essential idea is to find the eigenvector corresponding to the eigenvalue equal to zero. This eigenvector is a solution to the problem $\mathbb{A}_{ij}\mathbb{X}_j = \delta_{i'i}$. In practice, the smallest eigenvalue is found, and the corresponding eigenvector is used as a solution for \mathbb{V}_i defined in Eq. 4.53.

4.5 Numerical Solutions

In this section numerical solutions to the equations and a connection to their physical interpretation will be made. The parameters of the model appear in Table 4.1 with descriptions. The proton beta β_p , temperature ratio $T_{e,0}/T_{p,0}$,

Parameter	Description
$\lambda_{\text{mfp}}^{\text{eff}}$	Effective mean-free-path of protons
$\theta_{\hat{\mathbf{b}},\hat{\mathbf{k}}}$	Angle between wave vector and magnetic field
β_p	Proton beta
k	Norm of wavenumber
$T_{e,0}/T_{p,0}$	Electron to proton temperature ratio
$\lambda_{\text{mfp}}^{\text{eff}}/\lambda_{\text{mfp,electrons}}^{\text{eff}}$	Proton to electron effective mean-free-path ratio

Table 4.1: List of input parameters to solve the system of Eq. 4.23.

and wavenumber k can be directly measured in the solar wind. The remaining quantities do require a theory. Due to the observations presented by the solar wind, both β_p and k can be measured reliably enough to be dependent parameters in an ensemble study. This leaves four parameters, two of which ($\theta_{\hat{\mathbf{b}},\hat{\mathbf{k}}}$ and $\lambda_{\text{mfp}}^{\text{eff}}$) are to be measured. While $T_{e,0}/T_{p,0}$ can be measured, fixing the value along with fixing $\lambda_{\text{mfp}}^{\text{eff}}/\lambda_{\text{mfp,electrons}}^{\text{eff}}$, will simplify the final analysis

conducted in Chapter 5. The next sections show how these parameters effect the solutions, focussing on repeating past results, and justifying the fixing of model parameters.

The method of solution of Eq. 4.23 is to use analytical forms of the wave of choice for the initial guess of the root finding algorithm in Section 4.4.2. Then, a single parameter (Table 4.1) is changed slightly, using the previous solution as the initial guess. This allows dispersion relations $\omega(k)$ to be produced, and as a function of β etc. At these steps, the solution for V_j of Eq. 4.53 from the system of equations in Eq. 4.23 is computed numerically with the method of Section 4.4.3. This method forms the basis of all the numerical solutions shown throughout the Thesis.

The mode that is studied in this Chapter has the name ion-acoustic in the collisionless regime and the slow-mode in the collisional regime. This will be clarified in the next section. An introduction to the physics of these modes is given in Section 2.5.

4.5.1 Dispersion relation

The method for solving Eq. 4.23 for ω , the complex wave frequency, is detailed at the end of Section 4.5. The complex frequency will be decomposed,

$$\mathcal{R}\{\omega\} = \omega_r, \quad \mathcal{I}\{\omega\} = \gamma, \quad (4.40)$$

as is typical to look at the pseudo-normal mode frequency ω_r and the damping/growth rate γ . The parameters from Table 4.1 will be examined in the coming sections. The focus will be on how $\lambda_{\text{mfp}}^{\text{eff}}$, $\theta_{\mathbf{b},\mathbf{k}}$, β_p , k effect the solutions. The remaining two parameters will be set to values of,

$$\frac{T_{p,0}}{T_{e,0}} = 1, \quad \frac{\lambda_{\text{mfp}}^{\text{eff}}}{\lambda_{\text{mfp,electrons}}^{\text{eff}}} = 1, \quad (4.41)$$

for now and then discussed briefly at the end. These parameters are varied in Sections 4.5.2 and 4.5.3.

4.5.1.1 As a function of wavenumber

The solutions as a function of wavenumber and the effective mean-free-path will be displayed in this section. The reasoning behind this pair of parameters is in the argument of the plasma dispersion function,

$$\zeta_s = \frac{\omega}{k_{\parallel} v_s} + \frac{i}{k_{\parallel} \lambda_{\text{mfp}}^{\text{eff}}}, \quad (4.42)$$

from Eq. 4.17, using $\nu_s = v_s/\lambda_{\text{mfp}}^{\text{eff}}$. The transition between the collisional and collisionless regime can be understood through the product, by taking $k = 2\pi/\lambda_{\text{wave}}$,

$$\frac{1}{k_{\parallel} \lambda_{\text{mfp}}^{\text{eff}}} = \frac{2\pi\lambda_{\text{wave}}}{\cos(\theta_{\hat{\mathbf{b}},\hat{\mathbf{k}}})\lambda_{\text{mfp}}^{\text{eff}}}, \quad (4.43)$$

where λ_{wave} is the wavelength of the compressive wave-mode being considered. For the parallel propagation case ($\theta_{\hat{\mathbf{b}},\hat{\mathbf{k}}} = 0$), consider the wavelength to be much larger than the mean-free-path. The spatial extent of the density or pressure impulse from the wave, will be much larger than mean-free-path, so the vibration of the wave will be supported by plasma that is at collisional equilibrium, or crudely, it will be collisionally supported. The propagation angle plays a simple but effective role as the cosine function. In the opposite case where the effective mean-free-path is large, the fluctuation, e.g., δb_{\parallel} can interact with the individual particle magnetic moment, damping the wave and energizing the particle. The general picture of compressive waves and transit-time damping is discussed in Section 2.5.

These arguments are clarified by the two cases,

$$\begin{aligned} k_{\parallel} \lambda_{\text{mfp}}^{\text{eff}} \gg 1, & \quad (\text{collisionless regime}), \\ k_{\parallel} \lambda_{\text{mfp}}^{\text{eff}} \ll 1, & \quad (\text{collision dominated regime}). \end{aligned} \quad (4.44)$$

At this point it is necessary to connect the various compressive wave-modes shown in these sections to their textbook names. Analytical dispersion relations will be taken from Section 6 of Schekochihin et al. [2009], where some differences should be mentioned, a more complicated collision operator is employed, the “reduced” approximation $k_{\perp}/k_{\parallel} \gg 1$ is used, and the electrons are assumed isothermal. Eqs. 4.23 encapsulate this system since the BGK operator recovers the linear physics of the collision operator. The analytical limits are,

$$\omega \simeq k_{\parallel} v_A - i \frac{\eta_{\parallel,p} k_{\parallel}^2}{2}, \quad k_{\parallel} \lambda_{\text{mfp}}^{\text{eff}} \ll 1, \beta \gg 1, \quad (4.45)$$

$$\omega \simeq -i \frac{|k_{\parallel}| v_p}{\sqrt{\pi} \beta_p}, \quad k_{\parallel} \lambda_{\text{mfp}}^{\text{eff}} \gg 1, \beta \gg 1, \quad (4.46)$$

which are Eqs. 175 and 190 from Schekochihin et al. [2009], respectively. The value of η_{\parallel} , the parallel viscosity (see Section 2.2.2), has been taken from Eq. 73 of Hunana et al. [2022], which is $\eta_{\parallel} = p_p/\nu_{\text{eff}}$. Equation 4.46 is the non-propagating mode as found by Howes et al. [2006], which is not severely damped

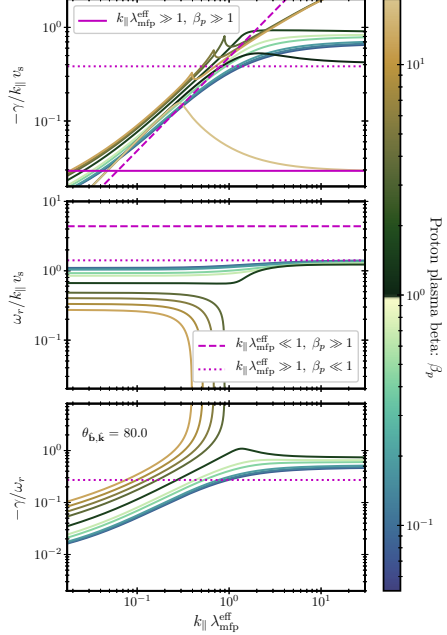


Figure 4.6: Dispersion relation of the slow-mode at $\theta_{\hat{\mathbf{b}}, \hat{\mathbf{k}}} = 80.0^\circ$. The non-magenta curves are produced from the numerical method described in the text. The color corresponds to the proton plasma beta. The legend reports the assumptions behind the analytical functions corresponding to Eqs. 4.45, 4.46, and 4.47. The value of β_p chosen for the analytical curves is the maximum or minimum of the range corresponding to whether the approximation for β_p is \gg or \ll than 1.

at high β_p . The collisionless low beta limit,

$$\omega \simeq k_{\parallel} c_s - i |k_{\parallel}| c_s \sqrt{\pi} \frac{c_s^3}{(v_{\parallel}^p)^3} \frac{\exp\{-c_s^3/(v_{\parallel}^p)^3\}}{1 + 3c_s^2/(v_{\parallel}^p)^2}, \quad k_{\parallel} \lambda_{\text{mfp}}^{\text{eff}} \gg 1, \beta \ll 1, \quad (4.47)$$

is taken from Verscharen et al. [2017] introducing the acoustic speed,

$$c_s = \sqrt{\frac{3k_B T_{p,0} + k_B T_{e,0}}{m_p}}, \quad (4.48)$$

where the collisionless result is used. In the fluid case, the coefficients out front of the temperatures are known as the specific heats, and are determined from the equation of state [Gary, 1993]. To get a better grasp on the β_p dependence of the fluid regime the MHD slow-mode will be considered,

$$\omega = k v_A \sqrt{\frac{1}{2} \left(1 + \frac{\kappa}{2} \beta_p \right) - \frac{1}{2} \left[\left(1 + \frac{\kappa}{2} \beta_p \right)^2 - 2\kappa \beta_p (\cos(\theta_{\hat{\mathbf{b}}, \hat{\mathbf{k}}}))^2 \right]^{1/2}}, \quad (4.49)$$

where $\kappa = 5/3$ is the adiabatic specific heat ratio. Due to the unestablished nomenclature of all the intermediate regimes explored in these sections, they will be referred to as slow-modes and the regimes of parameter space will be indicated when comparing to analytical dispersion relations. If the physics, e.g., the restoring force of the ion-acoustic wave, being the electron mobility, is referred to, then the textbook names will be used.

The slow-mode dispersion relations as a function of the product $k_{\parallel} \lambda_{\text{mfp}}^{\text{eff}}$ are displayed in Figs. 4.6 and 4.7 where the line color corresponds to the colorbar; a span of proton beta. The magenta curves are the analytical limits, indicated in the captions of Figs. 4.6 and 4.7. In the top panel of Fig. 4.6, the normalized damping rate, all of the numerical solutions are increasing functions with the $k_{\parallel} \lambda_{\text{mfp}}^{\text{eff}}$ -product, splitting near $k_{\parallel} \lambda_{\text{mfp}}^{\text{eff}} \sim 1$ depending on the plasma beta. In the low beta regime, the normalized damping rate for $\lambda_{\text{mfp}}^{\text{eff}} \gg 1$, $\beta \ll 1$ for Eq. 4.47, or the ion-acoustic damping rate, is a good approximation. As β_p is further increased, the dark-yellow curves, some of the modes continue to increase becoming highly damped. At a value of $\beta_p = 19.2$ the numerical solutions begin to asymptote to the high-beta damping rate, given by Eq. 4.46, which is a non-propagating mode. This can be seen in the middle and bottom panels, where the real part of the complex frequency ω_r is shown to go to zero in the $\beta_p > 1$ regime. It is clear that when all of the regimes β_p , $k_{\parallel} \lambda_{\text{mfp}}^{\text{eff}}$, are taken into consideration, the ion-acoustic, slow-mode and non-propagating mode are all connected.

Figure 4.6 does deserve further attention. The high beta curve, that asymptotes to the solid magenta line was found by Barnes et al. [2009] (see Figure 6) using a sophisticated gyrokinetic simulation with a Fokker-Planck collision operator. This is the dissipative scenario considered in Schekochihin et al. [2009] (see Figure 6) for the fate of the slow-mode. This shows how viscosity and collisionless damping (here it is Barnes damping) are both present and fit together nicely when looking at the dependence with the collisionality parameter $k_{\parallel} \lambda_{\text{mfp}}^{\text{eff}}$.

The first thorough investigation of the transition between the collisional and collisionless regimes is reported in an article by Stubbe [1994] (see Figures 6 and 7). In this article he compares laboratory measurements of the damping rate to a Braginskii fluid model [Braginskii, 1957] and another that incorporates Landau damping. The Braginskii fluid models have only viscosity, so the damping rate drops dramatically in the collisionless regime, where collisionless damping takes over. This is the most clear reason that Braginskii fluid model is insufficient for this analysis. The numerical code constructed in this thesis can describe both the high beta [Schekochihin et al., 2009] and low beta damping [Stubbe, 1994] scenarios.

In Fig. 4.7 the same parameters are considered, only decreasing the prop-

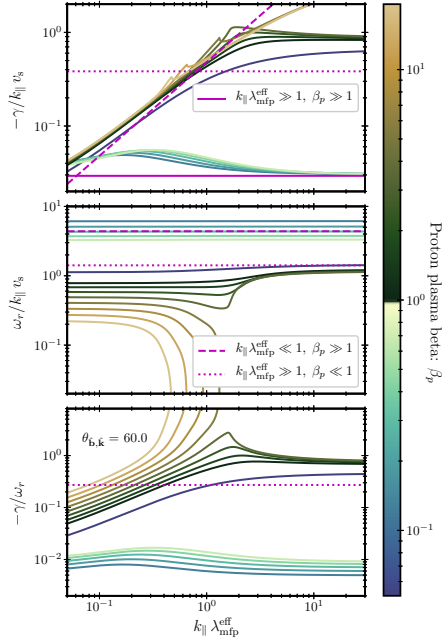


Figure 4.7: Dispersion relation of the slow-mode for $\theta_{\hat{b},\hat{k}} = 60.0^\circ$. The non-magenta curves are produced from the numerical method described in the text. The color corresponds to the proton plasma beta. The legend reports the assumptions behind the analytical functions corresponding to Eqs. 4.45, 4.46, and 4.47. The value of β_p chosen for the analytical curves is the maximum or minimum of the range corresponding to whether the approximation for β_p is \gg or \ll than 1.

agation angle. In the bottom panel it can be seen that the damping factor is much decreased for low beta.

4.5.1.2 As a function of propagation angle

The first notable investigation of compressive fluctuations for a collisionless plasma was carried out by Barnes [1966] who showed that compressive fluctuations are severely damped (also covered in Section 2.5). One of the primary results of Barnes [1966] was to investigate the dispersion relations as a function of the propagation angle $\theta_{\hat{b},\hat{k}}$ i.e., the angle between the background magnetic field and propagation vector.

The numerical method to solve the dispersion relations as a function of $\theta_{\hat{b},\hat{k}}$ is discussed in a general manner in Section 4.5. The only notable difficulty is that the step size when sweeping through a parameter needs to be very small when nearing $\theta_{\hat{b},\hat{k}} = 90^\circ$. This is because the argument of the dispersion relation function is inversely proportional to k_{\parallel} so that near $\simeq 90^\circ$ the cosine function

makes the argument go to infinity.

The dispersion relations as a function of propagation angle $\theta_{\hat{b},\hat{k}}$ for $k \lambda_{\text{mfp}}^{\text{eff}} = 50.0$ is shown in Fig. 4.8 for a range of β_p . The bottom panel of the figure corresponds well with Figure 3 of Barnes [1966]. There is an error in the labelling of the lines from this article, which becomes clear in the text discussing it. The results here also clarify the labelling error. From Fig. 4.8 it is clear that damping of the slow-mode is severe except for angles near $\approx 60^\circ$ and $\simeq 90^\circ$ at $\beta_p \geq 1$. The collisionless low beta analytical dispersion relation from Eq. 4.47 (dotted magenta line) is a good approximation regardless of the propagation angle. As stressed earlier, the product $k_{\parallel} \lambda_{\text{mfp}}^{\text{eff}}$ determines the collisionless versus fluid nature of the compressive mode, so for oblique angles of $\theta_{\hat{b},\hat{k}} \simeq 90^\circ$, it is inevitable that system transitions to the fluid regime. This can be seen in the top panel of Fig. 4.8, where the dashed magenta line (Eq. 4.45) begins to be a good approximation. This also coincides with the fact that there must be a parallel component of the wave k_{\parallel} for the “resonance” to occur, leading to Barnes or Landau Damping, so at oblique angles the damping rate goes to zero.

The opposing case to Fig. 4.8 is plotted in Fig. 4.9 for $k \lambda_{\text{mfp}}^{\text{eff}} = 0.2$. Comparing the bottom panel to Figure 3 of Barnes [1966] shows that in the fluid regime, the damping factor $-\gamma/\omega_r$ is smaller, especially for parallel propagation. This is the primary effect of the $i\nu_s$ in Eq. 4.42 on the linear physics, to lessen the damping rate. The analytical curve shown as a dashed magenta line corresponds to the fluid high beta regime (Eq. 4.45), and does well to capture the low beta regime damping rate. While contradictory, the derivation for the analytical solutions assumes $k_{\perp} \gg k_{\parallel}$, so it is not expected to be a good approximation when varying the ratio of k_{\perp}/k_{\parallel} .

4.5.1.3 Plasma beta

The proton plasma beta (β_p) is important to investigate since it parameterises two very different regimes of plasma, where thermal pressures dominate for $\beta_s \gg 1$ and magnetic pressure dominates for $\beta_s \ll 1$. A fairly drastic change in dynamics is to be expected when considering $\beta_s \simeq 1$. Since equal temperature, quasi-neutral plasmas, are considered, only the parameter β_p is discussed.

Figure 4.10 has been provided to show how the dispersion relations between the collisional and collisionless regimes behave as a function of the proton plasma beta. The top panel demonstrates that the damping rate is small in collisional regime (blue colors) and increases with beta. The collisionless regime is more damped. The middle panel shows that at low beta the collisionality regime has little effect on the phase speed, but at high beta the solution diverge. The

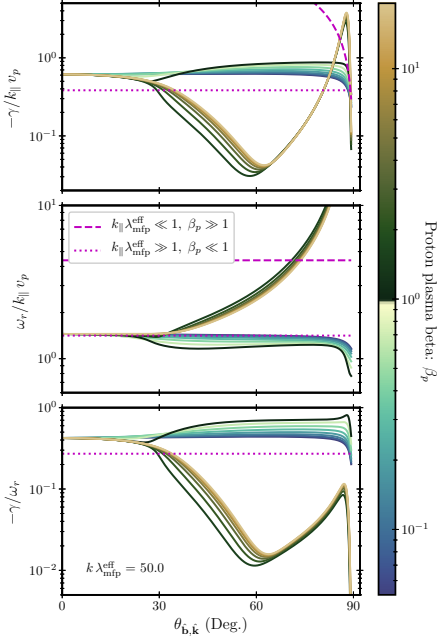


Figure 4.8: The slow-mode dispersion relations as a function of propagation angle. The non-magenta curves are produced from the numerical method described in the text. The color corresponds to the proton plasma beta. The legend reports the assumptions behind the analytical functions corresponding to Eqs. 4.45, 4.46, and 4.47. The value of β_p chosen for the analytical curves is the maximum or minimum of the range corresponding to whether the approximation for β_p is \gg or \ll than 1. In the bottom left corner of the bottom panel, the parameters $k \lambda_{\text{mfp}}^{\text{eff}} = 50.0$ are reported, corresponding to the collisionless regime.

solutions respect the limits, and in fact recover the MHD slow-mode (see caption of Fig. 4.10), which is an essential limit to capture for our study. The connection to the non-propagating mode for moderate collisionality $k_{\parallel} \lambda_{\text{mfp}}^{\text{eff}} \leq 1$ becomes clear for only high beta. The bottom panel shows that the damping factor is very small in the collisional regime and severe in the collisionless regime, respecting both of the limits (described in the caption of Fig. 4.10).

This result, the decrease in damping in the collisional regime, deserves to be highlighted. The article Barnes [1966] is very influential in plasma physics since it shows that compressive fluctuations are severely damped for moderate values of plasma beta and any propagation angle. The essential addition to our study is the effective mean-free-path which modifies the damping rate significantly.

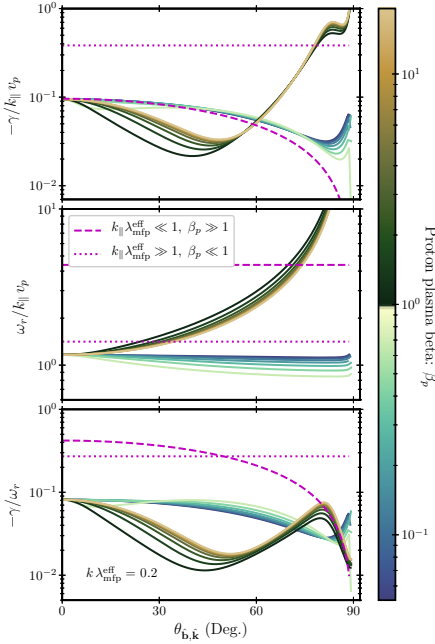


Figure 4.9: The slow-mode dispersion relations as a function of propagation angle. The non-magenta curves are produced from the numerical method described in the text. The color corresponds to the proton plasma beta. The legend reports the assumptions behind the analytical functions corresponding to Eqs. 4.45, 4.46, and 4.47. The value of β_p chosen for the analytical curves is the maximum or minimum of the range corresponding to whether the approximation for β_p is \gg or \ll than 1. In the bottom left corner of the bottom panel, the parameters $k \lambda_{\text{mfp}}^{\text{eff}} = 0.2$ are reported.

4.5.2 The ratio of electron to proton temperature

The restoring force of the ion-acoustic wave is the electron response to charge separation caused by a disturbance of the more massive protons; the mobility of the electrons is vital to the propagation of the wave [Gary, 1993]. The dispersion relations from Fig. 4.10 has been repeated for two values of $k_{\parallel} \lambda_{\text{mfp}}^{\text{eff}}$ by varying the species temperature ratio.

Two cases will be considered, the first is in the kinetic regime, $k_{\parallel} \lambda_{\text{mfp}}^{\text{eff}} = 15.0$, appearing as Fig. 4.11. In the top panel the damping rate is relatively smaller at low beta for large electron temperature (see the colorbar). The middle panel shows that the phase speed is increased for large electron temperature, resulting in the much decreased damping factor (bottom panel) for large electron temperature. The primary result here is that in the collisionless regime, the temperature ratio only affects the dynamics at small proton beta.

The fluid case is shown in Fig. 4.12 where $k_{\parallel} \lambda_{\text{mfp}}^{\text{eff}} = 0.05$. Varying the

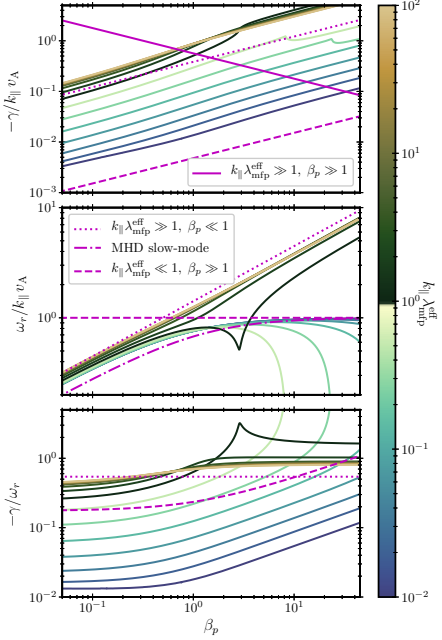


Figure 4.10: The slow-mode dispersion relations as a function of plasma beta. The non-magenta curves are produced from the numerical method described in the text. The color corresponds to the proton plasma beta. The legend reports the assumptions behind the analytical functions corresponding to Eqs. 4.45, 4.46, 4.47, and 4.49. The value of β_p chosen for the analytical curves is the maximum or minimum of the range corresponding to whether the approximation for β_p is \gg or \ll than 1. In the bottom left corner of the bottom panel, the parameters $k_{\parallel} \lambda_{\text{mfp}}^{\text{eff}} = 0.5$ are reported, corresponding to the fluid regime.

temperature ratio in the fluid regime is less familiar since the electrons are usually ignored or modelled as an isothermal fluid. In the top panel it can be seen that the damping rate follows differently than the collisionless case, that for larger relative electron temperature the damping rate increases. In the collisional regime propagation of this mode relies on the magnetic and thermal pressure. The phase speeds are more sensible, the MHD slow-mode (see caption of Fig. 4.12) ignores the electron pressure in the momentum equation. The blue lines follow the MHD slow-mode almost exactly. The large electron temperature solutions, in yellow lines, begin to follow the dashed magenta line. The damping factors increase with proton beta, as expected. The primary result is that the phase speeds, in the middle panel, are only largely effected at low and high beta. The span in temperature ratio for 4 order of magnitude, so the changes are exaggerated.

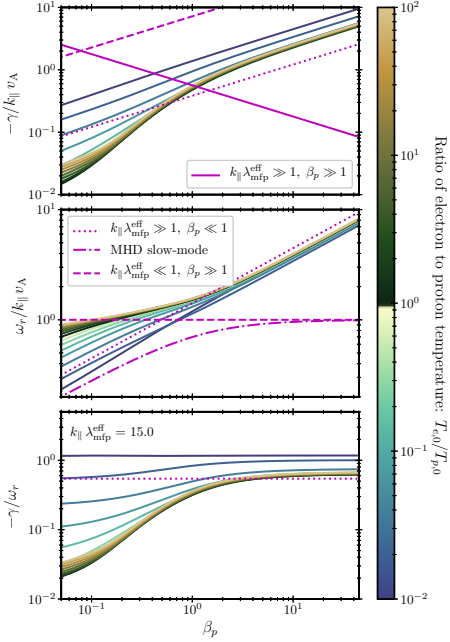


Figure 4.11: The slow-mode dispersion relations as a function of temperature ratio. The non-magenta curves are produced from the numerical method describe in the text. The color corresponds to the temperature ratio. The legend reports the assumptions behind the analytical functions corresponding to Eqs. 4.45, 4.46, 4.47, and 4.49. In the upper left corner of the bottom panel, the parameters $k_{\parallel}\lambda_{\text{mfp}}^{\text{eff}} = 15.0$ are reported, corresponding to the collisionless regime.

4.5.3 The ratio of proton to electron mean-free-path

The ratio of mean-free-paths is a quantity that is almost entirely unexplored in literature. The effects are only explored in terms of the stability of the code. To better see the effects, the electron to proton temperature has been increased to 4. Defining the ratio,

$$\mathcal{L} = \frac{\lambda_{\text{mfp}}^{\text{eff}}}{\lambda_{\text{mfp},\text{electrons}}^{\text{eff}}} , \quad (4.50)$$

and recalling the collisionality argument,

$$k_{\parallel}\lambda_{\text{mfp}}^{\text{eff}} = c, \Rightarrow k_{\parallel}\lambda_{\text{mfp},\text{electrons}}^{\text{eff}} = \frac{c}{\mathcal{L}}, \quad (4.51)$$

therefore \mathcal{L} determines the relative collisionality of the electrons. The three figures in this section all have a propagation angle of $\theta_{\hat{b},\hat{k}} = 60^\circ$ which is near a minimum of the damping factor for the high beta solutions (e.g., see Fig. 4.8). Three different $k_{\parallel}\lambda_{\text{mfp}}^{\text{eff}}$ are considered in this section. Figure 4.13 is the

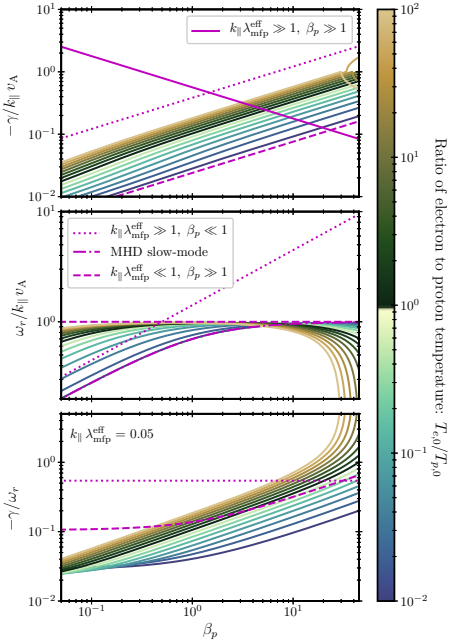


Figure 4.12: The slow-mode dispersion relations as a function of temperature ratio. The non-magenta curves are produced from the numerical method describe in the text. The color corresponds to the temperature ratio. The legend reports the assumptions behind the analytical functions corresponding to Eqs. 4.45, 4.46, 4.47, and 4.49. In the upper left corner of the bottom panel, the parameters $k_{\parallel}\lambda_{mfp}^{eff} = 0.05$ are reported, corresponding to the fluid regime.

collisional regime, where the top panel shows that the low beta damping rate is increased for more fluid-like electrons. The phase speed, in the second panel, is not affected by the mean-free-path ratio.

Continuing, with same set of parameters, but increasing k to the intermediate regime, seen in Fig. 4.14 shows that the effects on the damping rate (top panel) are not present, but in the middle panel, the phase speed is slightly altered.

The final figure, Fig. 4.15, shows that in the collisionless regime, the mean-free-path ratio has no effect. Other angles and temperatures were investigated, but the same results were found.

The collisionless range, Fig. 4.14, shows that increasing the mean-free-path ratio will increase the value of beta that connects the propagating to non-propagating mode. This connection is difficult to handle numerically. At high collisionality, the only effects on the complex frequency are for the damping rate at low beta. For these two reasons, the value settled on for the mean-free-path ratio is 1.

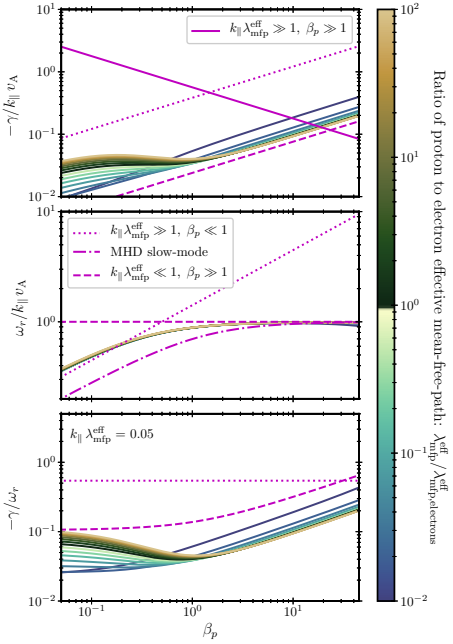


Figure 4.13: The slow-mode dispersion relations as a function of the mean-free-path ratio. The non-magenta curves are produced from the numerical method described in the text. The color corresponds to the mean-free-path ratio. The legend reports the assumptions behind the analytical functions corresponding to Eqs. 4.45, 4.46, 4.47, and 4.49. In the upper left corner of the bottom panel, the parameters $k_{\parallel} \lambda_{\text{mfp}}^{\text{eff}} = 0.05$ are reported, corresponding to the fluid regime.

4.6 Method of correlations and amplitudes

In this section, this method for solving for the fluctuating variables (e.g., the proton density δn_p) which lead to polarisations will be presented. These fluctuations, and consequently the polarisations, are readily measurable with spacecraft data, so a comparison among the two can lead to a measurement. This technique has been long used in space physics to indicate waves and their properties with single spacecraft measurements [Gary, 1993].

To obtain the fluctuating quantities, recall the system of equations \mathbb{K}_{ij} (Eq. 4.23), which is written in full in Section 4.3,

$$\mathbb{K}_{ij} V_j = \delta_{i'i} \quad (4.52)$$

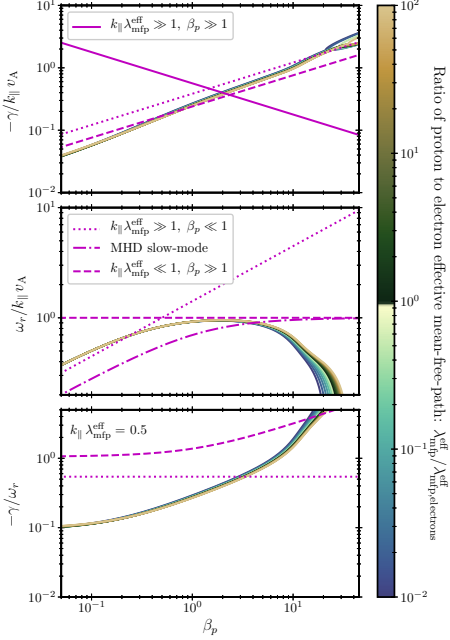


Figure 4.14: The slow-mode dispersion relations as a function of the mean-free-path ratio. The non-magenta curves are produced from the numerical method described in the text. The color corresponds to the mean-free-path ratio. The legend reports the assumptions behind the analytical functions corresponding to Eqs. 4.45, 4.46, 4.47, and 4.49. In the upper left corner of the bottom panel, the parameters $k_{\parallel} \lambda_{\text{mfp}}^{\text{eff}} = 0.5$ are reported, corresponding to the intermediate regime.

where it is written like this in Section 4.4.2, with the definitions

$$\mathbb{V}_j = \begin{bmatrix} \tilde{u}_{\perp} \\ \tilde{u}_{\parallel} \\ \tilde{b}_{\perp} \\ \tilde{b}_{\parallel} \\ \tilde{n} \\ \tilde{p}_{\perp}^p \\ \tilde{p}_{\parallel}^p \\ \tilde{p}_{\perp}^e \\ \tilde{p}_{\parallel}^e \end{bmatrix}, \quad \delta_{i'i} = \begin{bmatrix} 0 \\ 0 \\ 0 \\ 0 \\ 0 \\ 0 \\ 0 \\ 0 \\ 0 \end{bmatrix}. \quad (4.53)$$

The vector \mathbb{V}_j are the quantities of interest in this section. They can be numerically solved for with the SVD method described in Section 4.4.3. The routine is sketched like this, solve for the null space of the determinant to obtain ω , the complex frequency, and then insert ω and solve for the null space of the matrix,

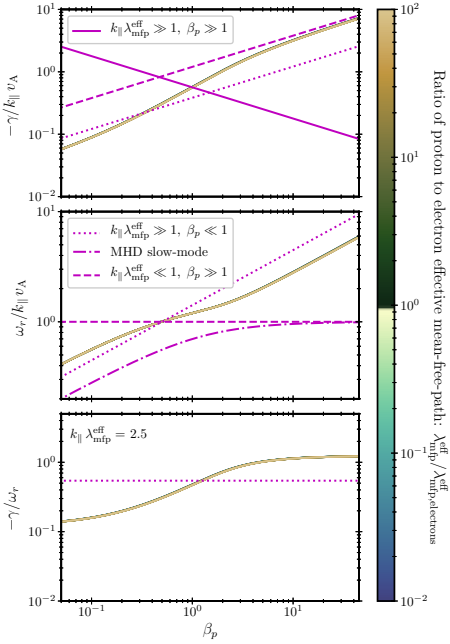


Figure 4.15: The slow-mode dispersion relations as a function of the mean-free-path ratio. The non-magenta curves are produced from the numerical method described in the text. The color corresponds to the mean-free-path ratio. The legend reports the assumptions behind the analytical functions corresponding to Eqs. 4.45, 4.46, 4.47, and 4.49. In the upper left corner of the bottom panel, the parameters $k_{\parallel} \lambda_{\text{mfp}}^{\text{eff}} = 2.5$ are reported, corresponding to the collisionless regime.

for the non-trivial \mathbb{V}_j . This provides the vector \mathbb{V}_j for the parameters imposed.

To generate cross-correlations and amplitude ratios, using the density as an example, the fluctuations are constructed,

$$\delta n = \tilde{n} \exp\{i\omega_r t\} \quad (4.54)$$

where ω_r is the real part of the complex frequency and $t = [0, 2\pi\omega_r^{-1}]$. If $\omega_r \approx 0$, then the wavenumber is used. Figure 4.16 plots four quantities relevant to the compressive wave for the fluid regime (see caption). Here, $\delta B = \delta|b_{\perp} + b_{\parallel}|$ is the fluctuation of the magnetic field strength. Defining the cross-correlation,

$$C(x, y) = \left\langle \frac{\delta x (\delta y)^*}{\langle |\delta x| \rangle \langle |\delta y| \rangle} \right\rangle, \quad (4.55)$$

where the average is over time t . The asterisk denotes the complex conjugate and $|...|$ denotes the conjugate norm. Now, comparing δB and the other three quantities, for the same β , it becomes clear that their cross-correlation is less

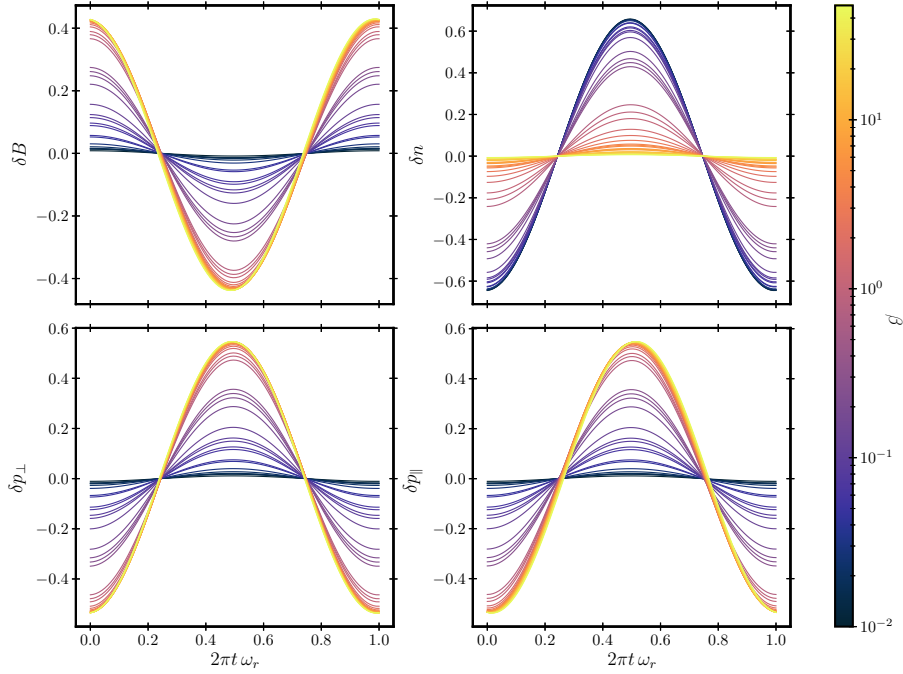


Figure 4.16: The fluctuations, defined as Eq. 4.54, are plotted as a function of time, displayed on the horizontal axis. The different curves are mapped to the color bar, which is the proton beta. The parameters for these solutions are $\theta_{\hat{\mathbf{b}}, \hat{\mathbf{k}}} = 80^\circ$ and $k_{\parallel} \lambda_{\text{mfp}}^{\text{eff}} = 0.01$, the fluid regime.

than zero, this is the unique polarization of the slow-mode wave. Comparing δp_{\perp} and δp_{\parallel} the curves are nearly identical, so the fluctuations are fairly isotropic. This is indicative of the fluid regime.

Now turning to the kinetic regime, plotted as Fig. 4.17, the scenario changes drastically. The density and magnetic field strength have similar properties to the fluid regime, that they are anti-correlated, but the pressure is different. The parallel pressure is out of phase with the other fluctuations so the magnitude of the cross-correlation of the parallel pressure and the other quantities will be less than one. The perpendicular pressure is positively correlated with the magnetic field strength for beta less than one and negatively correlated for beta greater than one. The fluctuations of the total pressure are no longer isotropic.

From the vertical axis limits of Fig. 4.17, the amplitudes of the fluctuations quantities clearly becomes important. Here, the amplitude is introduced,

$$A(x, y) = \frac{\langle x \rangle \langle |\delta y| \rangle}{\langle y \rangle \langle |\delta x| \rangle}, \quad (4.56)$$

which is normalized to the averages of the quantities.

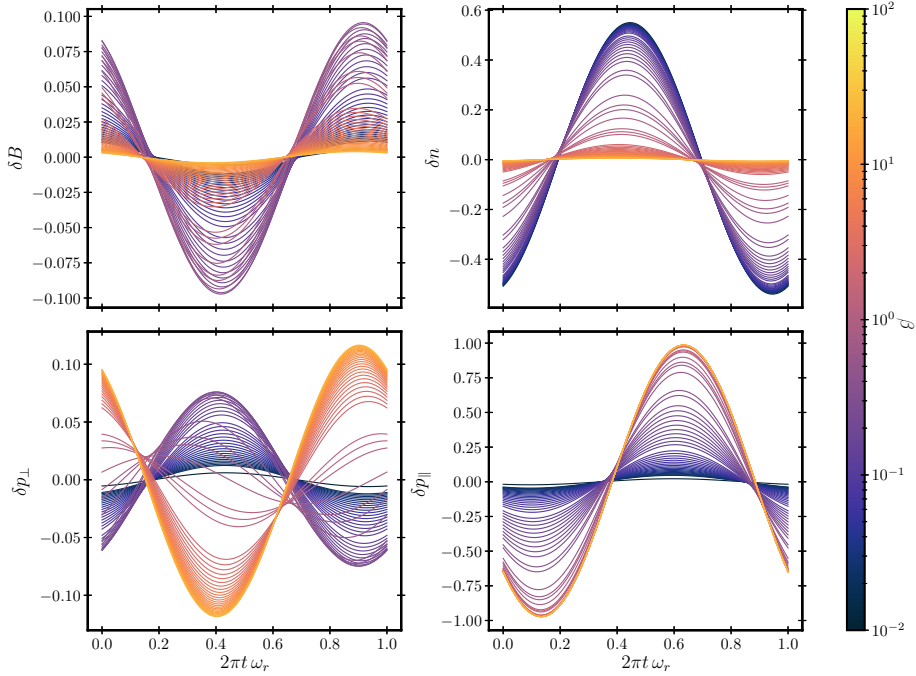


Figure 4.17: The fluctuations, defined as Eq. 4.54, are plotted as a function of time, displayed on the horizontal axis. The different curves are mapped to the color bar, which is the proton beta. The parameters for these solutions are $\hat{\theta}_{\mathbf{b},\mathbf{k}} = 80^\circ$ and $k_{\parallel} \lambda_{\text{mfp}}^{\text{eff}} = 10$.

These correlations can be studied as a function of other variables, for example, the proton beta. The correlations (Eq. 4.55) and amplitudes (Eq. 4.56) are plotted as a function of the plasma beta for different angles in Fig. 4.18 for $k_{\parallel} \lambda_{\text{mfp}}^{\text{eff}} = 10$, the collisionless case. The pressures are not correlated with each other indicating that the pressure anisotropy of the wave is a fluctuating quantity. Due to the definition of the amplitude, the parallel pressure fluctuations always dominates and becomes very large near $\beta \approx 0.8$. There does not appear to be an angular dependence on the location in β .

The correlations for the density and magnetic field strength have less angular dependence. The correlation is definitively negative and the amplitude of the density is always larger, increasingly so for low beta. This follows simply from the beta dependence in the definition of the amplitude considered here.

The collisional regime has been considered in Fig. 4.19 where the $k_{\parallel} \lambda_{\text{mfp}}^{\text{eff}} = 0.01$. The system is nearly isotropic with a slight departure at high beta.

The same thing can be done for different values of $k_{\parallel} \lambda_{\text{mfp}}^{\text{eff}}$ as a function of the beta, which appears as Fig. 4.20. The collisional limits are well respected from before, in that the pressures are isotropic. The magnetic field strength

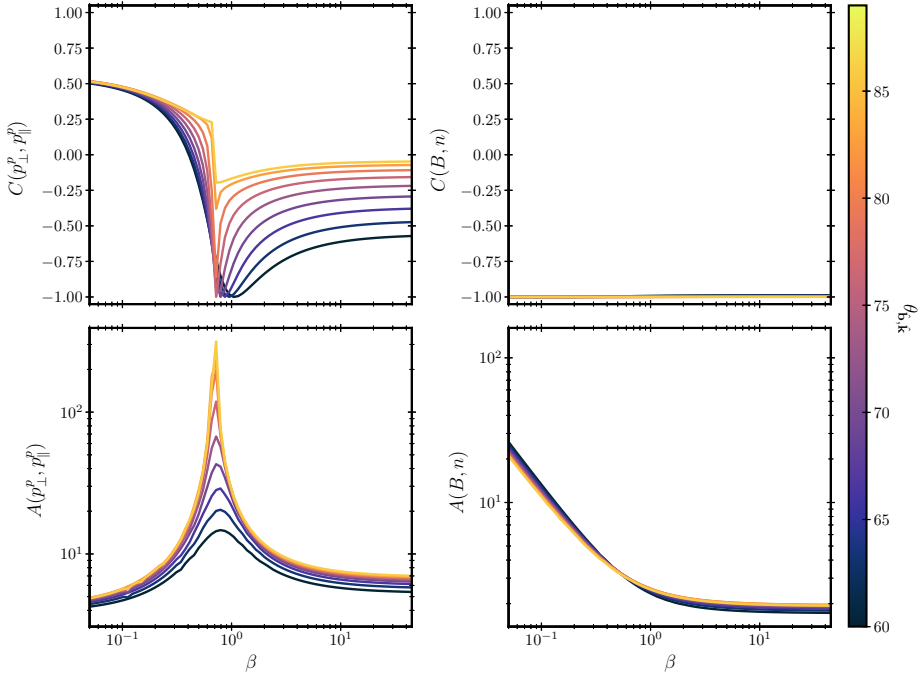


Figure 4.18: The correlations (Eq. 4.55) and amplitudes (Eq. 4.56) are plotted as a function of the plasma beta for different angles. The different curves are mapped to the color bar, which is the propagation angle. The parameters for these solutions are set to $k_{\parallel} \lambda_{\text{mfp}}^{\text{eff}} = 10$.

and density correlation is in general not influenced by the collisionality. This varying behaviour can be used as a probe for the collisionality.

The general point is that correlations, for example for a value of β , can be predicted by the model, for a set of parameters $k, \theta_{\hat{b}, \hat{k}}, \lambda_{\text{mfp}}^{\text{eff}}$. By measuring these correlations, as a function of beta, a comparison can be made between the observations and numerical predictions to measure remaining quantities, such as the $\lambda_{\text{mfp}}^{\text{eff}}$.

4.7 Conclusion

In this chapter the KMHD-BGK equations were derived and the eigen-problem was written. The numerical methods for treating this problem were explained and some results on the plasma dispersion relation function were displayed. This provides the numerical treatment of the compressive slow-mode wave.

The slow-mode wave was investigated for a range of $k, \lambda_{\text{mfp}}^{\text{eff}}, \theta_{\hat{b}, \hat{k}}$, and β . In Fig. 4.6 the damping scenario for a span of plasma beta was considered where the analytical expectations do well to match the numerical solutions according

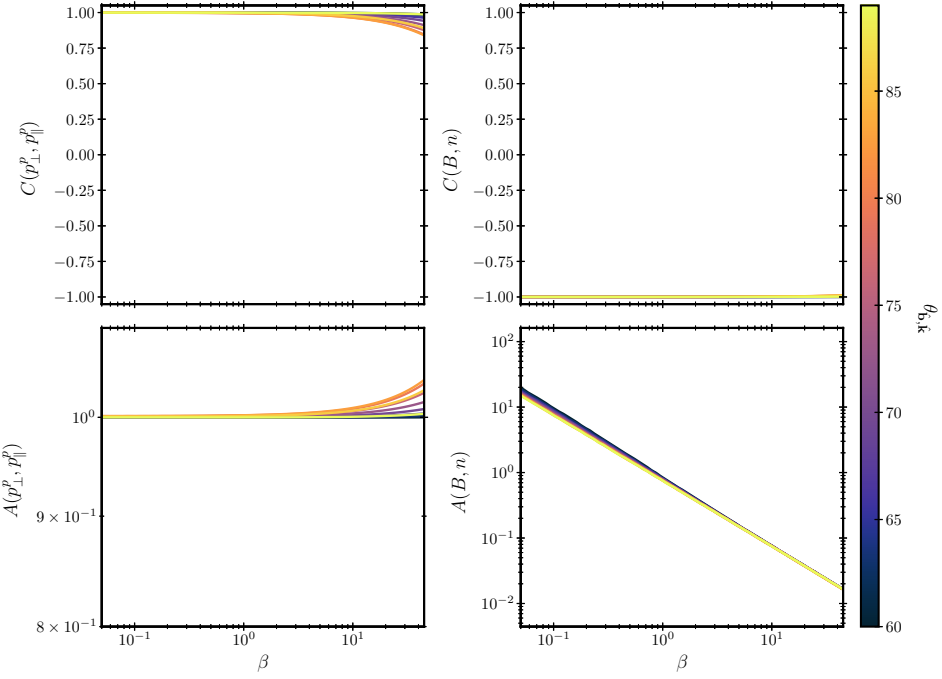


Figure 4.19: The correlations (Eq. 4.55) and amplitudes (Eq. 4.56) are plotted as a function of the plasma beta for different angles. The different curves are mapped to the color bar, which is the propagation angle. The parameters for these solutions are set to $k_{\parallel} \lambda_{\text{mfp}}^{\text{eff}} = 0.01$.

to the limits considered. In general, the waves are not severely damped in the fluid regime. In the collisionless regime, the damping rate becomes more significant showing strong beta dependence, as well as angular dependence as seen in Fig. 4.6, where the low beta solutions are weakly damped. At low beta phase speeds match the classic results for the slow-mode and ion-acoustic wave, but at high beta, the mode ceases to propagate.

The angular dependence was investigated further with Fig. 4.9 where $k \lambda_{\text{mfp}}^{\text{eff}} = 0.2$ corresponding to the fluid regime. Figure 4.8 has a $k \lambda_{\text{mfp}}^{\text{eff}} = 50.0$ where the damping factors match the classic results of Barnes [1966]. These two figures stress the importance of the propagation angle, in how much the damping factors change, as well as a drastic difference in the behaviour between high and low beta.

Due to this drastic change in behaviour of the slow-mode, the plasma beta turns out to be a good indicator of the collisionality of the system. Figure 4.10 displays the numerical solutions as a function of the plasma beta and collisionality. The damping rate increases with decreasing collisionality (and beta), as expected. The phase speeds show a drastic difference in behavior

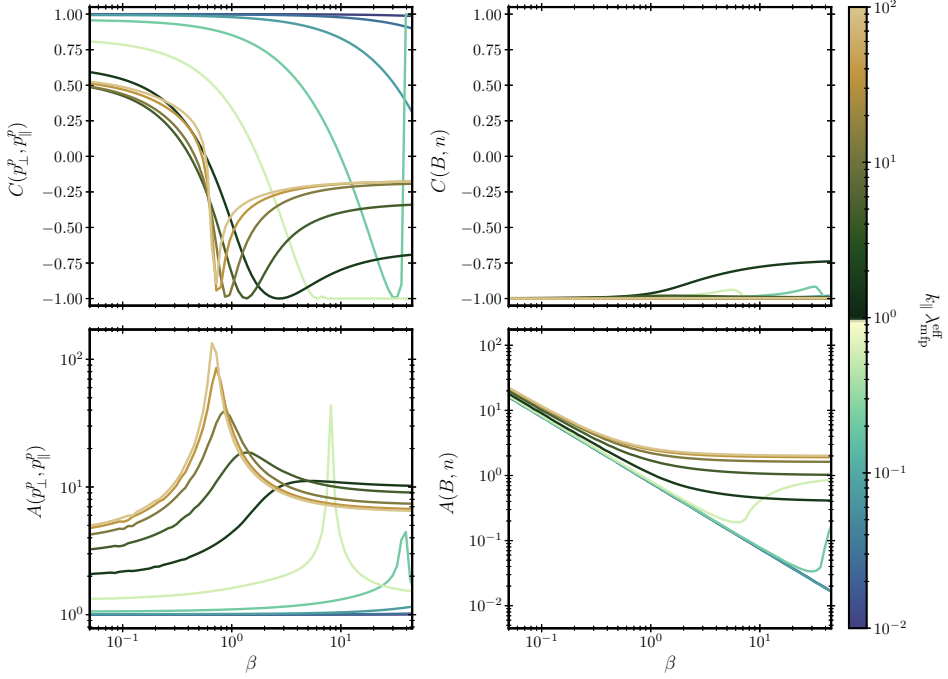


Figure 4.20: The correlations (Eq. 4.55) and amplitudes (Eq. 4.56) are plotted as a function of the plasma beta for different angles. The different curves are mapped to the color bar, which is $k_{\parallel} \lambda_{\text{mfp}}^{\text{eff}}$. The parameters for these solutions are set to $\theta_{\mathbf{b},\mathbf{k}} = 75^\circ$.

based on the collisionality until they are entirely collisionless. This is important for indicating the collisionality.

The temperature ratio and mean-free-path ratio were investigated to justify fixing the parameters. The temperature ratio does not significantly affect the dispersion relations at high beta in the fluid regime (Fig. 4.12) and less so in the collisionless regime (Fig. 4.11), also considering the color scale spans 4 orders of magnitude. For this reason the proton temperature is set equal to the electron temperature. The effective mean-free-path ratio does not appear to have a large effect on the system and is set to one, following the arguments from Sec. 4.5.3.

In Section 4.6 the method of correlations and amplitudes was presented. The dispersion relations are not measurable, so they cannot be used to identify wave properties of the observations. The classic test for the compressive wave mode is the cross-correlation of the density and magnetic field strength (see Section 3.6 for a review of observations), which have been shown to not strongly depend on the propagation angle and effective mean-free-path. In Chapter 5, different correlations are sought out, that are sensitive to the effective mean-free-path. These are then compared with observations.

This concludes the Chapter. A tool for investigating the properties of compressive slow-mode waves has been constructed. The full parameter regimes of k , $\lambda_{\text{mfp}}^{\text{eff}}$, $\theta_{\hat{\mathbf{b}}, \hat{\mathbf{k}}}$, and β can be investigated. The highlight of this tool, is the ability to investigate the spectrum of solutions that exist in between the collisional and collisionless limits. This provides a much better understanding of scale dependence, in particular through $k_{\parallel} \lambda_{\text{mfp}}^{\text{eff}}$, of compressive fluctuations. This tool will be used to model compressive fluctuations, compare with solar wind observations, and make a measurement of the effective mean-free-path of the solar wind in Chapter 5.

Chapter 5

Measuring the effective mean-free-path

In this Chapter, the methods for obtaining numerical predictions of cross-correlations (developed in Chapter 4) is appropriated for directly testing the equation of state. The effective collision frequency is the rate at which the distribution function is restored to equilibrium so it controls the influence of high order-moment such as the heat flux. Therefore, the equation of state depends sensitively on the effective mean-free-path. These predictions are then compared to solar wind observations to measure the effective mean-free-path and the scale-dependent anisotropy of the compressive fluctuations. These are the major results of the thesis. The essential finding is that the effective mean-free-path is much smaller than the collisional mean-free-path. This is shown to support the use of fluid theory to much smaller scales than the estimate from the collisional mean-free-path.

The solar wind proton pressure observations made by the electrostatic analyzer on the Wind spacecraft, have not been used for science previous to this work, so the validation of the dataset is shown by making comparisons with other datasets and repeating past results. The comparison between the dataset and the numerical methods required a comprehensive statistical method to be developed.

5.1 Chew-Goldberger-Low correlations

In Section 4.6 the method of producing quantities that are measurable by space-crafts was presented. Correlations of various variables can indicate waves and their properties [Gary, 1993]. Additionally, in Section 4.6, it was shown that the cross-correlations between the density and magnetic field fluctuations are

generally insensitive to the effective mean-free-path. Here it is shown that an excellent indicator can be produced by studying the Chew-Goldberger-Low (CGL) equations [Chew et al., 1956].

5.1.1 Equations of state and the Chew-Goldberger-Low equations

A quick sketch of the adiabatic equation of state follows from considering the pressure tensor moment of the drift kinetic equation (derived in Appendix B),

$$\begin{aligned} \frac{\partial}{\partial t} p_{ij}^s + \frac{\partial}{\partial x_k} (u_k^s p_{ij}^s + q_{ijk}^s) + \left(p_{kj}^s \frac{\partial}{\partial x_k} u_i^s + p_{ki}^s \frac{\partial}{\partial x_k} u_j^s \right) \\ - \frac{q_s}{m_s c} b_l (\epsilon_{ikl} p_{kj}^s + \epsilon_{jkl} p_{ki}^s) = \nu_s (p^s \delta_{ij} - p_{ij}^s), \end{aligned} \quad (5.1)$$

where the superscript “s” identifies the species for p_{ij}^s pressure tensor, u_i^s the bulk velocity, q_{ijk}^s the heat flux tensor, q_s the charge, m_s the mass, c the speed of light, b_l the magnetic field and ν_s the effective collision frequency. If the heat flux is zero, the trace (multiplying by δ_{ij}) gives,

$$\begin{aligned} \frac{\partial}{\partial t} p_{ii}^s + \frac{\partial}{\partial x_k} (u_k^s p_{ii}^s) + 2p_{ki}^s \frac{\partial}{\partial x_k} u_i^s \\ - \frac{q_s}{m_s c} b_l (\epsilon_{ikl} p_{ki}^s + \epsilon_{ikl} p_{ki}^s) = 0, \end{aligned} \quad (5.2)$$

if the pressure is diagonal in some frame ($p_{ii'}^s = 0$ if $i' \neq i$),

$$\frac{\partial}{\partial t} p_{ii}^s + \frac{\partial}{\partial x_k} (u_k^s p_{ii}^s) + 2p_{ki}^s \frac{\partial}{\partial x_k} u_i^s = 0, \quad (5.3)$$

the magnetic field term goes to zero and now considering the pressure to be isotropic $p^s = p_{ii}^s/3$,

$$3 \frac{\partial}{\partial t} p^s + 3 \frac{\partial}{\partial x_k} (u_k^s p^s) + 2p^s \frac{\partial}{\partial x_i} u_i^s = 0, \quad (5.4)$$

with $p_{ik}^s = \delta_{ik} p^s$. This is the adiabatic law,

$$\frac{1}{p^s} \frac{d}{dt} p^s = - \frac{5}{3} \frac{\partial}{\partial x_i} u_i^s = \frac{5}{3} \frac{1}{n_s} \frac{d}{dt} n^s. \quad (5.5)$$

where the continuity equation was used.

Now, if instead the pressure is symmetric but is anisotropic to the magnetic field, the situation is different. In Chew et al. [1956], the so-called Chew-Low-Golberger (CGL) invariants were presented. The equations, which include heat fluxes and collisional terms are derived in Appendix C from the drift-kinetic

equation. They are comprised of the density moment, perpendicular/parallel pressure moments, and the ideal induction equation. The same result can be derived from the Vlasov equation, taking the same moments, and then setting the non-gyrotropic terms to zero [Hunana et al., 2019a].

The perpendicular equation,

$$n_p |b_i| \frac{d}{dt} \left(\frac{p_\perp^p}{n_p |b_i|} \right) = -\frac{\partial}{\partial x_i} q_\perp^p \hat{b}_i - q_\perp^p \frac{\partial \hat{b}_i}{\partial x_i} + \frac{\nu_p}{3} (p_\parallel^p - p_\perp^p). \quad (5.6)$$

and the parallel equation,

$$\frac{n_p^3}{|b_i|^2} \frac{d}{dt} \left(\frac{p_\parallel^p |b_i|^2}{n_p^3} \right) = -\frac{\partial}{\partial x_i} \hat{b}_i q_\parallel^p + 2q_\perp^p \frac{\partial \hat{b}_i}{\partial x_i} + \frac{2\nu_p}{3} (p_\perp^p - p_\parallel^p), \quad (5.7)$$

where the proton density is n_p , the magnetic field is b_i , the perpendicular pressure is p_\perp^p , the perpendicular heat flux q_\perp^p , the effective proton collision frequency ν_p , the parallel pressure p_\parallel^p , and the parallel heat flux q_\parallel^p . The d/dt is the convective derivative with u_i^p supplying the convection.

The CGL equations are the extension of the adiabatic equation to a gyrotropic pressure. Some clarifying points need to be made. Looking at Eq. 5.6 and Eq. 5.7, for the purely Maxwellian case ($p_\perp^s = p_\parallel^s$), so that there is also no heat flux, the CGL invariants would appear to not be broken; they would not be broken in the fluid case. This is incorrect, and the point is subtle, but important.

The mathematical point of view is that Eq. 5.3 and Eq. 5.4 are independent of each other i.e., $\delta_{ij} p^s = p_{ij}^s$ is a constraint, not an algebraic manipulation. The resulting Eq. 5.6 and Eq. 5.7 have been derived considering the pressure-stress to be finite, which does not arise if the pressure is a scalar; so taking ($p_\perp^s = p_\parallel^s$) is not equivalent. This leads to the physical view point. Returning to Eq. 5.3, the final term is the pressure-stress, which is activated by anisotropic pressure, which is dictated by the magnetic field direction [Squire et al., 2019]. In the absence of these stresses, the magnetic field does not enter into the equations. This can be seen in Eq. C.18, using ($p_\perp^s = p_\parallel^s \Rightarrow \delta_{ij} = 3\hat{b}_i \hat{b}_j$). Thus, the magnetic field does not enter into the final invariants. So, with this context clearly laid, in the isotropic case, the CGL invariants are broken by the magnetic field, because it does not cause pressure-stresses.

In the absence of heat fluxes and collisions, the quantities in the big parentheses are conserved and are called the CGL invariants, which do appear in Chew et al. [1956], or are called the double adiabatic invariants. The breaking of the CGL invariants is considered in many applications of plasma physics since they are also broken by non-gyrotropic effects, neglected here, and by heating

of the plasma.

5.1.2 The CGL cross-correlations

The CGL equations (Eqs. 5.6, 5.7) are a sensitive test of the collision frequency in both the collisional $k_{\parallel} \lambda_{\text{mfp}}^{\text{eff}} \ll 1$ and collisionless regime $k_{\parallel} \lambda_{\text{mfp}}^{\text{eff}} \gg 1$. In the collisionless regime, the heat fluxes are finite, since the system is not at equilibrium, and will break the CGL invariants. The terms proportional to the effective collision frequency will break the invariants in the collisional regime. In the purely isotropic case they are broken as well, see the end of Section 5.1.1.

To test the CGL invariants, with cross-correlations and amplitude ratios from Section 4.6, the following are considered,

$$C_{\parallel} = \frac{\langle \delta p_{\parallel}^{\text{P}} \delta(n_{\text{p}}^3/B^2) \rangle}{\langle |\delta p_{\parallel}^{\text{P}}|^2 \rangle^{1/2} \langle |\delta(n_{\text{p}}^3/B^2)|^2 \rangle^{1/2}}, \quad (5.8a)$$

$$A_{\parallel} = \frac{\langle |\delta(n_{\text{p}}^3/B^2)|^2 \rangle^{1/2}}{\langle n_{\text{p}}^3/B^2 \rangle} \frac{\langle p_{\parallel}^{\text{P}} \rangle}{\langle |\delta p_{\parallel}^{\text{P}}|^2 \rangle^{1/2}}, \quad (5.8b)$$

$$C_{\perp} = \frac{\langle \delta p_{\perp}^{\text{P}} \delta(n_{\text{p}}B) \rangle}{\langle |\delta p_{\perp}^{\text{P}}|^2 \rangle^{1/2} \langle |\delta(n_{\text{p}}B)|^2 \rangle^{1/2}}, \quad (5.8c)$$

$$A_{\perp} = \frac{\langle |\delta(n_{\text{p}}B)|^2 \rangle^{1/2}}{\langle n_{\text{p}}B \rangle} \frac{\langle p_{\perp}^{\text{P}} \rangle}{\langle |\delta p_{\perp}^{\text{P}}|^2 \rangle^{1/2}}, \quad (5.8d)$$

where the $\delta\chi = \chi - \langle \chi \rangle$. The numerical predictions of these quantities are plotted, as a function of the proton beta, for a large range of the product $k_{\parallel} \lambda_{\text{mfp}}^{\text{eff}}$ in Fig. 5.1.

The trends in $k_{\parallel} \lambda_{\text{mfp}}^{\text{eff}}$ are fairly straight forward except for C_{\perp} , where some explanation follows. Starting with the fluid case (the lighter blue curves), the transition from low to high beta is sharp, and the sharpness decreases going towards the collisionless case, until $k_{\parallel} \lambda_{\text{mfp}}^{\text{eff}} \approx 1$ when the trends begin to become more sharp, and eventually (the most black curve) mimics the fluid case. This is because the slow-mode wave is recovered in the kinetic MHD limit from perpendicular pressure balance.

The measurements, that will be presented in Section 5.4.2, are in the fluid regime. Taking this to be a fact, the correlations C_{\perp} , C_{\parallel} , in the fluid regime, are more sharp for smaller relative wavenumber. The C_{\perp} curves in the collisionless regime, are more sharp for larger relative wavenumber. The wavenumber dependence is an important indicator that the technique we have used here is consistent. For example, if the measured sharpness of the C_{\perp} curves increased by increasing the wavenumber, then it would indicate the measurements are more near to the collisionless regime. The opposite is the measured case, that the most sharp C_{\perp} curve is for the smallest wavenumber and so the measure-

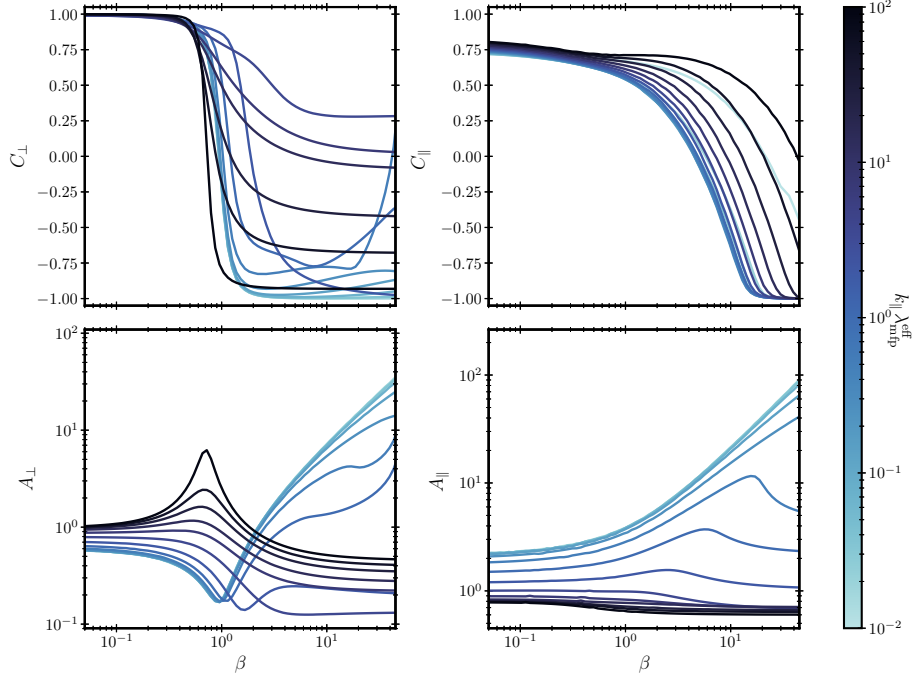


Figure 5.1: The correlations and amplitudes (Eqs. 5.8) are plotted as a function of the plasma beta for $k_{\parallel} \lambda_{\text{mfp}}^{\text{eff}}$, seen in the color bar. The obliqueness of the propagation angle $\theta_{\hat{b},\hat{k}}$ increases with k .

ments are in the fluid regime.

For example, looking at the C_{\perp} case in Fig. 5.1, and taking the propagation angle and effective mean-free-path constant, increasing the wavenumber, in the fluid regime (lighter blue), the correlation becomes less negative at high beta. In the collisionless regime (darker blues), the correlations becomes more negative by increasing the wavenumber. For this reason, two correlations, measured at different wavenumbers, are needed to indicate consistency with increasing wavenumber. Since there is another unknown parameter, the propagation angle, which needs to be determined as well, this requires one more case, for a total of three, to ensure the trends in wavenumber and propagation angle match between the observations and numerical solutions.

The amplitudes are more simple, but impose a basic check of the fluid regime. In the fluid regime, the amplitudes increase with beta, and in the collisionless regime, they decrease.

Figure 5.2 shows the influence of the propagation angle on the correlation and amplitudes. The importance here is on C_{\parallel} where the propagation angle does have a significant influence on the curves. This part of the analysis indicates that careful consideration of the propagation angle is necessary to recover the

correct trend with wavenumber. The propagation angle must increase sharply with increasing wavenumber to obtain the curves in Fig. 5.2, later in this Chapter observations will be presented that match this trend, indicating an increase in obliqueness with wavenumber is correct.

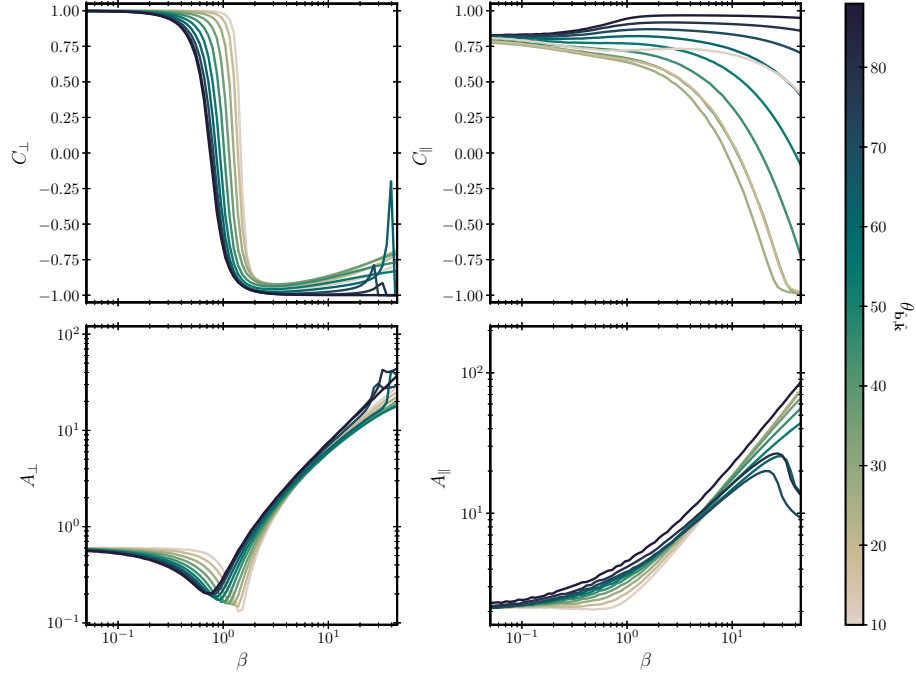


Figure 5.2: The correlations and amplitudes (Eqs. 5.8) are plotted as a function of the plasma beta for $k_{\parallel} \lambda_{\text{mfp}}^{\text{eff}} = 0.06$. a set of angles . The different curves are mapped to the color bar, which is $\theta_{\hat{b},\hat{k}}$.

To explore their meaning without going into the details of expanding the pressure, density and magnetic field fluctuations in Appendix B, instead some basic considerations will be made here. As was clearly displayed, in Chapter 4, these correlations are all parameterised by the $k, \beta, \lambda_{\text{mfp}}^{\text{eff}}, \theta_{\hat{b},\hat{k}}$, so that the numerical method was necessary, so here, a basic check of the expectations in the fluid regime are verified.

Dynamically, the isotropic pressure and magnetic field strengths follow,

$$\beta \gg 1, \quad \delta p_B \gg \delta p_p, \quad (5.9)$$

$$\beta \ll 1, \quad \delta p_B \ll \delta p_p, \quad (5.10)$$

where p_p is the proton pressure and $p_B = B^2/8\pi$ is the magnetic pressure. This says, that when the magnetic pressure is large, its perturbation is smaller, and same for the proton pressure. Next, for the fluid slow-mode, the anti-correlation

between the thermal and magnetic pressure, $\delta p_B \sim -\delta p_p$, identifies the mode. Last, adiabatically, $\delta p_p \sim \delta n_p$ the two quantities are correlated. It then follows that linearly,

$$\delta\left(\frac{n_p^3}{B^2}\right) \approx \frac{\bar{n}_p^3}{\bar{B}^2} \left(3\frac{\delta n_p}{\bar{n}_p} - 2\frac{\delta B}{\bar{B}}\right), \quad (5.11)$$

$$\delta\left(n_p B\right) \approx \bar{B}\delta n_p + \bar{n}_p\delta B, \quad (5.12)$$

where for simplicity the over bar is the average as well. The amplitude,

$$\begin{aligned} \left\langle \left| \delta\left(\frac{n_p^3}{B^2}\right) \right|^2 \right\rangle^{1/2} &\approx \left\langle \left| \frac{\bar{n}_p^3}{\bar{B}^2} \left(3\frac{\delta n_p}{\bar{n}_p} - 2\frac{\delta B}{\bar{B}}\right) \right|^2 \right\rangle^{1/2} \\ &= \left| \frac{\bar{n}_p^3}{\bar{B}^2} \right|^2 \left\langle 9\left|\frac{\delta n_p}{\bar{n}_p}\right|^2 + 4\left|\frac{\delta B}{\bar{B}}\right|^2 + 12\frac{\delta n_p}{\bar{n}_p}\frac{\delta B}{\bar{B}} \right\rangle^{1/2} \\ &\approx \left| \frac{\bar{n}_p^3}{\bar{B}^2} \right| \left\langle 9\left|\frac{\delta n_p}{\bar{n}_p}\right|^2 + 4\left|\frac{\delta B}{\bar{B}}\right|^2 \right\rangle^{1/2}, \end{aligned} \quad (5.13)$$

where in the second line, the third term will always be smaller than the other two. For the next important amplitude,

$$\begin{aligned} \left\langle \left| \delta\left(n_p B\right) \right|^2 \right\rangle^{1/2} &\approx \left\langle \left| \bar{B}\delta n_p + \bar{n}_p\delta B \right|^2 \right\rangle^{1/2} \\ &= \left\langle \left| \bar{B}\delta n_p \right|^2 + \left| \bar{n}_p\delta B \right|^2 + \bar{B}\bar{n}_p\delta n_p\delta B \right\rangle^{1/2} \\ &\approx |\bar{B}\bar{n}_p| \left\langle \left| \frac{\delta n_p}{\bar{n}_p} \right|^2 + \left| \frac{\delta B}{\bar{B}} \right|^2 \right\rangle^{1/2}, \end{aligned} \quad (5.14)$$

the cross correlation C_{\parallel} goes as,

$$\begin{aligned} C_{\parallel} &= \frac{\langle \delta p_{\parallel}^p \delta(n_p^3/B^2) \rangle}{\langle |\delta p_{\parallel}^p|^2 \rangle^{1/2} \langle |\delta(n_p^3/B^2)|^2 \rangle^{1/2}} \approx \frac{\left\langle \delta p_{\parallel}^p \frac{\bar{n}_p^3}{\bar{B}^2} \left(3\frac{\delta n_p}{\bar{n}_p} - 2\frac{\delta B}{\bar{B}}\right) \right\rangle}{\langle |\delta p_{\parallel}^p|^2 \rangle^{1/2} \left| \frac{\bar{n}_p^3}{\bar{B}^2} \right| \left\langle 9\left|\frac{\delta n_p}{\bar{n}_p}\right|^2 + 4\left|\frac{\delta B}{\bar{B}}\right|^2 \right\rangle^{1/2}}, \\ &\approx \frac{\left\langle \delta p_{\parallel}^p \left(3\frac{\delta n_p}{\bar{n}_p} - 2\frac{\delta B}{\bar{B}}\right) \right\rangle}{\langle |\delta p_{\parallel}^p|^2 \rangle^{1/2} \left\langle 9\left|\frac{\delta n_p}{\bar{n}_p}\right|^2 + 4\left|\frac{\delta B}{\bar{B}}\right|^2 \right\rangle^{1/2}}, \end{aligned} \quad (5.15)$$

for small and large β based on Eq. 5.9,

$$\beta \ll 1, \quad C_{\parallel} \approx \frac{\langle \delta p_{\parallel}^P \delta n_p \rangle}{\langle |\delta p_{\parallel}^P|^2 \rangle^{1/2} \left\langle \left| \delta n_p \right|^2 \right\rangle^{1/2}} > 0, \quad (5.16)$$

$$\beta \gg 1, \quad C_{\parallel} \approx -\frac{\langle \delta p_{\parallel}^P \delta B \rangle}{\langle |\delta p_{\parallel}^P|^2 \rangle^{1/2} \left\langle \left| \delta B \right|^2 \right\rangle^{1/2}} > 0, \quad (5.17)$$

where the low beta case corresponds to an adiabatic equation of state and the high beta case follows from the polarisation of the slow-mode wave. The C_{\perp} ,

$$\begin{aligned} C_{\perp} &= \frac{\langle \delta p_{\perp}^P \delta(n_p B) \rangle}{\langle |\delta p_{\perp}^P|^2 \rangle^{1/2} \langle |\delta(n_p B)|^2 \rangle^{1/2}} \approx \frac{\langle \delta p_{\perp}^P (\bar{B} \delta n_p + \bar{n}_p \delta B) \rangle}{\langle |\delta p_{\perp}^P|^2 \rangle^{1/2} |\bar{B} \bar{n}_p| \left\langle \left| \frac{\delta n_p}{\bar{n}_p} \right|^2 + \left| \frac{\delta B}{\bar{B}} \right|^2 \right\rangle^{1/2}}, \\ &\approx \frac{\langle \delta p_{\perp}^P \left(\frac{\delta n_p}{\bar{n}_p} + \frac{\delta B}{\bar{B}} \right) \rangle}{\langle |\delta p_{\perp}^P|^2 \rangle^{1/2} \left\langle \left| \frac{\delta n_p}{\bar{n}_p} \right|^2 + \left| \frac{\delta B}{\bar{B}} \right|^2 \right\rangle^{1/2}}. \end{aligned} \quad (5.18)$$

The argument of Eq. 5.9 gives,

$$\beta \ll 1, \quad C_{\perp} \approx \frac{\langle \delta p_{\perp}^P \delta n_p \rangle}{\langle |\delta p_{\perp}^P|^2 \rangle^{1/2} \left\langle \left| \delta n_p \right|^2 \right\rangle^{1/2}} > 0, \quad (5.19)$$

$$\beta \gg 1, \quad C_{\perp} \approx \frac{\langle \delta p_{\perp}^P \delta B \rangle}{\langle |\delta p_{\perp}^P|^2 \rangle^{1/2} \left\langle \left| \delta B \right|^2 \right\rangle^{1/2}} < 0. \quad (5.20)$$

Next, the A_{\parallel} ,

$$\begin{aligned} A_{\parallel} &= \frac{\langle |\delta(n_p^3/B^2)|^2 \rangle^{1/2}}{\langle n_p^3/B^2 \rangle} \frac{\langle p_{\parallel}^P \rangle}{\langle |\delta p_{\parallel}^P|^2 \rangle^{1/2}} \approx \frac{\left| \frac{\bar{n}_p^3}{B^2} \right| \left\langle \left| \frac{\delta n_p}{\bar{n}_p} \right|^2 + 4 \left| \frac{\delta B}{\bar{B}} \right|^2 \right\rangle^{1/2} \langle p_{\parallel}^P \rangle}{\langle n_p^3/B^2 \rangle \langle |\delta p_{\parallel}^P|^2 \rangle^{1/2}}, \\ &\approx \frac{\left\langle \left| \frac{\delta n_p}{\bar{n}_p} \right|^2 + 4 \left| \frac{\delta B}{\bar{B}} \right|^2 \right\rangle^{1/2} \langle p_{\parallel}^P \rangle}{\langle |\delta p_{\parallel}^P|^2 \rangle^{1/2}}, \end{aligned} \quad (5.21)$$

The argument of Eq. 5.9 gives,

$$\beta \ll 1, A_{\parallel} \approx 3 \left\langle \left| \frac{\delta n_p}{\bar{n}_p} \right|^2 \right\rangle^{1/2} \frac{\langle p_{\parallel}^p \rangle}{\langle |\delta p_{\parallel}^p|^2 \rangle^{1/2}}, \quad (5.22)$$

$$\beta \gg 1, A_{\parallel} \approx 2 \left\langle \left| \frac{\delta B}{B} \right|^2 \right\rangle^{1/2} \frac{\langle p_{\parallel}^p \rangle}{\langle |\delta p_{\parallel}^p|^2 \rangle^{1/2}}, \quad (5.23)$$

Where for high beta the amplitude will increase due to the average beta dependence. Finally, A_{\perp} ,

$$A_{\perp} = \frac{\langle |\delta(n_p B)|^2 \rangle^{1/2}}{\langle n_p B \rangle} \frac{\langle p_{\perp}^p \rangle}{\langle |\delta p_{\perp}^p|^2 \rangle^{1/2}} \approx \frac{|\bar{B} \bar{n}_p| \left(\left| \frac{\delta n_p}{\bar{n}_p} \right|^2 + \left| \frac{\delta B}{B} \right|^2 \right)^{1/2}}{\langle n_p B \rangle} \frac{\langle p_{\perp}^p \rangle}{\langle |\delta p_{\perp}^p|^2 \rangle^{1/2}},$$

$$\approx \left\langle \left| \frac{\delta n_p}{\bar{n}_p} \right|^2 + \left| \frac{\delta B}{B} \right|^2 \right\rangle^{1/2} \frac{\langle p_{\perp}^p \rangle}{\langle |\delta p_{\perp}^p|^2 \rangle^{1/2}} \quad (5.24)$$

The argument of Eq. 5.9 gives,

$$\beta \ll 1, A_{\perp} \approx \left\langle \left| \frac{\delta n_p}{\bar{n}_p} \right|^2 \right\rangle^{1/2} \frac{\langle p_{\perp}^p \rangle}{\langle |\delta p_{\perp}^p|^2 \rangle^{1/2}}, \quad (5.25)$$

$$\beta \gg 1, A_{\perp} \approx \left\langle \left| \frac{\delta B}{B} \right|^2 \right\rangle^{1/2} \frac{\langle p_{\perp}^p \rangle}{\langle |\delta p_{\perp}^p|^2 \rangle^{1/2}}, \quad (5.26)$$

where the amplitude follows similarly, in that it increases due to the beta dependence, at high beta. Returning to Fig. 5.1, these basic considerations are consistent for the correlations and amplitudes. To investigate them for moderate collisionality, the numerical method is necessary.

5.2 Breaking the parameter degeneracy

The general idea is to make comparisons between numerical predictions and observations of the cross-correlations and amplitude ratios. The set of parameters of the numerical predictions must be set or left free, to be determined, when making the comparison. A difficulty arises when determining the parameters due to the scale-dependent nature of the solutions in the collisional regime. Recall from Eq. 4.42 that the argument of the plasma dispersion function,

$$\zeta_s = \frac{\omega}{k_{\parallel} v_s} + \frac{i}{k_{\parallel} \lambda_{\text{mfp}}^{\text{eff}}}, \quad (5.27)$$

involves both the effective mean-free-path of protons $\lambda_{\text{mfp}}^{\text{eff}}$ and the propagation angle $\theta_{\hat{b}, \hat{k}}$. The collisional regime is defined by the dominance of the term

inversely proportional to $k_{\parallel} \lambda_{\text{mfp}}^{\text{eff}}$. Therefore, the solutions, non-trivially determined by the full set of equations in Section 4.5, are degenerate in $\lambda_{\text{mfp}}^{\text{eff}}$, $\theta_{\hat{\mathbf{b}},\hat{\mathbf{k}}}$. Recall that $k_{\parallel} = k \cos(\theta_{\hat{\mathbf{b}},\hat{\mathbf{k}}})$.

Figure 5.3 has been provided to illustrate the degeneracy. To illustrate the issue further, consider the following values,

$$k_{\parallel} \lambda_{\text{mfp}}^{\text{eff}} = 10^{-3}, \Rightarrow \theta_{\hat{\mathbf{b}},\hat{\mathbf{k}}} = \arccos \left\{ \frac{10^{-3}}{k \lambda_{\text{mfp}}^{\text{eff}}} \right\}, \quad (5.28)$$

where in Fig. 5.3, $\lambda_{\text{mfp}}^{\text{eff}} = [1, 2, 3] \times 10^5$ km are plotted as dashed lines; they have the same $k_{\parallel} \lambda_{\text{mfp}}^{\text{eff}}$ and will give the same solution. Notice that at a single wavenumber, say $k_{\text{SW}} = 10^{-7}$ km $^{-1}$ the dotted black lines are all crossed. So that for the same $k_{\parallel} \lambda_{\text{mfp}}^{\text{eff}} = 10^{-3}$ three pairs of $\lambda_{\text{mfp}}^{\text{eff}}$, $\theta_{\hat{\mathbf{b}},\hat{\mathbf{k}}}$ will give the same solution.

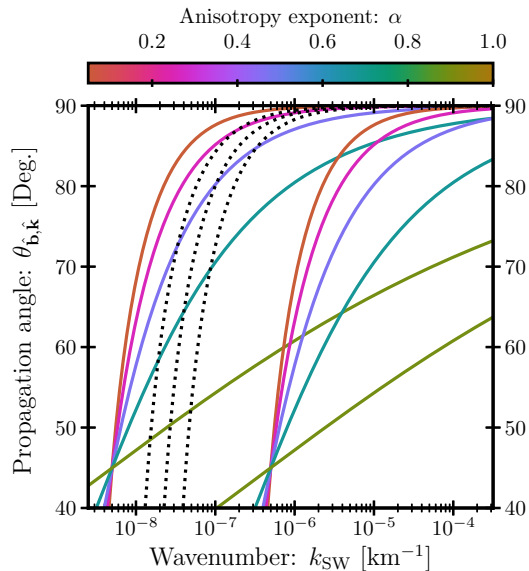


Figure 5.3: The dashed line is three different values of the $\lambda_{\text{mfp}}^{\text{eff}}$ and the same $k_{\parallel} \lambda_{\text{mfp}}^{\text{eff}}$. The function in Eq. 5.32 is plotted for a set of parameters, where α is mapped to the color bar and the values for k_{iso} are at 45 degrees where the colored lines meet.

To break this degeneracy a relation between the wavenumber and angle is established through a model so that $\lambda_{\text{mfp}}^{\text{eff}}$ can be determined. The model $k_{\parallel} \sim k_{\perp}^{\alpha}$, introduced here, is generalized from the critical balance model of Alfvénic turbulence [Goldreich and Sridhar, 1995]. To ensure the isotropic scale

is defined correctly,

$$\frac{k_{\parallel}}{k_{\text{iso}}/\sqrt{2}} = \left(\frac{k_{\perp}}{k_{\text{iso}}/\sqrt{2}} \right)^{\alpha}, \quad (5.29)$$

where α is the anisotropy exponent. Since, $k_{\parallel} = k \cos(\theta_{\hat{\mathbf{b}}, \hat{\mathbf{k}}})$, $k_{\perp} = k \sin(\theta_{\hat{\mathbf{b}}, \hat{\mathbf{k}}})$, this gives,

$$\frac{k \cos(\theta_{\hat{\mathbf{b}}, \hat{\mathbf{k}}})}{k_{\text{iso}}/\sqrt{2}} = \left(\frac{k \sin(\theta_{\hat{\mathbf{b}}, \hat{\mathbf{k}}})}{k_{\text{iso}}/\sqrt{2}} \right)^{\alpha} \Rightarrow k^{1-\alpha} = \left(\frac{k_{\text{iso}}}{\sqrt{2}} \right)^{1-\alpha} \cos(\theta_{\hat{\mathbf{b}}, \hat{\mathbf{k}}})^{-1} \sin(\theta_{\hat{\mathbf{b}}, \hat{\mathbf{k}}})^{\alpha}, \quad (5.30)$$

so that at $\theta_{\hat{\mathbf{b}}, \hat{\mathbf{k}}}^* = 45^\circ$, $\sin(\theta_{\hat{\mathbf{b}}, \hat{\mathbf{k}}}^*) = \cos(\theta_{\hat{\mathbf{b}}, \hat{\mathbf{k}}}^*) = 1/\sqrt{2}$,

$$k^{1-\alpha} = \left(\frac{k_{\text{iso}}}{\sqrt{2}} \right)^{1-\alpha} (\sqrt{2})^{1-\alpha} = (k_{\text{iso}})^{1-\alpha}, \quad (5.31)$$

so the isotropic scale $k = k_{\text{iso}}$ has been recovered. Thus, the wavenumber model appears as,

$$k = \frac{k_{\text{iso}}}{\sqrt{2}} [\sin(\theta_{\hat{\mathbf{b}}, \hat{\mathbf{k}}})]^{\alpha/(1-\alpha)} [\cos(\theta_{\hat{\mathbf{b}}, \hat{\mathbf{k}}})]^{1/(\alpha-1)}. \quad (5.32)$$

Some examples are plotted as colored lines in Fig. 5.3. Notice that for α, k_{iso} the wavenumber k determines $\theta_{\hat{\mathbf{b}}, \hat{\mathbf{k}}}$ like $\theta_{\hat{\mathbf{b}}, \hat{\mathbf{k}}} = f\{k; \alpha, k_{\text{iso}}\}$. Now, the degeneracy is in α, k_{iso} . Comparing solutions at multiple wavenumber can break the degeneracy.

The easiest way to see this is to notice that the best solution at a wavenumber has the value,

$$S_k = k \cos(f^{-1}\{k; \alpha, k_{\text{iso}}\}) \lambda_{\text{mfp}}^{\text{eff}}, \quad (5.33)$$

where f^{-1} is the inverse. Here, $\lambda_{\text{mfp}}^{\text{eff}}$ is determined at k for a set of α, k_{iso} (a set because the degeneracy is still an issue). Now, comparing at multiple wavenumbers k_0, k_1, k_2 gives solutions $S_{k_0}, S_{k_1}, S_{k_2}$, each with their own set of α, k_{iso} , which when comparing the sets, will eliminate α, k_{iso} that were reasonable for one solution, but not another. This final idea of reasonability will be quantified in Section 5.4.3.

In this way, the $\lambda_{\text{mfp}}^{\text{eff}}, \alpha, k_{\text{iso}}$ can be determined by finding the best solution at multiple wavenumbers. This is the method used to break the parameter degeneracy and determine the scale dependence of k_{\parallel} .

The wavenumber model has many freedoms, accounting for any scale dependent anisotropy of the $k_{\parallel} \sim k_{\perp}^{\alpha}$ kind, which includes slab models $\alpha = 0$

[Oughton et al., 2015], $\alpha_{GS} = 2/3$ from Goldreich and Sridhar [1995], and covers the measurements of α for compressive fluctuations [Chen, 2016], shown in Section 3.7.3. Some theoretical predictions based on turbulence were presented in Section 2.7.0.4 which are also covered by the generalized model.

5.3 The Wind dataset

The Wind data set is formed by measurements of the magnetic field made by the fluxgate magnetometer and proton measurements made by the electrostatic analyzer, both of which are covered in Section 3.8. The electrostatic analyzer takes onboard moments of the proton distribution function which provide the density, velocity and pressure tensor at the spacecraft spin frequency ≈ 3 seconds [Lin et al., 1995b]. To the best of my knowledge, the onboard proton pressure tensor data product has not been used for analysis in a published research article. When it first became apparent that the data product existed, the coordinate system and units were unknown. This section details the effort put into ensuring good quality of the dataset, the coordinate system, and the units.

The dataset covers the years 2005 - 2015 for any of the ensemble studies, and if it is not an ensemble study, the dates will be made clear. In these years Wind is at the L1 point in space so it is not influenced by Earth's magnetosphere. This dataset has approximately 100 million data points per quantity (e.g., proton density) where the nominal time cadence of 3 seconds is used to extrapolate that % 96 of the time, the spacecraft successfully recorded something. The single points are used in this section to make comparisons with other datasets. In the science section of this Chapter (section 5.3.4) the 10 years of data is used as streams of greater than 3 seconds, as a time series of the various quantities. These time series are then analyzed to produce the final results.

5.3.1 Comparison with ground moments

The method devised to understand the dataset is to compare on-ground moments calculated from proton distribution functions to onboard moments calculated by the microprocessors onboard the instrument. All of the observations are made by the 3DP instrument which is a set of electrostatic analyzers. The on-ground dataset is known as the "Proton Omnidirectional Fluxes and Moments" and is called PLSP, which is recorded at a 24 second cadence. The dataset intended for verification is known as Proton Moment (PM) and recorded at a 3 second cadence. The raw data is processed by SPEDAS (Space Physics Environment Data Analysis Software) [Angelopoulos et al., 2019]. Its capabilities range from plotting and analysis to performing post-calibration. Since the software

is capable of taking level zero data and outputting pristine data products like PLSP, it will be used to track down the data manipulations of the PM data.

The method employed to understand the dataset relies on two pieces of information: that SPEDAS takes level zero onboard data and outputs the data products that are on the “<https://cdaweb.gsfc.nasa.gov/pub/data/wind/3dp/>” website. Second, that on-ground 24 second moments are published. If the comparison between the 24 second data and the 3 second data is good, then the operations in SPEDAS contain the units and coordinate transforms. First, this is done with the velocity vector to ensure the technique will work (on a vector). If the comparison is good, then the same can be done for the pressure.

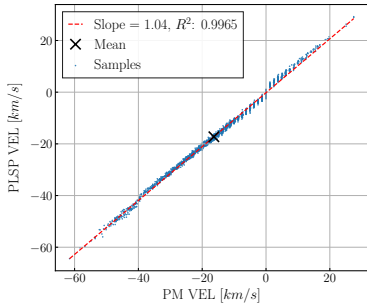


Figure 5.4: Component 2, see global caption.

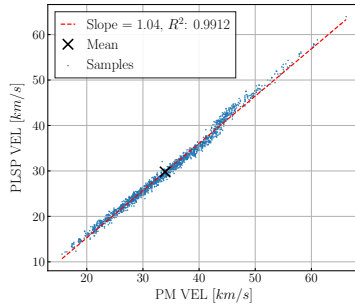


Figure 5.5: Component 1, see global caption.

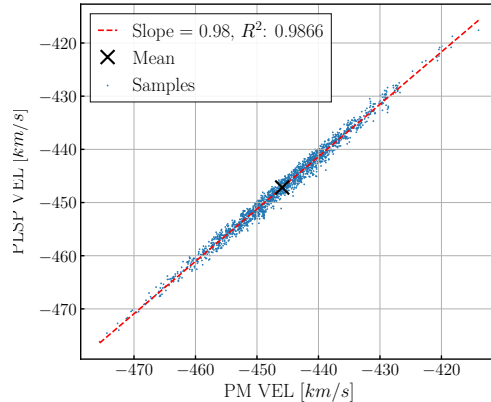


Figure 5.6: The blue dots are a scatter plot of the 24 second PLSP x-component of the velocity and 3 second PM x-component of the velocity from level 0, both in the geocentric coordinate system (see text for a description of the coordinate system). The time interval is one day: July 7th, 2007. The linear regression produced the slope (dashed red line) and the Pearson correlation coefficient. The mean can be ignored.

Figure 5.6 displays the comparison for three components of the velocity. To compare the 3 second data to the 24 second data, the closest data point, in time, was chosen. It was thought that some averaging would need to be done, but in the end, this was sufficient. While Fig. 5.6 is simple, it means that a comparison between the 24 second pressure tensor and the 3 second pressure tensor should reveal the units and coordinate system since the level zero data was used.

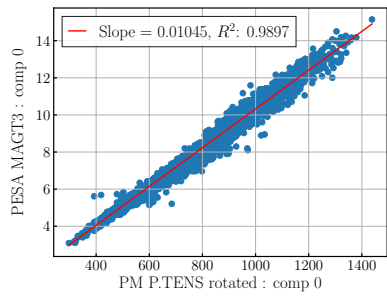


Figure 5.7: Component 00, see global caption.

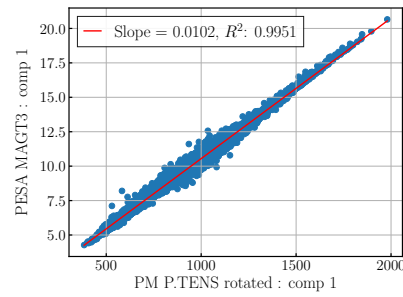


Figure 5.8: Component 11, see global caption.

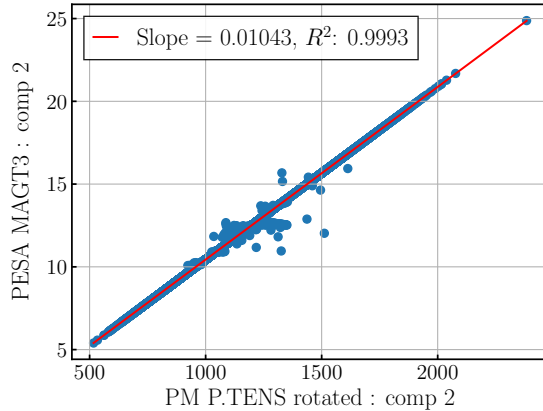


Figure 5.9: The blue dots are a scatter plot of the 24 second PLSP 22-component of the pressure tensor and the level zero 3 second PM 22-component of the velocity, both in the geocentric coordinate system. The time interval is one day: July 7th, 2007. The linear regression produced the slope (solid red line) and the Pearson correlation coefficient.

Figure 5.9 repeats the analysis of Fig. 5.6 on three components of the pressure tensor. The Pearson correlation coefficients are near unity. The slope

corresponds to the unit system used by the instrument. It corresponds to,

$$m_p = 938.272 \text{ eV}, \quad c = 2.99 \times 10^5 \text{ km/s} \Rightarrow \frac{m_p}{c^2} = 0.0104 \frac{\text{eV}}{(\text{km/s})^2}. \quad (5.34)$$

This number was later found to be commented-out in the IDL files that make up the SPEDAS software, along with the rotation matrix. This was the reason to pass the level zero data through SPEDAS, to track down these operations.

Next, the coordinate system of the two data products is geocentric solar ecliptic (GSE). The 0 component or “x” component points towards the sun, the 2 component or “z” component points perpendicular to the plane of the Earth’s orbit around the sun so that positive is consistent with the northern hemisphere of the Earth. The 1 component or “y” component, is then perpendicular to both of the other components.

The units of the 3DP 3 second dataset have been confirmed, so that the data product is a set of temperature tensors in T_{ij}^p [eV] and converted into any unit system. The pressure tensor is then easily obtained $p_{ij}^p = n_p k_B T_{ij}^p$, assuming the ideal gas law [[Landau and Lifshitz, 2013](#)]. The gyrotropic pressures are obtained by rotating into the local magnetic field coordinate system with the normalised magnetic field vector $\hat{b} = b_i / |b_i|$ where b_i is obtained from the magnetic field instrument. The decomposition appears like,

$$p_{ij}^p = p_\perp^p (\delta_{ij} - \hat{b}_i \hat{b}_j) + p_\parallel^p \hat{b}_i \hat{b}_j + \Pi_{ij}^p, \quad (5.35)$$

$$p_\perp^p = \frac{1}{2} p_{ij}^p (\delta_{ij} - \hat{b}_i \hat{b}_j), \quad p_\parallel^p = p_{ij}^p \hat{b}_i \hat{b}_j, \quad (5.36)$$

$$\Pi_{ij}^p = p_{ij}^p - (p_\perp^p (\delta_{ij} - \hat{b}_i \hat{b}_j) + p_\parallel^p \hat{b}_i \hat{b}_j), \quad (5.37)$$

where the perpendicular pressure p_\perp^p , parallel pressure p_\parallel^p , and non-gyrotropic pressure tensor Π_{ij}^p are all defined.

Comparison with the PLSP data has revealed the coordinate system and the units of the 3 second PM proton pressure tensor measurements. Next, the quality of the data needed to be checked. The dataset that follows is formed from the magnetic field instrument’s 3 second data product, linearly interpolated to time stamps of the 3 second PM proton pressure tensor, which is the same time stamp as the density and velocity.

5.3.2 Comparison with SWE

Numerous famous studies of the pressure have been completed with the Faraday cup instrument (SWE) on the Wind spacecraft (see Fig. 3.8) [[Ogilvie et al., 1995](#), [Kasper et al., 2002, 2006](#)]. A comparison with the SWE dataset has been made, starting with a repeat of Fig. 3.8, which appears here as Fig. 5.10. The

basic operation of a Faraday Cup is explained in Section 3.8.3.

The dataset is available as perpendicular and parallel thermal speeds. The definition used for the thermal speed by the SWE instrument is the 1 dimensional thermal speed $v^{1D} = \sqrt{k_B T/m_p}$ opposed to the most probable thermal speed in 3 dimensions $v^{3D} = \sqrt{2k_B T/m_p}$, used for the 3DP instrument. Therefore, the SWE temperature is divided by 2 to compare with the 3DP dataset.

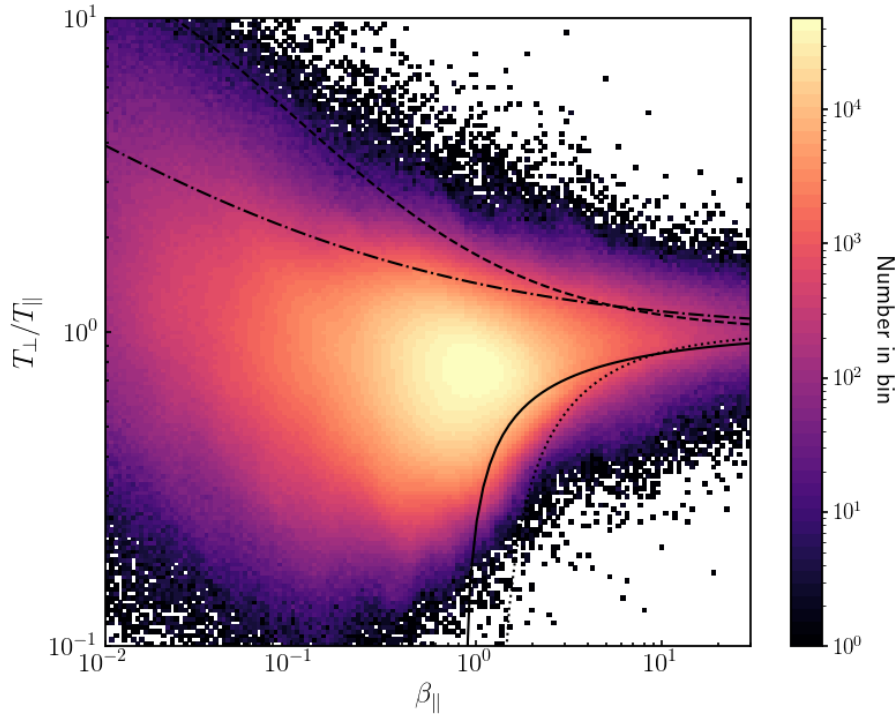


Figure 5.10: A repeat of the analysis employed by Hellinger et al. [2006]. The black lines are from the paper, corresponding to the mirror (dashed), proton cyclotron (dash-dot), parallel firehose (solid), and oblique firehose (dotted) instability thresholds. This is a joint histogram with logarithmically spaced boxes. The data is taken from years 2005 to 2008 as measured by the Wind 3DP electrostatic analyzer and the Wind MFI.

The general result, that the data is constrained by the thresholds, as seen in previous studies of these quantities. The data here tends to “spill over” the thresholds slightly more than as seen with the Faraday cup data. This is likely due to the time cadence of the measurement. These thresholds are calculated with the following reasoning: given β_{\parallel} what value of T_{\perp}/T_{\parallel} has $\gamma_{\max} = 10^{-3} \text{ s}^{-1}$. The maximum growth rate is roughly related to the rate at which the

temperature anisotropy is restored to isotropy (see Section 6.6 for more details). Therefore, as the plasma enters further into the unstable region, it spends less time there, so that at higher measurement cadence, the measured plasma will be observed deeper into the unstable region.

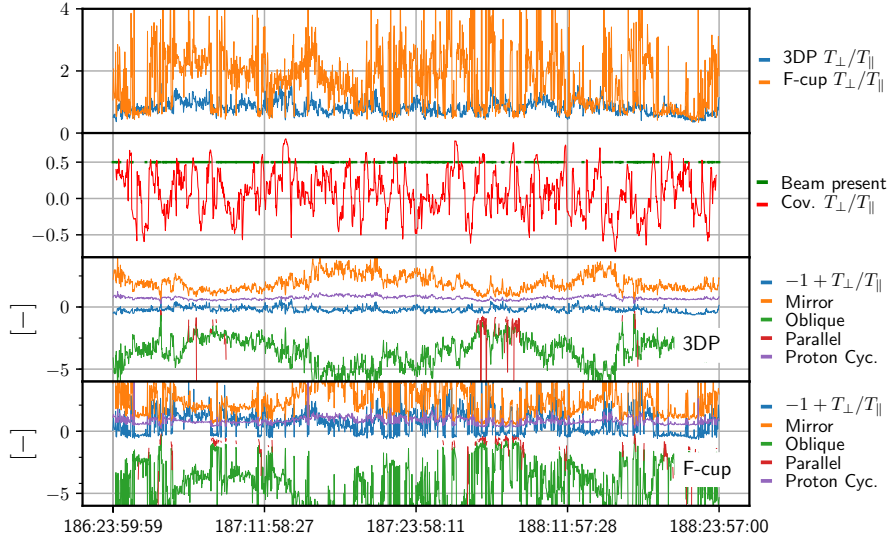


Figure 5.11: For the year 2007, the horizontal axis reads day:hour:minute:second. The top panel plots the temperature anisotropy ratio for the two instruments. The interval is nearly 2 days. The second panel from the top indicates when a beam is present by a green line, and the red line can be ignored. The next two panels plot the instability thresholds from Hellinger et al. [2006] where if $-1 + T_{\perp}/T_{\parallel}$ is larger in magnitude than the instabilities (see label), the plasma is unstable to the assumed growth rate.

To begin getting a sense of the two datasets, a time series of various quantities related to the instabilities is presented in Fig. 5.11. The period is chosen because there are intervals with and without a beam (indicated in the SWE data) and there are two times when 3DP measurements suggest the plasma is unstable to the temperature anisotropy instability thresholds. The Faraday cup measurements are available at 92 second cadence [Kasper et al., 2006] and the 3DP measurements is at a 3 second cadence. The top panel shows that the Faraday cup measurements have a large root-mean-square value with respect to the 3DP dataset.

The second panel has a green dot at 0.5 when the Faraday cup has detected a beam, which it then removes and calculates the perpendicular and parallel thermal speeds. Comparing panel 1 for times when there is a beam and no beam, it is clear that the two instruments agree when there is no beam (detected by the Faraday cup), and they do not agree when there is a beam present (which is

removed from the Faraday cup measurement). Therefore, 3DP does not remove the beam. When the beam is present, the temperature ratio, as defined, is larger, since the beam is typically located parallel to the magnetic field.

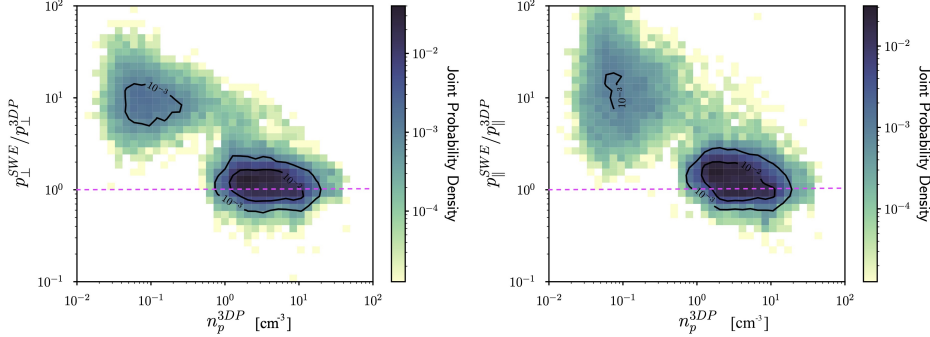


Figure 5.12: The joint probability density of the ratio of perpendicular pressures and 3DP density. See global caption for more details.

Figure 5.13: The joint probability density of the ratio of parallel pressures and 3DP density. See global caption for more details.

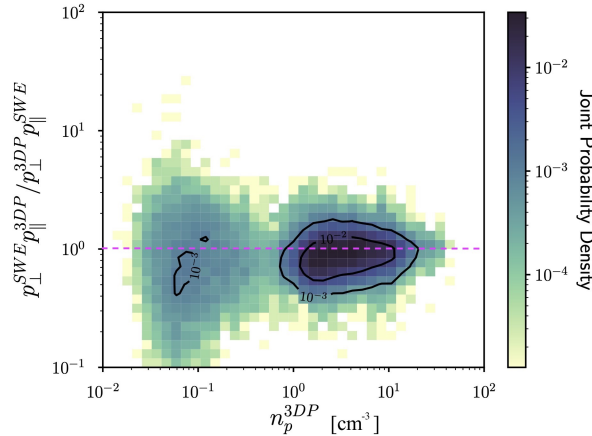


Figure 5.14: The joint probability density of the ratio of pressure anisotropy ratio and 3DP density. The dataset spans all the available data for SWE in 2007 and the nearest time stamp for 3DP. The dashed magenta line is for when the two data products are equal.

The bottom two panels hold a lot of information. The blue line corresponds to the instability parameter, for which, when it is larger in magnitude than the other lines (see label) the plasma is unstable, based on the assumed growth rate. In general, the 3DP data is more stable. The Faraday cup measurements suggests the plasma is consistently unstable to the proton cyclotron instability. Taking a look at the gaps where there is no beam (at the beginning and end of the interval), the Faraday cup measurements suggest that if there is a beam, the plasma is more likely to be unstable to the proton cyclotron instability

threshold, but that is not supported by the 3DP measurements.

Revisiting how these data products are made, the Faraday cup is a bi-Maxwellian fit to the core and beam. The 3DP data takes a direct moment of the proton distribution function. There will always be a discrepancy between these two datasets. Recall, the linear theory is derived from a bi-Maxwellian distribution function. Further differences between the dataset, while interesting, are not necessary to explore since 3DP provides exactly what is necessary for the science objectives: high cadence measurement of the proton pressure tensor.

It is interesting to note that, looking at the top panel, I would be convinced that the two signals have nothing to do with each other, and a cross-correlation does confirm that, so that I could be convinced, one of the signals is meaningless. Looking further into the details, for example, comparing the parallel firehose instability threshold, one can see that it is relevant at similar times in the time series. The time series has pointed out that the 3DP does contain the proton beam, now it is time to make direct comparisons. Now the SWE data, with the beam included in the parallel temperature, will be used.

Figures 5.12 - 5.14 plots joint probability density of the ratio of 3DP to SWE quantities versus the 3DP density. The top two panels show that there are two populations of points here, some that cluster around equality in the quantity on the vertical axis, and another that does not. The bottom panel makes it clear that whatever data product is wrong, it occurs when the density is low, not a complicated function of pressure and density.

Considering the instrument design, the electrostatic analyser relies on particle counts to build the distribution function, and the Faraday cup builds a reduced distribution from inferring the particle energy from the current. If the particle count is small, the distribution function will not be well approximated. The 3DP data needs to be limited to density greater than 1 particle per cm³.

Now that the density issue has been resolved and it is clear that the 3DP data does not remove the beam, a comparison between the SWE and 3DP data is shown as Fig. 5.17. The Pearson correlation coefficients are encouraging and the slope hints at a factor difference between the two data products. Looking closer at the joint probability density, the data has two trend lines, of which the linear regression slope, crosses in between. This issue was never resolved. It is interesting to investigate these issues further, but for the scientific goals of this thesis, satisfactory knowledge about the 3DP dataset has been gained, and it can now be used for scientific studies.

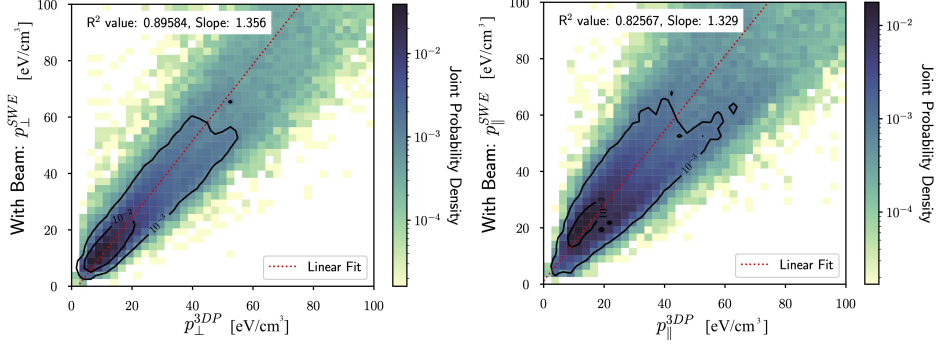


Figure 5.15: The joint probability density of the perpendicular pressures. See global caption for more details.

Figure 5.16: The joint probability density of the parallel pressures. See global caption for more details.

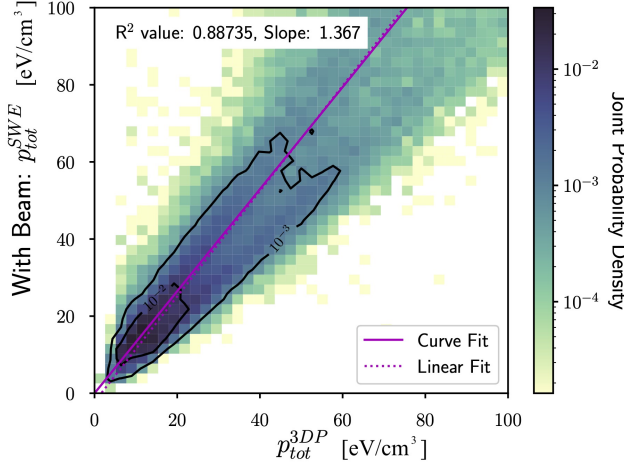


Figure 5.17: The joint probability density of the total pressure. The dataset spans all the available data for SWE in 2007 and the nearest time stamp for 3DP. The dotted lines are linear regressions, where the Pearson coefficient and slope are plotted annotated on the figures.

5.3.3 Measured length and time-scales

This dataset can be used to measure many of the proton plasma physics quantities. The collision length and time-scales are of particular interest. So they are measured here. Following the unit convention of the NRL Plasma formulary [Huba, 1987]. The Spitzer-Härm proton-proton collision frequency [Spitzer, 2006] for a proton-electron plasma with $T_p \leq T_e$, where T_p (T_e) is the proton (electron) temperature, is written,

$$\nu_{p,p}^{\text{SH}} = 4.8 \times 10^{-8} n_p T_p^{-3/2} \lambda (\text{s}^{-1}), \quad (5.38)$$

where n_p (cm^{-3}) is the proton number density, T_p is in eV and the Coulomb logarithm is λ . The Coulomb logarithm for proton-proton collisions,

$$\lambda = 23 - \ln \left| \frac{\sqrt{2n_p}}{T_p^{3/2}} \right|. \quad (5.39)$$

The dataset (the entire 10 years) provides the following averages,

$$n_p = 5.33 \text{ (cm}^{-3}\text{)}, \quad (5.40)$$

$$T_p = 30.0 \text{ (eV)}, \quad (5.41)$$

$$v_{\text{th}}^p = 48.3 \text{ (km/s)}, \quad (5.42)$$

where the proton thermal speed is v_{th}^p . With these measurements collision scales can be calculated,

$$\nu_{p,p}^{\text{SH}} = 4.23 \times 10^{-7} \text{ (s}^{-1}\text{)}, \quad (5.43)$$

$$\lambda_{\text{mfp}}^{\text{SH}} = v_{\text{th}}^p / \nu_{p,p}^{\text{SH}} = 1.14 \times 10^8 \text{ (km)}, \quad (5.44)$$

where $\lambda_{\text{mfp}}^{\text{SH}}$ is the Spitzer-Härm proton-proton mean-free-path. These are all consistent with other datasets that measure the scales at 1 AU [[Verscharen et al., 2019](#)].

The solar wind speed from this dataset is calculated to be,

$$\langle V_{\text{SW}} \rangle = 480 \pm 130 \text{ (km/s)} \quad (5.45)$$

where the \pm is the normal standard deviation.

5.3.4 The 3DP 3 second dataset

To make some concluding remarks about the dataset. The units and coordinate system were verified and then tracked down in the SPEDAS software to be verified. The dataset was then compared with the Faraday cup measurements which helped to confirm that the 3DP includes the proton beam and is poor at low density.

The pressure tensor at a 3 second cadence is a lifetime data product, so that it is nearly always available. For the consideration of the solar wind, Wind has been at L1 since 2005, so ensemble studies can be made. The onboard density and velocity, popular data products, have nearly identical availability to the pressure tensor. It has similar issues to the density and velocity, namely that the resolution of the proton distribution function can be poor, when the measured energy difference is comparable with the thermal energy, then the

resolution of the distribution function becomes poor. This new dataset will provide excellent science in the coming years due to its short time cadence and large sample number.

5.4 Comparing the observations and numerical methods

In this Section the primary data analysis is detailed. The numerical methods have been demonstrated in Section 5.1 to predict the relative breaking of the CGL invariants with cross-correlations. The key parameter of the numerical model is the effective mean-free-path. The analysis constructed in this section compares the solar wind observations (the database is described in Section 5.3) to the numerical model in a robust manner to measure the effective mean-free-path.

5.4.1 Conditioning the observations

The Wind dataset comprises the magnetic field data from the Magnetic Field Instrument (MFI) and the onboard proton density, velocity and pressure tensor from the electrostatic analyzer. The combined dataset covers years 2005-2015. The pressure tensor validation was described in Section 5.3. The general procedure is to calculate the cross-correlations, amplitude ratios, proton beta, and wind speed for a set of time intervals. The intervals are subjected to the following criteria:

1. Greater than %95 of the data must be present. The remaining is linearly interpolated.
2. The median of the density n_p must be greater than 1 particle - cm⁻³.
3. The norm of the non-gyrotropic tensor $|\Pi_{ij}^p|$ must be smaller than 0.3 $|p_{ij}^p|$.

The final item here uses the definitions from Eqs. 5.35. Figure 5.18 plots the following quantity,

$$\text{FLR ratio} = \frac{|\Pi_{ij}^p|}{|p_{ij}^p|}. \quad (5.46)$$

The figure shows that %86 of the single points are below 0.3. At larger time scales, considered here, the percentage of the data below 0.3 is even larger. This is expected since 3 seconds is slightly larger or near to the average gyroperiod of the solar wind at 1 AU.

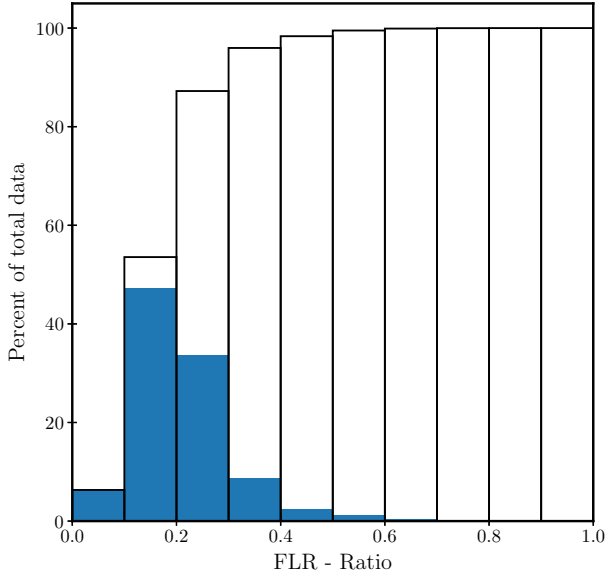


Figure 5.18: The FLR ratio (defined as Eq. 5.46) is plotted in blue as a histogram normalized to be the percent of the total data. This dataset here is for year 2007. The open boxes are a cumulative sum. There is %86 of data below 0.3.

Now the data is conditioned on two quantities, first the wavenumber, and then the proton beta, so that trends with β can be explored at different scales. The wavenumber is computed with Taylor's hypothesis [Taylor, 1938]. The general formula relating the spacecraft frame to the plasma frame for a wave is given by,

$$\omega_{\text{SC}} = \omega_{\text{plasma}} + |k_i|V_{\text{SW}} \cos(\theta_{\hat{V}_{\text{SW}}, \hat{k}}), \quad (5.47)$$

where ω_{SC} is the spacecraft frame frequency that is measured, ω_{plasma} is the frequency of the plasma wave in the plasma frame, k_i is the wavevector, V_{SW} is the magnitude of the solar wind velocity, and $\theta_{\hat{V}_{\text{SW}}, \hat{k}}$ is the angle between the wavenumber and the direction of the solar wind velocity [Huang and Sahraoui, 2019]. Now consider an ion-acoustic wave where $\omega_{\text{plasma}} = k \cos(\theta_{\hat{b}, \hat{k}}) c_s$ where the angle here is between the magnetic field direction and the wave propagation direction, and c_s is the sound speed. Taking $\tau = \omega_{\text{SC}}^{-1}$, where τ is the time cadence of the spacecraft instrument, yields,

$$|k_i| = \left[\tau V_{\text{SW}} \left(\cos(\theta_{\hat{b}, \hat{k}}) \frac{c_s}{V_{\text{SW}}} + \cos(\theta_{\hat{V}_{\text{SW}}, \hat{k}}) \right) \right]^{-1}. \quad (5.48)$$

Now, Taylor's assumption is often quoted as $c_s/V_{\text{SW}} \ll 1$, so the first term in

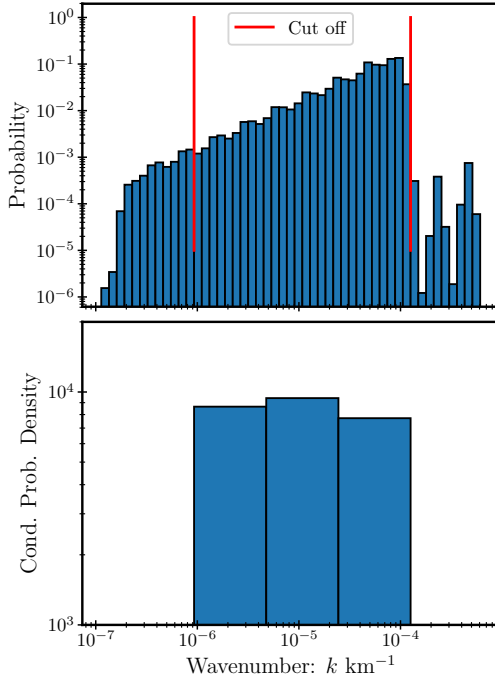


Figure 5.19: The wavenumbers computed via Taylor's hypothesis. The top panel is the probability function for an arbitrary bin number. The bottom panel is three near-to-equal conditioned probability density bins. The red lines are cutoffs, where the probability becomes less than 10^{-3} .

the parentheses can be neglected. In the solar wind the sound speed to solar wind speed ratio, along with the Alfvén speed to solar wind velocity v_A/v_{SW} , are about 0.1 [Matthaeus and Goldstein, 1982]. Notice this term also contains $\theta_{\hat{b},\hat{k}}$ which is difficult to measure. The next assumption is to take the fact that sound waves are longitudinal so the maximum power of any fluctuation will be measured when $\cos(\theta_{V_{SW},\hat{k}}) \simeq 1$. These two assumptions allow the wavenumber to be computed as,

$$k \approx \frac{1}{V_{SW} \tau}, \quad (5.49)$$

where $k = |k_i|$. This is the calculation of the wavenumber throughout this thesis.

This has been done for a set of time intervals $\tau = [30\text{s}, 1\text{min.}, 2\text{mins.}, \dots, 128\text{mins.}]$. A probability function of the wavenumbers k are plotted in Fig. 5.19. The top panel is the *probability* function where there are 9,035,008 total samples. This is used to identify outliers, defined arbitrarily as probability less than 10^{-3} . The outliers are removed and then three near-to-equal probability density bins

are constructed. This two-tiered histogram method is employed because a bin number estimate is unreliable for the unknown distribution (top panel of Fig. 5.19) and provides bins of equal probability density that are formed from the most probable bins of the original distribution.

These bins are now identified by their medians $k_{\text{SW}} = [0.288, 1.41, 6.34] \times 10^{-5} \text{ km}^{-1}$. Now there are a set of measurements that correspond to a wavenumber, so that statistics can be gathered at each median wavenumber. The number of samples in each bin are $[2.98, 16.6, 70.0] \times 10^5$, respectively.

Next, each wavenumber bin is conditioned on the proton beta. To ensure there is no internal bias between the two quantities, Fig. 5.20 is provided. It is the joint probability density function of the proton beta and the wavenumber. The first point, is that there is no trend, so the dataset can be conditioned in these two quantities without an internal bias. The next important condition that should be satisfied, is homogenous sampling, but unfortunately this property is not satisfied. To illustrate this property without testing it, drawing a vertical line, at $k = 10^{-5} \text{ km}^{-1}$, it crosses a few of the contours (in black), doing the same, at $k = 10^{-4} \text{ km}^{-1}$, the contours are crossed at different values of β . The same goes for flipping the line to be horizontal. For this study, the important span is in $\beta \in [0.5, 2]$, so the conditioning of the data is considered justified for this analysis. Recall from 5.1.2 that the numerical solutions over the interval $\beta \in [0.5, 2]$ change rapidly and diverge at higher beta. This region displays unique trends to aid the comparison between the numerical methods and observations.

Now that the method for the conditioning of the data has been presented, the statistics of the individual wavenumber bins (e.g., the average parallel magnetic field) can be conditioned on beta, to recover trends in beta, at a wavenumber. The technique does require a very large sample number.

5.4.2 Measurements of the CGL cross correlations

The cross-correlations and amplitude ratios defined in Section 5.1.2 are to be measured to compare with numerical solutions. The method to condition the data in wavenumber and proton beta is described in Section 5.4.1. Figure 5.21 shows the beta conditioned statistics for the median wavenumber bin $k_{\text{SW}} = 0.288 \times 10^{-5} \text{ km}^{-1}$. Notice that the trends are similar to that presented in Section 5.1.2. The samples have a spread around the beta conditioned statistics (see caption for magenta lines), but all follow a trend from $\beta < 1$ to $\beta > 1$.

This method has been repeated for the other two wavenumber bins appearing as Figs. 5.22 & 5.23. The trends are similar, but there are differences in the overall trends. For example, Fig. 5.21, the C_{\perp} descends sharper at the $\beta \approx 1$

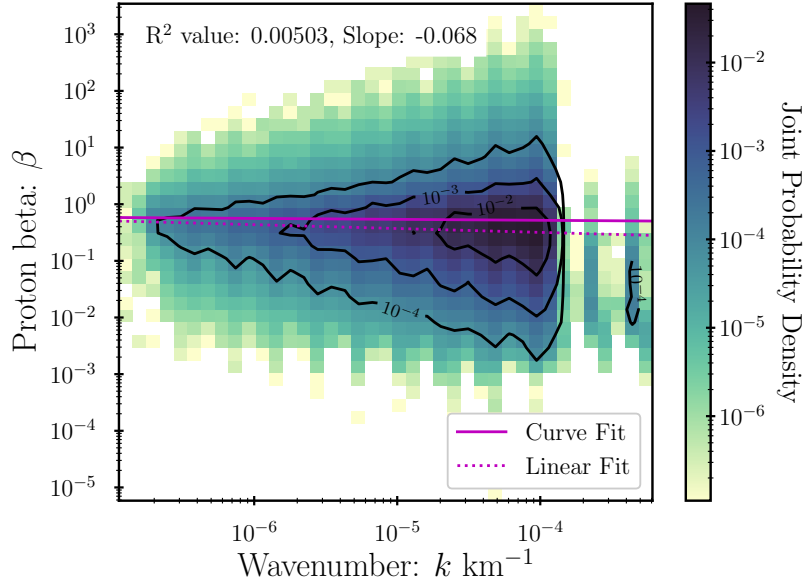


Figure 5.20: The joint probability function of the wavenumber and proton beta. The contours in black are constant values of the joint probability density. The annotated numbers are from the linear regression, seen as the dashed line.

transition, than does Fig. 5.23. This is also a feature of the numerical model developed in Section 5.1.2.

The three wavenumber bins here have provided a set of trends conditioned on the proton beta which can be compared to theoretical predictions from Section 5.1.2.

5.4.3 Comparing numerical solutions and observations

Section 5.1.2 detailed the method of obtaining solutions and Section 5.2 detailed the parameter degeneracy and how to resolve this issue. The method of comparison is to take the parameters of the model displayed in Table 4.5, with the caveat on $\theta_{b,k}$, making valid assumptions and leaving others free, to be determined by the analysis method. To recap, the wavenumber k is measured with the method in Section 5.4.1, the proton beta is measured directly, and the electron to proton temperature ratio is set to unity and the electron to proton mean-free-path ratio is set to unity, based on Section 4.5.3. This leaves the three parameters $\lambda_{mfp}^{\text{eff}}$, α , k_{iso} where $\theta_{b,k}$ being determined by the latter two parameters through the wavenumber model (Eq. 5.32).

The method of comparison is shown as a flow chart in Fig. 5.24. The top left box, labelled “Numerical model” classifies the parameters, leaving two free (Section 5.2 explains why this must be three parameters), and the box just below

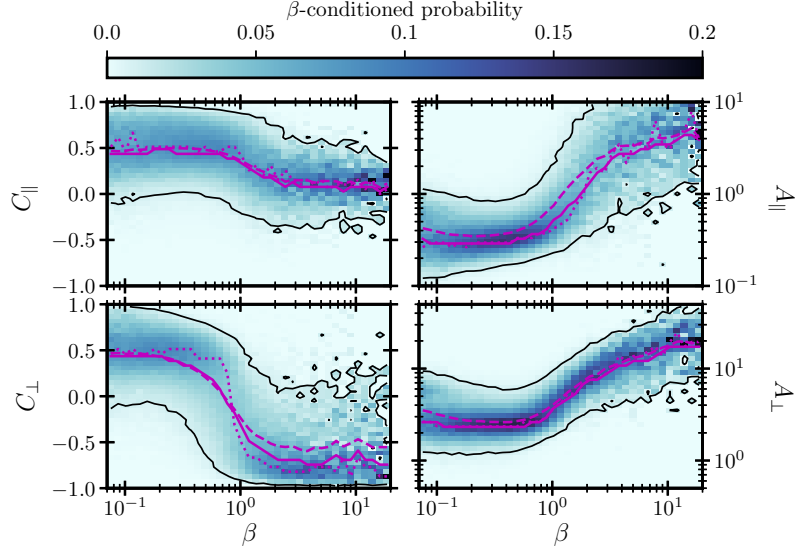


Figure 5.21: The cross-correlations and amplitudes defined in Section 5.1.2 mapped to a common color bar, that is conditioned on the proton beta. The wavenumber bin is $k_{SW} = 0.288 \times 10^{-5} \text{ km}^{-1}$. The thin black lines are the 10^{-2} contour. The magenta lines are the beta conditioned mean (dashed), median (solid), and maximum (dotted).

that is the “Observations”. The observations produce cross-correlations called the “Measured cross-correlations” and the numerical model produces the same cross-correlations called the “Numerical cross-correlation sensitive to $\theta_{\hat{b},\hat{k}}, \lambda_{\text{mfp}}^{\text{eff}}$ ”. The numerical cross-correlations are sensitive to parameters that will be measured, so the larger blue parallelogram on the right is put into a “for” loop sampling large parameter spaces in $\theta_{\hat{b},\hat{k}}, \lambda_{\text{mfp}}^{\text{eff}}$ and recording the “goodness of fit”. These are then used as weights to perform statistics.

The first piece of the analysis is to take the numerical solution, from Section 5.1.2, and normalise to the low beta value: the solid magenta curve from Fig. 5.21. This amounts to changing the numerical correlations by a factor so that it matches the observed trend, which can be seen clearly in Fig. 5.25 at low beta. Recalling the numerical correlations, say from Fig. 4.18, the correlations are a set value at low beta, to adjust them to the observed trends, the numerical correlations are then normalized so they match the observed trend.

This is argued to be physically reasonable since wave polarizations are approximately observed in turbulent plasmas. There is support for this using fluid simulations [Dmitruk and Matthaeus, 2009], kinetic simulations [Grošelj et al., 2019, Hunana et al., 2011], and in observations [Chen, 2016]. A long debate could ensue on this topic, but essentially, this work assumes that the magnitude

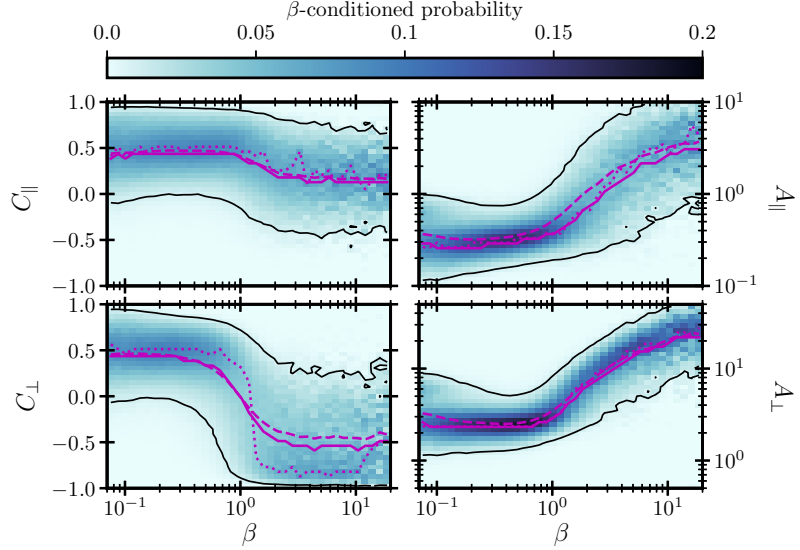


Figure 5.22: The cross-correlations and amplitudes defined in Section 5.1.2 mapped to a common color bar, that is conditioned on the proton beta. The wavenumber bin is $k_{\text{SW}} = 1.41 \times 10^{-5} \text{ km}^{-1}$. The thin black lines are the 10^{-2} contour. The magenta lines are the beta conditioned mean (dashed), median (solid), and maximum (dotted).

of the correlation is reduced by the turbulent behaviour, as one would expect from studying the correlation function, but the properties e.g, sign and change with parameters, are given by linear theories.

Now to quantify the comparison of the numerical solution and the observation, the statistic,

$$R(k, \lambda_{\text{mfp}}^{\text{eff}}, \alpha, k_{\text{iso}}) = \sqrt{N^{-1} \sum_i^N \left[\bar{y}(\beta_i, k) - \hat{y}(\beta_i, k, \lambda_{\text{mfp}}^{\text{eff}}, \alpha, k_{\text{iso}}) \right]^2}, \quad (5.50)$$

is introduced, where the subscript i denote the i th value of β . It is a root-mean-square where the mean is taken over beta. The measured trend is given by $\bar{y}(\beta_i, k)$ and the numerical solution is $\hat{y}(\beta_i, k, \lambda_{\text{mfp}}^{\text{eff}}, \alpha, k_{\text{iso}})$. The statistic is written so that if \bar{y}_i, \hat{y}_i are identical, $R \rightarrow 0$. The comparison is quantified by this statistic.

Considerable effort was put into ensuring the correct statistic was used for this comparison. Firstly, using the individual measurements that constitute the beta conditioned probability function in Fig. 5.21 (instead of the average trend) made a negligible difference. Next, R is just one of many possible statistics that can be used, but in the end there are only very slight differences for two reasons.

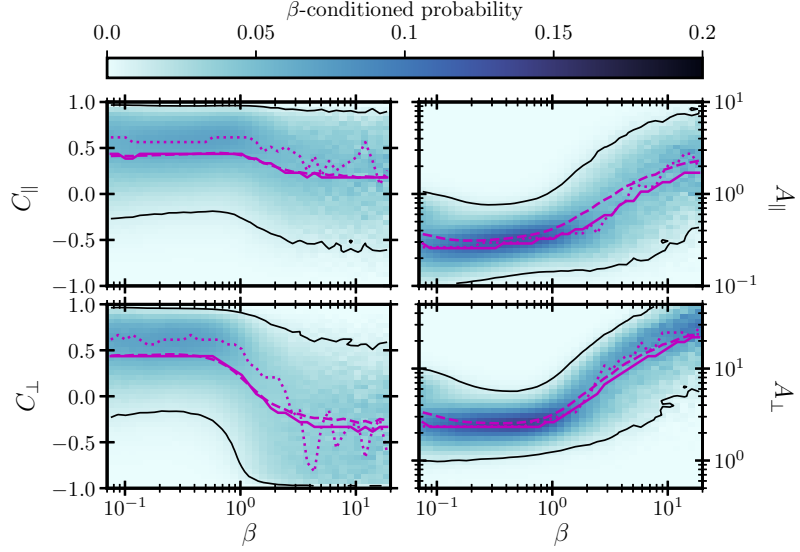


Figure 5.23: The cross-correlations and amplitudes defined in Section 5.1.2 mapped to a common color bar, that is conditioned on the proton beta. The wavenumber bin is $k_{\text{SW}} = 6.34 \times 10^{-5} \text{ km}^{-1}$. The thin black lines are the 10^{-2} contour. The magenta lines are the beta conditioned mean (dashed), median (solid), and maximum (dotted).

First, is that R is used as an unnormalized weight,

$$w(k, \lambda_{\text{mfp}}^{\text{eff}}, \alpha, k_{\text{iso}}) = \frac{1}{R(k, \lambda_{\text{mfp}}^{\text{eff}}, \alpha, k_{\text{iso}})}, \quad (5.51)$$

to calculate statistics so that only something along the lines of $w_{\text{max}}/w_{\text{median}}$ is important in determining the final statistics.

Figure 5.25 displays nearly 1000 solutions for different parameters, the choice of parameters will be made clear in Section 5.4.4. It can be seen that the darker lines, with larger weight, are more similar to the observed trend. The second reason the choice of R is best left simple, is that the distribution of weights are considered to indicate the underlying distribution, which then indicate the statistics to be used (e.g., Poisson, log-normal etc.) to calculate mean and standard deviations.

For now, just consider the weights calculated for a set of solutions given by ranges in the parameters $\lambda_{\text{mfp}}^{\text{eff}}, \alpha, k_{\text{iso}}$. Figure 5.26 displays the cumulative distribution function of the normalized weights w/w_{max} for the C_{\perp} statistic. The two distributions plotted that accompany the cumulative distribution function

Combining the measurements and numerical solutions

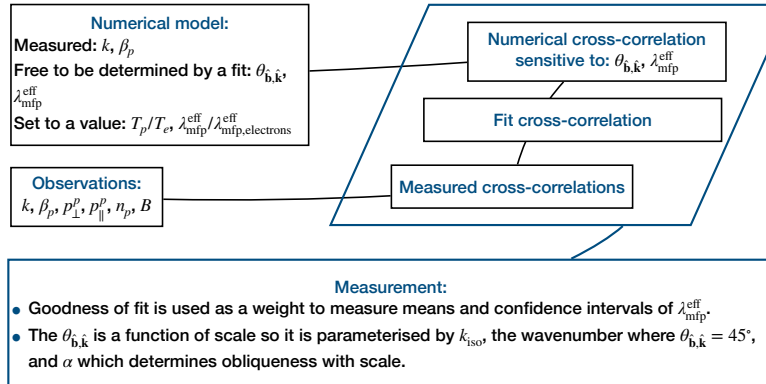


Figure 5.24: The “Numerical model” and the “Observations” are combined in the blue parallelogram by spanning a large parameter space in $\theta_{\hat{b},\hat{k}}$, $\lambda_{\text{mfp}}^{\text{eff}}$ and fitting the numerical solution to the observations. This is the data analysis technique implemented in the thesis to make the primary measurements of the thesis.

are defined respectively log-normal and normal,

$$\text{CDF}_{\log}(x) = \frac{1}{2} \left[1 + \text{erf} \left(\frac{\ln(x) - \mu}{\sigma \sqrt{2}} \right) \right], \quad (5.52)$$

$$\text{CDF}_{\text{norm}}(x) = \frac{1}{2} \left[1 + \text{erf} \left(\frac{x - \mu}{\sigma \sqrt{2}} \right) \right], \quad (5.53)$$

where μ , σ are the arithmetic mean and standard deviation, which are calculated directly from the data.

Notice that the log-normal distribution, from Fig. 5.26, better represents the data. It does appear that the normal distribution function does fit the largest weights better than the lognormal distribution function. To be brief, the mixed distribution function was considered, using the mean integrated standard error method [Marron and Wand, 1992], to show that the actual distribution is $\approx \%37$ normal and $\approx \%63$ log-normal. When generating statistics from the mixed distribution function the differences (again using the mean integrated standard error method), say in the mean of the distribution, are small. This can be seen from Fig. 5.26, that the distributions are similar.

This demonstrates that the best set of statistics to represent the data, are the weighted geometric statistics. If the observations x_i have unnormalised weights

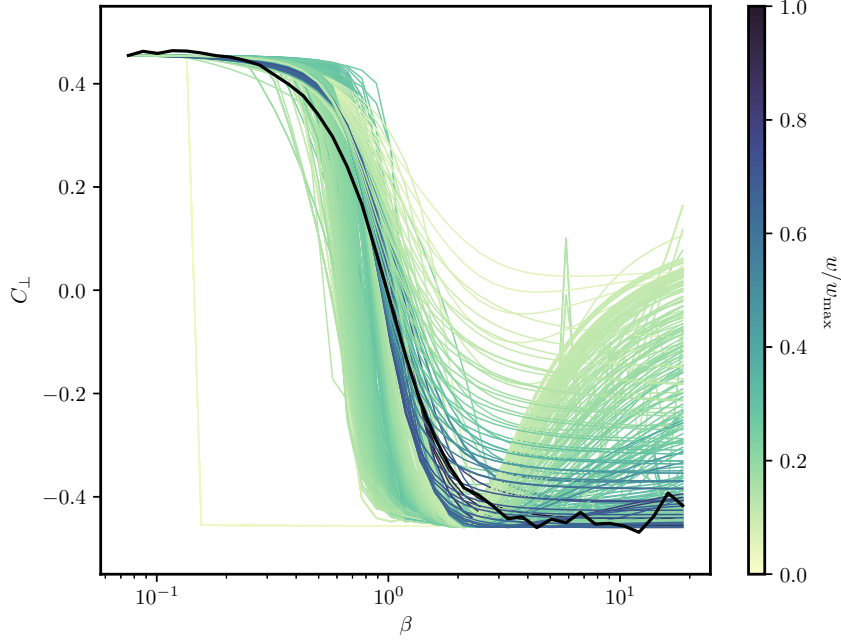


Figure 5.25: This figure is for C_{\perp} , $k_{SW} = 1.41 \times 10^{-5} \text{ km}^{-1}$. The numerical solutions colored by the normalized weight, mapped to the color bar. The black line is the observed beta conditioned median.

w_i , the definitions follow of the weighted geometric mean,

$$\mu^x = \exp \left\{ \sum_i^n \frac{w_i \ln|x_i|}{\sum_i^n w_i} \right\}, \quad (5.54)$$

weighted geometric covariance matrix,

$$(\sigma^{x,y})^2 = \exp \left\{ \frac{1}{\sum_i^n w_i} \sum_i^n w_i \ln \left| \frac{x_i}{\mu^x} \right| \ln \left| \frac{y_i}{\mu^y} \right| \right\}, \quad (5.55)$$

which defines,

$$\ln|\mu^x| \pm 2 \ln|(\sigma^{x,x})| \Rightarrow \text{CI}^x = [\mu^x (\sigma^{x,x})^2, \mu^x / (\sigma^{x,x})^2], \quad (5.56)$$

where CI^x is the weighted geometric two sigma confidence interval, following Norris [1940], Kendall and Stuart [1977]. These statistics are used to calculate means and covariances.

The method for comparing the numerical solutions to the measurements is to use the R statistic from Eq. 5.50. R is a semi-linear regression method, being that on the interval $d\beta$, a linear regression is considered, and the size of

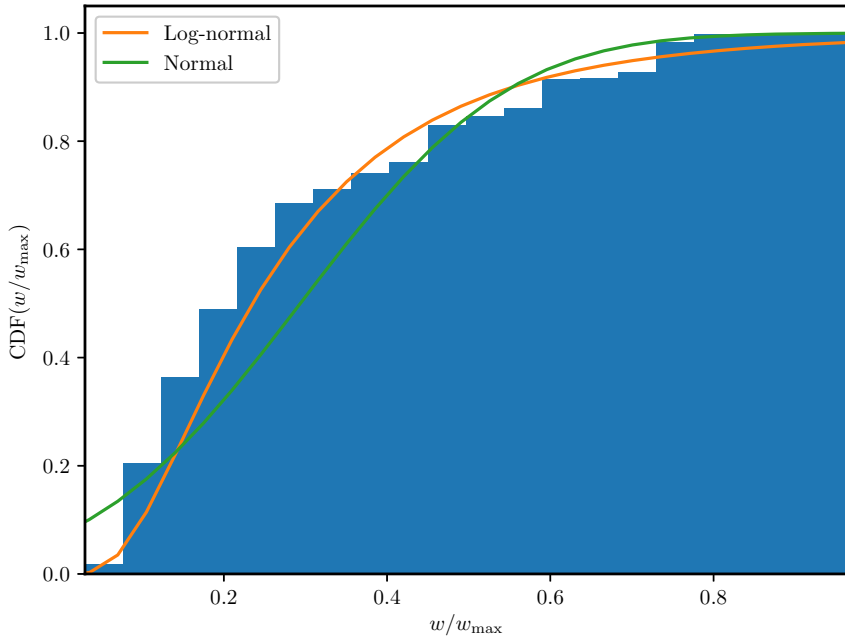


Figure 5.26: The normalized weights, where the weight is calculated from Eq. 5.51. The labelled curves are from Eqs. 5.52. The bin number was chosen arbitrarily.

$d\beta$ was chosen arbitrarily. Next, R is inverted to produce a weight, Eq. 5.51, for which the underlying distribution can be inferred. A mixed distribution was considered, but in the end was not used. With a method for determining $d\beta$, this method would serve as an excellent semi-linear model comparison method where the underlying distribution of the unknown parameters is not known.

5.4.4 Measuring the parameters

With the method of comparing the numerical model and observations detailed in Section 5.4.3 the results will be presented. Returning to Eq. 5.51, the weight is to be calculated. Recalling the degeneracy issue from Section 5.2, the parameters must be summed over wavenumber, to break the degeneracy, so that the important quantity to consider is,

$$\mathcal{W}(\lambda_{\text{mfp}}^{\text{eff}}, \alpha, k_{\text{iso}}) = \sum_{k_{\text{SW}}} w(k_{\text{SW}}, \lambda_{\text{mfp}}^{\text{eff}}, \alpha, k_{\text{iso}}), \quad (5.57)$$

where k_{SW} is the three wavenumber bins determined in Section 5.4.1. This weighted space, where examples of the solutions and the corresponding weights was shown in Fig. 5.25, will be shown. The weighted space is 3-dimensional

$(\lambda_{\text{mfp}}^{\text{eff}}, \alpha, k_{\text{iso}})$, so to visualize the space, the axis are integrated,

$$\mathcal{W}_\chi = \int_{\chi_0}^{\chi_n} d\chi \frac{\mathcal{W}(\alpha, k_{\text{iso}}, \lambda_{\text{mfp}}^{\text{eff}})}{\chi_n - \chi_0}, \quad (5.58)$$

where χ_n, χ_0 are the limits of the ranges. These 2-dimensional weight spaces are plotted for each of the cross-correlations and amplitude ratios in Figs. 5.27, 5.28, 5.29, and 5.30.

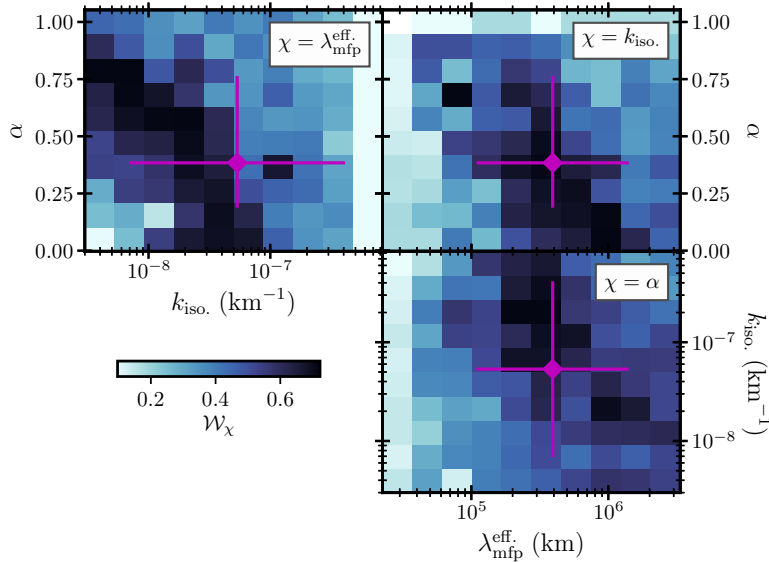


Figure 5.27: The integrated weights for C_\perp . The quantity of the color bar is defined as Eq. 5.58. The magenta diamonds are the weighted means from Eq. 5.54 and the magenta bars indicate the two sigma confidence interval from Eq. 5.56.

Besides the A_\perp amplitude ratio, the larger weights are clustered around similar values in the parameters $\lambda_{\text{mfp}}^{\text{eff}}, \alpha, k_{\text{iso}}$ and the magenta diamonds (the weighted geometric means calculated from Eq. 5.54) are central to the larger weights, with respect to the three panels, and the confidence intervals (the two sigma confidence intervals are calculated from Eq. 5.56).

To explain a bit more about the A_\perp case, Fig. 5.31 has been provided. It is a repeat of Fig. 5.25 for A_\perp . A few things are apparent, there are many solutions that do not match the observed trend. Next, there are many that match the trend only for beta near to one, and not so for higher beta, which then correspond to a small weight. This is not a feature of the other cross-correlations and amplitude ratios. This leads to A_\perp revealing many solutions that do not match the observed trend at high beta. It is probably this reason

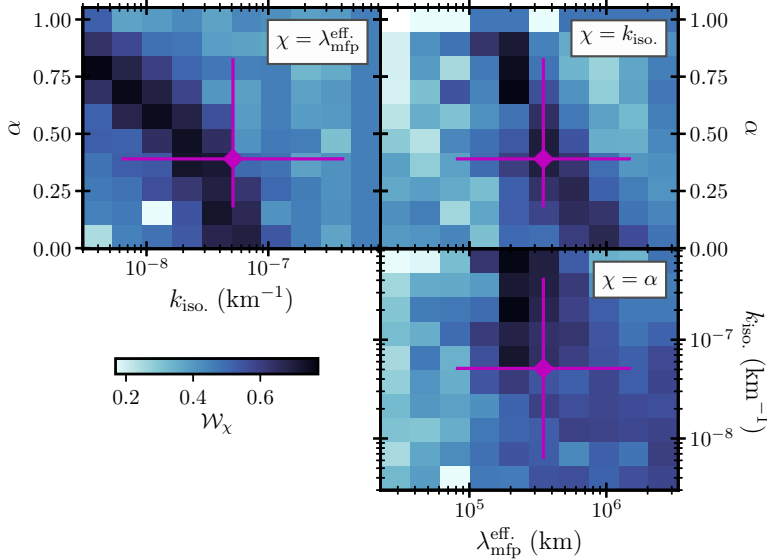


Figure 5.28: The integrated weights for C_{\parallel} . The quantity of the color bar is defined as Eq. 5.58. The magenta diamonds are the weighted means from Eq. 5.54 and the magenta bars indicate the two sigma confidence interval from Eq. 5.56.

that the other cross-correlations and amplitude ratios are good indicators and not A_{\perp} . One feature to notice is that A_{\perp} tends to larger values at larger beta, which is only a feature of the numerical solutions in the fluid regime.

The weighted geometric statistics for all of the quantities are plotted in Fig. 5.32. The statistics are very similar which is encouraging. For this reason, the statistics are combined, summing the four results and dividing by 4, and reported in Table 5.1. These are the primary measurements of this piece of work.

5.4.5 The wavenumber dependence

The parameters α , k_{iso} replaced $\theta_{\hat{\mathbf{b}}, \hat{\mathbf{k}}}$ to break the degeneracy with $\lambda_{\text{mfp}}^{\text{eff}}$. In Section 5.2, it was shown that this requires us to make sure the parameters α , k_{iso} are providing the correct $\theta_{\hat{\mathbf{b}}, \hat{\mathbf{k}}}$ at multiple wavenumbers.

Figure 5.33, displays the maximum weight (defined as Eq. 5.51) from the wavenumber bins for each of the cross-correlations and amplitude ratios, accompanied by the observed trend for each of the wavenumbers. The parameters of the maximum appear on the panel. Returning to Table 5.1, most of these parameters are within the confidence intervals.

The point here, is that the trend in wavenumber is similar for the numerical

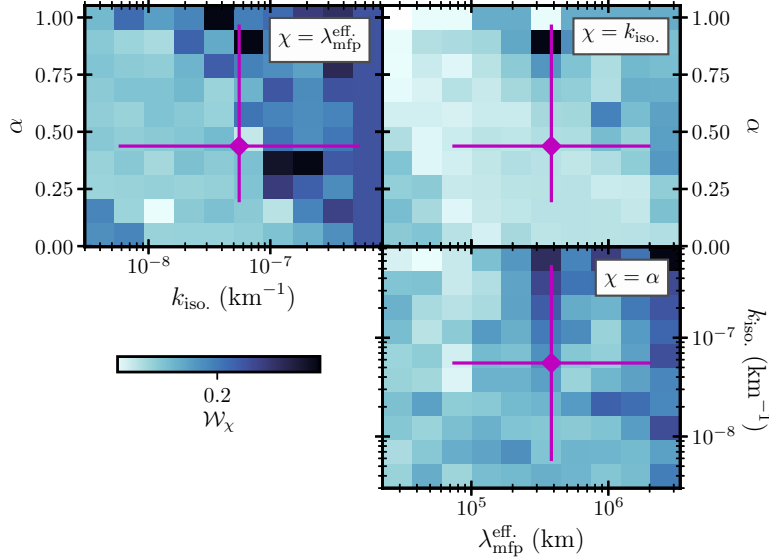


Figure 5.29: The integrated weights for A_{\perp} . The quantity of the color bar is defined as Eq. 5.58. The magenta diamonds are the weighted means from Eq. 5.54 and the magenta bars indicate the two sigma confidence interval from Eq. 5.56.

solutions. For example, for the C_{\perp} panel, the largest scale (black line) indicates the most sharp change from low beta to high beta, this feature becomes less sharp, going to larger wavenumber. There are some differences in the trends for A_{\perp} , but as discussed before, this measure is less reliable than the others.

This demonstrates that the determination of α , k_{iso} has resolved the degeneracy issue. The measurement of α , k_{iso} also provides the most probable propagation angle $\theta_{\mathbf{b},\mathbf{k}}$ as a function of wavenumber k , in particular k_{\parallel} .

5.4.6 Measuring the transition scale

In Section 4.5.1.1 the importance of the fluid and collisionless regimes was investigated numerically, where the transition between the two occurs in frequency or wavenumber. The proper definition of the transition frequency is $\nu_{\text{eff}} \simeq \omega$, where ν_{eff} is the effective collision frequency and ω is the temporal frequency of a plasma fluctuation. The measured effective mean-free-path and mean proton thermal speed (measured with this data set) gives an effective collision frequency of $\nu_{\text{eff}} = v_{\text{th}}^{\text{P}} / \lambda_{\text{mfp}}^{\text{eff}} = 1.11 \times 10^{-4} \text{ s}^{-1}$. The thermal speed is presented in Section 5.3.3. The sound wave dispersion relation can be used for the temporal frequency ω . Near to the transition scale, the dispersion relation is best described by the ion-acoustic dispersion relation $\omega_{\text{IA}} = k_{\parallel} c_s$. The transition scale

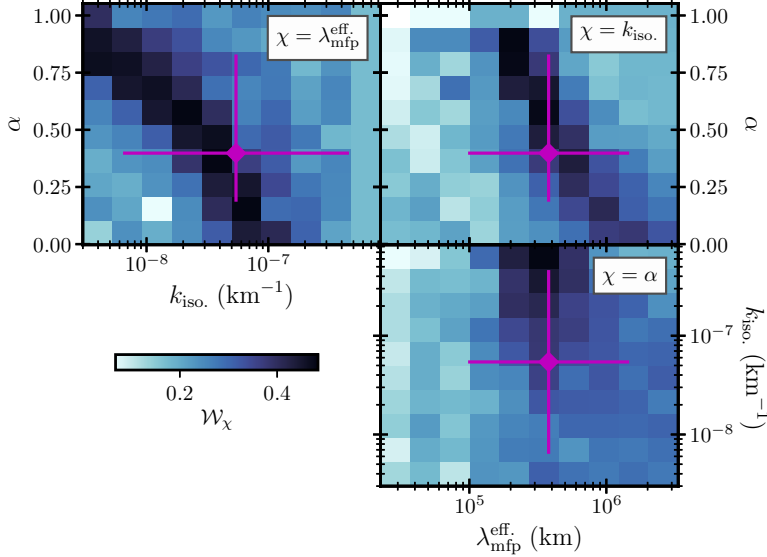


Figure 5.30: The integrated weights for A_{\parallel} . The quantity of the color bar is defined as Eq. 5.58. The magenta diamonds are the weighted means from Eq. 5.54 and the magenta bars indicate the two sigma confidence interval from Eq. 5.56.

is then defined when the parallel wavenumber satisfies $k_{\parallel}^{\text{trans}} = v_{\text{th}}^{\text{p}} / c_s \lambda_{\text{mfp}}^{\text{eff}}$. The wavenumber model can be used to rewrite the transition scale for k , which can then be compared directly to previous observations.

Rewriting the wavenumber model from Section 5.2,

$$k = \frac{k_{\text{iso}}}{\sqrt{2}} \cos(\theta_{\hat{\mathbf{b}}, \hat{\mathbf{k}}})^{1/(\alpha-1)} \sin(\theta_{\hat{\mathbf{b}}, \hat{\mathbf{k}}})^{\alpha/(1-\alpha)}, \quad (5.59)$$

which permits,

$$\frac{v_{\text{th}}^{\text{p}}}{c_s \lambda_{\text{mfp}}^{\text{eff}}} = k^{\text{trans}} \cos(\theta_{\hat{\mathbf{b}}, \hat{\mathbf{k}}}^{\text{trans}}) = \frac{k_{\text{iso}}}{\sqrt{2}} \tan(\theta_{\hat{\mathbf{b}}, \hat{\mathbf{k}}}^{\text{trans}})^{\alpha/(1-\alpha)}. \quad (5.60)$$

Solving for $\theta_{\hat{\mathbf{b}}, \hat{\mathbf{k}}}^{\text{trans}}$,

$$\theta_{\hat{\mathbf{b}}, \hat{\mathbf{k}}}^{\text{trans}} = \arctan \left\{ \left[\frac{\sqrt{2} v_{\text{th}}^{\text{p}}}{c_s k_{\text{iso}} \lambda_{\text{mfp}}^{\text{eff}}} \right]^{(1-\alpha)/\alpha} \right\}. \quad (5.61)$$

Now, k^{trans} can be written,

$$k^{\text{trans}} = \frac{k_{\text{iso}}}{\sqrt{2}} \cos(\theta_{\hat{\mathbf{b}}, \hat{\mathbf{k}}}^{\text{trans}})^{1/\alpha-1} \sin(\theta_{\hat{\mathbf{b}}, \hat{\mathbf{k}}}^{\text{trans}})^{\alpha/1-\alpha}. \quad (5.62)$$

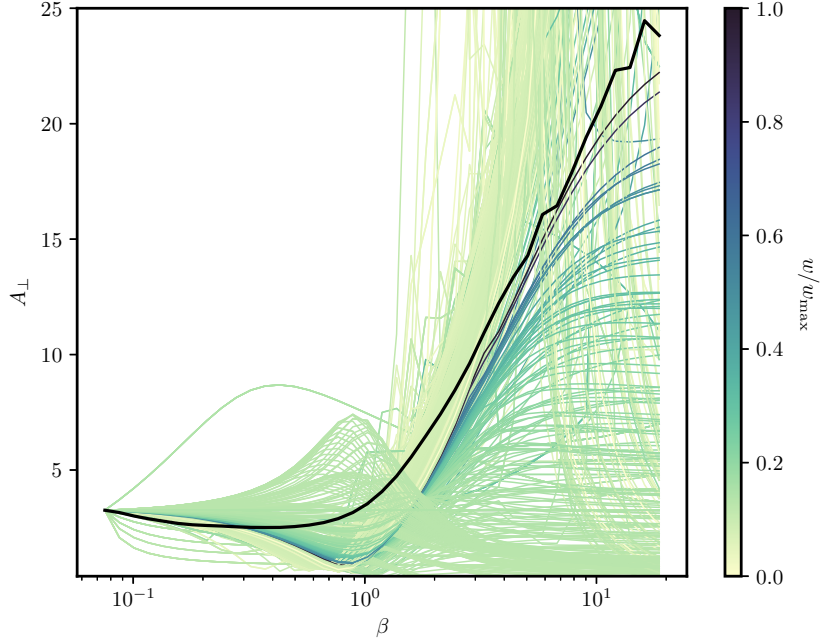


Figure 5.31: This figure is for A_{\perp} , $k_{\text{SW}} = 1.41 \times 10^{-5} \text{ km}^{-1}$. The numerical solutions colored by the normalized weight, mapped to the color bar. The black line is the observed beta conditioned median.

Using the trigonometric identities,

$$\cos(\arctan(x)) = \frac{1}{\sqrt{1+x^2}}, \quad \sin(\arctan(x)) = \frac{x}{\sqrt{1+x^2}}, \quad (5.63)$$

yields,

$$k^{\text{trans}} = \frac{k_{\text{iso}}}{\sqrt{2}} \left(\frac{1}{\sqrt{1+\chi^2}} \right)^{1/\alpha-1} \left(\frac{\chi}{\sqrt{1+\chi^2}} \right)^{\alpha/1-\alpha}, \quad (5.64)$$

where,

$$\chi = \left[\frac{\sqrt{2}v_{\text{th}}^{\text{p}}}{c_s k_{\text{iso}} \lambda_{\text{mfp}}^{\text{eff}}} \right]^{(1-\alpha)/\alpha} \quad (5.65)$$

which simplifies to,

$$k^{\text{trans}} = \frac{k_{\text{iso}}}{\sqrt{2}} \chi^{\alpha/(1-\alpha)} \sqrt{1+\chi^2}. \quad (5.66)$$

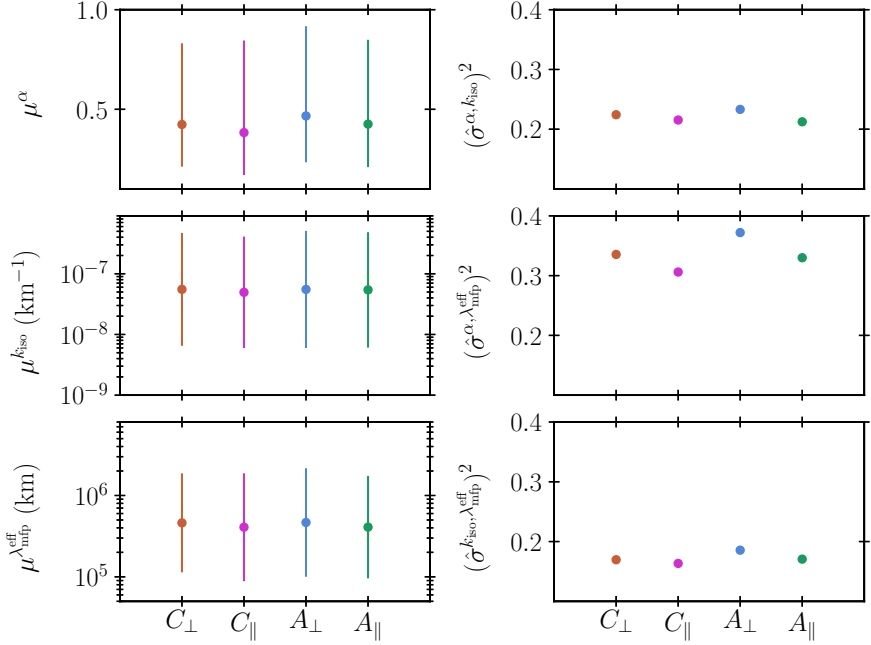


Figure 5.32: The statistics: weighted geometric mean μ_x (Eq. 5.54), covariance $\hat{\sigma}_{x,y}^2 = \sigma_{x,y}^2 / (\hat{\sigma}_{x,x} \hat{\sigma}_{y,y})$ (Eq. 5.55), and the two sigma confidence interval CI_x (Eq. 5.56) are calculated for the the amplitude ratios and cross-correlations.

Now inserting χ ,

$$k^{\text{trans}} = \frac{v_{\text{th}}^{\text{p}}}{c_s \lambda_{\text{mfp}}^{\text{eff}}} \sqrt{1 + \left[\frac{2(v_{\text{th}}^{\text{p}})^2}{c_s^2 k_{\text{iso}}^2 (\lambda_{\text{mfp}}^{\text{eff}})^2} \right]^{(1-\alpha)/\alpha}}. \quad (5.67)$$

The transition scale can be tested by inserting typical values for the solar wind. The $\lambda_{\text{mfp}}^{\text{eff}}$ and k_{iso} have been measured by this analysis, appearing in Table 5.1. Using a typical value of $v_{\text{th}}^{\text{p}}/c_s = \sqrt{1/2}$ for the solar wind, and using Taylor's assumption, the transition wavenumber in spacecraft-frame frequency at 1 AU is $\langle V_{\text{SW}} \rangle k^{\text{trans}} = f^{\text{trans}} = 0.19$ Hz, and $\text{CI}_{f^{\text{trans}}} = [0.046, 0.33]$ Hz. The uncertainties are propagated from V_{SW} and the four estimates of k^{trans} from C_{\parallel} , A_{\parallel} , C_{\perp} , A_{\perp} . The values of the average solar wind speed and standard deviation are reported in Section 5.3.3.

Equation 5.67 has some nice properties worth investigating. For $\alpha = 1$, the wavenumber anisotropy is isotropic $k_{\perp} = k_{\parallel}$ for all wavenumbers, which results in the transition wavenumber $k^{\text{trans}} \sim 1/\lambda_{\text{mfp}}^{\text{eff}}$, this would result in a prediction $480/4.4 \times 10^5 = 1.1^{-3}$ Hz, a difference of two orders of magnitude. The anisotropy is clearly an important factor in determining the transition scale. Looking to Figs. 5.27, 5.28, 5.29, and 5.30, there is some evidence for α near to

Statistic	Value(s)	Unit
μ_α	0.43	-
$\mu_{k_{\text{iso}}}$	5.4×10^{-8}	km^{-1}
$\mu_{\lambda_{\text{mfp}}^{\text{eff}}}$	4.4×10^5	km
CI_α	[0.21, 0.86]	-
$\text{CI}_{k_{\text{iso}}}$	$[0.064, 4.5] \times 10^{-7}$	km^{-1}
$\text{CI}_{\lambda_{\text{mfp}}^{\text{eff}}}$	$[1.0, 19] \times 10^5$	km
$\sigma_{\alpha, k_{\text{iso}}}^2 / (\sigma_{\alpha, \alpha} \sigma_{k_{\text{iso}}, k_{\text{iso}}})$	0.22	-
$\sigma_{\alpha, \lambda_{\text{mfp}}^{\text{eff}}}^2 / (\sigma_{\alpha, \alpha} \sigma_{\lambda_{\text{mfp}}^{\text{eff}}, \lambda_{\text{mfp}}^{\text{eff}}})$	0.34	-
$\sigma_{k_{\text{iso}}, \lambda_{\text{mfp}}^{\text{eff}}}^2 / (\sigma_{k_{\text{iso}}, k_{\text{iso}}} \sigma_{\lambda_{\text{mfp}}^{\text{eff}}, \lambda_{\text{mfp}}^{\text{eff}}})$	0.17	-

Table 5.1: The combined statistics: weighted geometric mean μ_x (Eq. 5.54), covariance $\hat{\sigma}_{x,y}^2$ (Eq. 5.55), and the two sigma confidence interval CI_x (Eq. 5.56).

1, but the most probable value for α is smaller.

Considering a slab model, where $\alpha = 0$, some interesting limits follow. Consulting Mathematica, if the quantity inside the exponent is less than 1 then $k^{\text{trans}} \sim 1/\lambda_{\text{mfp}}^{\text{eff}}$, if the quantity inside the exponent is larger than 1 then $k^{\text{trans}} \rightarrow \infty$, which is not physical. Values of $\alpha \notin [0, 1]$ are plausible, but beyond the scope of the discussion. In general, for there to be a compressive fluid inertial range, $k_{\text{iso}}\lambda_{\text{mfp}}^{\text{eff}} < 1$ (the quantity in the exponent is greater than 1), so that the isotropic scale length is larger than the transition scale. This immediately requires a scale dependent anisotropy $\alpha \neq 0$. If there is no fluid inertial range, where all the fluctuation energy is at scales below the effective mean-free-path, there is no restriction.

5.5 Conclusion

This Chapter synthesises the largest pieces of work. The numerical method of obtaining cross-correlations from Chapter 4 is extended to test the relative non-conservation of the Chew-Goldberger-Low invariants in Section 5.1. It is shown in Section 5.1.1 that these invariants are an excellent test of the equation of state of the plasma, in particular, they are related to the effective mean-free-path. The need to model the propagation angle leads to a parameter degeneracy, a difficult issue to overcome, but is shown in its entirety in Section 5.2 and resolved.

Next, the database for the study is presented in Section 5.3. This section includes the verification method and makes comparisons with other data products to understand the dataset and the quality. The quality of the pressure tensor is excellent and will serve to be useful in the future. The conditioning and preparation of the dataset is presented. The comparison of the numerical predictions

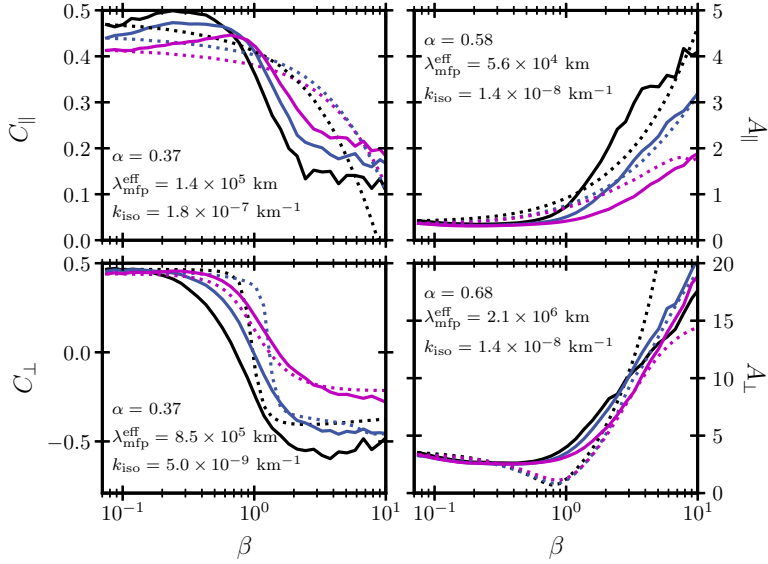


Figure 5.33: The four panels show the β -conditioned mean of cross-correlations and amplitudes for the three median wavenumber bins $k_{\text{SW}} = [0.288, 1.41, 6.34] \times 10^{-5} \text{ km}^{-1}$ as solid (black, blue, magenta) lines respectively. The dashed lines are the numerical solutions corresponding to the maximum \mathcal{W} ; the parameters of the maximum are reported in the panels.

of the CGL correlations and amplitudes to the observations is then presented in Section 5.4. The method of obtaining statistics is detailed and presented as a general method for comparing non-linear models to observations.

Most importantly, this Chapter presents the primary results of the thesis: the measurement of the effective mean-free-path, which appears in Table 5.1 in Section 5.4.4. Finally, the transition scale is measured in Section 5.4.6.

The primary result of the thesis is the robust measurement of the effective mean-free-path of solar wind protons at 1 AU, $\lambda_{\text{mfp}}^{\text{eff}} \approx 4 \times 10^5 \text{ km}$, which is approximately 10^3 times shorter than the Spitzer-Härm mean-free-path, which appears in Section 5.3.3. The effective mean-free-path is centred about the range of inverse wavenumbers (calculated by Taylor's hypothesis) for this analysis. This is encouraging because these are length scales that the analysis can resolve accurately (i.e., without extrapolation). Additionally, the inferred effective collision frequency $\nu_{\text{eff}} = 1.11 \times 10^{-4} \text{ s}^{-1}$ is not beyond the instrument time cadence, therefore a frequency of this magnitude can be resolved. Finally, due to the observed fluid behaviour, one would expect the mean-free-path to be shorter and the effective collision frequency to be larger than the Spitzer-Härm estimates, as found here. Physical limits on how short mean-free-path are difficult to impose due to the $k_{\parallel} \lambda_{\text{mfp}}^{\text{eff}}$ dependence, but the resulting transition scale

is probably limited by the gyroradius.

This measurement means that the range of scales of fluid behaviour extends to much higher frequencies or smaller scales than would be expected by the Spitzer-Härm estimate. In particular, the nature of compressive fluctuations, as they should be severely damped. This is the key solar wind observation that is inconsistent with the linear collisionless plasma theory. The caveat being that nonlinearly plasmas support effective collision processes.

The scale at which this transition from fluid to collisionless behaviour occurs is measured to be ≈ 0.2 Hz in the frame of the spacecraft. Returning to Fig. 3.10, the transition scale separates the inertial and kinetic ranges. This validates the use of fluid theories to frequencies smaller than that of the transitions scale. For decades fluid MHD theory has been successfully applied to the inertial range without a clear understanding as to why it can model all aspects of the solar wind behaviour. This serves as an explanation.

The measured effective mean-free-path and effective collision frequency are consistent with the known kinetic processes that are present at frequencies larger than 0.2 Hz. This point was explored numerically in Section 4.5.1.1, where it was shown that at scales $k_{\parallel} \lambda_{\text{mfp}}^{\text{eff}} \gg 1$ the collisional term is infinitesimally small, and the kinetic solutions are recovered. All of the perturbations to the distribution function that are responsible for kinetic effects are recovered at these scales. In the context of the solar wind, the ratio of the effective mean-free-path to the gyroradius for protons at 1AU is 10^3 . Gyroscale motion is not disrupted by the effective collisionality, it is only the Doppler shifted effective collision frequency that is near to the gyrofrequency. Therefore, processes such as cyclotron resonance and stochastic heating, which rely on the departure of the distribution function from the equilibrium, are not inhibited. It is likely not a coincidence that the gyroscale motion remains intact while the transitions scale is near to the gyroscale, which is why quasi-linear processes such as resonant heating and isotropization were studied in Section 6.6.

One of the primary difficulties of this piece of work was to model the propagation angle $\theta_{\hat{b}, \hat{k}}$ as a function of wavenumber. The parameterisation k_{iso}, α provided this description. This detail is necessary to produce numerical solutions that coincide with observations, this detail is shown in Section 5.1.2, in particular, due to the dependence of the solutions on $k_{\parallel} \lambda_{\text{mfp}}^{\text{eff}}$ the angle and effective mean-free-path can alter the solutions in the same manner. To highlight the importance of this measurement, one can use the effective mean-free-path and Taylor's hypothesis (see Section 5.4.6 for the details on the angle) to naively estimate the transition scale $\approx V_{\text{SW}} / \lambda_{\text{mfp}}^{\text{eff}} = 480 [\text{km/s}] / 4.4 \times 10^5 [\text{km}] = 1.1 \times 10^{-3} [\text{s}^{-1}]$, (using measurements from 5.3.3). This estimate is two orders of magnitude larger than the transition scale using the correct angle due to the inverse

cosine dependence. The naive estimate is two orders of magnitude larger than the observed magnetic field power spectral break.

The inapplicability of the Spitzer-Härm method to the solar wind has been discussed in detail in reviews such as Marsch [2006]. The question that arises, is *could the effective mean-free-path be a correction to the Spitzer-Härm method?* Since the solar wind is not near to a Maxwellian distribution function, the mean-free-path is likely different than the Spitzer-Härm estimate. It could be a correction, but due to the 10^3 difference, it is likely not a collisional process, but actually a collisionless process.

The collisionless processes that could be responsible for the enhanced effective collision frequency measured in the solar wind includes wave-particle interactions [Kellogg, 2000, Graham et al., 2022], instabilities [Gary et al., 2000, Yoon, 2017], and the plasma wave-echo [Schekochihin et al., 2016, Meyrand et al., 2019]. These processes have long been studied theoretically and numerically to explain a variety of processes such as galactic magnetic field amplification, reconnection, magnetorotational instability, magnetic dynamos and inhibition of pressure anisotropy in collisionless plasmas [Coroniti and Eviatar, 1977, Schekochihin and Cowley, 2006, Kunz et al., 2014, Rincon et al., 2016, Helderlander et al., 2016, Kunz et al., 2016, Squire et al., 2017b]. It is an open question as to how they are activated, but has been shown that compressive fluctuations and Alfvénic fluctuations can generate pressure anisotropy, thereby activating instabilities and regulating the departure from equilibrium [Verscharen et al., 2016, Squire et al., 2017, Kunz et al., 2020].

There is some evidence for these processes in the solar wind. In Bale et al. [2009], they showed that magnetic field fluctuations at the gyro-scale are enhanced near the instability thresholds, consistent with excitation of waves due to the unstable plasma. Additionally, the velocity distribution functions appear to follow the contours that would be stable to various wave-particle resonances [Tu and Marsch, 2002, He et al., 2015b]. To progress our understanding of these processes, better tools for analyzing the details of the velocity distribution functions are needed. This is considered in Chapter 6.

The solar wind presents a case where the effective mean-free-path is much shorter than the Spitzer-Härm mean-free-path. Given the potential effective collision mechanism discussed above, it is clear that the fluctuation amplitude (i.e., turbulence) plays a strong role in dictating the effective mean-free-path. For example, large amplitude fluctuations cause the plasma to become unstable, causing particle scattering and relaxation of the plasma. A collisionless plasma that is laminar would not be drastically governed by the effective mean-free-path, if it plays any role at all.

Chapter 6

Quasi-linear relaxation rate: numerical simulations

Quasi-linear theory was sketched in Section 2.6 and some evidence for quasi-linear heating occurring in the solar wind was presented in Section 3.5. Quasi-linear theory describes the relaxation of plasma towards equilibrium which is one of the potential effective collision mechanisms. Therefore, the primary objective of the Chapter is to develop a method to measure the quasi-linear relaxation rate directly from particle distribution functions. A numerical approach is taken, employing a simulation that evolves the particle distribution function, so that data can be obtained in a controlled setting. Analysis techniques are developed to obtain the gradient of the particle distribution function. This enables the measurement of the so-called quasi-linear heating rates, which are a proxy for the relaxation rate. These methods are developed to deal with noise in the particle distribution function so that they have a direct application to spacecraft measurements. While this analysis is widely applicable, the focus of the Chapter is on how to measure relaxation rates.

6.1 The VPIC simulation

To create a *proof of concept* project a simulation will be employed to test the analysis technique. The VPIC simulation, see [Bowers et al. \[2008\]](#), is a particle-in-cell (PIC) method to solve the particle distribution function in Boltzmann's equation which couple to Maxwell's equations, where the fields are solved with a finite-difference scheme.

A simulation that evolves the particle distribution function is necessary for this *proof of concept* project. For example, any fluid (e.g. MHD) or Landau Fluid code assumes a form for the distribution function so it is not a good

choice. Next, there are two classes, PIC codes and finite-difference or finite-element codes that evolve the distribution function. Either would be a good choice for this method, but there is a preference for the PIC code because a better understanding of the noise in a PIC code is useful for PIC simulation. Finally, the hybrid-PIC code is chosen, where electrons play the role of a fluid (i.e., the distribution function is not evolved) which is a good approximation because electrons do not play a kinetic role in the physical scenario considered here. Therefore, the hybrid-PIC simulation is perfectly suited for the task at hand.

Briefly, the PIC approach defines super-particles to represent many actual particles, essentially allowable because the Lorentz force is proportional to q_s/m_s , not the number of particles. The typical equations of motion for a particle in an electromagnetic field are solved with a finite-difference scheme where the electromagnetic fields are intermediate to the time step i.e., the leap-frog method. Macroscopic quantities and the fields are then calculated on grid points. When the time steps and grid sizes are smaller than the inverse electron plasma frequency and the Debye length the simulation is stable [Okuda, 1972].

Noise in the particle distribution function arises from representing a continuous system with a finite number of super-particles. The noise is evolved in the equations and is transferred “around” when calculating quantities on a grid. This is often reduced by introducing a shape function, but noise persists [Okuda, 1972]. The noise level is proportional to the inverse square root of the number of particles per cell, so that a larger number of particles leads to a more stable and less noisy simulation.

This approach is extremely efficient for problems where important geometry (e.g., the magnetic field shape) is on scales much larger than kinetic scales (e.g., the gyro radius or inertial radius) yet kinetic physics (e.g., particle trapping) is required to describe the system fully. An example of that is reconnection where large-scale magnetic field geometry dictates inflow physics, but the site of reconnection, where micro-scale physics of decoupled electrons and ions must be described to resolve particle acceleration. See for example, Guo et al. [2014], the VPIC simulation is able to resolve relativistic particles energized through the first order Fermi process in the reconnection outflows.

6.2 The parallel proton cyclotron instability as a case study

The anisotropic temperature parallel proton cyclotron instability was discussed in Section 2.5.1.2.2 and the role of the proton cyclotron wave in heating the

solar wind was shown in Section 3.4.2, and the role of the instability in the solar wind was discussed in Section 3.5.

Another reason for the choice, is because parallel propagating waves introduce considerable simplicity in the final form of the equations that govern the wave properties and the evolution of the distribution function. The hybrid-VPIC simulation is suitable for this instability since the electrons are nonresonant due to their relatively large thermal speed when the species temperatures are equal [Gary, 1993].

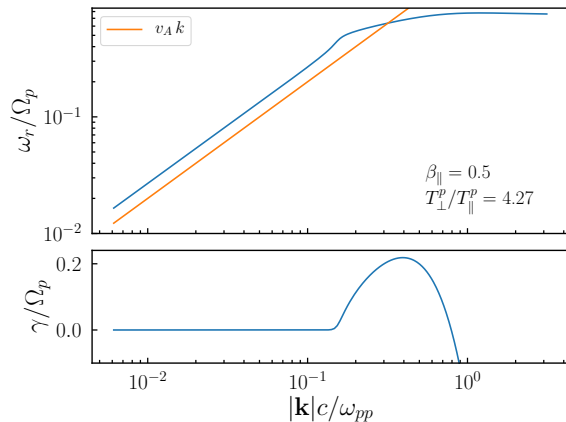


Figure 6.1: The dispersion relation for the parallel proton cyclotron instability for time 0 Ω_p^{-1} . The top panel is the real part of the complex frequency and bottom panel is the imaginary part. The parameters of the system are annotated on the top panel, in simulation units.

This method has a long history, see Davidson [1972] and Hamasaki [1973], and the review article by Yoon [2017], where the system is initialized to be unstable, so that there is a growth of waves at the expense of particle energy. This study, for proton cyclotron waves, was first considered by Davidson and Ogden [1975]. The most recent and advanced study of this kind has been done by Astfalk and Jenko [2018].

The simulation box is quasi-1D in space, $4 d_p$ in the perpendicular direction to the background magnetic field, and $512 d_p$ in the parallel direction where d_p is the proton inertial length. In velocity space the span is 8 Alfvén speeds in the three cartesian directions, which are then split into 100 grids in each direction. The boundaries are periodic. There are 10,000 particles per cell and only one run of the simulation is shown here.

The parameters for the simulation, shown in this section, are initialized so that the proton temperature ratio is $T_{\perp}^p/T_{\parallel}^p = 4.27$ and the parallel beta $\beta_{\parallel} = 0.5$. These initial conditions are unstable to the parallel proton cyclotron instability and not the mirror (see for example Fig. 3.8). This is also sufficient

initial conditions so that the generated waves are nearly parallel [Gary, 1993]. The velocity space in the 3D cylindrical space has a span of $v_{\parallel} = [-4v_A, 4v_A]$, $v_{\perp} = [0, 8v_A]$, and $v_{\phi} = [0, 2\pi]$. Defining $v_{\parallel} = v_z$, based on the background magnetic field direction, then $v_{\perp} = \sqrt{v_x^2 + v_y^2}$ and $v_{\phi} = \arctan\{v_y/v_x\}$. This requires some serious care, since the quasi-linear theory is derived in cylindrical coordinates, but the typical distribution function plotted is a reduced cartesian parameterized by the cylindrical coordinates. See the helpful demonstrative article Moseev and Salewski [2019] for more information and how to transform between various coordinate systems.

The dispersion relation for the proton cyclotron wave is shown at the initial time of the simulation in Fig. 6.1. The method to obtain the dispersion relation is described in Section 2.5.1. The top panel shows the normalized real part of the complex frequency, which is near to the Alfvén speed for small wavenumbers (normalized to the proton inertial length), then plateaus near the cyclotron frequency, due to the strong resonance at the cyclotron frequency. The bottom panel shows a positive imaginary part of the complex frequency, where there is significant growth over a bandwidth in wavenumber. The propagation direction of the new-born waves is symmetric, equal populations of parallel and anti-parallel [Davidson and Ogden, 1975]

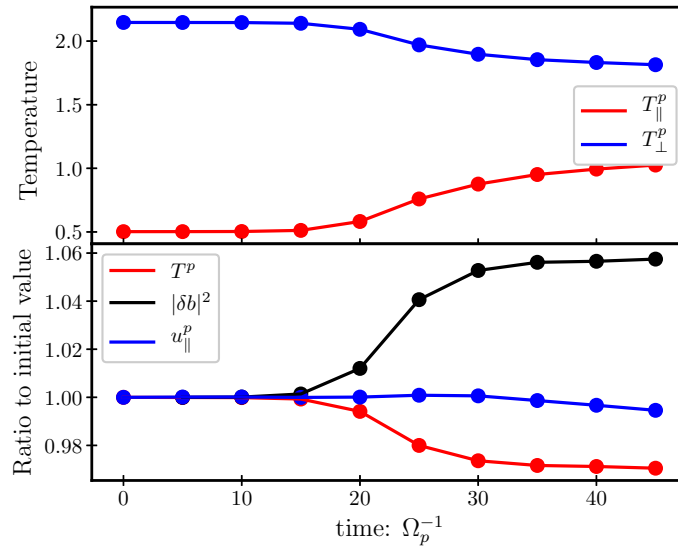


Figure 6.2: The initial parallel proton beta is 0.5, the initial temperatures are seen in the top panel, they are in simulation units. The bottom panel shows three quantities labelled in the legend, that are all normalized to the value at time = 0 Ω_p^{-1} .

Figure 6.2 displays the time history of the temperatures, parallel velocity,

and magnetic field energy. The top panel shows that the perpendicular temperature decreases (cooling) and the parallel temperature increases (heats). In the bottom panel, the three quantities labelled in the legend, are all normalized to their initial value so that fractional changes can be seen. It can be seen that the magnetic energy increases at the expense of the total temperature $T_p = (2T_\perp^p + T_\parallel^p)/3$. The parallel bulk velocity (e.g. parallel first-order moment) stays constant, since the waves are generated symmetric in wavenumber [Davidson, 1972], until the very late stages, where it is likely that the magnetic field amplitude is large enough to interact non-linearly with the plasma, in a stage called magnetic trapping.

The analysis that will be employed is to measure the heating rate, according to the quasi-linear theory prescription, and then integrate in time to recover the temperature profile. The primary issue addressed in this Chapter is noise in velocity space. PIC simulation noise results from representing a continuous distribution function as a discrete system of particles. The simulation is self-consistent with the noise. The system is physically accurate when the noise does not corrupt the system, for example in a low moment system (e.g., fluid), if the heat flux is noisy, the physics is still well captured. For this reason, removing the noise is advantageous when the quantity is not affected by the noise. It is assumed throughout the analysis that noise does corrupt the measurement, and should be removed for a better measurement.

6.3 The general problem of measuring quasi-linear heating rates

Section 2.6 introduced the quasi-linear equations and the derivation to discuss the microscopic picture of resonance between waves and particles, and the macroscopic picture of heating. The equations are reintroduced here. The time evolution equation for the background distribution function,

$$\frac{\partial}{\partial t} F_s = \int_{-\infty}^{\infty} \frac{d^3 k}{(2\pi)^3} \hat{B}(k_i) \frac{1}{v_\perp} \frac{\partial}{\partial \alpha} v_\perp \nu_s^{\text{scatt}}(k_i; v_\parallel, v_\perp) \frac{\partial}{\partial \alpha} F_s \quad (6.1)$$

where the normalized magnetic field power spectrum is,

$$\hat{B}(k_i) = \frac{8\pi}{B_0^2} \left(\frac{k_\parallel}{|k_i|} \right)^2 \frac{|\hat{b}_i(k_i)|^2}{1 - |\hat{k}_i e_i|^2}, \quad (6.2)$$

where $e_i = \delta_{ix}e_x + \delta_{iy}e_y + \delta_{iz}e_z$ is the polarization vector. The pitch-angle gradient is,

$$\frac{\partial}{\partial \alpha} = v_\perp \frac{\partial}{\partial v_\parallel} + \left(\frac{\omega_r(k_i)}{k_\parallel} - v_\parallel \right) \frac{\partial}{\partial v_\perp}, \quad (6.3)$$

where ω_r is the real part of the wave frequency. The relaxation or scattering rate,

$$\nu_s^{\text{scatt}}(k_i; v_\parallel, v_\perp) = \pi \frac{\Omega_s^2}{k_\parallel} \sum_{n=-\infty}^{\infty} \delta(v_{\text{res}} - v_\parallel) |\Psi_n|^2. \quad (6.4)$$

The resonant velocity is defined,

$$v_{\text{res}} = \frac{\omega_r - n\Omega_s}{k_\parallel}, \quad (6.5)$$

where Ω_s is the species cyclotron frequency. Additionally,

$$\Psi_n = \frac{1}{\sqrt{2}} \left[e_r J_{n+1}(\lambda_s) + e_l J_{n-1}(\lambda_s) \right] + \frac{v_\parallel}{v_\perp} e_z J_n(\lambda_s), \quad (6.6)$$

is defined where $\lambda_s = k_\perp v_\perp / \Omega_s$ is the argument of the Bessel functions J_n and the right/left handed polarization vectors,

$$e_r = \frac{e_x - ie_y}{\sqrt{2}}, \quad e_l = \frac{e_x + ie_y}{\sqrt{2}}. \quad (6.7)$$

Equation 6.1 is understood as the following, when an electromagnetic wave's phase speed matches a harmonic of the resonant velocity, the energy transfer between the two will occur if the pitch-angle gradient is non-zero.

Taking moments of Eq. 6.1 leads to the time-evolution of the momentum and temperatures, called acceleration and heating, in the quasi-linear framework. Concisely,

$$\begin{pmatrix} \dot{u}_\parallel^s \\ \dot{T}_\parallel^s \\ \dot{T}_\perp^s \end{pmatrix} = m_s n_s \int \frac{d^3 k}{(2\pi)^3} \left(\frac{\Omega_s}{k_\parallel} \right)^2 \hat{B}(k_i) \sum_{n=-\infty}^{\infty} \mathcal{R}(k_i, n) \begin{pmatrix} k_\parallel \\ 2k_\parallel v_{\text{res}} \\ n\Omega_s \end{pmatrix}, \quad (6.8)$$

where the resonance function is defined,

$$\mathcal{R}(k_i, n) = -2\pi^2 \frac{k_\parallel}{|k_\parallel|} \int_0^\infty dv_\perp v_\perp^2 |\Psi_n|^2 \left. \frac{\partial}{\partial \alpha} F_s \right|_{v_\parallel=v_{\text{res}}}, \quad (6.9)$$

Equation 6.8 is the focus of this Chapter. Dots represent the partial time derivative, giving the change in the quantities. On the right hand side, there is

the magnetic field power spectrum and the pitch-angle gradient of the distribution function evaluated at all of the resonances, due to the integral in k_i .

According to the quasi-linear prescription, and assumptions, if the magnetic field and distribution function can be measured with respect to the resonances (i.e., resolving the bandwidth of interacting waves), and the wave properties can be confirmed (e.g., polarization and propagation direction) then the analysis is reduced to measuring the magnetic field power spectrum and pitch-angle gradients.

6.4 Measuring the pitch-angle gradient

Equation 6.8 shows that the pitch-angle gradient (defined as Eq. 6.3) of the distribution function must be measured. The distribution function has been assumed to be gyrotropic during the quasi-linear derivation (which is not entirely necessary Melrose [1986]) and therefore, the only coordinates of the velocity distribution functions are the parallel and perpendicular coordinates. The distribution function will be expanded in Hermite-Laguerre coefficients. The coefficients are spectra, and just like the electromagnetic fields, have noise floors. The order of the spectral coefficient corresponding to the noise floor is then used to truncate the series of coefficients. The remaining coefficients are then used to calculate the terms in the pitch-angle gradient via the recursion relations that the Hermite and Laguerre polynomials permit.

6.4.1 Hermite-Laguerre functions

The Hermite functions,

$$\psi_m(x) = \frac{1}{(2^m m! \sqrt{\pi})^{1/2}} e^{-x^2/2} H_m(x), \quad (6.10)$$

$$H_m(x) = (-1)^m e^{x^2} \frac{d^m}{dx^m} e^{-x^2}, \quad (6.11)$$

$$\int_{-\infty}^{\infty} dx \psi_m(x) \psi_n(x) = \delta_{mn}, \quad (6.12)$$

are orthogonal over $(-\infty, \infty)$. They follow the recursion relations,

$$\frac{\partial}{\partial x} \psi_m(x) = \sqrt{\frac{m}{2}} \psi_{m-1}(x) - \sqrt{\frac{m+1}{2}} \psi_{m+1}(x) \quad (6.13)$$

$$x \psi_m(x) = \sqrt{\frac{m}{2}} \psi_{m-1}(x) + \sqrt{\frac{m+1}{2}} \psi_{m+1}(x). \quad (6.14)$$

The associated Laguerre functions,

$$\Gamma_n^k(x) = \sqrt{\frac{n!}{(n+k)!}} e^{-x/2} x^{k/2} L_n^k(x), \quad (6.15)$$

$$L_n^k(x) = \frac{e^x x^{-k}}{n!} \frac{d^n}{dx^n} (e^{-x} x^{n+k}), \quad (6.16)$$

$$\int_0^\infty dx \Gamma_n^k(x) \Gamma_m^k(x) = \delta_{nm}, \quad (6.17)$$

are orthogonal over $[0, \infty)$. They follow the recursion relations,

$$\frac{\partial}{\partial x^{1/2}} \Gamma_n^k(x) = \Gamma_n^k(x) \left(\frac{1}{x^{1/2}} - x^{1/2} + \frac{2n}{x^{1/2}} \right) - 2\Gamma_{n-1}^k(x) \frac{n+1}{x^{1/2}(n+k)}, \quad (6.18)$$

$$\sqrt{x} \Gamma_n^k(x) = \Gamma_n^{k+1}(x) \sqrt{n+k+1} - \sqrt{n} \Gamma_{n-1}^{k+1}(x). \quad (6.19)$$

The choice of these functions becomes clear when considering the following product,

$$\psi_0(x) \Gamma_0^1(y) = \pi^{-1/4} e^{-x^2/2} \sqrt{y} e^{-y/2}, \quad (6.20)$$

so that if $x = v_{\parallel}/v_s^{\parallel}$, the parallel velocity normalized to the parallel thermal speed and $y = (v_{\perp}/v_s^{\perp})^2$ the perpendicular velocity normalized to the perpendicular thermal speed - all squared,

$$\psi_0(v_{\parallel}/v_s^{\parallel}) \Gamma_0^1((v_{\perp}/v_s^{\perp})^2) = \pi^{-1/4} \frac{v_{\perp}}{v_s^{\perp}} \exp \left\{ -\frac{1}{2} \left(\frac{v_{\parallel}^2}{(v_s^{\parallel})^2} + \frac{v_{\perp}^2}{(v_s^{\perp})^2} \right) \right\}, \quad (6.21)$$

the bi-Maxwellian in 3D-cylindrical coordinates multiplied by a simply constant factor. The use of Laguerre function $k = 1$ puts the system in cylindrical coordinates, this will be discussed as appropriate throughout these sections.

Figure 6.3 shows the functions for a few orders of the polynomials. Notice the blue colors ($m = 0$) correspond to a 1D Maxwellian respective to the span of the coordinates for the perpendicular and parallel velocity. The first three orders show that features such as beams and skewness can be captured by the functions. The red lines are for $m = 10$, which describe fine-scale structure of the velocity distribution function.

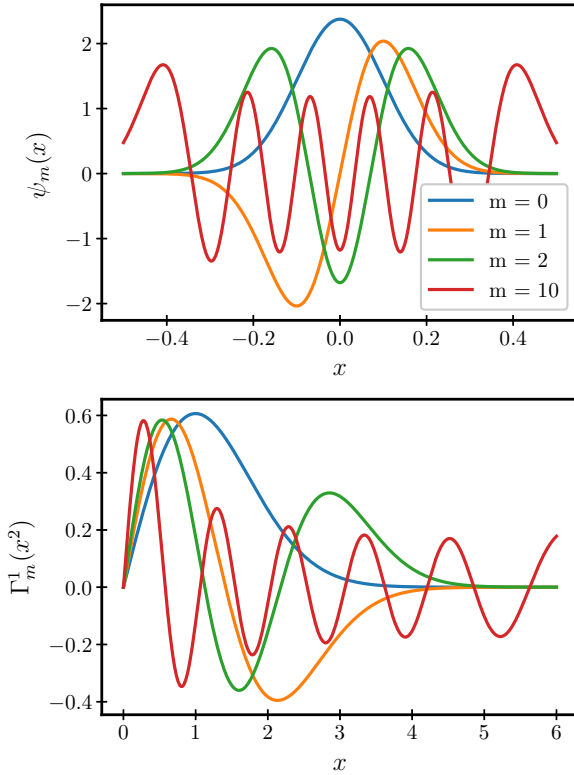


Figure 6.3: The top panel plots the Hermite functions from Eqs. 6.10 and the bottom panel plots the Laguerre functions from Eqs. 6.15. The horizontal axis x is the normalized velocity. The colors correspond to the legend, notice that red is $m = 10$.

6.4.2 Hermite-Laguerre transform

The Hermite-Laguerre transform,

$$c_{lm} = \int_{-\infty}^{\infty} dv_{\parallel} \int_0^{\infty} dv_{\perp} \psi_m(\hat{v}_{\parallel}) \Gamma_l^1(\hat{v}_{\perp}) F(v_{\parallel}, v_{\perp}) \quad (6.22)$$

$$F_{ML}(v_{\parallel}, v_{\perp}) = \sum_{m=0}^M \sum_{l=0}^L c_{lm} \psi_m(\hat{v}_{\parallel}) \Gamma_l^1(\hat{v}_{\perp}) \quad (6.23)$$

providing the coefficients c_{lm} and the inverse transform for $F_{ML}(v_{\parallel}, v_{\perp})$, based on maximum polynomial numbers M, L . The integral is in cylindrical coordinates where the angular integral has been completed, giving 2π due to gyrotropy, but it is ignored throughout the following sections. The Jacobian factor of v_{\perp} is held within the $k = 1$ Laguerre function, discussed at the end of Section 6.4.1.

These points deserves some attention, notice the hat used for the argument

of the functions, this is the normalised velocity e.g., $\hat{v}_{\parallel} = v_{\parallel}/v_{\parallel}^s$. There are a few known methods for normalisation, such as the maximum root of the Hermite polynomials considered [Tang, 1993]. If the normalisation is chosen poorly, it can take many orders of the polynomials to well approximate the distribution function. This can drastically affect the interpretation of the physics as well. This issue needs to be treated with great care when implementing this technique. The technique here is to use the first three moments of the distribution function to form the correct argument of functions. For example, the argument of the Hermite function

The technique will be demonstrated on a 1-dimensional slice of the distribution function produced by the simulation (the setup is described in Section 6.2). A slice in the parallel velocity direction appears in the top panel of Fig. 6.4 as a dashed orange line. The Hermite transform of the simulation data has been taken up to $m = 5$, then the inverse to produce a low pass filter of the distribution function.

The bottom panel is the central difference of the simulation data in orange and the blue line is produced by computing the derivative according to the recursion relations of Eq. 6.13. The difference between the blue line and orange line demonstrates the technique, that the orange line suffers from noise, amplified by taking the derivative.

A method for assessing the maximum polynomial number, e.g., m , must now be considered. The 1-dimensional case for v_{\parallel} is treated with the spectral coefficients,

$$c_m = \int_{-\infty}^{\infty} dv_{\parallel} \psi_m(\hat{v}_{\parallel}) F(v_{\parallel}, 0), \quad (6.24)$$

which are plotted in Fig. 6.5 for 4 time stamps in the simulation (see the legend). Near to $m = 10$ the power in the spectral coefficients levels off, indicating the classic noise floor. For orders less than $m = 10$ it can be noticed that there is amplification in the power from the initial time (blue line) of the spectral coefficients, which is possibly a physical process, not simulation noise.

To conclude the method,

1. Take the Hermite-Laguerre transform of the simulation data to obtain the spectral coefficients.
2. Assess the maximum polynomial order with the simulation noise floor.
3. Calculate the pitch-angle gradient via the recursion relations, with the spectral coefficients up to the maximum polynomial order.

Additionally this method provides information on the spectral coefficients, which

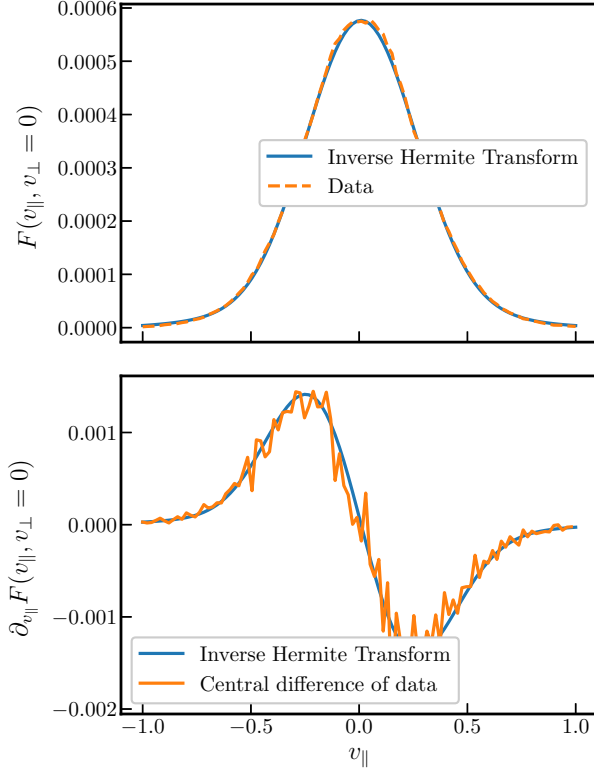


Figure 6.4: The top panel shows the distribution function produced by the simulation in parallel velocity coordinates as a dashed orange line and the inverse transform method in blue. The bottom panel is the central difference derivative of the distribution function and the blue line is the derivative produced from the recursion relations.

have a physical meaning, see Section 6.7.3.

6.4.3 Pitch-angle gradients

With the method for obtaining gradients for the 1-dimensional case demonstrated, now it is time to show the result for the pitch-angle gradient. Recall the pitch-angle gradient, from Eq. 6.3, contains both products and derivatives, so the recursion relations for the Hermite function (Eqs. 6.13) and Laguerre functions (Eqs. 6.18) are used. Additionally, the pitch-angle gradient involves the wave frequency ω_r . To further demonstrate the method, the full-pitch angle gradient has been calculated with maximum Hermite and Laguerre polynomial order of 10 and plotted as Fig. 6.6. The phase velocity of the wave is assumed to be $\omega_r/k_{\parallel} = 0.8$ for this Figure.

The Hermite-Laguerre method in the top panel shows the ability of the

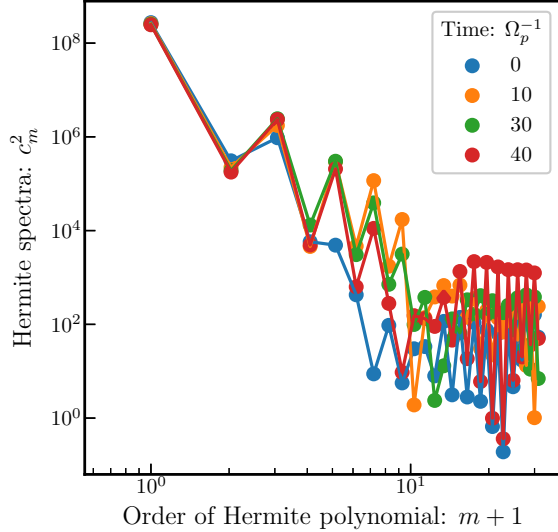


Figure 6.5: The 1-dimensional spectral coefficients (Eq. 6.24) are computed for simulation distribution function for multiple times, labelled in the legend. The order of the Hermite polynomial is on the horizontal axis.

technique to avoid incorporating noise into the calculation of the pitch-angle gradient. With a method to measure the pitch-angle gradient, one large piece of the quasi-linear heating rate is now measured.

6.4.4 Combining the resonance function with the magnetic field power spectrum

Turning to Eq. 6.25 (rewritten here from Eq. 6.8), with the pitch-angle gradient method described in Section 6.4.3, the resonance function (Eq. 6.9) is measured. The final part is to obtain the resonant velocities which are provided by solving for the dispersion relation from the dielectric tensor for the temperature anisotropic parallel proton cyclotron instability (see Section 2.5.1). The Bessel functions simplify since $k_{\perp} = 0$ so that only the harmonics of $n = \pm 1$ contribute. Then, the integral in v_{\perp} is computed numerically and the resonance function $\mathcal{R}(k_i, n)$ is measured.

For clarity, heating rates and acceleration are rewritten here,

$$\begin{pmatrix} \dot{u}_{\parallel}^s \\ \dot{T}_{\parallel}^s \\ \dot{T}_{\perp}^s \end{pmatrix} = m_s n_s \int \frac{d^3 k}{(2\pi)^3} \left(\frac{\Omega_s}{k_{\parallel}} \right)^2 \hat{B}(k_i) \sum_{n=-\infty}^{\infty} \mathcal{R}(k_i, n) \begin{pmatrix} k_{\parallel} \\ 2k_{\parallel}v_{\text{res}} \\ n\Omega_s \end{pmatrix}. \quad (6.25)$$

The normalised magnetic field power spectrum $\hat{B}(k_i)$ is measured with a simple

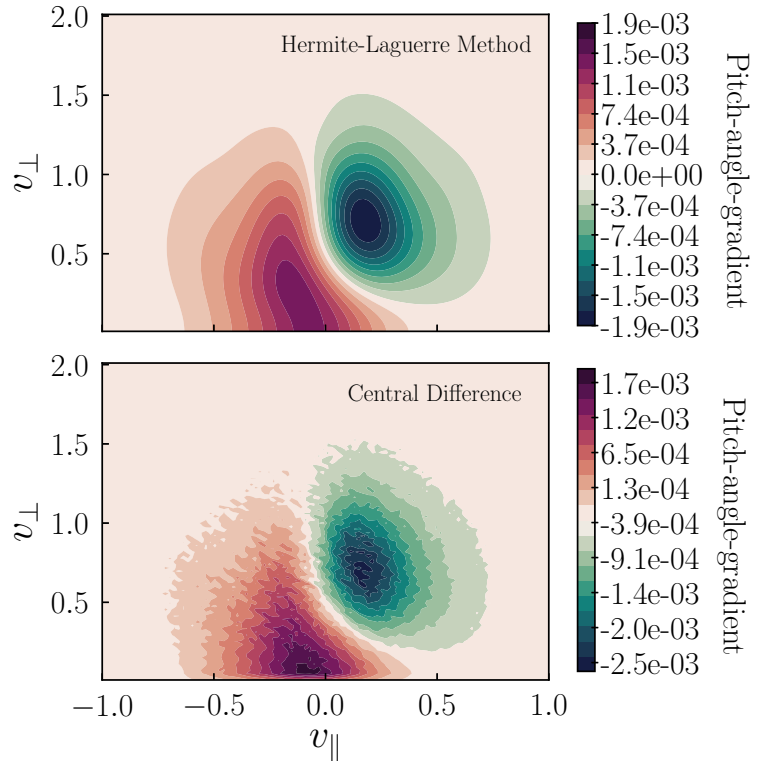


Figure 6.6: The pitch-angle gradient for time $t = 20\Omega_p^{-1}$ for a resonant wave frequency calculated with two methods. In the top panel is the Hermite-Laguerre method described in the text. The bottom panel is 2D central differences scheme. The color bars are the pitch-angle gradients. There is a slight difference in the range of the two color bars.

fast Fourier transform package provided by Python. The magnetic field power spectrum suffers from a few issues, which will be addressed in more detail, but at this point, a few ($\pm 0.01\Omega_p^{-1}$) time stamps, near to the time that the velocity distribution is computed, are averaged in spectral space to help with the non-smoothness of the power spectrum.

It is advantageous to plot the entire integrands of Eq. 6.25, seen in Fig. 6.7 to better understand the physical process and measurement issues. In the top panel the resonant velocity (Eq. 6.5) is displayed, which involves the phase velocity of the wave and the order of the resonance, which can be seen in the legend at the top of the figure. The top panel indicates where in velocity space the wave-particle interaction can happen due to the wave, with the wavenumber given on the horizontal axis. The interaction is weighted by the pitch-angle gradient and the power spectral density of the magnetic field, indicating if the interaction is happening.

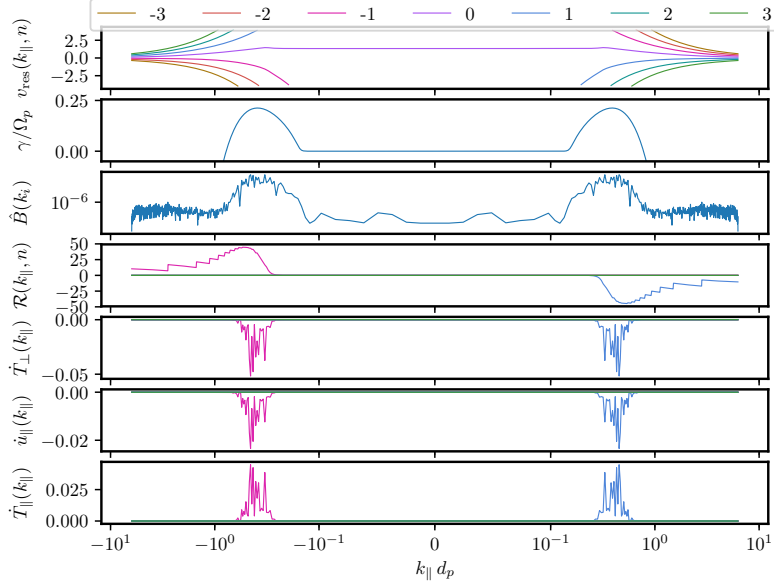


Figure 6.7: Various quantities plotted for $t = 15 \Omega_p^{-1}$, plotted as a function of the parallel wavenumber times the proton inertial length. The horizontal axis is symmetrical logarithm, so that at $\pm 10^{-1}$ the scale becomes linear to pass from < 0 to > 0 . The colors of the lines correspond to the legend at the very top, which is the order of the resonance, n , where only pink and blue lines contribute to the bottom panels, denoting -1, 1, respectively.

The second panel down is the complex frequency γ from solving the dispersion relation, it can be seen that there is growth, (positive complex frequency) for a span of wavenumbers. The third panel down is the magnetic field power spectrum, computed from the simulation. The magnetic field appears to be peaked in the same wavenumber range as the growth rate, suggesting the magnetic field power is the power of the proton cyclotron waves.

The fourth panel down is the resonance function which is made up of integrals over the pitch-angle gradient, a function of the wavenumber. The function is fairly smooth with small jumps, due to discreteness in velocity space. The theory says that the resonance function is calculated for $v_{\parallel} = v_{\text{res}}$, where in the simulation, v_{\parallel} is discrete due to the finite resolution of the simulation. For a span of k_{\parallel} , the resonant velocity will change only slightly, and therefore the same v_{\parallel} will be $v_{\parallel} \approx v_{\text{res}}$. This can be confirmed by recalling that the phase velocity, seen in Fig. 6.1, for large wavenumber, flattens near to the cyclotron order 1 resonance, and therefore, changes very little. This explains why the stepped nature of the function is more pronounced at larger absolute wavenumber.

Notice that the stepped feature, does not contribute to the bumpy nature of the curves in the next three panels. For this reason, an analysis technique has

not been implemented to deal with this issue, but should be considered in the future. The following bumpy nature in the bottom three panels, is due to the magnetic field power spectrum (see Eq. 6.25).

The bottom three panels are the entire integrand of Eq. 6.25. Writing them as a function of k_{\parallel} is slightly misleading, but it serves its purpose, it shows that the resonance is indeed working. Notice that there is perpendicular cooling and parallel heating, seen from the sign of the functions. Next, there is a small amount of parallel deceleration, but the actual value is very small when compared to the total velocity. This is confirmed by Fig. 6.2.

As mentioned before the magnetic field power spectrum is averaged local in time to the time stamp of the quantities measured here. However, the non-smoothness of the power spectrum is clearly seen in the bottom three panels. This issue will be further analyzed in Section 6.7.1. Finally, the bottom three panels can be numerically integrated in k_{\parallel} to measure the heating rates and acceleration.

6.5 Comparing the time history

The time history, shown in Fig. 6.8, displays the rates for the time history of the simulation. The bottom two panels compare the VPIC temperature, the basic moments of the distribution function, to the Hermite-Laguerre temperature, which is computed by integrating the heating rate,

$$\text{HL Temperature}_{\alpha}(t) = T_{\alpha}(t_0) + \int_{t_0}^t dt' \dot{T}_{\alpha}(t'), \quad (6.26)$$

where α is \perp or \parallel . The integrand $\dot{T}_{\alpha}(t')$ has been computed via quasi-linear theory.

For the comparison to be exact, the physics (e.g., the time evolution) must be valid in the quasi-linear assumptions, and the simulation must be capturing this evolution appropriately. For this set of initial conditions, it has been reported that quasi-linear theory is valid by Yoon [2017], and this will be visited later in Section 6.7.2.

The parallel temperature profile appears to be correct at the maximum time of the simulation, but there is a mismatch of the rates throughout the time history. The parallel temperature appears to get the asymptotic state correct, but there is a mismatch of the rates throughout the time history. The perpendicular case is a bit worse, where both the asymptotic state and the time history of the rates do not match. The method is promising, but the discreteness of the magnetic field power spectrum makes it difficult to address if the Hermite-Laguerre

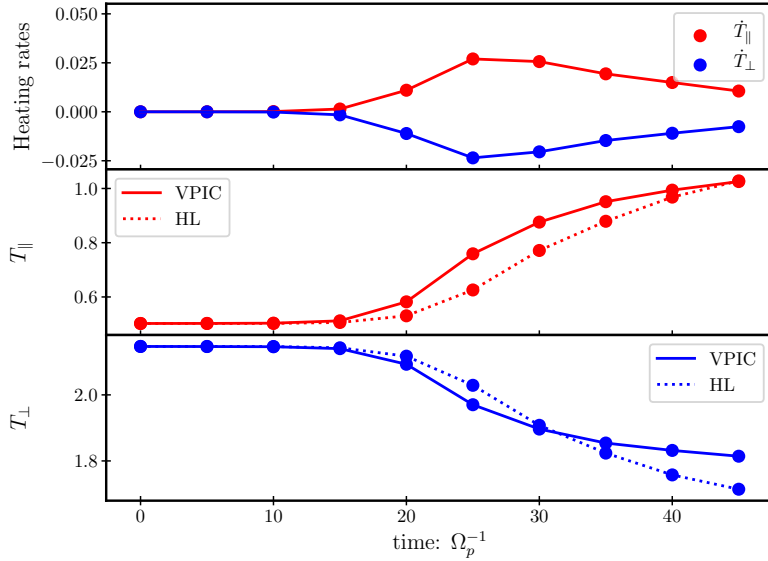


Figure 6.8: The top panel are the heating rates which are labelled in the legend. The bottom two panels are the VPIC simulation temperatures and the Hermite-Laguerre method (HL) (see Eq. 6.26) temperatures. The time unit is in inverse proton cyclotron frequency.

method is providing sufficiently accurate pitch-angle gradients to measure the heating rates. The causes of discrepancy are:

1. PIC noise corrupting the pitch-angle gradient (or the noise floor not being a sufficient indicator of noise).
2. Inaccuracy in the Hermite-Laguerre method.
3. The evolution departing from quasi-linear theory.
4. Noise or discreteness of the magnetic field power spectrum causing the measurement to be inaccurate.

In the final section a few of these issues are assessed directly.

6.6 Relaxation time

Quasi-linear relaxation is a possible explanation for the effective collisionality of the solar wind, the primary topic of this thesis. A numerical model is built in Chapter 4 and a measurement with solar wind observations is made in Chapter 5. This analysis contained in this Chapter has been built to measure the collisionless relaxation rate in the quasi-linear regime.

Hamasaki [1973] studied the electron whistler instability in the same context as shown here, initialising an unstable plasma, to study the collisionless relaxation. In their article, a relaxation time is derived from the inverse of the maximum growth rate, which is then related to the temperature, and well-explains the simulations that they ran. It is then considered as a proxy for comparison to the effective collision frequency in articles such as Davidson and Ogden [1975] and extended to more initial conditions (e.g., β_{\parallel} , $T_{\perp}^p/T_{\parallel}^p$) by Gary et al. [2000]. Equation 3 of Gary et al. [2000] gives an estimate for the collisionless relaxation,

$$\nu_p^{\text{P.G.}} = \Omega_p 0.15 \exp \left\{ -\frac{5.5}{(\beta_{\parallel})^{0.8} (T_{\perp}^p/T_{\parallel}^p - 1)^2} \right\}, \quad (6.27)$$

by studying the rate at which $T_{\perp}^p/T_{\parallel}^p - 1$ decreases in the quasi-linear phase. This rate is compared to a few others in Fig. 6.9. The red and blue lines are the normalized rate of change. The magenta line is the actual rate of change of the quantity considered by Gary et al. [2000], defined to be positive,

$$\nu_p^{\text{anis}} = \frac{-1}{T_{\parallel}} \left(\dot{T}_{\perp} - \frac{T_{\perp}}{T_{\parallel}} \dot{T}_{\parallel} \right), \quad (6.28)$$

which is calculated with the rates measured by the Hermite-Laguerre method.

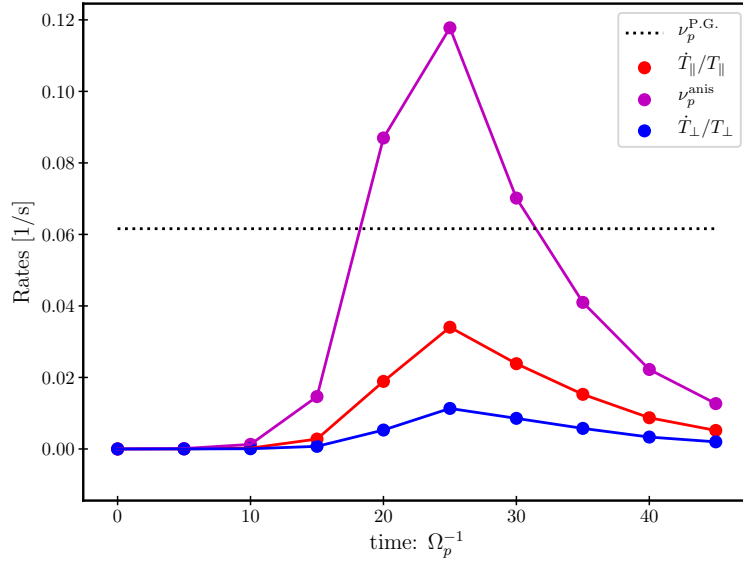


Figure 6.9: The rates calculated in a few different ways. The dotted line is defined as Eq. 6.27 and the magenta line is defined as Eq. 6.28. The blue and red lines are discussed in Section 6.5. The horizontal axis is the time in units of inverse proton cyclotron frequency.

The dotted line of Fig. 6.9 is Eq. 6.27, which is the rate, given the initial parameters, which is clearly very restrictive, but it serves the purpose for large ensemble studies. The magenta line from Fig. 6.9, is Eq. 6.28, which is essentially the instantaneous version of Eq. 6.27, and clearly has the advantage of indicating if the wave-particle interaction is occurring.

This does call to question: what rate should be considered for an effective collision frequency? The decrease in the temperature anisotropy is just a proxy, one that is ultimately linked to only the second-order moment. For now, Eq. 6.28, is a good proxy, but this should be reconsidered in the future.

Figure 6.9 represents the connection between this project and the main observation of the Thesis, presented in Chapter 5, to measure the effective collision frequency. The measured effective collision frequency is likely due to collisionless processes, of which there is evidence for instabilities being the cause of this. The analysis technique here is the key to not only measuring the quasi-linear relaxation rate, to answer if it is a sufficient mechanism to produce such an enhanced collision frequency, but is also suited to measure any wave-particle interaction.

6.7 Future work

This section demonstrates a few projects that are ongoing and will likely be a part of the completed analysis in the future, and some projects that have been inspired by this analysis.

6.7.1 Magnetic field power spectrum

The quasi-linear rates, shown as a function of wavenumber in Fig. 6.7, that lead to the rates shown in Fig. 6.8, are not smooth. Clearly this is due to the non-smoothness from the discrete nature of the power spectrum, seen also in Fig. 6.7. There are methods to smooth the power spectrum, but they lead to a loss of power and only capture particular kinds of noise, which is not the idea to pursue here. A method with marginal success is to return to the growth rate and compare it to the power spectrum. Figure 6.10, is a repeat of Fig. 6.7 at time $40 \Omega_p^{-1}$, a later time in the simulation, when the heating should calm down. This is evidenced by the offset between the resonance function (the fourth panel down) and the magnetic field power spectrum (the third panel down). To better capture the expected magnetic field power spectrum, a window is used, where it is 1 for when the growth rate is positive, and 10^3 smaller when it is not. The windowed power spectrum can be seen in the third panel down of Fig. 6.10, see the caption. The rates, in the bottom three panels, are then calculated with the

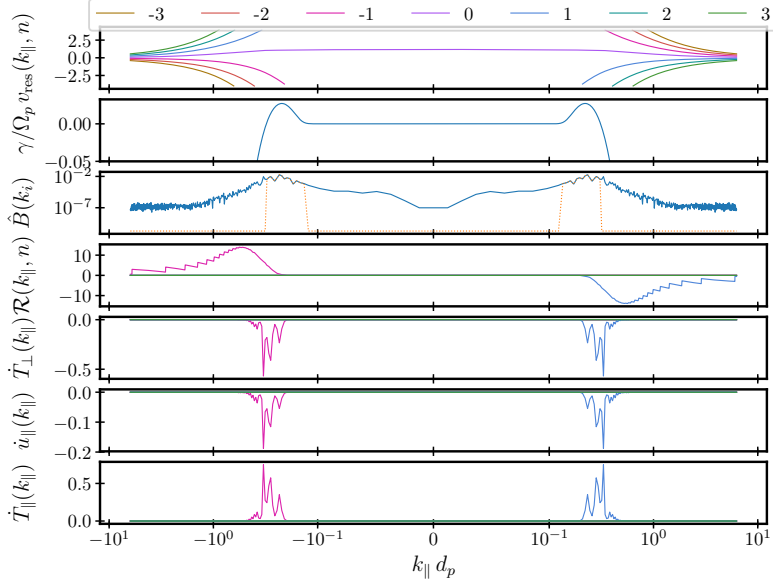


Figure 6.10: This is a repeat of Fig. 6.7, plotted for $t = 40 \Omega_p^{-1}$. The third panel down shows the magnetic field power spectrum, where the windowed power spectrum is the dashed orange line.

windowed magnetic field power spectrum.

The comparison of temperatures and integrated heating rates, made in Fig. 6.8, has been done for the windowed power spectrum version, shown as Fig. 6.11. The results are slightly contradictory, where the asymptotic state of the parallel temperature is now worse, and the perpendicular temperature is nearly perfect. The very encouraging point is that the heating rates appear to react better to changes in temperature, as they should. While this technique needs to be refined, among other points, such as the power spectrum, it is promising.

6.7.2 Comparison with bi-Maxwellian

Section 2.6 discussed the macroscopic and microscopic picture of quasi-linear theory, in particular, how finite resonance regions can cause the distribution function to depart from the simple bi-Maxwellian distribution function (see Fig. 2.6 for details on this discussion). The method derived here, is capable of alleviating this issue. Since the results are not perfect (e.g., the time evolution of the temperatures), it is difficult to make conclusive remarks, but some points can be illustrated.

Figure 6.12 is a repeat of 6.11, note that this is the windowed power spectrum version, with the bi-Maxwellian case also plotted for comparison. The bi-Maxwellian evolution was discussed in relation to Fig. 2.6, and here it can

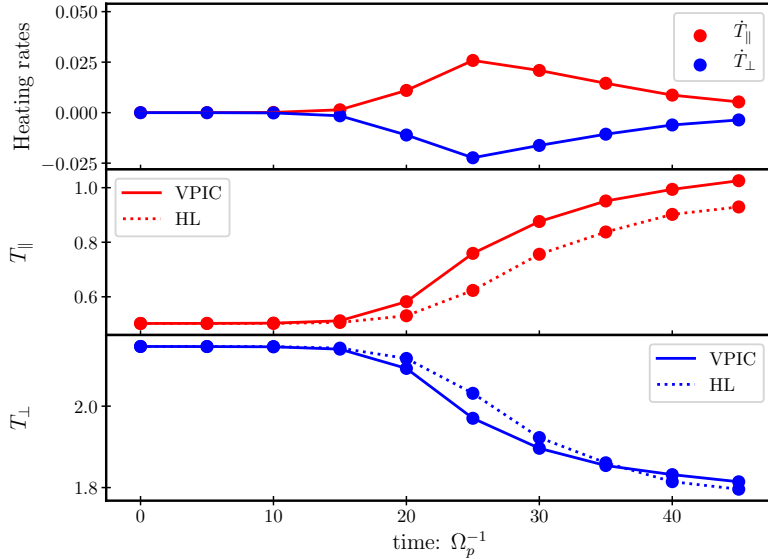


Figure 6.11: This is a repeat of Fig. 6.8 for the windowed power spectrum.

be given some more clarity. Returning to the heating and acceleration from Eq. 6.25, and using a bi-Maxwellian distribution function to describe the distribution function, notably, throughout the entire evolution, those equations become simple differential equations that can be solved, along with an equation for the magnetic field energy. This procedure is described in great detail in the review article by Yoon [2017], leading to the dashed lines in Fig. 6.12.

The bi-Maxwellian evolution does well to capture asymptotic states, but does not capture the time at which heating takes place, which can be seen in the top panel of the figure; the dashed line, lags behind the solid line. The dashed lines peak near to $20\Omega_p^{-1}$, but the maximum change in temperature (seen in the bottom two panels) clearly happens near to $25\Omega_p^{-1}$. The solid line, the Hermite-Laguerre method, does coincide better with the actual changes in temperature (from the simulation) seen in the bottom panel.

Figure 6.13 has been provided to ensure that the maximum order of the Hermite-Laguerre polynomials has not been analyzed incorrectly. For example, the bi-Maxwellian case is maximum order 0 for both polynomials, it has been argued that orders up to about 10, are physical, based on the noise floor (see Section 6.4.2). Figure 6.13 repeats Fig. 6.8 for a set of maximum Hermite-Laguerre polynomial orders, labelled in the legend. The axis limits have changed so that the slight differences can be seen.

A few points can be made, first is that the maximum polynomial order does not drastically affect the results, which is expected due to the large resonance

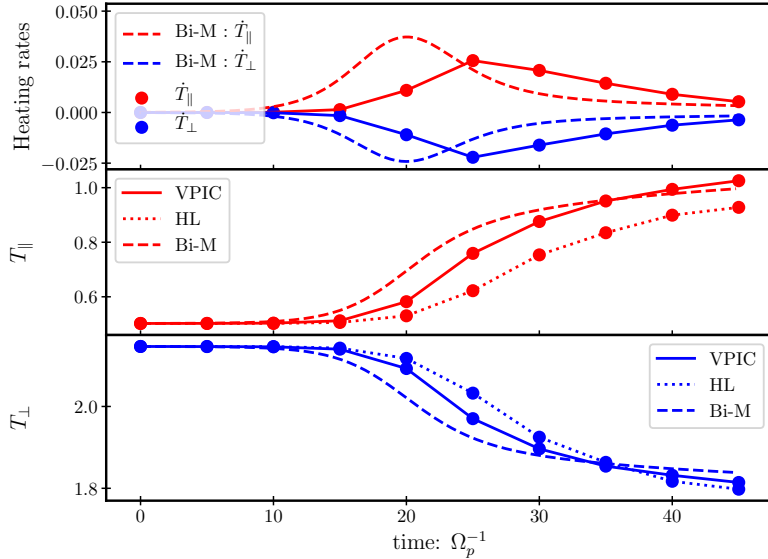


Figure 6.12: This is a repeat of Fig. 6.11 compared with the bi-Maxwellian (Bi-M) time evolution.

region, i.e., the fine details of the distribution function do not play a large role in the evolution. In fact, recalling Fig. 6.5, most the power, in velocity space, is stored in the the low-orders and stays there throughout the time of the simulation. It is only for orders 4 and larger, disregarding the noise, that show evolution, and they possess considerably less power than the lower orders. Therefore, it is expected that a low order treatment of the Hermite-Laguerre analysis should not differ greatly from a higher-order analysis.

This analysis suggests that the inaccuracy of the analysis presented here is related to the magnetic field power spectral density. The bi-Maxwellian time evolution, presented in Fig. 6.12, evolves the magnetic field coupled to the evolution of the distribution function, and since this evolution is not recovered for low order Hermite-Laguerre moments, it is probably the inability of the method to capture necessary information about the magnetic field.

Once this method is perfected, it can be used to better understand quasi-linear heating, beyond simple distribution functions. This idea is further explored in Section 6.7.3.

6.7.3 High-order quasi-linear theory

The Hermite-Laguerre analysis allows a higher-order (finer-details) theory of quasi-linear theory to be constructed. The ideas will be sketched in this section. Figure 6.14 shows the normalised power in the Hermite-Laguerre coefficients

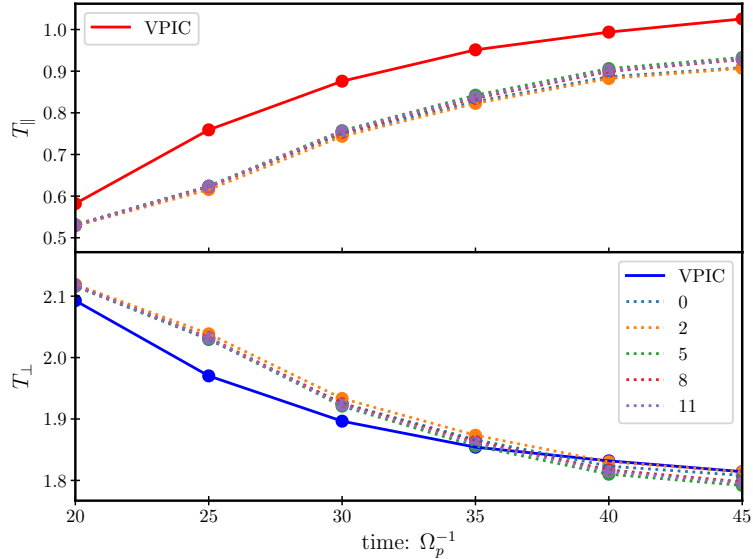


Figure 6.13: This is a repeat of Fig. 6.11 for varying maximum Hermite-Laguerre polynomial order, which is indicated in the legend. The horizontal axis has been shifted so the variation in time-evolution of the temperatures can be seen.

for four different times of the simulation (see the caption). Notice, that higher order Hermite indices are excited in the first time step, and then up through the Laguerre index. There is a preference in the even Hermite indices which is not present in the Laguerre indices.

The extended power in Laguerre indices for initial time of the simulation, suggest that there might be an issue with the analysis, which has been checked many times, or it is possible there is an issue with how the simulation is initialized. This is future work.

The evolution of the coefficients c_{ml} can be studied as well, where inserting the Hermite-Laguerre decomposed distribution function into Eq. 6.1 allows for an equation of the form,

$$\frac{\partial}{\partial t} c_{ml} = \sum_{m'=m-2}^{m+2} \sum_{l'=l-2}^{l+2} a_{m'l'}(t) c_{m'l'}, \quad (6.29)$$

where $a_{m'l'}(t)$ are time dependent coefficients determined by the magnetic field power spectrum, coefficients from the recursion relations, and the resonant velocity. The sum is from $-2, +2$ due to the double pitch-angle gradient in the full operator. This is a promising approach to better understanding the full details of quasi-linear theory. For example, how is free energy distributed in Hermite-

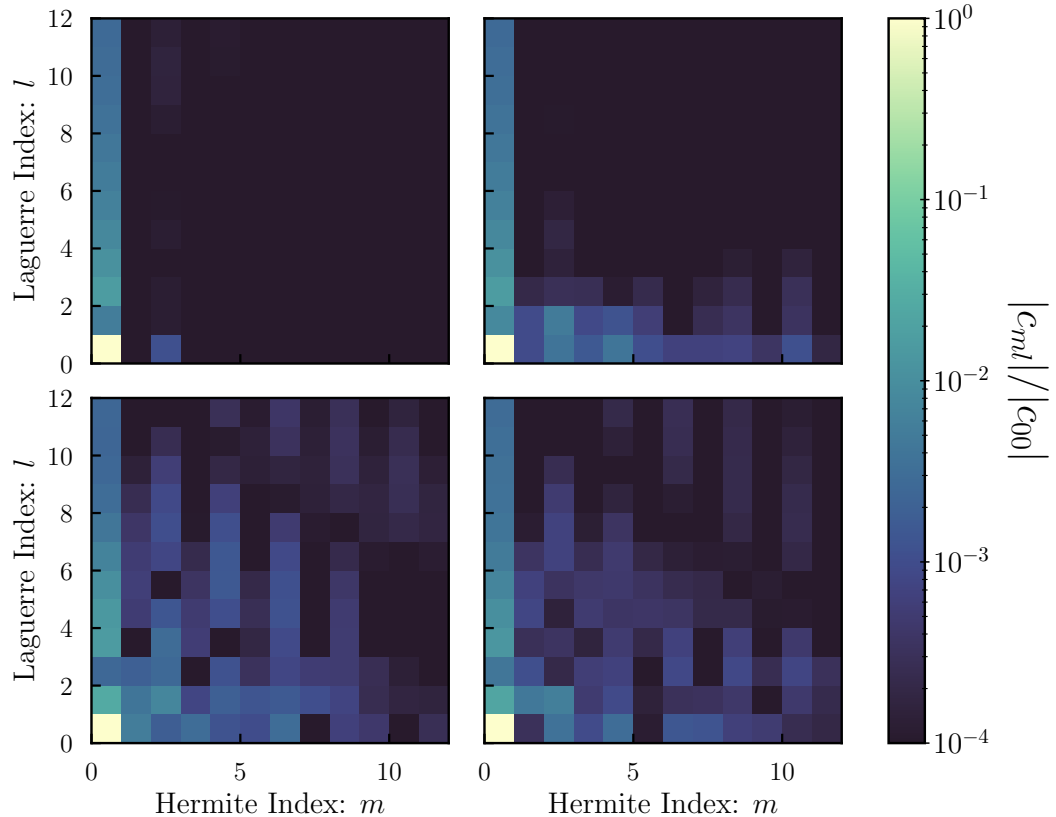


Figure 6.14: The Hermite-Laguerre coefficients, defined in Section 6.4.1 for times $0 \Omega_p^{-1}$ (top left), $15 \Omega_p^{-1}$ (top right), $30 \Omega_p^{-1}$ (bottom left), and $45 \Omega_p^{-1}$ (bottom right). The vertical axes are the Laguerre indicies, where the tick label is below the box. The horizontal axes are the Hermite indicies, where the tick label is to the left of the box. The color bar is normalized to the c_{00} box, which is nearly constant throughout the time evolution.

Laguerre space by various instabilities? Does it maintain free energy in the low orders, or does it prefer to send free energy to higher orders where it will be eventually thermalized by collisions. Can a non-linear theory be produced from this analysis?

Last, this decomposition can also be done for the dielectric tensor, and a Hermite-Laguerre dispersion relation solver can be constructed. Both of these projects are well underway.

6.8 Conclusion

This chapter is dedicated to creating analyses techniques to measure quasi-linear heating rates and acceleration. The methods were tested with a PIC simulation

as a *proof of concept* for spacecraft data. The analysis of the pitch-angle gradient of the distribution function permits a measurement of the quasi-linear relaxation rate. This allows the direct measurement of various proxies for the quasi-linear relaxation rate. While the method is not yet fully optimised, some important results are to be emphasised here.

The focus was on removing noise from velocity space, essentially with a low-pass filter, which was constructed from the Hermite-Laguerre functions. This method can be employed immediately to spacecraft data. This technique was also used to find the pitch-angle gradient via the recursion relations permitted by the Hermite-Laguerre functions. To test the accuracy of the gradient method, it was used to measure the quasi-linear heating rates. The method is convincing, but the results thus far are not correct. A closer look at the method proved that it is likely the analysis of magnetic field, or combining it, that leads to the errors, and so the pitch-angle gradient method can probably be applied to spacecraft data immediately.

At this point, since the method is not restricted to approximate velocity distribution functions, it can be applied to any instability, and since all wave-particle interactions (non-linear) involve velocity space gradients, this method will serve to also make measurements beyond quasi-linear theory.

Chapter 7

Conclusions and future work

The problem of the fluid nature of weakly collisional plasmas has been addressed by modelling relaxation processes in the kinetic equation and comparing to solar wind observations to measure the effective mean-free-path of the solar wind protons. The effective mean-free-path is measured to be approximately 4×10^5 km. In addition, the scale-dependent anisotropy exponent of the compressive fluctuations has been measured to be approximately 0.4. These measurements are used to determine the scale separating the fluid and collisionless regimes, called the transition scale, in the solar wind, which in spacecraft frame is approximately 0.2 Hz. The measurements show that the fluid description of the solar wind extends to much smaller scales than previously thought. The transition scale is consistent with past measurements of fluid and collisionless behaviour in the solar wind.

To conclude, a summary of the results of the Thesis is presented. Last, the implications of the results, physical interpretation, and connection to future work is presented.

7.1 Summary

In Chapter 4 the kinetic magnetohydrodynamic equations are supplemented with a relaxation operator to model effective collision processes. The system is linearized and compressive wave modes are produced. The model has freedom in propagation angle, wavenumber, plasma beta and effective mean-free-path, as well as electron to proton ratio of temperature and effective mean-free-path. The former parameters are shown to reproduce a list of past results on compressive waves, including the severe damping in the collisionless regime, and the lack of damping in the fluid regime. The model shows a natural connection between the MHD slow-mode, ion-acoustic mode, and the non-propagating mode. The

model is then shown to produce cross-correlations of the plasma fluctuations (e.g., density, magnetic field strength) which are non-trivial considering the effective mean-free-path and propagation angle. These cross-correlations can be compared with solar wind observations to determine if the plasma fluctuations are consistent with a particular wave mode.

Chapter 5 extends the cross-correlations to sensitive tests of the equation of state, which are based on the Chew-Goldberger-Low invariants or the double adiabatic equations. The dataset used in this chapter was not previously used for scientific publication so considerable attention is paid to the verification of the quality and the correctness by making comparison with other datasets and repeating previous studies. The observations were prepared for a data analysis to make a comparison with the numerical model. The analysis is not simple due to the fact that in the fluid regime, the predicted cross-correlations depend on the wavenumber, propagation angle, and effective-mean-free path. A model connecting the wavenumber and propagation angle is implemented and shown to alleviate these issues, also permitting a straight forward measurement of the scale-dependent anisotropy. The method of statistics is a new method that does not assume underlying statistical distribution of the parameters, general to the comparison of non-linear models and observations. Finally, the measurement of the effective mean-free-path, scale-dependent anisotropy, and the transition scale are presented.

Chapter 6 constructs data analysis techniques to measure the key ingredient of collisionless relaxation processes: the pitch-angle gradient. The gradient is not simple to measure from the standpoint of spacecraft measurements due to noise. An analysis technique that uses the Hermite-Laguerre polynomials as a basis for a transform is implemented to low pass filter the velocity distribution function in spectral space. This technique is used to measure the pitch-angle gradient of the distribution function, one of the essential pieces of the quasi-linear heating and momentum transfer rates, and is shown to be marginally successful. The collisionless relaxation rate is measured and compared with previous methods. The new method is a promising analysis technique to measure gradients of the velocity distribution function.

7.2 Discussion and future work

In this Section the discussion of a few major topics is expanded upon to connect to future work. The discussion relates to implications for the understanding of the solar wind and of plasma physics.

7.2.1 The fluid nature of plasmas

The fluid nature of the solar wind is not expected due to the long collisional mean-free-path of the protons. In particular, compressive waves should be severely damped in the collisionless case, as presented in the influential paper by Barnes [1966]. Some years later, in the review article Council [1979], the section titled, “Hydromagnetic waves and turbulence in the solar wind,” is written by A. Barnes, where there appears to be some reluctance in reviewing fluid MHD theory when presenting wave modes. The review focusses on which parts of the MHD theory survive in the kinetic theory (e.g., purely transverse small-amplitude Alfvén waves, non-propagating mode), of which guided my ideas through Chapter 4.

The idea presented here, is that collisionless relaxation processes shorten the mean-free-path so that collisionless damping is weak. While the mechanism that shortens the mean-free-path is yet to be determined, this serves as an explanation for why compressive waves are observed. The damping rate is proportional to $k_{\parallel}v_p$, but if the relaxation rate ν_{eff} is faster, the damping is interrupted. When the relaxation is slower, then damping occurs and the collisionless regime is recovered. The wavenumber dependence, of these processes, connects the collisionless and fluid regimes.

The fluid nature is consistent with decades of research that uses fluid models to explore energetics of the solar wind. Consider how drastic of an effect the effective collisionality is on the solar wind, with the shortening of the mean-free-path and the wave number geometry, the frequency of the transition scale is increased by six orders of magnitude. This piece of the thesis, while the mechanism has not been identified, is the primary contribution of this work to the field of space plasma physics. Future work must focus on the processes that retain the fluid nature of the solar wind plasma. This is a difficult undertaking, but without doubt, the gradient of the distribution function must be accurately measured. This is the focus of Chapter 6.

7.2.2 The transport coefficients

The transport coefficients (e.g., heat, viscosity) are applicable in the collisional regime. The neoclassical regime is essentially born from Braginskii’s finding that transport is anisotropic. The turbulent transport regime incorporates microinstabilities, but presents a massive complication since microinstabilities in a turbulent environment require detailed accuracy of the fields and particles in space and time. This thesis emphasises two important concepts worth discussing.

The scale-dependence of these processes is clear from the discussion of the

transition scale, the scale separating the fluid and collisionless scales; transport processes are scale dependent. Looking back to Fig. 4.6, it is clear that the damping rates connect smoothly between the estimate from viscosity and collisionless damping, so the actual “viscosity” is a simple function of scale. The other transport coefficients probably follow the same line of thinking.

The second point, is that above the transitions scale, the details of the distribution function do not matter. This is a very important finding of this Thesis. The actual effective collision frequency is determined by complicated plasma physics, that do depend on the details of the distribution function, but at large-scales, the system is fluid.

Future work should better understand the transition of the transport coefficients between these two regimes to better understand how transport occurs in multi-scale plasmas.

7.2.3 Compressive turbulence

In Chapter 5 the scale-dependent anisotropy of the compressive fluctuations and the transition scale are measured. With this, the picture of compressive turbulence can be updated. Figure 7.1 updates our understanding of turbulence in the solar wind. Previously, the critical balance curve could be drawn for the Alfvénic fluctuations; the compressive curve is more anisotropic and connects to the kinetic slow-mode and ion-acoustic mode. The damping of these modes is how compressive fluctuations heat the plasma.

The non-severe damping of the compressive waves reopens the plausibility that some of the particle energetics of the solar wind must be due to compressive waves. This was considered in Narita and Marsch [2015] where some features of these modes are presented (with gyroscale effects). The general conclusion is that the kinetic slow-mode is efficient at heating particles through the 0th order resonances. While most of the focus in the solar wind community has been on how the kinetic Alfvén wave and proton cyclotron wave heat the solar wind, this is not the whole story, the compressive mode will need to be considered for the entire heating scenario to be understood. This would be an interesting avenue for future work.

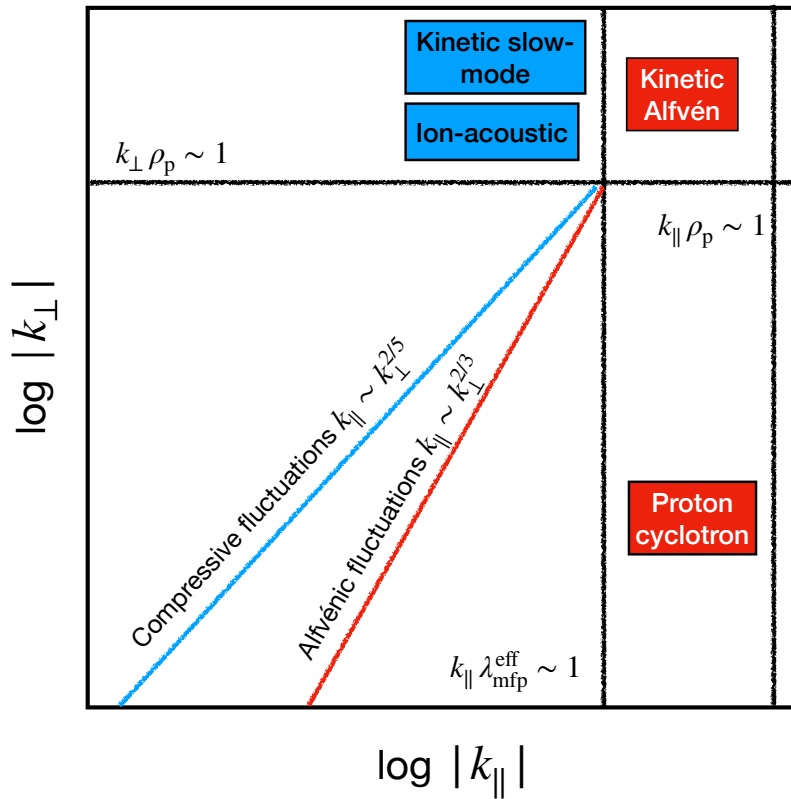


Figure 7.1: A schematic of the anisotropy of compressive and Alfvénic fluctuations in the inertial range, up to the kinetic ranges. The vertical axis is the logarithm of the perpendicular wavenumber and the horizontal axis is the parallel wavenumber. The coloured lines are labelled, corresponding to contours of maximum power in wavenumber space. The colour then corresponds to the kinetic waves associated with the inertial range (fluid) waves. The black lines are indicated where the wavenumber becomes comparable to important length scales. Notice that the $k_{\parallel} \lambda_{\text{mfp}}^{\text{eff}} \sim k_{\perp} \rho_p$ for the compressive and Alfvénic fluctuations.

Appendix A

Derivation of electromagnetic dielectric tensor

Beginning with the collisionless Vlasov equation, by setting the collision frequency to zero in Eq. 2.37,

$$\left[\frac{\partial}{\partial t} + v_j \frac{\partial}{\partial x_j} + \frac{q_s}{m_s} \left(E'_i + c^{-1} \epsilon_{ijk} v_j B'_k \right) \frac{\partial}{\partial v_i} \right] f'_s = 0 \quad (\text{A.1})$$

the electric field $E'_i = E'_i(t, x_i)$, magnetic field $B'_i = B'_i(t, x_i)$ and species distribution function $f'_s = f'_s(t, x_i, v_i)$. Maxwell's equations from Eqs. 2.38,

$$\epsilon_{ijk} \frac{\partial}{\partial x_j} B'_k - c^{-1} \frac{\partial}{\partial t} E'_i = \frac{4\pi}{c} \sum_s q_s \int d^3v v_i f'_s, \quad (\text{A.2})$$

$$\frac{\partial}{\partial x_i} B'_i = 0, \quad (\text{A.3})$$

$$\frac{\partial}{\partial x_i} E'_i = 4\pi \sum_s q_s \int d^3v f'_s, \quad (\text{A.4})$$

$$\epsilon_{ijk} \frac{\partial}{\partial x_j} E'_k + c^{-1} \frac{\partial}{\partial t} B'_i = 0. \quad (\text{A.5})$$

Decomposing,

$$f'_s(t, x_i, v_i) = F_s(t, v_i) + f_s(t, x_i, v_i), \quad (\text{A.6})$$

$$E'_i(t, x_i) = E_i(t, x_i), \quad (\text{A.7})$$

$$B'_i(t, x_i) = B_i + b_i(t, x_i), \quad (\text{A.8})$$

so that an ensemble average $\langle \dots \rangle$ leaves,

$$\langle f'_s(t, x_i, v_i) \rangle = F_s(t, v_i) \quad (\text{A.9})$$

$$\langle E_i(t, x_i) \rangle = 0 \quad (\text{A.10})$$

$$\langle B'_i(t, x_i) \rangle = B_i = B_0 \delta_{iz} \quad (\text{A.11})$$

where these are all assumptions, and δ_{iz} is the direction parallel to the background magnetic field equation. Rewriting Equation A.1 with the decomposition,

$$\begin{aligned} & \left[\frac{\partial}{\partial t} + \frac{q_s}{m_s} \left(E_i + c^{-1} \epsilon_{ijk} v_j (B_k + b_k) \right) \frac{\partial}{\partial v_i} \right] F_s \\ &= - \left[\frac{\partial}{\partial t} + v_j \frac{\partial}{\partial x_j} + \frac{q_s}{m_s} \left(E_i + c^{-1} \epsilon_{ijk} v_j (B_k + b_k) \right) \frac{\partial}{\partial v_i} \right] f_s \end{aligned} \quad (\text{A.12})$$

taking an ensemble average,

$$\begin{aligned} & \underbrace{\left[\frac{\partial}{\partial t} + \frac{q_s}{m_s} \left(c^{-1} \epsilon_{ijk} v_j B_k \right) \frac{\partial}{\partial v_i} \right]}_{\text{A}} F_s \\ &= - \left\langle \left[\frac{q_s}{m_s} \left(E_i + c^{-1} \epsilon_{ijk} v_j b_k \right) \frac{\partial}{\partial v_i} \right] f_s \right\rangle \end{aligned} \quad (\text{A.13})$$

writing the velocity in cylindrical coordinates,

$$v_i = \delta_{ix} v_\perp \cos[v_\phi] + \delta_{iy} v_\perp \sin[v_\phi] + \delta_{iz} v_\perp, \quad v_\parallel = v_i \hat{b}_i, \quad v_\perp = |v_i - v_\parallel \hat{b}_i| \quad (\text{A.14})$$

where v_ϕ is the gyrophase angle and the perpendicular and parallel definitions stem from the unit magnetic field vector $\hat{b}_i = b_i / |b_i|$. Working with term “A” $\times F_s$,

$$\begin{aligned} & \frac{q_s}{m_s} \left(c^{-1} \epsilon_{ijk} v_j B_k \right) \partial_{v_i} F_s = \frac{q_s}{c m_s} \left(\delta_{ix} v_y B_0 - \delta_{iy} v_x B_0 \right) \frac{\partial}{\partial v_i} F_s \\ &= \frac{q_s}{c m_s} \left(\delta_{ix} v_\perp \sin[v_\phi] B_0 - \delta_{iy} v_\perp \cos[v_\phi] B_0 \right) \frac{\partial}{\partial v_i} F_s, \end{aligned} \quad (\text{A.15})$$

noticing,

$$\frac{\partial}{\partial v_\phi} v_x = -v_\perp \sin[v_\phi], \quad \frac{\partial}{\partial v_\phi} v_y = v_\perp \cos[v_\phi], \quad \frac{\partial}{\partial v_\phi} v_z = 0 \quad (\text{A.16})$$

substituting,

$$\begin{aligned} \frac{q_s}{cm_s} & \left(\delta_{ix} v_\perp \sin[v_\phi] B_0 - \delta_{iy} v_\perp \cos[v_\phi] B_0 \right) \frac{\partial}{\partial v_i} F_s \\ &= -\frac{q_s B_0}{cm_s} \left(\delta_{ix} \frac{\partial}{\partial v_\phi} v_x + \delta_{iy} \frac{\partial}{\partial v_\phi} v_y + \delta_{iz} \frac{\partial}{\partial v_\phi} v_z \right) \frac{\partial}{\partial v_i} F_s \end{aligned} \quad (\text{A.17})$$

and with chain rule,

$$\frac{q_s}{m_s} \left(c^{-1} \epsilon_{ijk} v_j B_k \right) \partial_{v_i} F_s - \frac{q_s B_0}{cm_s} \frac{\partial}{\partial v_\phi} F_s. \quad (\text{A.18})$$

Now write rewrite Eq. A.13,

$$\left[\partial_t - \Omega_s \frac{\partial}{\partial v_\phi} \right] F_s = - \left\langle \left[\frac{q_s}{m_s} \left(E_i + c^{-1} \epsilon_{ijk} v_j b_k \right) \frac{\partial}{\partial v_i} \right] f_s \right\rangle, \quad (\text{A.19})$$

where the definition of the species gyrofrequency is $\Omega_s = q_s B_0 / cm_s$. Returning to Equation A.12 and inserting Equation A.19

$$\begin{aligned} & \left[\partial_t + v_j \frac{\partial}{\partial x_j} + \frac{q_s}{m_s} \left(E_i + c^{-1} \epsilon_{ijk} v_j (B_k + b_k) \right) \frac{\partial}{\partial v_i} \right] f_s \\ &= -\frac{q_s}{m_s} \left(E_i + c^{-1} \epsilon_{ijk} v_j b_k \right) \frac{\partial}{\partial v_i} F_s + \left\langle \left[\frac{q_s}{m_s} \left(E_i + c^{-1} \epsilon_{ijk} v_j b_k \right) \frac{\partial}{\partial v_i} \right] f_s \right\rangle, \end{aligned} \quad (\text{A.20})$$

linearise,

$$\left[\partial_t + v_j \frac{\partial}{\partial x_j} + \frac{q_s}{cm_s} \epsilon_{ijk} v_j B_k \frac{\partial}{\partial v_i} \right] f_s = -\frac{q_s}{m_s} \left(E_i + c^{-1} \epsilon_{ijk} v_j b_k \right) \frac{\partial}{\partial v_i} F_s. \quad (\text{A.21})$$

The terms in the brackets on the left hand side constitute the 0th order evolution of a particle, so this is perfectly setup for the "Method of unperturbed orbits" following Stix [1992] and Gary [1993].

A.0.1 The perturbation in the unperturbed orbit frame

The Lagrangian frame of unperturbed orbits (or the characteristics or the zero-order trajectory),

$$\frac{d}{dt'} x_i(t') = v_i(t'), \quad \frac{d}{dt'} v_i(t') = \frac{q_s}{m_s c} \epsilon_{ijk} v_j(t') B_k \quad (\text{A.22})$$

where $v'_j = v_j(t')$, $x'_j = x_j(t')$, for the rate of change of the zero-order distribution function,

$$\left(\frac{d}{dt'} F'_s \right)_0 = \left[\partial'_t + v'_j \frac{\partial}{\partial x'_j} + c^{-1} \epsilon_{ijk} v'_j B_k \frac{\partial}{\partial v'_i} \right] F'_s = 0 \quad (\text{A.23})$$

the zero-order distribution does not evolve on the unperturbed orbits¹. Consider the first-order distribution function (using Equation A.21) along the zero-order orbits,

$$\begin{aligned} \left(\frac{d}{dt'} f'_s \right)_0 &= \left[\partial'_t + v'_j \frac{\partial}{\partial x'_j} + \frac{q_s}{cm_s} \epsilon_{ijk} v'_j B_k \frac{\partial}{\partial v'_i} \right] f'_s \\ &= -\frac{q_s}{m_s} \left(E'_i + c^{-1} \epsilon_{ijk} v'_j b'_k \right) \frac{\partial}{\partial v'_i} F'_s, \end{aligned} \quad (\text{A.24})$$

giving the rate of change of the perturbation along the unperturbed orbits on the left hand side. Integrating in time,

$$f_s(t, x_i, v_i) - f_s(t_0, x_i(t_0), v_i(t_0)) = -\frac{q_s}{m_s} \int_{t_0}^t dt' \left(E'_i + c^{-1} \epsilon_{ijk} v'_j b'_k \right) \frac{\partial}{\partial v'_i} F'_s. \quad (\text{A.25})$$

For the evolution of the distribution function the initial perturbation is ignored² and the lower limit on the integral is set to $t_0 = -\infty$,

$$f_s(t, x_i, v_i) = -\frac{q_s}{m_s} \int_{-\infty}^t dt' \left(E'_i + c^{-1} \epsilon_{ijk} v'_j b'_k \right) \frac{\partial}{\partial v'_i} F'_s. \quad (\text{A.26})$$

The perturbation of the distribution function is now a complicated integral involving the perturbed field and the background distribution function.

A.0.2 The unperturbed orbits

The orbits can be solved for by integrating Eq. A.22, where the perpendicular and parallel velocity are constant giving,

$$\begin{aligned} \frac{d}{dt'} v_i(t') &= -\delta_{ix} v_\perp \sin[v'_\phi] \frac{d}{dt'} v'_\phi + \delta_{iy} v_\perp \cos[v'_\phi] \frac{d}{dt'} v'_\phi \\ &= \frac{q_s}{m_s c} \epsilon_{ijk} v_j(t') B_k = \frac{q_s B_0}{cm_s} \left(\delta_{ix} v_\perp \sin[v'_\phi] - \delta_{iy} v_\perp \cos[v'_\phi] \right) \\ &\Rightarrow \frac{d}{dt'} v'_\phi = -\Omega_s \end{aligned} \quad (\text{A.27})$$

¹This is only true in the linear phase

²See page 248 - 249 of "Waves in Plasmas", Stix for a full treatment of this issue. This is ignores the ballistic response the ballistic response.

integrating,

$$\begin{aligned} v_\phi(t') &= -\Omega_s(t' - t) + v_\phi(t) \\ \Rightarrow v'_i &= \delta_{ix}v_\perp \cos[-\Omega_s(t' - t) + v_\phi] + \delta_{iy}v_\perp \sin[-\Omega_s(t' - t) + v_\phi] + \delta_{iz}v_\parallel. \end{aligned} \quad (\text{A.28})$$

Integrating over time for the position,

$$\begin{aligned} x'_i - x_i &= -\delta_{ix}\frac{v_\perp}{\Omega_s} \left(\sin[-\Omega_s(t' - t) + v_\phi] - \sin[v_\phi] \right) \\ &\quad + \delta_{iy}\frac{v_\perp}{\Omega_s} \left(\cos[-\Omega_s(t' - t) + v_\phi] - \cos[v_\phi] \right) + \delta_{iz}v_\parallel(t' - t). \end{aligned} \quad (\text{A.29})$$

These results lead to a change of coordinates,

$$v'_x = v_\perp \cos[v_\Phi], \quad v'_y = v_\perp \sin[v_\Phi], \quad v'_z = v_\parallel \quad (\text{A.30})$$

using $v_\Phi = -\Omega_s(t' - t) + v_\phi$, which gives,

$$dv'_x = dv_\perp \cos[v_\Phi] - v_\perp \sin[v_\Phi] dv_\Phi, \quad (\text{A.31})$$

$$dv'_y = dv_\perp \sin[v_\Phi] + v_\perp \cos[v_\Phi] dv_\Phi, \quad (\text{A.32})$$

$$dv'_z = dv_\parallel \quad (\text{A.33})$$

considering,

$$\begin{aligned} dg &= dv'_x \frac{\partial}{\partial v'_x} g + dv'_y \frac{\partial}{\partial v'_y} g + dv'_z \frac{\partial}{\partial v'_z} g, \\ dg &= dv_\perp \frac{\partial}{\partial v_\perp} g + dv_\Phi \frac{\partial}{\partial v_\Phi} g + dv_\parallel \frac{\partial}{\partial v_\parallel} g, \end{aligned} \quad (\text{A.34})$$

for arbitrary function g , so that upon substitution,

$$\begin{aligned} dg &= \left(dv_\perp \cos[v_\Phi] - v_\perp \sin[v_\Phi] dv_\Phi \right) \frac{\partial}{\partial v'_x} g \\ &\quad + \left(dv_\perp \sin[v_\Phi] + v_\perp \cos[v_\Phi] dv_\Phi \right) \frac{\partial}{\partial v'_y} g + dv_\parallel \frac{\partial}{\partial v'_z} g \\ &= \left(\cos[v_\Phi] \frac{\partial}{\partial v'_x} g + \sin[v_\Phi] \frac{\partial}{\partial v'_y} g \right) dv_\perp \\ &\quad + \left(v_\perp \cos[v_\Phi] \frac{\partial}{\partial v'_y} g - v_\perp \sin[v_\Phi] \frac{\partial}{\partial v'_x} g \right) dv_\Phi + dv_\parallel \frac{\partial}{\partial v'_z} g, \end{aligned} \quad (\text{A.35})$$

so that,

$$\begin{aligned}\frac{\partial}{\partial v_{\perp}}g &= \cos[v_{\Phi}]\frac{\partial}{\partial v'_x}g + \sin[v_{\Phi}]\frac{\partial}{\partial v'_y}g \\ \frac{\partial}{\partial v_{\Phi}}g &= v_{\perp}\cos[v_{\Phi}]\frac{\partial}{\partial v'_y}g - v_{\perp}\sin[v_{\Phi}]\frac{\partial}{\partial v'_x}g \\ \frac{\partial}{\partial v_{\parallel}}g &= \frac{\partial}{\partial v'_z}g.\end{aligned}\tag{A.36}$$

If the function g' does not depend on v_{Φ} then,

$$\cos[v_{\Phi}]\frac{\partial}{\partial v'_y}g' = \sin[v_{\Phi}]\frac{\partial}{\partial v'_x}g',\tag{A.37}$$

giving,

$$\begin{aligned}\frac{\partial}{\partial v_{\perp}}g' &= \cos[v_{\Phi}]\frac{\partial}{\partial v'_x}g' + \sin[v_{\Phi}]\tan[v_{\Phi}]\frac{\partial}{\partial v'_x}g' \\ &= (\cos[v_{\Phi}])^{-1}\frac{\partial}{\partial v'_x}g' = (\sin[v_{\Phi}])^{-1}\frac{\partial}{\partial v'_y},\end{aligned}\tag{A.38}$$

collecting the results for later,

$$\frac{\partial}{\partial v'_x} = \cos[v_{\Phi}]\frac{\partial}{\partial v_{\perp}}, \quad \frac{\partial}{\partial v'_y} = \sin[v_{\Phi}]\frac{\partial}{\partial v_{\perp}}, \quad \frac{\partial}{\partial v'_z} = \frac{\partial}{\partial v_{\parallel}},\tag{A.39}$$

which are valid for a function that doesn't depend on v_{Φ} .

A.0.3 Fourier Transform

For the late-time (weak damping/growth) dispersive properties it is sufficient to assume all perturbations evolve in space and time as,

$$g(t, x_i) = \int d^3k \hat{g}(k_i) \exp\{ik_j x_j - i\omega(k_i)t\}\tag{A.40}$$

$$\hat{g}(k_i) = (2\pi)^{-3} \int d^3x g(t, x_i) \exp\{-ik_j x_j + i\omega(k_i)t\}\tag{A.41}$$

where the complex frequency $\omega(k_i) = \omega^r(k_i) + i\gamma(k_i)$ gives the time dependence. This is the form of the Fourier transform used throughout this appendix. Since all of the functions are real the general statement is valid,

$$\begin{aligned}g(t, x_i) &= \int d^3k \hat{g}(k_i) \exp\{ik_j x_j - i\omega(k_i)t\} \\ &= g^*(t, x_i) = \int d^3k \hat{g}^*(k_i) \exp\{-ik_j x_j + i\omega^*(k_i)t\},\end{aligned}\tag{A.42}$$

where $*$ denotes of the complex conjugate. Taking the Fourier transform,

$$\begin{aligned}
& (2\pi)^{-3} \int d^3x \exp\{-ip_j x_j + i\omega(p_i)t\} g(t, x_i) \\
&= (2\pi)^{-3} \int d^3x \exp\{-ip_j x_j + i\omega(p_i)t\} \int d^3k \hat{g}(k_i) \exp\{ik_j x_j - i\omega(k_i)t\} \\
&= (2\pi)^{-3} \int d^3k \hat{g}(k_i) \exp\{i(\omega(p_i) - \omega(k_i))t\} \int d^3x \exp\{i(k_j - p_j)x_j\} \\
&= (2\pi)^{-3} \int d^3k \hat{g}(k_i) \exp\{i(\omega(p_i) - \omega(k_i))t\} \delta(k_j - p_j) \\
&= \hat{g}(k_i),
\end{aligned} \tag{A.43}$$

and the right hand side,

$$\begin{aligned}
& (2\pi)^{-3} \int d^3x \exp\{-ip_j x_j + i\omega(p_i)t\} g^*(t, x_i) \\
&= (2\pi)^{-3} \int d^3x \exp\{-ip_j x_j + i\omega(p_i)t\} \int d^3k \hat{g}^*(k_i) \exp\{-ik_j x_j + i\omega^*(k_i)t\} \\
&= (2\pi)^{-3} \int d^3k \hat{g}^*(k_i) \exp\{i(\omega(p_i) + \omega^*(k_i))t\} \int d^3x \exp\{-i(p_j + k_j)x_j\} \\
&= \int d^3k \hat{g}^*(k_i) \exp\{i(\omega(p_i) + \omega^*(k_i))t\} \delta(p_j + k_j) \\
&= \hat{g}^*(-p_i) \exp\{i(\omega(p_i) + \omega^*(-p_i))t\},
\end{aligned} \tag{A.44}$$

so that $p_i \rightarrow k_i$ gives,

$$\omega_r(k_i) + i\gamma(k_i) = -\omega_r(-k_i) + i\gamma(-k_i), \tag{A.45}$$

giving the reality condition,

$$\omega_r(k_i) = -\omega_r(-k_i), \quad \gamma(k_i) = \gamma(-k_i), \quad \hat{g}(k_i) = \hat{g}^*(-k_i), \tag{A.46}$$

the reality condition.

Applying the Fourier transform to Faraday's law (introduced as Eq. D.97 in this appendix),

$$\epsilon_{ijk} \frac{\partial}{\partial x_j} E_k + \frac{1}{c} \frac{\partial}{\partial t} b_i = 0, \tag{A.47}$$

gives,

$$\hat{b}_i = \frac{c}{\omega(k_i)} \epsilon_{ijk} k_j \hat{E}_k. \tag{A.48}$$

Applying the Fourier transform to Ampere's Law gives,

$$i\epsilon_{ijk}k_j\hat{b}_k + \frac{i\omega(k_i)}{c}\hat{E}_i = \frac{4\pi}{c} \sum_s q_s \int d^3v v_i \hat{f}_s \quad (\text{A.49})$$

inserting Fourier transformed Farady's Law,

$$\frac{c^2}{\omega(k_i)^2} \epsilon_{ijk} \epsilon_{klm} k_j k_l \hat{E}_m + \hat{E}_i = -\frac{4\pi i}{\omega(k_i)} \sum_s q_s \int d^3v v_i \hat{f}_s, \quad (\text{A.50})$$

with vector identities,

$$\frac{c^2}{\omega(k_i)^2} (k_i k_j \hat{E}_j - k_j^2 \hat{E}_i) + \hat{E}_i = -\frac{4\pi i}{\omega(k_i)} \sum_s q_s \int d^3v v_i \hat{f}_s, \quad (\text{A.51})$$

which is the dielectric tensor, where a solution for the perturbed distribution function is required.

Applying the Fourier transform to Equation A.26,

$$\begin{aligned} (2\pi)^{-3} \int d^3x f_s \exp\{-ip_j x_j + i\omega_p t\} &= \hat{f}_s \\ &= -\frac{q_s}{m_s} \int_{-\infty}^t dt' (2\pi)^{-3} \int d^3x \exp\{-ip_j x_j + i\omega(p_i)t'\} \\ &\quad \times \left(E'_i + c^{-1} \epsilon_{ijk} v'_j b'_k \right) \frac{\partial}{\partial v'_i} F'_s, \end{aligned} \quad (\text{A.52})$$

and writing out the perturbed quantities E'_i, b'_k gives,

$$\begin{aligned} \hat{f}_s &= -\frac{q_s}{m_s} \int_{-\infty}^t dt' (2\pi)^{-3} \int d^3x \int d^3k \exp\{-ip_j x_j + i\omega_p t'\} \\ &\quad \times \exp\{ik_j x'_j - i\omega_k t'\} \left(\hat{E}_i + c^{-1} \epsilon_{ijk} v'_j \hat{b}_k \right) \frac{\partial}{\partial v'_i} F'_s, \end{aligned} \quad (\text{A.53})$$

so that here the quantities with hats are functions of k_i . Introduce $\Delta x_j = x'_j - x_j$

which depends on $t' - t$ (see Equation A.29) to write,

$$\begin{aligned}
\hat{f}_s &= -\frac{q_s}{(2\pi)^3 m_s} \int_{-\infty}^t dt' \int d^3k \exp\{ik_j \Delta x_j - i\omega(k_i)t' + i\omega(p_i)t\} \\
&\quad \times \left(\hat{E}_i + c^{-1} \epsilon_{ijk} v'_j \hat{b}_k \right) \frac{\partial}{\partial v'_i} F'_s \int d^3x \exp\{ix_j(k_j - p_j)\} \\
&= -\frac{q_s}{m_s} \int_{-\infty}^t dt' \int d^3k \exp\{ik_j \Delta x_j - i\omega(k_i)t' + i\omega(p_i)t\} \\
&\quad \times \left(\hat{E}_i + c^{-1} \epsilon_{ijk} v'_j \hat{b}_k \right) \delta(k_j - p_j) \frac{\partial}{\partial v'_i} F'_s \\
&= -\frac{q_s}{m_s} \int_{-\infty}^t dt' \exp\{ik_j(x'_j - x_j) - i\omega(k_i)(t' - t)\} \\
&\quad \times \left(\hat{E}_i + c^{-1} \epsilon_{ijk} v'_j \hat{b}_k \right) \frac{\partial}{\partial v'_i} F'_s. \tag{A.54}
\end{aligned}$$

The first step uses homogeneity in x_i (i.e., to ignore the integral of Δx_i) and the next steps use properties of the Dirac delta function. Now the result on Faraday's law can be used to re-write the magnetic field term,

$$c^{-1} \epsilon_{ijk} v'_j \hat{b}_k = \omega(k_i)^{-1} \epsilon_{ijk} v'_j \epsilon_{klm} k_l \hat{E}_m = \omega(k_i)^{-1} (v'_j k_i \hat{E}_j - v'_j k_j \hat{E}_i), \tag{A.55}$$

giving,

$$\begin{aligned}
\hat{f}_s &= -\frac{q_s}{m_s} \int_{-\infty}^t dt' \exp\{ik_j(x'_j - x_j) - i\omega(k_i)(t' - t)\} \\
&\quad \times \left(\hat{E}_i + \omega(k_i)^{-1} (v'_j k_i \hat{E}_j - v'_j k_j \hat{E}_i) \right) \frac{\partial}{\partial v'_i} F'_s \\
&= -\frac{q_s}{m_s} \int_{-\infty}^t dt' \exp\{ik_j(x'_j - x_j) - i\omega(k_i)(t' - t)\} \\
&\quad \times \hat{E}_l [\delta_{il}(1 - \omega(k_i)^{-1} v'_j k_j) + \omega(k_i)^{-1} v'_j k_i \delta_{jl}] \frac{\partial}{\partial v'_i} F'_s. \tag{A.56}
\end{aligned}$$

Now some vector products and algebra needs to be done. It is best to write out

the vector algebra in the integrand,

$$\begin{aligned}
& \hat{E}_l \left[\delta_{il} (1 - \omega(k_i)^{-1} v'_j k_j) + \omega(k_i)^{-1} v'_j k_i \delta_{jl} \right] \frac{\partial}{\partial v'_i} F'_s \\
&= \hat{E}_i \left(1 - \omega(k_i)^{-1} v'_j k_j \right) \frac{\partial}{\partial v'_i} F'_s + \hat{E}_j \omega(k_i)^{-1} v'_j k_i \frac{\partial}{\partial v'_i} F'_s \\
&= \left[1 - \omega(k_i)^{-1} (v'_x k_x + v'_y k_y + v'_z k_z) \right] \left(\hat{E}_x \frac{\partial}{\partial v'_x} F'_s + \hat{E}_y \frac{\partial}{\partial v'_y} F'_s + \hat{E}_z \frac{\partial}{\partial v'_z} F'_s \right) \\
&\quad + \omega(k_i)^{-1} \left(\hat{E}_x v'_x + \hat{E}_y v'_y + \hat{E}_z v'_z \right) \left(k_x \frac{\partial}{\partial v'_x} + k_y \frac{\partial}{\partial v'_y} + k_z \frac{\partial}{\partial v'_z} \right) F'_s \\
&= \hat{E}_x \left[\frac{\partial}{\partial v'_x} - \omega(k_i)^{-1} \left(v'_y k_y + v'_z k_z \right) \frac{\partial}{\partial v'_x} + \omega(k_i)^{-1} v'_x \left(k_y \frac{\partial}{\partial v'_y} + k_z \frac{\partial}{\partial v'_z} \right) \right] F'_s \\
&\quad + \hat{E}_y \left[\frac{\partial}{\partial v'_y} - \omega(k_i)^{-1} \left(v'_x k_x + v'_z k_z \right) \frac{\partial}{\partial v'_y} + \omega(k_i)^{-1} v'_y \left(k_x \frac{\partial}{\partial v'_x} + k_z \frac{\partial}{\partial v'_z} \right) \right] F'_s \\
&\quad + \hat{E}_z \left[\frac{\partial}{\partial v'_z} - \omega(k_i)^{-1} \left(v'_x k_x + v'_y k_y \right) \frac{\partial}{\partial v'_z} + \omega(k_i)^{-1} v'_z \left(k_x \frac{\partial}{\partial v'_x} + k_y \frac{\partial}{\partial v'_y} \right) \right] F'_s
\end{aligned} \tag{A.57}$$

now consider cylindrical coordinates, the same change of coordinates detailed at the end of Section A.0.2, for the wavenumber. Now, introduce $k_x = k_\perp \cos[\theta]$, $k_y = k_\perp \sin[\theta]$, $k_z = k_\parallel$ where θ is in the plane perpendicular to the magnetic field. Additionally, reintroduce the cylindrical coordinates for the velocity (from Eqs. A.39) so that,

$$\begin{aligned}
& \frac{\partial}{\partial v'_x} - \omega(k_i)^{-1} \left(v'_y k_y + v'_z k_z \right) \frac{\partial}{\partial v'_x} + \omega(k_i)^{-1} v'_x \left(k_y \frac{\partial}{\partial v'_y} + k_z \frac{\partial}{\partial v'_z} \right) \\
&= \cos[v'_\Phi] \frac{\partial}{\partial v'_\perp} - \omega(k_i)^{-1} \left(k_y v'_\perp \sin[v'_\Phi] + v'_\parallel k_z \right) \cos[v'_\Phi] \frac{\partial}{\partial v'_\perp} \\
&\quad + \omega(k_i)^{-1} v'_\perp \cos[v'_\Phi] \left(k_y \sin[v'_\Phi] \frac{\partial}{\partial v'_\perp} + k_z \frac{\partial}{\partial v'_\parallel} \right) \\
&= \cos[v'_\Phi] \left[\frac{\partial}{\partial v'_\perp} + \omega(k_i)^{-1} k_\parallel \left(v'_\perp \frac{\partial}{\partial v'_\parallel} - v'_\parallel \frac{\partial}{\partial v'_\perp} \right) \right],
\end{aligned} \tag{A.58}$$

and,

$$\begin{aligned}
\frac{\partial}{\partial v'_y} - \omega(k_i)^{-1} & \left(v'_x k_x + v'_z k_z \right) \frac{\partial}{\partial v'_y} + \omega(k_i)^{-1} v'_y \left(k_x \frac{\partial}{\partial v'_x} + k_z \frac{\partial}{\partial v'_z} \right) \\
& = \sin[v'_\Phi] \frac{\partial}{\partial v'_\perp} - \omega(k_i)^{-1} \left(k_x v'_\perp \cos[v'_\Phi] + v'_\parallel k_z \right) \sin[v'_\Phi] \frac{\partial}{\partial v'_\perp} \\
& \quad + \omega(k_i)^{-1} v'_\perp \sin[v'_\Phi] \left(k_x \cos[v'_\Phi] \frac{\partial}{\partial v'_\perp} + k_z \frac{\partial}{\partial v'_\parallel} \right) \\
& = \sin[v'_\Phi] \left[\frac{\partial}{\partial v'_\perp} + \omega(k_i)^{-1} k_\parallel \left(v'_\perp \frac{\partial}{\partial v'_\parallel} - v'_\parallel \frac{\partial}{\partial v'_\perp} \right) \right], \tag{A.59}
\end{aligned}$$

last,

$$\begin{aligned}
\frac{\partial}{\partial v'_z} - \omega(k_i)^{-1} & \left(v'_x k_x + v'_y k_y \right) \frac{\partial}{\partial v'_z} + \omega(k_i)^{-1} v'_z \left(k_x \frac{\partial}{\partial v'_x} + k_y \frac{\partial}{\partial v'_y} \right) \\
& = \frac{\partial}{\partial v'_\parallel} - \omega(k_i)^{-1} \left(v'_\perp k_x \cos[v'_\Phi] + v'_\perp k_y \sin[v'_\Phi] \right) \frac{\partial}{\partial v'_\parallel} \\
& \quad + \omega(k_i)^{-1} v'_\parallel \left(k_x \cos[v'_\Phi] \frac{\partial}{\partial v'_\perp} + k_y \sin[v'_\Phi] \frac{\partial}{\partial v'_\perp} \right) \\
& = \frac{\partial}{\partial v'_\parallel} + \omega(k_i)^{-1} k_\perp \left(\cos[\theta] \cos[v'_\Phi] + \sin[\theta] \sin[v'_\Phi] \right) \left(v'_\parallel \frac{\partial}{\partial v'_\perp} - v'_\perp \frac{\partial}{\partial v'_\parallel} \right) \\
& = \frac{\partial}{\partial v'_\parallel} + \omega(k_i)^{-1} k_\perp \cos[\theta - v_\Phi] \left(v'_\parallel \frac{\partial}{\partial v'_\perp} - v'_\perp \frac{\partial}{\partial v'_\parallel} \right) \tag{A.60}
\end{aligned}$$

so the perturbation can be written,

$$\begin{aligned}
\hat{f}_s & = -\frac{q_s}{m_s} \int_{-\infty}^t dt' \exp\{ik_j(x'_j - x_j) - i\omega(k_i)(t' - t)\} \\
& \times \left[\hat{E}_x \cos[v'_\Phi] \frac{\partial}{\partial \alpha'_+} + \hat{E}_y \sin[v'_\Phi] \frac{\partial}{\partial \alpha'_+} + \hat{E}_z \left(\frac{\partial}{\partial \alpha'_+} v'_\parallel + \cos[\theta - v'_\Phi] \frac{\partial}{\partial \beta'_+} \right) \right] F_s. \tag{A.61}
\end{aligned}$$

where,

$$\frac{\partial}{\partial \alpha_\pm} = \frac{\partial}{\partial v_\perp} \pm \omega(\pm k)^{-1} k_\parallel \left(v_\perp \frac{\partial}{\partial v_\parallel} - v_\parallel \frac{\partial}{\partial v_\perp} \right) \tag{A.62}$$

$$\frac{\partial}{\partial \beta_\pm} = \pm \omega(\pm k)^{-1} k_\perp \left(v_\parallel \frac{\partial}{\partial v_\perp} - v_\perp \frac{\partial}{\partial v_\parallel} \right). \tag{A.63}$$

Here $v_\Phi = -\Omega_s(t' - t) + v_\phi$ involves t' . At this point, recall that v_\perp, v_\parallel are constants of motion for the unperturbed orbits, so only v_ϕ, v_Φ have t' dependence.

A.0.4 Introducing the Bessel functions

Now put the exponential function into a form that is better suited for introducing Bessel functions. The first thing to do is set the angle $\theta = 0$ so that, $k_i = \delta_{ix}k_\perp + \delta_{iy}0 + \delta_{iz}k_\parallel$. Next, rewrite the exponential in Equation A.61 by recalling the unperturbed orbits from section A.0.2,

$$ik_j(x'_j - x_j) - i\omega(k_i)(t' - t) = -i \frac{k_\perp v_\perp}{\Omega_s} [\sin[v'_\Phi] - \sin[v_\phi]] + i[k_\parallel v_\parallel - \omega(k_i)](t' - t). \quad (\text{A.64})$$

The time dependence t' has been considered now, that only v_Φ depends on time, which initial condition is v_ϕ . Recognizing the Bessel function (first kind) identities,

$$\exp\{i\lambda_s \sin[x]\} = \sum_{n=-\infty}^{\infty} J_n(\lambda_s) \exp\{inx\}, \quad (\text{A.65})$$

$$\sum_{n=-\infty}^{\infty} J_n(\lambda_s) \exp\{inx\} \cos[x] = \sum_{n=-\infty}^{\infty} \frac{n}{\lambda_s} J_n(\lambda_s) \exp\{inx\}, \quad (\text{A.66})$$

$$\sum_{n=-\infty}^{\infty} J_n(\lambda_s) \exp\{inx\} \sin[x] = -i \sum_{n=-\infty}^{\infty} \frac{\partial}{\partial \lambda_s} J_n(\lambda_s) \exp\{inx\}, \quad (\text{A.67})$$

where $\lambda_s = k_\perp v_\perp / \Omega_s$ is the argument of the Bessel function J_n of the first kind. The later two identities can be proven with recursion relations. Now the exponential can be written,

$$\begin{aligned} & \exp\left\{-i \frac{k_\perp v_\perp}{\Omega_s} (\sin[v_\Phi] - \sin[v_\phi]) + i[k_\parallel v_\parallel - \omega(k_i)](t' - t)\right\} \\ &= \exp\{i[k_\parallel v_\parallel - \omega(k_i)](t' - t)\} \sum_{n,m=-\infty}^{\infty} J_m(\lambda_s) J_n(\lambda_s) \exp\{-inv_\Phi + imv_\phi\}, \end{aligned} \quad (\text{A.68})$$

giving the two relations,

$$\begin{aligned}
& \cos[v'_\Phi] \exp \left\{ -i \frac{k_\perp v_\perp}{\Omega_s} (\sin[v_\Phi] - \sin[v_\phi]) + i[k_\parallel v_\parallel - \omega(k_i)](t' - t) \right\} \\
&= \cos[-v'_\Phi] \exp \{ i[k_\parallel v_\parallel - \omega(k_i)](t' - t) \} \\
&\quad \times \sum_{n,m=-\infty}^{\infty} J_m(\lambda_s) J_n(\lambda_s) \exp \{ -i n v'_\Phi + i m v_\phi \} \\
&= \exp \{ i[k_\parallel v_\parallel - \omega(k_i)](t' - t) \} \\
&\quad \times \sum_{n,m=-\infty}^{\infty} \frac{n}{\lambda_s} J_m(\lambda_s) J_n(\lambda_s) \exp \{ -i n v'_\Phi + i m v_\phi \} \\
&= \sum_{n,m=-\infty}^{\infty} \frac{n}{\lambda_s} J_m(\lambda_s) J_n(\lambda_s) \exp \{ i(m-n)v_\phi \} \\
&\quad \times \exp \{ i[k_\parallel v_\parallel - \omega(k_i) + n\Omega_s](t' - t) \} \tag{A.69}
\end{aligned}$$

$$\begin{aligned}
& \sin[v'_\Phi] \exp \left\{ -i \frac{k_\perp v_\perp}{\Omega_s} (\sin[v'_\Phi] - \sin[v_\phi]) + i[k_\parallel v_\parallel - \omega(k_i)](t' - t) \right\} \\
&= -\sin[-v'_\Phi] \exp \{ i[k_\parallel v_\parallel - \omega(k_i)](t' - t) \} \\
&\quad \times \sum_{n,m=-\infty}^{\infty} J_m(\lambda_s) J_n(\lambda_s) \exp \{ -i n v'_\Phi + i m v_\phi \} \\
&= i \exp \{ i[k_\parallel v_\parallel - \omega(k_i)](t' - t) \} \\
&\quad \times \sum_{n,m=-\infty}^{\infty} J_m(\lambda_s) \frac{\partial}{\partial \lambda_s} J_n(\lambda_s) \exp \{ -i n v'_\Phi + i m v_\phi \} \\
&= i \sum_{n,m=-\infty}^{\infty} J_m(\lambda_s) \frac{\partial}{\partial \lambda_s} J_n(\lambda_s) \exp \{ i(m-n)v_\phi \} \\
&\quad \times \exp \{ i[k_\parallel v_\parallel - \omega(k_i) + n\Omega_s](t' - t) \} \tag{A.70}
\end{aligned}$$

where $v'_\Phi = -\Omega_s(t' - t) + v_\phi$ was used. Now Eq. A.61 can be rewritten with relations,

$$\begin{aligned}
\hat{f}_s &= -\frac{q_s}{m_s} \int_{-\infty}^t dt' \sum_{n,m=-\infty}^{\infty} J_m(\lambda_s) \exp \{ i(m-n)v_\phi \} \exp \{ i[k_\parallel v_\parallel - \omega(k_i) + n\Omega_s](t' - t) \} \\
&\quad \left[\hat{E}_x \frac{n}{\lambda_s} J_n(\lambda_s) \frac{\partial}{\partial \alpha_+} + i \hat{E}_y \frac{\partial}{\partial \lambda_s} J_n(\lambda_s) \frac{\partial}{\partial \alpha_+} + \hat{E}_z J_n(\lambda_s) \left(\frac{\partial}{\partial v_\parallel} + \frac{n}{\lambda_s} \frac{\partial}{\partial \beta_+} \right) \right] F_s. \tag{A.71}
\end{aligned}$$

Now only the only t' dependence is written explicitly! Consider the substitution $\tau = t' - t$ and use,

$$\begin{aligned} \frac{\partial}{\partial \tau} \exp\{i[k_{\parallel}v_{\parallel} - \omega(k_i) + n\Omega_s]\tau\} \\ = i[k_{\parallel}v_{\parallel} - \omega(k_i) + n\Omega_s] \exp\{i[k_{\parallel}v_{\parallel} - \omega(k_i) + n\Omega_s]\tau\}, \end{aligned} \quad (\text{A.72})$$

so that the integral in t' can be performed. Rearranging with product rule, the integral is simple. The initial condition is ignored $t' = -\infty$, as discussed earlier. The result is,

$$\begin{aligned} \hat{f}_s = -\frac{q_s}{m_s} \sum_{n,m=-\infty}^{\infty} \frac{J_m(\lambda_s) \exp\{i(m-n)v_{\phi}\}}{i[k_{\parallel}v_{\parallel} - \omega(k_i) + n\Omega_s]} \\ \times \left[\hat{E}_x \frac{n}{\lambda_s} J_n(\lambda_s) \frac{\partial}{\partial \alpha_+} + i \hat{E}_y \frac{\partial}{\partial \lambda_s} J_n(\lambda_s) \frac{\partial}{\partial \alpha_+} + \hat{E}_z J_n(\lambda_s) \left(\frac{\partial}{\partial v_{\parallel}} + \frac{n}{\lambda_s} \frac{\partial}{\partial \beta_+} \right) \right] F_s. \end{aligned} \quad (\text{A.73})$$

This is the general result for a small amplitude spatially homogeneous perturbation of the distribution function.

Appendix B

Derivation of kinetic magnetohydrodynamics and normal modes

B.1 Drift Kinetic Equation

The Boltzmann equation,

$$\left[\frac{\partial}{\partial t} + v_i \frac{\partial}{\partial x_i} + a_i^s(v_i; E_i(t, x_i), b_i(t, x_i)) \frac{\partial}{\partial v_i} \right] f_s(t, x_i, v_i) = \mathcal{C}[f_s(t, x_i, v_i)], \quad (\text{B.1})$$

and the acceleration vector $a_i^s(v_i; E_i(t, x_i), b_i(t, x_i))$,

$$a_i^s(v_i; E_i(t, x_i), b_i(t, x_i)) = \frac{q_s}{m_s} \left[E_i(t, x_i) + \epsilon_{ijk} \frac{v_j b_k(t, x_i)}{c} \right], \quad (\text{B.2})$$

where $E_i(t, x_i)$ is the electric field, $b_i(t, x_i)$ is the magnetic field, $\partial/\partial x_i$ is the partial derivative with respect to x_i -space, $\partial/\partial v_i$ is the partial derivative with respect to v_i -space, q_s is the species “ s ” charge, m_s is the species “ s ” mass and c is the speed of light. The species “ s ” distribution function is $f_s(t, x_i, v_i)$. The collisional operator is the single species (no interspecies drifts) Bhatnagar-Gross-Krook (BGK) operator so it takes on the form,

$$\mathcal{C}[f_s(t, x_i, v_i)] = -\nu_s [f_s(t, x_i, v_i) - F_s(v_i; n_s(t, x_i), u_i^s(t, x_i), T_s(t, x_i))], \quad (\text{B.3})$$

and $F_s(v_i; n_s(t, x_i), u_i^s(t, x_i), T_s(t, x_i))$ is the BGK equilibrium distribution function which we take to be the Maxwellian distribution function (Eq. B.52). This operator conserves particle number, momentum and energy.

B.1.1 Derivation of drift kinetic equation

Now all implicit dependence will be dropped. Start by writing out an infinitesimal change in the distribution function,

$$df_s = \frac{\partial f_s}{\partial t} dt + \frac{\partial f_s}{\partial x_i} dx_i + \frac{\partial f_s}{\partial v_i} dv_i, \quad (\text{B.4})$$

where no terms appear $\partial v_i / \partial t$ because they are zero. Just to be clear, if a derivative's argument appears in the fraction, that is the only argument, if it is open, the derivative carries to the right in a normal fashion. Now change variables $v_i \rightarrow w_i = v_i - u_i^s(t, x_i)$ where $u_i^s(t, x_i)$ can be any frame, yielding,

$$\begin{aligned} df_s &= \frac{\partial f_s}{\partial t} dt + \frac{\partial w_i}{\partial t} \frac{\partial f_s}{\partial w_i} dt \\ &\quad + \frac{\partial f_s}{\partial x_i} dx_i + \frac{\partial w_j}{\partial x_i} \frac{\partial f_s}{\partial w_j} dx_i \\ &\quad + \frac{\partial w_j}{\partial v_i} \frac{\partial f_s}{\partial w_j} dv_i, \end{aligned} \quad (\text{B.5})$$

where $\partial w_j / \partial v_i = \delta_{ij}$ and equivalence of the terms gives,

$$\begin{aligned} \frac{\partial}{\partial t} &\rightarrow \frac{\partial}{\partial t} - \frac{\partial u_i^s}{\partial t} \frac{\partial}{\partial w_i} \\ \frac{\partial}{\partial x_i} &\rightarrow \frac{\partial}{\partial x_i} - \frac{\partial u_j^s}{\partial x_i} \frac{\partial}{\partial w_j} \\ \frac{\partial}{\partial v_i} &\rightarrow \frac{\partial}{\partial w_i}. \end{aligned} \quad (\text{B.6})$$

The acceleration term,

$$a_i^s \frac{\partial}{\partial w_i} f_s = \frac{q_s}{m_s} \left[E_i + \epsilon_{ijk} \frac{(w_j + u_j^s) b_k}{c} \right] \frac{\partial}{\partial w_i} f_s, \quad (\text{B.7})$$

so rewriting the equation gives,

$$\begin{aligned} &\left\{ \frac{\partial}{\partial t} - \frac{\partial u_i^s}{\partial t} \frac{\partial}{\partial w_i} + (w_i + u_i^s) \frac{\partial}{\partial x_i} - (w_i + u_i^s) \frac{\partial u_j^s}{\partial x_i} \frac{\partial}{\partial w_j} \right. \\ &\quad \left. + \frac{q_s}{m_s} \left[E_i + \epsilon_{ijk} \frac{(w_j + u_j^s) b_k}{c} \right] \frac{\partial}{\partial w_i} \right\} f_s = \nu_s [f_s - F_s], \end{aligned} \quad (\text{B.8})$$

rearranging to separate terms,

$$\begin{aligned} &\left\{ \frac{\partial}{\partial t} - \left[\frac{\partial u_i^s}{\partial t} + u_j^s \frac{\partial u_i^s}{\partial x_j} - \frac{q_s}{c m_s} \epsilon_{ijk} u_j^s b_k \right] \frac{\partial}{\partial w_i} + (w_i + u_i^s) \frac{\partial}{\partial x_i} \right. \\ &\quad \left. + \left[\frac{q_s}{m_s} E_i + \frac{q_s}{c m_s} \epsilon_{ijk} w_j b_k - w_j \frac{\partial u_i^s}{\partial x_j} \right] \frac{\partial}{\partial w_i} \right\} f_s = \nu_s [f_s - F_s]. \end{aligned} \quad (\text{B.9})$$

The cylindrical coordinate system is introduced by defining $\hat{b} = b_i/|b_j|$, local (t, x_i) magnetic field direction. The norm is defined, $|\chi_i| = \sqrt{\chi_i^2}$. Any vector χ_i can be decomposed,

$$\chi_{\parallel} = \hat{b}_i \chi_i, \quad (\text{B.10})$$

$$\chi_{\perp} = |\chi_i - \chi_{\parallel} \hat{b}_i|. \quad (\text{B.11})$$

Now focus on the term,

$$\frac{q_s}{c m_s} \epsilon_{ijk} w_j b_k \frac{\partial}{\partial w_i} f_s, \quad (\text{B.12})$$

and write the peculiar velocity vector in cylindrical notation,

$$w_i = \delta_{ix} w_{\perp} \cos(w_{\phi}) + \delta_{iy} w_{\perp} \sin(w_{\phi}) + \delta_{iz} w_{\parallel}, \quad (\text{B.13})$$

where δ_{ix} is the unit vector in the x-direction of x_i -space. This gives,

$$\frac{q_s}{c m_s} \epsilon_{ijk} w_j b_k \frac{\partial}{\partial w_i} f_s = \frac{q_s}{c m_s} (\delta_{ix} b_z w_{\perp} \sin(w_{\phi}) - \delta_{iy} b_z w_{\perp} \cos(w_{\phi})) \frac{\partial}{\partial w_i} f_s, \quad (\text{B.14})$$

and notice that,

$$\frac{\partial w_x}{\partial w_{\phi}} = -w_{\perp} \sin(w_{\phi}), \quad \frac{\partial w_y}{\partial w_{\phi}} = w_{\perp} \cos(w_{\phi}), \quad \frac{\partial w_z}{\partial w_{\phi}} = 0 \quad (\text{B.15})$$

and with chain rule we find,

$$\frac{q_s}{c m_s} \epsilon_{ijk} w_j b_k \frac{\partial}{\partial w_i} f_s = -\frac{q_s b_z}{c m_s} \frac{\partial}{\partial w_{\phi}} f_s \quad (\text{B.16})$$

we now have,

$$\left\{ \frac{\partial}{\partial t} - \left[\frac{\partial u_i^s}{\partial t} + u_j^s \frac{\partial u_i^s}{\partial x_j} - \frac{q_s}{c m_s} \epsilon_{ijk} u_j^s b_k \right] \frac{\partial}{\partial w_i} + (w_i + u_i^s) \frac{\partial}{\partial x_i} \right. \\ \left. + \left[\frac{q_s}{m_s} E_i - w_j \frac{\partial u_i^s}{\partial x_j} \right] \frac{\partial}{\partial w_i} - \frac{q_s b_z}{c m_s} \frac{\partial}{\partial w_{\phi}} \right\} f_s = -\nu_s [f_s - F_s]. \quad (\text{B.17})$$

The $\partial/\partial w_{\phi}$ term is zero since the distribution function is assumed to be gyroscopic. Now the variables of w_i are changed to w, w_{\parallel} to simplify the gyro-angle average. The definitions

$$w = (w_i^2)^{1/2}, \quad w_{\parallel} = w_i \hat{b}_i, \quad \hat{b}_i = \frac{b_i}{(b_j^2)^{1/2}}, \quad w_{\perp,i} = w_j (\delta_{ij} - \hat{b}_i \hat{b}_j), \\ w_{\perp} = (w^2 - w_{\parallel}^2)^{1/2}, \quad w_i = \hat{b}_i w_{\parallel} + (\delta_{ij} - \hat{b}_i \hat{b}_j) w_j, \quad (\text{B.18})$$

are necessary. The change of variables looks like,

$$\begin{aligned} df_s &= \frac{\partial f_s}{\partial t} dt + \frac{\partial w_{||}}{\partial t} \frac{\partial f_s}{\partial w_{||}} dt, \\ &+ \frac{\partial f_s}{\partial x_i} dx_i + \frac{\partial w_{||}}{\partial x_i} \frac{\partial f_s}{\partial w_{||}} dx_i, \\ &+ \frac{\partial w_{||}}{\partial w_i} \frac{\partial f_s}{\partial w_{||}} dw_i + \frac{\partial w}{\partial w_i} \frac{\partial f_s}{\partial w} dw_i, \end{aligned} \quad (\text{B.19})$$

and so we have,

$$\frac{\partial f_s}{\partial t} \rightarrow \frac{\partial f_s}{\partial t} + w_i \frac{\partial \hat{b}_i}{\partial t} \frac{\partial f_s}{\partial w_{||}}, \quad (\text{B.20})$$

$$\frac{\partial f_s}{\partial x_i} \rightarrow \frac{\partial f_s}{\partial x_i} + w_j \frac{\partial \hat{b}_j}{\partial x_i} \frac{\partial f_s}{\partial w_{||}}, \quad (\text{B.21})$$

$$\frac{\partial f_s}{\partial w_i} \rightarrow \hat{b}_i \frac{\partial f_s}{\partial w_{||}} + \frac{w_i}{w} \frac{\partial f_s}{\partial w}, \quad (\text{B.22})$$

giving,

$$\left\{ \underbrace{\frac{\partial}{\partial t} + w_i \frac{\partial \hat{b}_i}{\partial t} \frac{\partial}{\partial w_{||}} - \left[\frac{\partial u_i^s}{\partial t} + u_j^s \frac{\partial u_i^s}{\partial x_j} - \frac{q_s}{c m_s} \epsilon_{ijk} u_j^s b_k \right]}_{\text{a}} \right. \\ \times \left(\hat{b}_i \frac{\partial}{\partial w_{||}} + \frac{w_i}{w} \frac{\partial}{\partial w} \right) + (w_i + u_i^s) \left(\frac{\partial}{\partial x_i} + w_j \frac{\partial \hat{b}_j}{\partial x_i} \frac{\partial}{\partial w_{||}} \right) \\ \left. + \left[\frac{q_s}{m_s} E_i - w_j \frac{\partial u_i^s}{\partial x_j} \right] \left(\hat{b}_i \frac{\partial}{\partial w_{||}} + \frac{w_i}{w} \frac{\partial}{\partial w} \right) \right\} f_s = -\nu_s [f_s - F_s]. \quad (\text{B.23})$$

Now we gyro-average the kinetic equation,

$$\begin{aligned} \frac{1}{2\pi} \int dw_\phi \left\{ \underbrace{\frac{\partial}{\partial t} + w_i \frac{\partial \hat{b}_i}{\partial t} \frac{\partial}{\partial w_{||}} - \left[\frac{\partial u_i^s}{\partial t} + u_j^s \frac{\partial u_i^s}{\partial x_j} - \frac{q_s}{c m_s} \epsilon_{ijk} u_j^s b_k \right]}_{\text{a}} \right. \\ \times \underbrace{\left(\hat{b}_i \frac{\partial}{\partial w_{||}} + \frac{w_i}{w} \frac{\partial}{\partial w} \right)}_{\text{b}} + \underbrace{(w_i + u_i^s) \left(\frac{\partial}{\partial x_i} + w_j \frac{\partial \hat{b}_j}{\partial x_i} \frac{\partial}{\partial w_{||}} \right)}_{\text{c}} + \underbrace{\left[\frac{q_s}{m_s} E_i - w_j \frac{\partial u_i^s}{\partial x_j} \right]}_{\text{d}} \underbrace{\left(\hat{b}_i \frac{\partial}{\partial w_{||}} + \frac{w_i}{w} \frac{\partial}{\partial w} \right)}_{\text{e}} \\ \left. + \underbrace{\left(\hat{b}_i \frac{\partial}{\partial w_{||}} + \frac{w_i}{w} \frac{\partial}{\partial w} \right)}_{\text{b}} \right\} f_s = -\underbrace{\nu_s \frac{1}{2\pi} \int dw_\phi [f_s - F_s]}_{\text{f}}. \end{aligned} \quad (\text{B.24})$$

Term “a” in completeness for later use,

$$\begin{aligned}
\frac{1}{2\pi} \int dw_\phi w_i \frac{\partial \hat{b}_i}{\partial t} \frac{\partial}{\partial w_\parallel} f_s &= \frac{1}{2\pi} \frac{\partial \hat{b}_i}{\partial t} \frac{\partial f_s}{\partial w_\parallel} \int dw_\phi w_i \\
&= \frac{1}{2\pi} \frac{\partial \hat{b}_i}{\partial t} \frac{\partial f_s}{\partial w_\parallel} \int dw_\phi (\delta_{ix} w_\perp \cos(w_\phi) + \delta_{iy} w_\perp \sin(w_\phi) + \delta_{iz} w_\parallel) \\
&= \frac{\partial \hat{b}_i}{\partial t} \frac{\partial f_s}{\partial w_\parallel} \delta_{iz} w_\parallel,
\end{aligned} \tag{B.25}$$

where the trigonometric functions integrate to zero, and the z-component gives 2π , noting from the definition of $w_i \delta_{iz} = w_\parallel = w_i \hat{b}_i$ identifies $\delta_{iz} = \hat{b}_i$. Equation B.25 will be referenced to show the gyro-average over w_i . Rearranging,

$$\frac{1}{2\pi} \int dw_\phi w_i \frac{\partial \hat{b}_i}{\partial t} \frac{\partial}{\partial w_\parallel} f_s = \frac{1}{2} \frac{\partial \hat{b}_i^2}{\partial t} w_\parallel \frac{\partial f_s}{\partial w_\parallel} = 0, \tag{B.26}$$

since $\hat{b}_i^2 = \text{const}$. Term “b”,

$$\frac{1}{2\pi} \int dw_\phi \left(\hat{b}_i \frac{\partial}{\partial w_\parallel} + \frac{w_i}{w} \frac{\partial}{\partial w} \right) f_s = \hat{b}_i \left(\frac{\partial}{\partial w_\parallel} + \frac{w_\parallel}{w} \frac{\partial}{\partial w} \right) f_s. \tag{B.27}$$

Term “c”,

$$\begin{aligned}
&\frac{1}{2\pi} \int dw_\phi (w_i + u_i^s) \left(\frac{\partial}{\partial x_i} + w_j \frac{\partial \hat{b}_j}{\partial x_i} \frac{\partial}{\partial w_\parallel} \right) f_s \\
&= \frac{1}{2\pi} \int dw_\phi \left(w_i \frac{\partial}{\partial x_i} + w_i w_j \frac{\partial \hat{b}_j}{\partial x_i} \frac{\partial}{\partial w_\parallel} + u_i^s \frac{\partial}{\partial x_i} + u_i^s w_j \frac{\partial \hat{b}_j}{\partial x_i} \frac{\partial}{\partial w_\parallel} \right) f_s.
\end{aligned} \tag{B.28}$$

The integration in the first and fourth terms are just like Eq. B.25 and the third term is ignorant to the integral giving,

$$\begin{aligned}
&\frac{1}{2\pi} \int dw_\phi (w_i + u_i^s) \left(\frac{\partial}{\partial x_i} + w_j \frac{\partial \hat{b}_j}{\partial x_i} \frac{\partial}{\partial w_\parallel} \right) f_s \\
&= \hat{b}_i w_\parallel \frac{\partial}{\partial x_i} f_s + \frac{1}{2\pi} \frac{\partial \hat{b}_j}{\partial x_i} \frac{\partial f_s}{\partial w_\parallel} \int dw_\phi w_i w_j + u_i^s \frac{\partial}{\partial x_i} f_s + \frac{1}{2} u_i^s w_\parallel \frac{\partial \hat{b}_j^2}{\partial x_i} \frac{\partial}{\partial w_\parallel} f_s,
\end{aligned} \tag{B.29}$$

The fourth term is zero since $\hat{b}_i^2 = \text{const}$. The second term with the tensor $w_i w_j$,

$$\begin{aligned} \frac{1}{2\pi} \int dw_\phi w_i w_j &= \frac{1}{2\pi} \int dw_\phi \left[\delta_{ix} w_\perp \cos(w_\phi) + \delta_{iy} w_\perp \sin(w_\phi) + \delta_{iz} w_\parallel \right] \\ &\quad \times \left[\delta_{jx} w_\perp \cos(w_\phi) + \delta_{jy} w_\perp \sin(w_\phi) + \delta_{jz} w_\parallel \right] \\ &= \frac{1}{2\pi} \int dw_\phi \left\{ \delta_{ix} w_\perp \cos(w_\phi) \left[\delta_{jx} w_\perp \cos(w_\phi) + \delta_{jy} w_\perp \sin(w_\phi) + \delta_{jz} w_\parallel \right] \right. \\ &\quad + \delta_{iy} w_\perp \sin(w_\phi) \left[\delta_{jx} w_\perp \cos(w_\phi) + \delta_{jy} w_\perp \sin(w_\phi) + \delta_{jz} w_\parallel \right] \\ &\quad \left. + \delta_{iz} w_\parallel \left[\delta_{jx} w_\perp \cos(w_\phi) + \delta_{jy} w_\perp \sin(w_\phi) + \delta_{jz} w_\parallel \right] \right\}, \quad (\text{B.30}) \end{aligned}$$

any term that is left with a single trigonometric function or the product $\sin(w_\phi) \cos(w_\phi)$ will integrate to zero,

$$\frac{1}{2\pi} \int dw_\phi w_i w_j = \frac{1}{2\pi} \int dw_\phi (\delta_{ix} \delta_{jx} w_\perp^2 \cos^2(w_\phi) + \delta_{iy} \delta_{jy} w_\perp^2 \sin^2(w_\phi) + \delta_{iz} \delta_{jz} w_\parallel^2), \quad (\text{B.31})$$

where the squared trigonometric functions both give π after the integral and using $\delta_{ix} \delta_{jx} + \delta_{iy} \delta_{jy} = \delta_{ij} - \delta_{iz} \delta_{jz}$ reveals,

$$\frac{1}{2\pi} \int dw_\phi w_i w_j = \frac{1}{2} w_\perp^2 (\delta_{ij} - \hat{b}_i \hat{b}_j) + \hat{b}_i \hat{b}_j w_\parallel^2. \quad (\text{B.32})$$

Now returning to the term in Eq. B.29,

$$\frac{1}{2\pi} \frac{\partial \hat{b}_j}{\partial x_i} \frac{\partial f_s}{\partial w_\parallel} \int dw_\phi w_i w_j = \frac{\partial \hat{b}_j}{\partial x_i} \frac{\partial f_s}{\partial w_\parallel} \left[\frac{1}{2} w_\perp^2 (\delta_{ij} - \hat{b}_i \hat{b}_j) + \hat{b}_i \hat{b}_j w_\parallel^2 \right] \quad (\text{B.33})$$

where any term that is $\hat{b}_j \partial \hat{b}_j / \partial x_i = 0$, since $\hat{b}_j^2 = \text{const}$. Finally, Eq. B.29 simplifies,

$$\begin{aligned} \frac{1}{2\pi} \int dw_\phi (w_i + u_i^s) \left(\frac{\partial}{\partial x_i} + w_j \frac{\partial \hat{b}_j}{\partial x_i} \frac{\partial}{\partial w_\parallel} \right) f_s \\ = \left(\hat{b}_i w_\parallel \frac{\partial}{\partial x_i} + u_i^s \frac{\partial}{\partial x_i} + \frac{w_\perp^2}{2} \frac{\partial \hat{b}_i}{\partial x_i} \frac{\partial}{\partial w_\parallel} \right) f_s. \quad (\text{B.34}) \end{aligned}$$

The term “d” \times “b” gives,

$$\frac{q_s}{m_s} E_i \hat{b}_i \left(\frac{\partial}{\partial w_\parallel} + \frac{w_\parallel}{w} \frac{\partial}{\partial w} \right) f_s = \frac{q_s}{m_s} E_\parallel \left(\frac{\partial}{\partial w_\parallel} + \frac{w_\parallel}{w} \frac{\partial}{\partial w} \right) f_s. \quad (\text{B.35})$$

The term “e” × “b”,

$$\begin{aligned}
& -\frac{1}{2\pi} \int dw_\phi w_j \frac{\partial u_i^s}{\partial x_j} \left(\hat{b}_i \frac{\partial}{\partial w_\parallel} + \frac{w_i}{w} \frac{\partial}{\partial w} \right) f_s \\
& = -w_\parallel \hat{b}_i \hat{b}_j \frac{\partial u_i^s}{\partial x_j} \frac{\partial f_s}{\partial w_\parallel} - \frac{\partial u_i^s}{\partial x_j} \frac{1}{w} \frac{\partial f_s}{\partial w} \frac{1}{2\pi} \int dw_\phi w_i w_j \\
& = -w_\parallel \hat{b}_i \hat{b}_j \frac{\partial u_i^s}{\partial x_j} \frac{\partial f_s}{\partial w_\parallel} - \frac{\partial u_i^s}{\partial x_j} \frac{1}{w} \frac{\partial f_s}{\partial w} \left(\frac{1}{2} w_\perp^2 (\delta_{ij} - \hat{b}_i \hat{b}_j) + \hat{b}_i \hat{b}_j w_\parallel^2 \right), \quad (\text{B.36})
\end{aligned}$$

where the first equal sign uses the result from Eq. B.29, and for the second equal sign the result on the tensor $w_i w_j$ from Eq. B.32 is used. The last term “f”,

$$-\nu_s \frac{1}{2\pi} \int dw_\phi [f_s - F_s] = -\nu_s [f_s - F_s], \quad (\text{B.37})$$

is ignorant to the gyro-average since both the perturbation and equilibrium F_s are gyrotropic.

Collecting all of the terms,

$$\begin{aligned}
& \left\{ \frac{\partial}{\partial t} - \left[\frac{\partial u_i^s}{\partial t} + u_j^s \frac{\partial u_i^s}{\partial x_j} - \underbrace{\frac{q_s}{cm_s} \epsilon_{ijk} u_j^s b_k}_{\text{g}} \right] \hat{b}_i \left(\frac{\partial}{\partial w_\parallel} + \frac{w_\parallel}{w} \frac{\partial}{\partial w} \right) \right. \\
& + \left(\hat{b}_i w_\parallel \frac{\partial}{\partial x_i} + u_i^s \frac{\partial}{\partial x_i} + \frac{w_\perp^2}{2} \frac{\partial \hat{b}_i}{\partial x_i} \frac{\partial}{\partial w_\parallel} \right) + \frac{q_s}{m_s} E_\parallel \left(\frac{\partial}{\partial w_\parallel} + \frac{w_\parallel}{w} \frac{\partial}{\partial w} \right) \\
& \left. - w_\parallel \hat{b}_i \hat{b}_j \frac{\partial u_i^s}{\partial x_j} \frac{\partial}{\partial w_\parallel} - \frac{\partial u_i^s}{\partial x_j} \left(\frac{1}{2} w_\perp^2 (\delta_{ij} - \hat{b}_i \hat{b}_j) + \hat{b}_i \hat{b}_j w_\parallel^2 \right) \frac{1}{w} \frac{\partial}{\partial w} \right\} f_s \\
& = -\nu_s [f_s - F_s]. \quad (\text{B.38})
\end{aligned}$$

Term “g” is zero because \hat{b}_i is orthogonal to $\epsilon_{ijk} u_j^s b_k$. The equation can then be rearranged to produce,

$$\begin{aligned}
& \left\{ \frac{\partial}{\partial t} + (\hat{b}_i w_\parallel + u_i^s) \frac{\partial}{\partial x_i} + \frac{w_\perp^2}{2} \frac{\partial \hat{b}_i}{\partial x_i} \frac{\partial}{\partial w_\parallel} \right. \\
& + \left[\frac{q_s}{m_s} E_\parallel - \hat{b}_i \left(\frac{\partial u_i^s}{\partial t} + u_j^s \frac{\partial u_i^s}{\partial x_j} \right) \right] \left(\frac{\partial}{\partial w_\parallel} + \frac{w_\parallel}{w} \frac{\partial}{\partial w} \right) \\
& \left. - \frac{w_\perp^2}{2w} \frac{\partial u_i^s}{\partial x_i} \frac{\partial}{\partial w} + \hat{b}_i \hat{b}_j \frac{\partial u_i^s}{\partial x_j} \left[\left(\frac{w_\perp^2}{2} - w_\parallel^2 \right) \frac{1}{w} \frac{\partial}{\partial w} - w_\parallel \frac{\partial}{\partial w_\parallel} \right] \right\} f_s \\
& = -\nu_s [f_s - F_s] \quad (\text{B.39})
\end{aligned}$$

This is the form of the drift kinetic equation studied in this thesis. This derivation emphasized the non-reduced version so F_s can be a gyrotropic equilibrium

distribution function that is a function of space and time. Other versions of this equation can be produced by transforming variables to w_\perp , w_\parallel or $w_\perp^2/2|b_i|$, w_\parallel .

B.1.2 Linearization

This section shows the linearization Eq. B.39. The perturbations are,

$$\begin{aligned}
b_i &= b'_i + b_0 \hat{b}_i, \\
E_\parallel &= E'_\parallel, \\
u_i^s &= u_i^{s'}, \\
f_s &= f'_s + F_s^0, \\
F_s^0 &= n_{s,0} \left(\frac{m_s}{2\pi k_B T_{s,0}} \right)^{3/2} \exp \left\{ -\frac{m_s}{2k_B T_{s,0}} v^2 \right\}, \\
n_s &= n_{0,s} + n'_s \rightarrow n^s + n'_s, \\
p_\perp &= p_{\perp,0}^s + p_{\perp}^{s,\prime} \rightarrow p_\perp^s + p_\perp^{s,\prime}, \\
p_\parallel &= p_{\parallel,0}^s + p_\parallel^{s,\prime} \rightarrow p_\parallel^s + p_\parallel^{s,\prime},
\end{aligned} \tag{B.40}$$

where the primed variables are the fluctuations about the unprimed variables (static background). The distribution function f_s is perturbed about a static Maxwellian F_s^0 and the equilibrium distribution function used in the BGK operator F_s is the local Maxwellian, so n_s , u_i^s , T_s are perturbed.

Some useful calculations,

$$\hat{b}_i = \frac{b'_i + b_0 \delta_{\parallel i}}{\sqrt{(b'_i + b_0 \delta_{\parallel i})^2}} \stackrel{0\text{th}}{=} \frac{2b_0 \delta_{\parallel i}}{\sqrt{(2b_0 \delta_{\parallel i})^2}} = \frac{\delta_{\parallel i}}{\sqrt{\delta_{\parallel i} \delta_{\parallel i}}} = \delta_{\parallel i}, \tag{B.41}$$

$$\frac{\partial}{\partial x_i} \hat{b}_i = -\frac{\hat{b}_i \hat{b}_l}{\sqrt{b_k^2}} \frac{\partial}{\partial x_i} b_l \stackrel{1\text{st}}{=} -\frac{1}{|b_0|} \frac{\partial}{\partial x_\parallel} b'_\parallel, \tag{B.42}$$

$$\frac{\partial}{\partial x_j} \hat{b}_i = \frac{1}{|b_l|} \left[\frac{\partial}{\partial x_j} b_i - \hat{b}_i \hat{b}_l \frac{\partial}{\partial x_j} b_l \right] \stackrel{1\text{st}}{=} \frac{1}{|b_0|} \left[\frac{\partial}{\partial x_j} b'_i - \delta_{\parallel i} \frac{\partial}{\partial x_j} b'_\parallel \right], \tag{B.43}$$

where $\delta_{\parallel i}$ is unit vector pointing in the direction of the background magnetic field, and the text “0th”, of above the equal signs means “to the zeroth order”

and similarly for “1st”. Rewriting the kinetic equation with labels,

$$\begin{aligned}
& \underbrace{\frac{\partial}{\partial t} f_s + \left(u_i^s + w_{\parallel} \hat{b}_i \right) \frac{\partial}{\partial x_i} f_s}_{\text{A}} + \underbrace{\frac{w_{\perp}^2}{2} \frac{\partial \hat{b}_i}{\partial x_i} \frac{\partial}{\partial w_{\parallel}} f_s}_{\text{B}} \\
& + \underbrace{\left[\frac{q_s}{m_s} E_{\parallel} - \hat{b}_i \left(\frac{\partial u_i^s}{\partial t} + u_j^s \frac{\partial u_i^s}{\partial x_j} \right) \right]}_{\text{C}} \underbrace{\left[\frac{w_{\parallel}}{w} \frac{\partial}{\partial w} f_s + \frac{\partial}{\partial w_{\parallel}} f_s \right]}_{\text{E}} \\
& - \underbrace{\frac{\partial u_i^s}{\partial x_i} \frac{w_{\perp}^2}{2w} \frac{\partial}{\partial w} f_s}_{\text{F}} + \underbrace{\hat{b}_i \hat{b}_j \frac{\partial u_i^s}{\partial x_j}}_{\text{G}} \underbrace{\left[\left(\frac{w_{\perp}^2}{2} - w_{\parallel}^2 \right) \frac{1}{w} \frac{\partial}{\partial w} f_s - w_{\parallel} \frac{\partial}{\partial w_{\parallel}} f_s \right]}_{\text{H}} \\
& = \underbrace{-\nu_s (f_s - F_s)}_{\text{J}}. \tag{B.44}
\end{aligned}$$

Now use the perturbations from Eqs. B.40 for the linearization. Part A,

$$\frac{\partial}{\partial t} f_s + (u_i^s + w_{\parallel} \hat{b}_i) \frac{\partial}{\partial x_i} f_s \stackrel{\text{1st}}{=} \frac{\partial}{\partial t} f'_s + w_{\parallel} \frac{\partial}{\partial x_{\parallel}} f'_s. \tag{B.45}$$

Part B,

$$\frac{w_{\perp}^2}{2} \frac{\partial \hat{b}_i}{\partial x_i} \frac{\partial}{\partial w_{\parallel}} f_s \stackrel{\text{1st}}{=} -\frac{w_{\perp}^2}{2|b_0|} \frac{\partial b'_{\parallel}}{\partial x_{\parallel}} \frac{\partial}{\partial w_{\parallel}} F_s^0. \tag{B.46}$$

Part C \times E,

$$\frac{q_s}{m_s} E_{\parallel} \left[\frac{w_{\parallel}}{w} \frac{\partial}{\partial w} f_s + \frac{\partial}{\partial w_{\parallel}} f_s \right] \stackrel{\text{1st}}{=} \frac{q_s}{m_s} E'_{\parallel} \left[\frac{w_{\parallel}}{w} \frac{\partial}{\partial w} F_s^0 + \frac{\partial}{\partial w_{\parallel}} F_s^0 \right]. \tag{B.47}$$

Part D \times E,

$$\hat{b}_i \left(\frac{\partial u_i^s}{\partial t} + u_j^s \frac{\partial u_i^s}{\partial x_j} \right) \left[\frac{w_{\parallel}}{w} \frac{\partial}{\partial w} f_s + \frac{\partial}{\partial w_{\parallel}} f_s \right] \stackrel{\text{1st}}{=} \frac{\partial u_{\parallel}^{s'}}{\partial t} \left[\frac{w_{\parallel}}{w} \frac{\partial}{\partial w} F_s^0 + \frac{\partial}{\partial w_{\parallel}} F_s^0 \right]. \tag{B.48}$$

Part F,

$$\frac{\partial u_i^s}{\partial x_i} \frac{w_{\perp}^2}{2w} \frac{\partial}{\partial w} f_s \stackrel{\text{1st}}{=} \frac{\partial u_i^{s'}}{\partial x_i} \frac{w_{\perp}^2}{2w} \frac{\partial}{\partial w} F_s^0. \tag{B.49}$$

Part G \times H,

$$\hat{b}_i \hat{b}_j \frac{\partial u_i^s}{\partial x_j} \left(\frac{w_{\perp}^2}{2} - w_{\parallel}^2 \right) \frac{1}{w} \frac{\partial}{\partial w} f_s \stackrel{\text{1st}}{=} \frac{\partial u_{\parallel}^{s'}}{\partial x_{\parallel}} \left(\frac{w_{\perp}^2}{2} - w_{\parallel}^2 \right) \frac{1}{w} \frac{\partial}{\partial w} F_s^0. \tag{B.50}$$

Part G \times I,

$$\hat{b}_i \hat{b}_j \frac{\partial u_i^s}{\partial x_j} w_{\parallel} \frac{\partial}{\partial w_{\parallel}} f_s \stackrel{1st}{=} \frac{\partial u_{\parallel}^{s'}}{\partial x_{\parallel}} w_{\parallel} \frac{\partial}{\partial w_{\parallel}} F_s^0 \quad (\text{B.51})$$

Last, part J, requires linearization of the equilibrium distribution function, the Maxwellian distribution function,

$$F_s = n_s \left(\frac{m_s}{2\pi k_B T_s} \right)^{3/2} \exp \left\{ - \frac{m_s}{2k_B T_s} w^2 \right\}. \quad (\text{B.52})$$

Quantities $n_s, u_{\parallel}^s, T_s$ need to be perturbed, but it is more simple to perturb $n_s, u_{\parallel}^s, p_s$ where $p_s = n_s k_B T_s$ so that,

$$p'_s = k_B (n'_s T_s + n_s T'_s). \quad (\text{B.53})$$

First rewrite the distribution function,

$$F_s = n_s^{5/2} \left(\frac{m_s}{2\pi p_s} \right)^{3/2} \exp \left\{ - \frac{m_s n_s}{2p_s} w^2 \right\}, \quad (\text{B.54})$$

and to be clear at zeroth order $u_{\parallel} = 0$ since this is the parallel component of the frame we have changed to. Start by writing the partial derivatives,

$$\frac{\partial}{\partial n_s} F_s = \frac{F_s}{n_s} \left[\frac{5}{2} - \frac{m_s n_s}{2p_s} w \right], \quad (\text{B.55})$$

$$\frac{\partial}{\partial p_s} F_s = \frac{F_s}{p_s} \left[\frac{m_s n_s}{2p_s} w^2 - \frac{3}{2} \right], \quad (\text{B.56})$$

so the perturbation appears,

$$F_s \stackrel{1st}{=} F_s^0 \left\{ \frac{n'_s}{n_s} \left[\frac{5}{2} - \frac{m_s n_s}{2p_s} w^2 \right] + \frac{p'_s}{p_s} \left[\frac{m_s n_s}{2p_s} w^2 - \frac{3}{2} \right] \right\}, \quad (\text{B.57})$$

where F_s^0 is now set to 0th order in the perturbation. Writing part J,

$$\left[\frac{\partial}{\partial t} f_s \right]_C \stackrel{1st}{=} -\nu_s f'_s + \nu_s F_s^0 \left\{ \frac{n'_s}{n_s} \left[\frac{5}{2} - \frac{m_s n_s}{2p_s} w^2 \right] + \frac{p'_s}{p_s} \left[\frac{m_s n_s}{2p_s} w^2 - \frac{3}{2} \right] \right\}. \quad (\text{B.58})$$

Collecting all the terms we have,

$$\begin{aligned}
& \frac{\partial}{\partial t} f'_s + w_{\parallel} \frac{\partial}{\partial x_{\parallel}} f'_s - \frac{w_{\perp}^2}{2|b_0|} \frac{\partial b'_{\parallel}}{\partial x_{\parallel}} \frac{\partial}{\partial w_{\parallel}} F_s^0 + \frac{q_s}{m_s} E'_{\parallel} \left[\frac{w_{\parallel}}{w} \frac{\partial}{\partial w} F_s^0 + \frac{\partial}{\partial w_{\parallel}} F_s \right] \\
& - \frac{\partial u_{\parallel}^{s'}}{\partial t} \left[\frac{w_{\parallel}}{w} \frac{\partial}{\partial w} F_s^0 + \frac{\partial}{\partial w_{\parallel}} F_s^0 \right] - \frac{\partial u_i^{s'}}{\partial x_i} \frac{w_{\perp}^2}{2w} \frac{\partial}{\partial w} F_s^0 \\
& + \frac{\partial u_{\parallel}^{s'}}{\partial x_{\parallel}} \left(\frac{w_{\perp}^2}{2} - w_{\parallel}^2 \right) \frac{1}{w} \frac{\partial}{\partial w} F_s^0 - \frac{\partial u_{\parallel}^{s'}}{\partial x_{\parallel}} w_{\parallel} \frac{\partial}{\partial w_{\parallel}} F_s^0 \\
& = -\nu_s f'_s + \nu_s F_s^0 \left\{ \frac{n'_s}{n_s} \left[\frac{5}{2} - \frac{m_s n_s}{2p_s} w^2 \right] + \frac{p'_s}{p_s} \left[\frac{m_s n_s}{2p_s} w^2 - \frac{3}{2} \right] \right\}. \quad (\text{B.59})
\end{aligned}$$

This is the full linearised drift kinetic equation.

B.1.3 Fourier analysis

Using the Fourier ansatz,

$$\begin{aligned}
f'_s(x_{\perp}, x_{\parallel}, v_{\parallel}, v, t) &= \tilde{f}_s(v_{\parallel}, v) \exp\{i(k_{\perp}x_{\perp} + k_{\parallel}x_{\parallel} - \omega t)\}, \\
b'_i(x_{\perp}, x_{\parallel}, t) &= \tilde{b}_i \exp\{i(k_{\perp}x_{\perp} + k_{\parallel}x_{\parallel} - \omega t)\}, \\
u'_i(x_{\perp}, x_{\parallel}, t) &= \tilde{u}_i \exp\{i(k_{\perp}x_{\perp} + k_{\parallel}x_{\parallel} - \omega t)\}, \\
E'_{\parallel}(x_{\perp}, x_{\parallel}, t) &= \tilde{E}_{\parallel} \exp\{i(k_{\perp}x_{\perp} + k_{\parallel}x_{\parallel} - \omega t)\}, \\
\tilde{n}_s(x_{\perp}, x_{\parallel}, t) &= \int d^3w \tilde{f}_s(w_{\parallel}, w, t) \\
&= n'_s(x_{\perp}, x_{\parallel}, t) \exp\{i(-k_{\perp}x_{\perp} - k_{\parallel}x_{\parallel} + \omega t)\}, \\
\tilde{p}_{\perp}^s(x_{\perp}, x_{\parallel}, t) &= \frac{m_s}{2} \int d^3w w_{\perp}^2 \tilde{f}_s(w_{\parallel}, w, t) \\
&= p_{\perp}^{s'}(x_{\perp}, x_{\parallel}, t) \exp\{i(-k_{\perp}x_{\perp} - k_{\parallel}x_{\parallel} + \omega t)\}, \\
\tilde{p}_{\parallel}^s(x_{\perp}, x_{\parallel}, t) &= m_s \int d^3w w_{\parallel}^2 \tilde{f}_s(w_{\parallel}, w, t) \\
&= p_{\parallel}^{s'}(x_{\perp}, x_{\parallel}, t) \exp\{i(-k_{\perp}x_{\perp} - k_{\parallel}x_{\parallel} + \omega t)\}, \quad (\text{B.60})
\end{aligned}$$

where k_{\perp} , k_{\parallel} are the perpendicular, parallel wavenumbers and ω is the complex frequency. Making the Fourier ansatz here is appropriate to asymptotic solutions since it ignores the ballistic response, see Section 8.5 of Krall and Trivelpiece [1973]. Applying this ansatz,

$$\frac{\partial}{\partial t} \rightarrow -i\omega, \quad \frac{\partial}{\partial x_{\parallel}} \rightarrow ik_{\parallel}, \quad \frac{\partial}{\partial x_{\perp}} \rightarrow ik_{\perp}, \quad (\text{B.61})$$

to the linearized kinetic equation (Eq. B.59) leads to,

$$\begin{aligned} -i\omega \tilde{f}_s + ik_{\parallel} w_{\parallel} \tilde{f}_s - \frac{m_s n_s}{p_s} w_{\parallel} F_s \left(\frac{q_s}{m_s} \tilde{E}_{\parallel} + i\omega \tilde{u}_{\parallel}^s \right) \\ + i \frac{m_s n_s}{p_s} F_s \left(\frac{w_{\perp}^2}{2} \omega \frac{\tilde{b}_{\parallel}}{b_0} + k_{\parallel} w_{\parallel}^2 \tilde{u}_{\parallel}^s \right) = -\nu_s \tilde{f}_s \\ + \nu_s F_s \left\{ \frac{\tilde{n}_s}{n_s} \left[\frac{5}{2} - \frac{m_s n_s}{2p_s} w^2 \right] + \frac{\tilde{p}_s}{p_s} \left[\frac{m_s n_s}{2p_s} w^2 - \frac{3}{2} \right] \right\}, \end{aligned} \quad (\text{B.62})$$

where Eq. B.122 is used to replace \tilde{u}_{\perp} with \tilde{b}_{\parallel} . Reorganising the equation slightly,

$$\begin{aligned} -i\omega \tilde{f}_s + ik_{\parallel} w_{\parallel} \tilde{f}_s - \frac{n_s q_s}{p_s} \tilde{E}_{\parallel} w_{\parallel} F_s - i\omega \frac{m_s n_s}{p_s} \frac{\tilde{b}_{\parallel}}{b_0} F_s \frac{w_{\perp}^2}{2} \\ + \frac{i m_s n_s}{p_s} w_{\parallel} \tilde{u}_{\parallel}^s (k_{\parallel} w_{\parallel} - \omega) F_s = -\nu_s \tilde{f}_s \\ + \nu_s F_s \left\{ \frac{\tilde{n}_s}{n_s} \left[\frac{5}{2} - \frac{m_s n_s}{2p_s} w^2 \right] + \frac{\tilde{p}_s}{p_s} \left[\frac{m_s n_s}{2p_s} w^2 - \frac{3}{2} \right] \right\}, \end{aligned} \quad (\text{B.63})$$

now modify the \tilde{u}_{\parallel} term to ease the manipulations, solving for the Fourier amplitude of the perturbed distribution function,

$$\begin{aligned} \tilde{f}_s = \frac{1}{i(-\omega + k_{\parallel} w_{\parallel} - i\nu_s)} & \left(\frac{n_s q_s}{p_s} \tilde{E}_{\parallel} w_{\parallel} F_s - i\omega \frac{m_s n_s}{p_s} \frac{\tilde{b}_{\parallel}}{b_0} F_s \frac{w_{\perp}^2}{2} \right) \\ & - \frac{k_{\parallel} w_{\parallel} - \omega - i\nu_s + i\nu_s}{i(-\omega + k_{\parallel} w_{\parallel} - i\nu_s)} \frac{i m_s n_s}{p_s} w_{\parallel} \tilde{u}_{\parallel}^s F_s \\ & + \frac{\nu_s}{i(-\omega + k_{\parallel} w_{\parallel} - i\nu_s)} F_s \left\{ \frac{\tilde{n}_s}{n_s} \left[\frac{5}{2} - \frac{m_s n_s}{2p_s} w^2 \right] + \frac{\tilde{p}_s}{p_s} \left[\frac{m_s n_s}{2p_s} w^2 - \frac{3}{2} \right] \right\}. \end{aligned} \quad (\text{B.64})$$

Now working the \tilde{u}_{\parallel} term for convenience,

$$\begin{aligned} \tilde{f}_s = \frac{1}{i(-\omega + k_{\parallel} w_{\parallel} - i\nu_s)} & \left(\frac{n_s q_s}{p_s} \tilde{E}_{\parallel} w_{\parallel} F_s - i\omega \frac{m_s n_s}{p_s} \frac{\tilde{b}_{\parallel}}{b_0} F_s \frac{w_{\perp}^2}{2} \right) \\ & - \frac{i\nu_s}{(-\omega + k_{\parallel} w_{\parallel} - i\nu_s)} \frac{m_s n_s}{p_s} w_{\parallel} \tilde{u}_{\parallel}^s F_s - \frac{m_s n_s}{p_s} w_{\parallel} \tilde{u}_{\parallel}^s F_s \\ & + \frac{\nu_s}{i(-\omega + k_{\parallel} w_{\parallel} - i\nu_s)} F_s \left\{ \frac{\tilde{n}_s}{n_s} \left[\frac{5}{2} - \frac{m_s n_s}{2p_s} w^2 \right] + \frac{\tilde{p}_s}{p_s} \left[\frac{m_s n_s}{2p_s} w^2 - \frac{3}{2} \right] \right\}, \end{aligned} \quad (\text{B.65})$$

and now we can determine $\tilde{p}_{\perp}^s, \tilde{p}_{\parallel}^s, \tilde{n}^s$ with the respective moments.

B.1.4 Moments of the kinetic equation

At this point, changing variables from $w, w_{\parallel} \rightarrow w_{\perp}, w_{\parallel}$ is fine since no derivatives appear, and then moments can be taken for \tilde{p}_{\perp}^s . The velocity space integral is,

$$\int_{\tau(\mathbf{w})} d^3w = 2\pi \int_0^\infty dw_{\perp} \int_{-\infty}^\infty dw_{\parallel}, \quad (\text{B.66})$$

and to put the integrals in the form of the plasma dispersion function we will make the substitution,

$$u = \sqrt{\frac{m_s n_s}{2p_s}} w_{\parallel} \Rightarrow dw_{\parallel} = du \sqrt{\frac{2p_s}{m_s n_s}}, \quad (\text{B.67})$$

and limits $\pm\infty$. The argument of the plasma dispersion function will be,

$$\zeta_s = \sqrt{\frac{m_s n_s}{2p_s}} \frac{1}{|k_{\parallel}|} (\omega + i\nu_s). \quad (\text{B.68})$$

more on this can be found in Appendix B.5. The important integrals have been worked out in Appendix B.6.

B.1.4.1 Density moment

The density moment,

$$\begin{aligned} \tilde{n}_s &= \int_{\tau(\mathbf{w})} d^3w \tilde{f}_s = \int_{\tau(\mathbf{w})} d^3w \left\{ \frac{1}{i(-\omega + k_{\parallel} w_{\parallel} - i\nu_s)} \right. \\ &\quad \times \left(\frac{n_s q_s}{p_s} \tilde{E}_{\parallel} w_{\parallel} F_s - i\omega \frac{m_s n_s}{p_s} \frac{\tilde{b}_{\parallel}}{b_0} F_s \frac{w_{\perp}^2}{2} \right) \\ &\quad - \frac{i\nu_s}{(-\omega + k_{\parallel} w_{\parallel} - i\nu_s)} \frac{m_s n_s}{p_s} w_{\parallel} \tilde{u}_{\parallel}^s F_s - \frac{m_s n_s}{p_s} w_{\parallel} \tilde{u}_{\parallel}^s F_s \\ &\quad + \frac{\nu_s}{i(-\omega + k_{\parallel} w_{\parallel} - i\nu_s)} F_s \left[\frac{\tilde{n}_s}{n_s} \left(\frac{5}{2} - \frac{m_s n_s}{2p_s} w^2 \right) \right. \\ &\quad \left. \left. + \frac{\tilde{p}_s}{p_s} \left(\frac{m_s n_s}{2p_s} w^2 - \frac{3}{2} \right) \right] \right\} \end{aligned} \quad (\text{B.69})$$

first, the term \tilde{u}_\parallel that doesn't contain a pole is zero when integrating over $w_\parallel F_s$. The integrals of interest out are written in Appendix B.6,

$$\begin{aligned}\tilde{n}_s = & -i \frac{n_s q_s}{p_s} \tilde{E}_\parallel \frac{n_s}{|k_\parallel|} [1 + \zeta_s Z(\zeta_s)] - \omega \frac{m_s n_s}{2p_s} \frac{\tilde{b}_\parallel}{b_0} \frac{n_s}{|k_\parallel|} \left(\frac{2p_s}{m_s n_s} \right)^{1/2} Z(\zeta_s) \\ & - i\nu_s \frac{m_s n_s}{p_s} \tilde{u}_\parallel^s \frac{n_s}{|k_\parallel|} [1 + \zeta_s Z(\zeta_s)] \\ & - i\nu_s \frac{\tilde{n}_s}{n_s} \left(\frac{m_s n_s}{2p_s} \right)^{1/2} \frac{n_s}{|k_\parallel|} \left[\frac{5}{2} Z(\zeta_s) - \left(Z(\zeta_s) + \zeta_s [1 + \zeta_s Z(\zeta_s)] \right) \right] \\ & - i\nu_s \frac{\tilde{p}_s}{p_s} \left(\frac{m_s n_s}{2p_s} \right)^{1/2} \frac{n_s}{|k_\parallel|} \left[\left(Z(\zeta_s) + \zeta_s [1 + \zeta_s Z(\zeta_s)] \right) - \frac{3}{2} Z(\zeta_s) \right],\end{aligned}\tag{B.70}$$

and now introduce the thermal speed as $w_s^2 = 2p_s/m_s n_s$ and make more simplifications,

$$\begin{aligned}\tilde{n}_s = & -i \frac{n_s q_s}{p_s} \tilde{E}_\parallel \frac{n_s}{|k_\parallel|} [1 + \zeta_s Z(\zeta_s)] - \omega \frac{\tilde{b}_\parallel}{b_0} \frac{n_s}{|k_\parallel| w_s} Z(\zeta_s) \\ & - i \frac{2\nu_s}{w_s^2} \tilde{u}_\parallel^s \frac{n_s}{|k_\parallel|} [1 + \zeta_s Z(\zeta_s)] \\ & - i \frac{\nu_s}{w_s} \frac{\tilde{n}_s}{n_s} \frac{n_s}{|k_\parallel|} \left[\frac{3}{2} Z(\zeta_s) - \zeta_s [1 + \zeta_s Z(\zeta_s)] \right] \\ & - i \frac{\nu_s}{w_s} \frac{\tilde{p}_s}{p_s} \frac{n_s}{|k_\parallel|} \left[\zeta_s [1 + \zeta_s Z(\zeta_s)] - \frac{1}{2} Z(\zeta_s) \right],\end{aligned}\tag{B.71}$$

and now $\mathcal{R}(\zeta_s) = 1 + \zeta_s Z(\zeta_s)$,

$$\begin{aligned}\tilde{n}_s = & -i \frac{n_s q_s}{p_s} \tilde{E}_\parallel \frac{n_s}{|k_\parallel|} \mathcal{R}(\zeta_s) - \omega \frac{\tilde{b}_\parallel}{b_0} \frac{n_s}{|k_\parallel| w_s} Z(\zeta_s) - i \frac{2\nu_s}{w_s^2} \tilde{u}_\parallel^s \frac{n_s}{|k_\parallel|} \mathcal{R}(\zeta_s) \\ & - i \frac{\nu_s}{w_s} \frac{\tilde{n}_s}{n_s} \frac{n_s}{|k_\parallel|} \left[\frac{3}{2} Z(\zeta_s) - \zeta_s \mathcal{R}(\zeta_s) \right] - i \frac{\nu_s}{w_s} \frac{\tilde{p}_s}{p_s} \frac{n_s}{|k_\parallel|} \left[\zeta_s \mathcal{R}(\zeta_s) - \frac{1}{2} Z(\zeta_s) \right].\end{aligned}\tag{B.72}$$

This result is left like this to be combined with the pressure moments for further simplifications.

B.1.4.2 Perpendicular pressure moment

The moment,

$$\begin{aligned} \frac{m_s}{2} \int_{\tau(\mathbf{w})} d^3 w w_\perp^2 \tilde{f}_s &= \frac{m_s}{2} \int_{\tau(\mathbf{w})} d^3 w w_\perp^2 \left\{ \frac{1}{i(-\omega + k_\parallel w_\parallel - i\nu_s)} \right. \\ &\times \left(\frac{n_s q_s}{p_s} \tilde{E}_\parallel w_\parallel F_s - i\omega \frac{m_s n_s}{p_s b_0} \tilde{b}_\parallel F_s \frac{w_\perp^2}{2} \right) - \frac{i\nu_s}{(-\omega + k_\parallel w_\parallel - i\nu_s)} \frac{m_s n_s}{p_s} w_\parallel \tilde{u}_\parallel^s F_s \\ &- \frac{m_s n_s}{p_s} w_\parallel \tilde{u}_\parallel^s F_s + \frac{\nu_s}{i(-\omega + k_\parallel w_\parallel - i\nu_s)} \\ &\times F_s \left[\frac{\tilde{n}_s}{n_s} \left(\frac{5}{2} - \frac{m_s n_s}{2 p_s} w^2 \right) + \frac{\tilde{p}_s}{p_s} \left(\frac{m_s n_s}{2 p_s} w^2 - \frac{3}{2} \right) \right] \end{aligned} \quad (\text{B.73})$$

will lead to the perpendicular pressure, recalling that $v_i = w_i + u_i^s$. In the Appendix B.6 we have worked out the integrals, so we can replace them immediately,

$$\begin{aligned} \tilde{p}_\perp^s &= -i \frac{n_s q_s}{|k_\parallel|} \tilde{E}_\parallel [1 + \zeta_s Z(\zeta_s)] - \omega \frac{\tilde{b}_\parallel}{b_0} \frac{2 m_s n_s}{k_\parallel} \left(\frac{2 p_s}{m_s n_s} \right)^{1/2} Z(\zeta_s) \\ &- i\nu_s \frac{m_s n_s}{|k_\parallel|} \tilde{u}_\parallel^s [1 + \zeta_s Z(\zeta_s)] \\ &- i\nu_s \frac{n_s m_s}{2 |k_\parallel|} \left(\frac{2 p_s}{m_s n_s} \right)^{1/2} \frac{\tilde{n}_s}{n_s} \left[\frac{1}{2} Z(\zeta_s) - \zeta_s [1 + \zeta_s Z(\zeta_s)] \right] \\ &- i\nu_s \frac{n_s m_s}{2 |k_\parallel|} \left(\frac{2 p_s}{m_s n_s} \right)^{1/2} \frac{\tilde{p}_s}{p_s} \left[\frac{1}{2} Z(\zeta_s) + \zeta_s [1 + \zeta_s Z(\zeta_s)] \right], \end{aligned} \quad (\text{B.74})$$

introduce $w_s^2 = m_s n_s / 2 p_s$,

$$\begin{aligned} \tilde{p}_\perp^s &= -i \frac{n_s q_s}{|k_\parallel|} \tilde{E}_\parallel [1 + \zeta_s Z(\zeta_s)] - \omega \frac{\tilde{b}_\parallel}{b_0} \frac{m_s n_s w_s}{k_\parallel} Z(\zeta_s) \\ &- i\nu_s \frac{m_s n_s}{|k_\parallel|} \tilde{u}_\parallel^s [1 + \zeta_s Z(\zeta_s)] \\ &- i\nu_s \frac{n_s m_s}{2 |k_\parallel|} w_s \frac{\tilde{n}_s}{n_s} \left[\frac{1}{2} Z(\zeta_s) - \zeta_s [1 + \zeta_s Z(\zeta_s)] \right] \\ &- i\nu_s \frac{n_s m_s}{2 |k_\parallel|} w_s \frac{\tilde{p}_s}{p_s} \left[\frac{1}{2} Z(\zeta_s) + \zeta_s [1 + \zeta_s Z(\zeta_s)] \right], \end{aligned} \quad (\text{B.75})$$

and now introduce $\mathcal{R}(\zeta_s) = 1 + \zeta_s Z(\zeta_s)$,

$$\begin{aligned}\tilde{p}_\perp^s &= -i \frac{n_s q_s}{|k_\parallel|} \tilde{E}_\parallel \mathcal{R}(\zeta_s) - \omega \frac{\tilde{b}_\parallel}{b_0} \frac{m_s n_s w_s}{k_\parallel} Z(\zeta_s) - i \nu_s \frac{m_s n_s}{|k_\parallel|} \tilde{u}_\parallel^s \mathcal{R}(\zeta_s) \\ &\quad - i \nu_s \frac{n_s m_s}{2|k_\parallel|} w_s \frac{\tilde{n}_s}{n_s} \left[\frac{1}{2} Z(\zeta_s) - \zeta_s \mathcal{R}(\zeta_s) \right] \\ &\quad - i \nu_s \frac{n_s m_s}{2|k_\parallel|} w_s \frac{\tilde{p}_s}{p_s} \left[\frac{1}{2} Z(\zeta_s) + \zeta_s \mathcal{R}(\zeta_s) \right].\end{aligned}\tag{B.76}$$

This result will be simplified later when it is more simple to do so.

B.1.4.3 Parallel pressure moment

The parallel pressure moment,

$$\begin{aligned}m_s \int_{\tau(\mathbf{w})} d^3 w w_\parallel^2 \tilde{f}_s &= m_s \int_{\tau(\mathbf{w})} d^3 w w_\parallel^2 \left\{ \frac{1}{i(-\omega + k_\parallel w_\parallel - i\nu_s)} \right. \\ &\quad \times \left(\frac{n_s q_s}{p_s} \tilde{E}_\parallel w_\parallel F_s - i\omega \frac{m_s n_s}{p_s} \frac{\tilde{b}_\parallel}{b_0} F_s \frac{w_\perp^2}{2} \right) \\ &\quad - \frac{i\nu_s}{(-\omega + k_\parallel w_\parallel - i\nu_s)} \frac{m_s n_s}{p_s} w_\parallel \tilde{u}_\parallel^s F_s - \frac{m_s n_s}{p_s} w_\parallel \tilde{u}_\parallel^s F_s \\ &\quad \left. + \frac{\nu_s}{i(-\omega + k_\parallel w_\parallel - i\nu_s)} F_s \left[\frac{\tilde{n}_s}{n_s} \left(\frac{5}{2} - \frac{m_s n_s}{2p_s} w^2 \right) \frac{\tilde{p}_s}{p_s} \left(\frac{m_s n_s}{2p_s} w^2 - \frac{3}{2} \right) \right] \right\},\end{aligned}\tag{B.77}$$

where the integrals in Appendix B.6 can be substituted,

$$\begin{aligned}\tilde{p}_\parallel &= -i \frac{n_s q_s}{|k_\parallel|} \tilde{E}_\parallel [1 + 2\zeta_s^2 (1 + \zeta_s Z(\zeta_s))] - \omega \left(\frac{2p_s}{m_s n_s} \right)^{1/2} \frac{\tilde{b}_\parallel}{b_0} \frac{m_s n_s}{k_\parallel} \zeta_s [1 + \zeta_s Z(\zeta_s)] \\ &\quad - i \nu_s \frac{m_s n_s}{|k_\parallel|} \tilde{u}_\parallel^s [1 + 2\zeta_s^2 (1 + \zeta_s Z(\zeta_s))] \\ &\quad - i \nu_s \left(\frac{2p_s}{m_s n_s} \right)^{1/2} \frac{m_s n_s}{|k_\parallel|} \frac{\tilde{n}_s}{n_s} \left[\frac{3}{2} \zeta_s [1 + \zeta_s Z(\zeta_s)] - \frac{1}{2} \zeta_s [1 + 2\zeta_s^2 (1 + \zeta_s Z(\zeta_s))] \right] \\ &\quad - i \nu_s \left(\frac{2p_s}{m_s n_s} \right)^{1/2} \frac{m_s n_s}{2|k_\parallel|} \frac{\tilde{p}_s}{p_s} \left[\zeta_s [1 + 2\zeta_s^2 (1 + \zeta_s Z(\zeta_s))] - \zeta_s [1 + \zeta_s Z(\zeta_s)] \right],\end{aligned}\tag{B.78}$$

introducing $v_s^2 = 2p_s/m_s n_s$

$$\begin{aligned} \tilde{p}_\parallel &= -i \frac{n_s q_s}{|k_\parallel|} \tilde{E}_\parallel [1 + 2\zeta_s^2(1 + \zeta_s Z(\zeta_s))] - \omega \frac{\tilde{b}_\parallel}{b_0} \frac{m_s n_s v_s}{k_\parallel} \zeta_s [1 + \zeta_s Z(\zeta_s)] \\ &\quad - i\nu_s \frac{m_s n_s}{|k_\parallel|} \tilde{u}_\parallel^s [1 + 2\zeta_s^2(1 + \zeta_s Z(\zeta_s))] \\ &\quad - i\nu_s \frac{m_s n_s v_s}{|k_\parallel|} \frac{\tilde{n}_s}{n_s} \left[\frac{3}{2} \zeta_s [1 + \zeta_s Z(\zeta_s)] - \frac{1}{2} \zeta_s [1 + 2\zeta_s^2(1 + \zeta_s Z(\zeta_s))] \right] \\ &\quad - i\nu_s \frac{m_s n_s v_s}{2|k_\parallel|} \frac{\tilde{p}_s}{p_s} \left[\zeta_s [1 + 2\zeta_s^2(1 + \zeta_s Z(\zeta_s))] - \zeta_s [1 + \zeta_s Z(\zeta_s)] \right], \end{aligned} \quad (\text{B.79})$$

and now introduce $\mathcal{R}(\zeta_s) = 1 + \zeta_s Z(\zeta_s)$,

$$\begin{aligned} \tilde{p}_\parallel &= -i \frac{n_s q_s}{|k_\parallel|} \tilde{E}_\parallel [1 + 2\zeta_s^2 \mathcal{R}(\zeta_s)] - \omega \frac{\tilde{b}_\parallel}{b_0} \frac{m_s n_s w_s}{k_\parallel} \zeta_s \mathcal{R}(\zeta_s) \\ &\quad - i\nu_s \frac{m_s n_s}{|k_\parallel|} \tilde{u}_\parallel^s [1 + 2\zeta_s^2 \mathcal{R}(\zeta_s)] \\ &\quad - i\nu_s \frac{m_s n_s v_s}{|k_\parallel|} \frac{\tilde{n}_s}{n_s} \left[\frac{3}{2} \zeta_s \mathcal{R}(\zeta_s) - \frac{1}{2} \zeta_s [1 + 2\zeta_s^2 \mathcal{R}(\zeta_s)] \right] \\ &\quad - i\nu_s \frac{m_s n_s v_s}{2|k_\parallel|} \frac{\tilde{p}_s}{p_s} \left[\zeta_s [1 + 2\zeta_s^2 \mathcal{R}(\zeta_s)] - \zeta_s \mathcal{R}(\zeta_s) \right] \end{aligned} \quad (\text{B.80})$$

. This result is left until it can be simplified more simply.

B.1.4.4 Simplifying the moment equations

Rewriting the result on the density after dividing by n_s and rearranging the coefficient in front of the \tilde{u}_\parallel term,

$$\begin{aligned} \frac{\tilde{n}_s}{n_s} &= -i \frac{n_s q_s}{|k_\parallel| p_s} \tilde{E}_\parallel \mathcal{R}(\zeta_s) - \frac{\omega}{|k_\parallel| v_s} \frac{\tilde{b}_\parallel}{b_0} Z(\zeta_s) - i \frac{\nu_s m_s n_s}{|k_\parallel| p_s} \tilde{u}_\parallel^s \mathcal{R}(\zeta_s) \\ &\quad - i \frac{\nu_s}{v_s |k_\parallel|} \frac{\tilde{n}_s}{n_s} \left[\frac{3}{2} Z(\zeta_s) - \zeta_s \mathcal{R}(\zeta_s) \right] - i \frac{\nu_s}{v_s |k_\parallel|} \frac{\tilde{p}_s}{p_s} \left[\zeta_s \mathcal{R}(\zeta_s) - \frac{1}{2} Z(\zeta_s) \right], \end{aligned} \quad (\text{B.81})$$

and dividing the perpendicular pressure fluctuations by the total pressure and using the relation between p_s , v_s ,

$$\begin{aligned} \frac{\tilde{p}_\perp^s}{p_s} = & -i \frac{n_s q_s}{|k_\parallel| p_s} \tilde{E}_\parallel \mathcal{R}(\zeta_s) - \omega \frac{\tilde{b}_\parallel}{b_0} \frac{2}{|k_\parallel| v_s} Z(\zeta_s) - i \nu_s \frac{m_s n_s}{|k_\parallel| p_s} \tilde{u}_\parallel^s \mathcal{R}(\zeta_s) \\ & - i \frac{\nu_s}{|k_\parallel| v_s} \frac{\tilde{n}_s}{n_s} \left[\frac{1}{2} Z(\zeta_s) - \zeta_s \mathcal{R}(\zeta_s) \right] - i \frac{\nu_s}{|k_\parallel| v_s} \frac{\tilde{p}_s}{p_s} \left[\frac{1}{2} Z(\zeta_s) + \zeta_s \mathcal{R}(\zeta_s) \right]. \end{aligned} \quad (\text{B.82})$$

Subtracting the new equations, the \tilde{E}_\parallel , \tilde{u}_\parallel terms cancel,

$$\begin{aligned} \frac{\tilde{n}_s}{n_s} - \frac{\tilde{p}_\perp^s}{p_s} = & -\frac{\omega}{|k_\parallel| v_s} \frac{\tilde{b}_\parallel}{b_0} Z(\zeta_s) - i \frac{\nu_s}{v_s |k_\parallel|} \frac{\tilde{n}_s}{n_s} \left[\frac{3}{2} Z(\zeta_s) - \zeta_s \mathcal{R}(\zeta_s) \right] \\ & - i \frac{\nu_s}{v_s |k_\parallel|} \frac{\tilde{p}_s}{p_s} \left[\zeta_s \mathcal{R}(\zeta_s) - \frac{1}{2} Z(\zeta_s) \right] + \omega \frac{\tilde{b}_\parallel}{b_0} \frac{2}{|k_\parallel| v_s} Z(\zeta_s) \\ & + i \frac{\nu_s}{|k_\parallel| v_s} \frac{\tilde{n}_s}{n_s} \left[\frac{1}{2} Z(\zeta_s) - \zeta_s \mathcal{R}(\zeta_s) \right] + i \frac{\nu_s}{|k_\parallel| v_s} \frac{\tilde{p}_s}{p_s} \left[\frac{1}{2} Z(\zeta_s) + \zeta_s \mathcal{R}(\zeta_s) \right], \end{aligned} \quad (\text{B.83})$$

and further simplifications occur,

$$\frac{\tilde{n}_s}{n_s} - \frac{\tilde{p}_\perp^s}{p_s} = \frac{\omega}{|k_\parallel| v_s} \frac{\tilde{b}_\parallel}{b_0} Z(\zeta_s) - i \frac{\nu_s}{v_s |k_\parallel|} \frac{\tilde{n}_s}{n_s} Z(\zeta_s) + i \frac{\nu_s}{v_s |k_\parallel|} \frac{\tilde{p}_s}{p_s} Z(\zeta_s). \quad (\text{B.84})$$

Write out the total pressure fluctuations as $\tilde{p}_s = 2\tilde{p}_\perp/3p_s + \tilde{p}_\parallel/3p_s$, and rearrange,

$$\begin{aligned} \frac{\tilde{n}_s}{n_s} - \frac{\tilde{p}_\perp^s}{p_s} = & \frac{\omega}{|k_\parallel| v_s} \frac{\tilde{b}_\parallel}{b_0} Z(\zeta_s) - i \frac{\nu_s}{v_s |k_\parallel|} \frac{\tilde{n}_s}{n_s} Z(\zeta_s) + i \frac{\nu_s}{v_s |k_\parallel|} \left(\frac{2}{3} \frac{\tilde{p}_\perp^s}{p_s} + \frac{1}{3} \frac{\tilde{p}_\parallel^s}{p_s} \right) Z(\zeta_s) \\ \Rightarrow \frac{\tilde{n}_s}{n_s} \left(1 + i \frac{\nu_s}{v_s |k_\parallel|} Z(\zeta_s) \right) - \frac{\tilde{p}_\perp^s}{p_s} \left(1 + i \frac{2}{3} \frac{\nu_s}{v_s |k_\parallel|} Z(\zeta_s) \right) \\ & - \frac{\omega}{|k_\parallel| v_s} \frac{\tilde{b}_\parallel}{b_0} Z(\zeta_s) - \frac{1}{3} i \frac{\nu_s}{v_s |k_\parallel|} \frac{\tilde{p}_\parallel^s}{p_s} Z(\zeta_s) = 0. \end{aligned} \quad (\text{B.85})$$

Now the same thing can be done by multiplying the original density equation by $[1 + 2\zeta_s^2 \mathcal{R}(\zeta_s)]/n_s$,

$$\begin{aligned} [1 + 2\zeta_s^2 \mathcal{R}(\zeta_s)] \frac{\tilde{n}_s}{n_s} &= [1 + 2\zeta_s^2 \mathcal{R}(\zeta_s)] \left\{ -i \frac{n_s q_s}{|k_\parallel| p_s} \tilde{E}_\parallel \mathcal{R}(\zeta_s) - \frac{\omega}{|k_\parallel| v_s} \frac{\tilde{b}_\parallel}{b_0} Z(\zeta_s) \right. \\ &\quad - i \frac{\nu_s m_s n_s}{|k_\parallel| p_s} \tilde{u}_\parallel^s \mathcal{R}(\zeta_s) - i \frac{\nu_s}{v_s |k_\parallel|} \frac{\tilde{n}_s}{n_s} \left[\frac{3}{2} Z(\zeta_s) - \zeta_s \mathcal{R}(\zeta_s) \right] \\ &\quad \left. - i \frac{\nu_s}{v_s |k_\parallel|} \frac{\tilde{p}_s}{p_s} \left[\zeta_s \mathcal{R}(\zeta_s) - \frac{1}{2} Z(\zeta_s) \right] \right\}. \end{aligned} \quad (\text{B.86})$$

Then multiply the parallel pressure equation by $\mathcal{R}(\zeta_s)/p_s$ and use $v_s^2 = 2p_s/m_s n_s$,

$$\begin{aligned} \mathcal{R}(\zeta_s) \frac{\tilde{p}_\parallel}{p_s} &= \mathcal{R}(\zeta_s) \left\{ -i \frac{n_s q_s}{|k_\parallel| p_s} \tilde{E}_\parallel [1 + 2\zeta_s^2 \mathcal{R}(\zeta_s)] - \omega \frac{\tilde{b}_\parallel}{b_0} \frac{2}{k_\parallel v_s} \zeta_s \mathcal{R}(\zeta_s) \right. \\ &\quad - i \nu_s \frac{m_s n_s}{|k_\parallel| p_s} \tilde{u}_\parallel^s [1 + 2\zeta_s^2 \mathcal{R}(\zeta_s)] \\ &\quad - i 2 \frac{\nu_s}{|k_\parallel| v_s} \frac{\tilde{n}_s}{n_s} \left[\frac{3}{2} \zeta_s \mathcal{R}(\zeta_s) - \frac{1}{2} \zeta_s [1 + 2\zeta_s^2 \mathcal{R}(\zeta_s)] \right] \\ &\quad \left. - i \frac{\nu_s}{|k_\parallel| v_s} \frac{\tilde{p}_s}{p_s} \left[\zeta_s [1 + 2\zeta_s^2 \mathcal{R}(\zeta_s)] - \zeta_s \mathcal{R}(\zeta_s) \right] \right\}, \end{aligned} \quad (\text{B.87})$$

and now taking the difference,

$$\begin{aligned} [1 + 2\zeta_s^2 \mathcal{R}(\zeta_s)] \frac{\tilde{n}_s}{n_s} - \mathcal{R}(\zeta_s) \frac{\tilde{p}_\parallel}{p_s} &= \\ [1 + 2\zeta_s^2 \mathcal{R}(\zeta_s)] \left\{ &- \frac{\omega}{|k_\parallel| v_s} \frac{\tilde{b}_\parallel}{b_0} Z(\zeta_s) - i \frac{\nu_s}{v_s |k_\parallel|} \frac{\tilde{n}_s}{n_s} \left[\frac{3}{2} Z(\zeta_s) - \zeta_s \mathcal{R}(\zeta_s) \right] \right. \\ &- i \frac{\nu_s}{v_s |k_\parallel|} \frac{\tilde{p}_s}{p_s} \left[\zeta_s \mathcal{R}(\zeta_s) - \frac{1}{2} Z(\zeta_s) \right] \left. \right\} + \omega \frac{\tilde{b}_\parallel}{b_0} \frac{2}{k_\parallel v_s} \zeta_s \mathcal{R}^2(\zeta_s) \\ &+ i 2 \frac{\nu_s}{|k_\parallel| v_s} \frac{\tilde{n}_s}{n_s} \mathcal{R}(\zeta_s) \left[\frac{3}{2} \zeta_s \mathcal{R}(\zeta_s) - \frac{1}{2} \zeta_s \mathcal{R}(\zeta_s) [1 + 2\zeta_s^2 \mathcal{R}(\zeta_s)] \right] \\ &+ i \frac{\nu_s}{|k_\parallel| v_s} \frac{\tilde{p}_s}{p_s} \mathcal{R}(\zeta_s) \left[\zeta_s [1 + 2\zeta_s^2 \mathcal{R}(\zeta_s)] - \zeta_s \mathcal{R}(\zeta_s) \right]. \end{aligned} \quad (\text{B.88})$$

The rearrangements are a bit tedious, but simplify to,

$$\begin{aligned} [1 + 2\zeta_s^2 \mathcal{R}(\zeta_s)] \frac{\tilde{n}_s}{n_s} - \mathcal{R}(\zeta_s) \frac{\tilde{p}_\parallel}{p_s} &= \frac{\omega}{|k_\parallel| v_s} \frac{\tilde{b}_\parallel}{b_0} [2\zeta_s \mathcal{R}(\zeta_s) - Z(\zeta_s)] \\ &+ i \frac{3}{2} \frac{\nu_s}{v_s |k_\parallel|} \frac{\tilde{n}_s}{n_s} [2\zeta_s \mathcal{R}(\zeta_s) - Z(\zeta_s)] + i \frac{1}{2} \frac{\nu_s}{|k_\parallel| v_s} \frac{\tilde{p}_s}{p_s} [Z(\zeta_s) - 2\zeta_s \mathcal{R}(\zeta_s)] \end{aligned} \quad (\text{B.89})$$

using $\tilde{p}_s = 2\tilde{p}_\perp/3p_s + \tilde{p}_\parallel^s/3p_s$ and rearranging,

$$\begin{aligned} [1 + 2\zeta_s^2 \mathcal{R}(\zeta_s)] \frac{\tilde{n}_s}{n_s} - \mathcal{R}(\zeta_s) \frac{\tilde{p}_\parallel}{p_s} &= \frac{\omega}{|k_\parallel| v_s b_0} \frac{\tilde{b}_\parallel}{[2\zeta_s \mathcal{R}(\zeta_s) - Z(\zeta_s)]} \\ &+ i \frac{3}{2} \frac{\nu_s}{v_s |k_\parallel|} \frac{\tilde{n}_s}{n_s} [2\zeta_s \mathcal{R}(\zeta_s) - Z(\zeta_s)] \\ &+ i \frac{1}{2} \frac{\nu_s}{|k_\parallel| v_s} \left(\frac{2}{3} \frac{\tilde{p}_\perp^s}{p_s} + \frac{1}{3} \frac{\tilde{p}_\parallel^s}{p_s} \right) [Z(\zeta_s) - 2\zeta_s \mathcal{R}(\zeta_s)]. \end{aligned} \quad (\text{B.90})$$

B.2 Continuity

The 0th order moment of the Boltzmann equation (Eq. B.1) for a collision operator that conserves particle number (e.g., the BGK operator),

$$\frac{\partial}{\partial t} n_s + \frac{\partial}{\partial x_i} u_i^s n_s = 0. \quad (\text{B.91})$$

B.2.1 Linearization

The necessary perturbations from Eq. 4.9 for this section are,

$$\begin{aligned} u_i^s &= u_i^{s'}, \\ n_s &= n_{0,s} + n'_s \rightarrow n^s + n'_s, \end{aligned} \quad (\text{B.92})$$

so that for protons ($s = p$) of Eq. B.91,

$$\frac{\partial}{\partial t} n_p + \frac{\partial}{\partial x_i} u_i^p n_p \stackrel{\text{1st}}{=} \frac{\partial}{\partial t} n'_p + n_p \frac{\partial}{\partial x_i} u_i^{p'} = 0. \quad (\text{B.93})$$

Due to the ignorance of the electron momentum through the quasi-neutrality equation, the single-fluid approximation, and smallness of the ion inertial length, the momentum of the electrons do not enter into the description.

B.2.2 Fourier Analysis

The relevant Fourier amplitudes from Eq. 4.10 for this section are,

$$\begin{aligned} f'_s(x_\perp, x_\parallel, v_\parallel, v, t) &= \tilde{f}_s(v_\parallel, v) \exp\{i(k_\perp x_\perp + k_\parallel x_\parallel - \omega t)\}, \\ u'_i(x_\perp, x_\parallel, t) &= \tilde{u}_i \exp\{i(k_\perp x_\perp + k_\parallel x_\parallel - \omega t)\}, \\ \tilde{n}_s(x_\perp, x_\parallel, t) &= \int d^3 w \tilde{f}_s(w_\parallel, w, t) \\ &= n'_s(x_\perp, x_\parallel, t) \exp\{i(-k_\perp x_\perp - k_\parallel x_\parallel + \omega t)\}, \end{aligned} \quad (\text{B.94})$$

so that Eq. B.93 becomes,

$$-i\omega \tilde{n}_s + i n_s (k_{\perp} \tilde{u}_{\perp}^p + k_{\parallel} \tilde{u}_{\parallel}^p) = 0. \quad (\text{B.95})$$

B.3 Single-fluid momentum

The 1st momentum of the Boltzmann equation (Eq. B.1) produces Eq. 4.3 and the single-fluid momentum (Eq. 4.6) is explained in the text of Section 4.1 giving,

$$\begin{aligned} m_p \left(\frac{\partial}{\partial t} n_p u_i^p + \frac{\partial}{\partial x_j} n_p u_i^p u_j^p \right) \\ = - \frac{\partial}{\partial x_j} (p_{ij}^p + p_{ij}^e) + \frac{1}{4\pi} b_k \left(\frac{\partial}{\partial x_k} b_i - \frac{\partial}{\partial x_i} b_k \right). \end{aligned} \quad (\text{B.96})$$

B.3.1 Linearization

The relevant perturbations from Eq. 4.9 are,

$$\begin{aligned} b_i &= b'_i + b_0 \hat{b}_i, \\ u_i^s &= u_i^{s'}, \\ n_s &= n_{0,s} + n'_s \rightarrow n^s + n'_s, \\ p_{\perp} &= p_{\perp,0}^s + p_{\perp}^{s'} \rightarrow p_{\perp}^s + p_{\perp}^{s'}, \\ p_{\parallel} &= p_{\parallel,0}^s + p_{\parallel}^{s'} \rightarrow p_{\parallel}^s + p_{\parallel}^{s'}, \end{aligned} \quad (\text{B.97})$$

Labelling the single-fluid momentum equation from Eq. B.96,

$$\underbrace{m_p n \left(\frac{\partial}{\partial t} + u_j^p \frac{\partial}{\partial x_j} \right) u_i^p}_{\text{K}} + \underbrace{\frac{\partial}{\partial x_j} \left(p_{ij}^p + p_{ij}^e \right)}_{\text{L}} + \underbrace{(4\pi)^{-1} b_j \left(\frac{\partial}{\partial x_i} b_j - \frac{\partial}{\partial x_j} b_i \right)}_{\text{M}} = 0. \quad (\text{B.98})$$

For part K,

$$m_p n \left(\frac{\partial}{\partial t} + u_j^p \frac{\partial}{\partial x_j} \right) u_i^p \stackrel{\text{1st}}{=} m_p n \frac{\partial}{\partial t} u_i^{p'}, \quad (\text{B.99})$$

Part L,

$$\frac{\partial}{\partial x_j} \left(p_{ij}^p + p_{ij}^e \right) \stackrel{\text{1st}}{=} \frac{\partial}{\partial x_j} \left(p_{ij}^{p'} + p_{ij}^{e'} \right), \quad (\text{B.100})$$

where if the pressure is gyrotropic p_{ij}^s ,

$$p_{ij}^s = p_\perp^s (\delta_{ij} - \hat{b}_i \hat{b}_j) + p_\parallel^s \hat{b}_i \hat{b}_j \quad (\text{B.101})$$

$$p_\perp = \frac{1}{2} p_{ij}^s (\delta_{ij} - \hat{b}_i \hat{b}_j), \quad p_\parallel^s = p_{ij}^s \hat{b}_i \hat{b}_j \quad (\text{B.102})$$

can be decomposed into the perpendicular p_\perp^s and parallel p_\parallel^s pressures, giving to first order,

$$\begin{aligned} p_{ij}^s &= \delta_{ij} p_\perp^s + \hat{b}_i \hat{b}_j (p_\parallel^s - p_\perp^s) \\ &\stackrel{\text{1st}}{=} \delta_{ij} p_\perp^{s'} + \hat{b}'_i \delta_{j\parallel} (\bar{p}_\parallel^s - \bar{p}_\perp^s) + \delta_{i\parallel} \hat{b}'_j (\bar{p}_\parallel^s - \bar{p}_\perp^s) + \delta_{i\parallel} \delta_{j\parallel} (p_\parallel^{s'} - p_\perp^{s'}). \end{aligned} \quad (\text{B.103})$$

The spatial derivative acts,

$$\begin{aligned} \frac{\partial}{\partial x_j} p_{ij}^s &\stackrel{\text{1st}}{=} \frac{\partial}{\partial x_j} \left(\delta_{ij} p_\perp^{s'} + \hat{b}'_i \delta_{j\parallel} (\bar{p}_\parallel^s - \bar{p}_\perp^s) + \delta_{i\parallel} \hat{b}'_j (\bar{p}_\parallel^s - \bar{p}_\perp^s) + \delta_{i\parallel} \delta_{j\parallel} (p_\parallel^{s'} - p_\perp^{s'}) \right) \\ &= \frac{\partial}{\partial x_i} p_\perp^{s'} + \frac{1}{|b_0|} \delta_{j\parallel} (p_\parallel^s - p_\perp^s) \left[\frac{\partial}{\partial x_j} b'_i - \delta_{\parallel i} \frac{\partial}{\partial x_j} b'_\parallel \right] \\ &\quad - \frac{1}{|b_0|} \delta_{i\parallel} (p_\parallel^s - p_\perp^s) \frac{\partial}{\partial x_\parallel} b'_\parallel + \delta_{i\parallel} \frac{\partial}{\partial x_\parallel} (p_\parallel^{s'} - p_\perp^{s'}) \\ &= \frac{\partial}{\partial x_i} p_\perp^{s'} + \frac{1}{|b_0|} (p_\parallel^s - p_\perp^s) \left[\frac{\partial}{\partial x_\parallel} b'_i - \delta_{i\parallel} \frac{\partial}{\partial x_\parallel} b'_\parallel \right] \\ &\quad - \frac{1}{|b_0|} \delta_{i\parallel} (p_\parallel^s - p_\perp^s) \partial_i b'_\parallel + \delta_{i\parallel} \frac{\partial}{\partial x_\parallel} (p_\parallel^{s'} - p_\perp^{s'}) \\ &= \frac{\partial}{\partial x_i} p_\perp^{s'} + \frac{1}{|b_0|} (p_\parallel^s - p_\perp^s) \left[\frac{\partial}{\partial x_\parallel} b'_i - \delta_{\parallel i} \frac{\partial}{\partial x_\parallel} b'_\parallel \right] \\ &\quad - \frac{1}{|b_0|} \delta_{i\parallel} (p_\parallel^s - p_\perp^s) \frac{\partial}{\partial x_\parallel} b'_\parallel + \delta_{i\parallel} \frac{\partial}{\partial x_\parallel} (p_\parallel^{s'} - p_\perp^{s'}). \end{aligned} \quad (\text{B.104})$$

Part L,

$$\begin{aligned} \frac{\partial}{\partial x_j} (p_{ij}^p + p_{ij}^e) &\stackrel{\text{1st}}{=} \frac{\partial}{\partial x_i} p_\perp^{p'} + \frac{1}{|b_0|} (p_\parallel^p - p_\perp^p) \left[\frac{\partial}{\partial x_\parallel} b'_i - 2\delta_{i\parallel} \frac{\partial}{\partial x_\parallel} b'_\parallel \right] \\ &\quad + \delta_{i\parallel} \frac{\partial}{\partial x_\parallel} (p_\parallel^{p'} - p_\perp^{p'}) + \frac{\partial}{\partial x_i} p_\perp^{e'} + \frac{1}{|b_0|} (p_\parallel^e - p_\perp^e) \\ &\quad \times \left[\frac{\partial}{\partial x_\parallel} b'_i - 2\delta_{i\parallel} \frac{\partial}{\partial x_\parallel} b'_\parallel \right] + \delta_{i\parallel} \frac{\partial}{\partial x_\parallel} (p_\parallel^{e'} - p_\perp^{e'}) \end{aligned} \quad (\text{B.105})$$

and part M,

$$b_j \left(\frac{\partial}{\partial x_i} b_j - \frac{\partial}{\partial x_j} b_i \right) \stackrel{1st}{=} b_0 \delta_{j\parallel} \left(\frac{\partial}{\partial x_i} b'_j - \frac{\partial}{\partial x_j} b'_i \right) = b_0 \frac{\partial}{\partial x_i} b'_{\parallel} - b_0 \frac{\partial}{\partial x_{\parallel}} b'_i. \quad (\text{B.106})$$

Collecting all of the terms,

$$\begin{aligned} m_p n_0 \frac{\partial}{\partial t} u'_i + \frac{\partial}{\partial x_i} p'^{\perp} + \frac{1}{|b_0|} (p^p_{\parallel} - p^p_{\perp}) & \left[\frac{\partial}{\partial x_{\parallel}} b'_i - 2\delta_{\parallel i} \frac{\partial}{\partial x_{\parallel}} b'_{\parallel} \right] \\ + \delta_{i\parallel} \frac{\partial}{\partial x_{\parallel}} (p'^{\parallel} - p'^{\perp}) + \frac{\partial}{\partial x_i} p'^{\perp} + \frac{1}{|b_0|} (p^e_{\parallel} - p^e_{\perp}) & \left[\frac{\partial}{\partial x_{\parallel}} b'_i - 2\delta_{\parallel i} \frac{\partial}{\partial x_{\parallel}} b'_{\parallel} \right] \\ + \delta_{i\parallel} \frac{\partial}{\partial x_{\parallel}} (p'^{\parallel} - p'^{\perp}) + (4\pi)^{-1} \left(b_0 \frac{\partial}{\partial x_i} b'_{\parallel} - b_0 \frac{\partial}{\partial x_{\parallel}} b'_i \right) & = 0. \end{aligned} \quad (\text{B.107})$$

Setting the background distribution functions to isotropic, $p^p_{\perp} = p^p_{\parallel}$, $p^e_{\perp} = p^e_{\parallel}$, simplifies considerably,

$$\begin{aligned} m_p n \frac{\partial}{\partial t} u'_i + \frac{\partial}{\partial x_i} p'^{\perp} + \delta_{i\parallel} \frac{\partial}{\partial x_{\parallel}} (p'^{\parallel} - p'^{\perp}) \\ + \frac{\partial}{\partial x_i} p'^{\perp} + \delta_{i\parallel} \frac{\partial}{\partial x_{\parallel}} (p'^{\parallel} - p'^{\perp}) + (4\pi)^{-1} \left(b_0 \frac{\partial}{\partial x_i} b'_{\parallel} - b_0 \frac{\partial}{\partial x_{\parallel}} b'_i \right) & = 0. \end{aligned} \quad (\text{B.108})$$

B.3.2 Fourier analysis

The Fourier amplitudes from Eq. 4.10 relevant to this section are,

$$\begin{aligned} b'_i(x_{\perp}, x_{\parallel}, t) &= \tilde{b}_i \exp\{i(k_{\perp}x_{\perp} + k_{\parallel}x_{\parallel} - \omega t)\}, \\ u'_i(x_{\perp}, x_{\parallel}, t) &= \tilde{u}_i \exp\{i(k_{\perp}x_{\perp} + k_{\parallel}x_{\parallel} - \omega t)\}, \\ \tilde{n}_s(x_{\perp}, x_{\parallel}, t) &= \int d^3 w \tilde{f}_s(w_{\parallel}, w, t) \\ &= n'_s(x_{\perp}, x_{\parallel}, t) \exp\{i(-k_{\perp}x_{\perp} - k_{\parallel}x_{\parallel} + \omega t)\}, \\ \tilde{p}_{\perp}^s(x_{\perp}, x_{\parallel}, t) &= \frac{m_s}{2} \int d^3 w w_{\perp}^2 \tilde{f}_s(w_{\parallel}, w, t) \\ &= p_{\perp}^{s,\prime}(x_{\perp}, x_{\parallel}, t) \exp\{i(-k_{\perp}x_{\perp} - k_{\parallel}x_{\parallel} + \omega t)\}, \\ \tilde{p}_{\parallel}^s(x_{\perp}, x_{\parallel}, t) &= m_s \int d^3 w w_{\parallel}^2 \tilde{f}_s(w_{\parallel}, w, t) \\ &= p_{\parallel}^{s,\prime}(x_{\perp}, x_{\parallel}, t) \exp\{i(-k_{\perp}x_{\perp} - k_{\parallel}x_{\parallel} + \omega t)\}. \end{aligned} \quad (\text{B.109})$$

Fourier transforming Eq. B.108 gives,

$$\begin{aligned} -im_p n \omega \tilde{u}_i + ik_i \tilde{p}_\perp^p + i \delta_{i\parallel} k_\parallel (\tilde{p}_\parallel^p - \tilde{p}_\perp^p) \\ + ik_i \tilde{p}_\perp^e + i \delta_{i\parallel} k_\parallel (\tilde{p}_\parallel^e - \tilde{p}_\perp^e) + \frac{ib_0}{4\pi} (k_i \tilde{b}_\parallel - k_\parallel \tilde{b}_i) = 0. \end{aligned} \quad (\text{B.110})$$

It is more useful to split this into parallel and perpendicular components. For the parallel component, multiply by $\delta_{i\parallel}$,

$$\begin{aligned} \delta_{i\parallel} \left\{ -im_p n \omega \tilde{u}_i + ik_i \tilde{p}_\perp^p + i \delta_{i\parallel} k_\parallel (\tilde{p}_\parallel^p - \tilde{p}_\perp^p) \right. \\ \left. + ik_i \tilde{p}_\perp^e + i \delta_{i\parallel} k_\parallel (\tilde{p}_\parallel^e - \tilde{p}_\perp^e) + \frac{ib_0}{4\pi} (k_i \tilde{b}_\parallel - k_\parallel \tilde{b}_i) \right\} \\ = -im_p n \omega \tilde{u}_\parallel + ik_\parallel \tilde{p}_\perp^p + ik_\parallel (\tilde{p}_\parallel^p - \tilde{p}_\perp^p) \\ + ik_\parallel \tilde{p}_\perp^e + ik_\parallel (\tilde{p}_\parallel^e - \tilde{p}_\perp^e) + \frac{ib_0}{4\pi} (k_\parallel \tilde{b}_\parallel - k_\parallel \tilde{b}_\parallel) \\ = -im_p n \omega \tilde{u}_\parallel + ik_\parallel \tilde{p}_\parallel^p + ik_\parallel \tilde{p}_\parallel^e = 0. \end{aligned} \quad (\text{B.111})$$

Finally,

$$\omega m_p n \tilde{u}_\parallel = k_\parallel (\tilde{p}_\parallel^p + \tilde{p}_\parallel^e) \quad (\text{B.112})$$

and now for the perpendicular equation, multiplying the Fourier transformed momentum equation by $\delta_{i\perp}$,

$$\begin{aligned} \delta_{i\perp} \left\{ -im_p n \omega \tilde{u}_i + ik_i \tilde{p}_\perp^p + i \delta_{i\parallel} k_\parallel (\tilde{p}_\parallel^p - \tilde{p}_\perp^p) \right. \\ \left. + ik_i \tilde{p}_\perp^e + i \delta_{i\parallel} k_\parallel (\tilde{p}_\parallel^e - \tilde{p}_\perp^e) + \frac{ib_0}{4\pi} (k_i \tilde{b}_\parallel - k_\parallel \tilde{b}_i) \right\} \\ = -im_p n \omega \tilde{u}_\perp + ik_\perp \tilde{p}_\perp^p + ik_\perp \tilde{p}_\perp^e + \frac{ib_0}{4\pi} (k_\perp \tilde{b}_\parallel - k_\parallel \tilde{b}_\perp). \end{aligned} \quad (\text{B.113})$$

Finally,

$$m_p n \omega \tilde{u}_\perp = k_\perp \tilde{p}_\perp^p + k_\perp \tilde{p}_\perp^e + \frac{b_0}{4\pi} (k_\perp \tilde{b}_\parallel - k_\parallel \tilde{b}_\perp). \quad (\text{B.114})$$

B.4 Induction equation

The induction equation is derived by inserting a simplified electric field (Omh's Law) into Faraday's law. The simplified electric field is derived by writing a time evolution equation for the current from the momentum equations (Eq. 4.3) and then using Ampere's and Faraday's Laws, the single-fluid approximation, smallness of the ion inertial length, and the non-relativistic approximation to

arrive at the ideal Ohm's Law,

$$E_i = -\epsilon_{ijk} u_j^p b_k \quad (\text{B.115})$$

and inserting into Faraday's law,

$$\frac{\partial}{\partial t} b_i = \epsilon_{ijk} \partial_j \epsilon_{klm} u_l^p b_m = b_j \frac{\partial}{\partial x_j} u_i^p - \frac{\partial}{\partial x_j} u_j^p b_i. \quad (\text{B.116})$$

B.4.1 Linearization

Now linearize with the perturbations from Eq. 4.9,

$$\begin{aligned} b_i &= b'_i + b_0 \hat{b}_i, \\ u_i^s &= u_i^{s'}, \end{aligned} \quad (\text{B.117})$$

giving,

$$\frac{\partial}{\partial t} b'_i = \delta_{j\parallel} b_0 \frac{\partial}{\partial x_j} u_i^{p'} - \delta_{i\parallel} b_0 \frac{\partial}{\partial x_j} u_j^{p'} = b_0 \frac{\partial}{\partial x_\parallel} u_i^{p'} - \delta_{i\parallel} b_0 \frac{\partial}{\partial x_j} u_j^{p'}. \quad (\text{B.118})$$

B.4.2 Fourier analysis

Using the definitions from Eq. 4.10 relevant to this section,

$$\begin{aligned} b'_i(x_\perp, x_\parallel, t) &= \tilde{b}_i \exp\{i(k_\perp x_\perp + k_\parallel x_\parallel - \omega t)\}, \\ u'_i(x_\perp, x_\parallel, t) &= \tilde{u}_i \exp\{i(k_\perp x_\perp + k_\parallel x_\parallel - \omega t)\}, \end{aligned} \quad (\text{B.119})$$

yielding,

$$-i\omega \tilde{b}_i = i b_0 k_\parallel \tilde{u}_i^p - i \delta_{i\parallel} b_0 k_j \tilde{u}_j^p \quad (\text{B.120})$$

and now taking the perpendicular and parallel parts,

$$i = \perp \Rightarrow -\omega \tilde{b}_\perp = b_0 k_\parallel \tilde{u}_\perp^p, \quad (\text{B.121})$$

$$i = \parallel \Rightarrow \omega \tilde{b}_\parallel = b_0 k_\perp \tilde{u}_\perp^p. \quad (\text{B.122})$$

B.5 Plasma dispersion function

Defining the plasma dispersion function,

$$\sqrt{\pi} Z(\zeta_s) = \int_{C_L} du \frac{\exp\{-u^2\}}{u - \zeta_s}, \quad (\text{B.123})$$

The path C_L is called the Landau contour in plasma physics, it is the analytical continuation of the path between $(-\infty, \infty)$, necessary when there is a pole at ζ_s . This integral can be treated numerically or with expansions for large/small $|\zeta_s|$.

Replacing the integral path with the actual path $[-\infty, \infty]$ taking the partial derivative with respect to the argument of Eq. B.123,

$$\begin{aligned}\frac{\partial}{\partial \zeta_s} Z(\zeta_s) &= \frac{1}{\sqrt{\pi}} \int_{-\infty}^{\infty} du \exp\{-u^2\} \frac{\partial}{\partial \zeta_s} \frac{1}{u - \zeta_s} \\ &= \frac{-1}{\sqrt{\pi}} \int_{-\infty}^{\infty} du \exp\{-u^2\} \frac{\partial}{\partial u} \frac{1}{u - \zeta_s},\end{aligned}\quad (\text{B.124})$$

integrate by parts,

$$\begin{aligned}&\frac{-1}{\sqrt{\pi}} \int_{-\infty}^{\infty} du \exp\{-u^2\} \frac{\partial}{\partial u} \frac{1}{u - \zeta_s} \\ &= \frac{-1}{\sqrt{\pi}} \left(\left[\frac{\exp\{-u^2\}}{u - \zeta_s} \right]_{-\infty}^{\infty} + 2 \int_{-\infty}^{\infty} du \frac{u \exp\{-u^2\}}{u - \zeta_s} \right),\end{aligned}\quad (\text{B.125})$$

the first term inside the parentheses goes to zero and the second term is a common integral that was solved later in this Appendix, to give,

$$\frac{\partial}{\partial \zeta_s} Z(\zeta_s) = -2[1 + \zeta_s Z(\zeta_s)].\quad (\text{B.126})$$

This is a ordinary differential equation,

$$\frac{dy}{dx} y(x) + b(x) y(x) = a,\quad (\text{B.127})$$

where the integral factor is,

$$\int d\zeta_s 2\zeta_s = \zeta_s^2,\quad (\text{B.128})$$

with undefined limits. This yields,

$$\frac{\partial}{\partial \zeta_s} Z(\zeta_s) \exp\{\zeta_s^2\} = -2 \exp\{\zeta_s^2\}.\quad (\text{B.129})$$

Integrating once more,

$$Z(\zeta_s) \exp\{\zeta_s^2\} \Big|_{\mathcal{B}} = -2 \int_{\mathcal{B}} d\zeta_s \exp\{\zeta_s^2\},\quad (\text{B.130})$$

where the boundary conditions \mathcal{B} must be determined. To do this, use the

$$\zeta_s = 0,$$

$$Z(0) = \frac{1}{\sqrt{\pi}} \text{P.V.} \int_{-\infty}^{\infty} du \frac{\exp\{-u^2\}}{u} + i\sqrt{\pi} \quad (\text{B.131})$$

by the Sokhotski–Plemelj theorem, where P.V. is the Cauchy principal value. Rewriting Eq. B.130 with the bounds,

$$Z(\zeta_s) = \exp\{-\zeta_s^2\} \left(i\sqrt{\pi} - 2 \int_0^{\zeta_s} dx \exp\{x^2\} \right), \quad (\text{B.132})$$

where the integral is imaginary error function. Integrals of this kind can be handled by modern computational mathematics programs. This is the method employed to treat the plasma dispersion function numerically.

The plasma dispersion function can be expanded in terms of its argument, often used for analytical treatment,

$$Z(\zeta_s) \approx i\sqrt{\pi} \exp\{-\zeta_s^2\} - 2\zeta_s \left(1 - 2\frac{\zeta_s^2}{3} + 4\frac{\zeta_s^4}{15} + \dots \right), \quad |\zeta_s| \gg 1, \quad (\text{B.133})$$

$$Z(\zeta_s) \approx i\sigma\sqrt{\pi} \exp\{-\zeta_s^2\} - \frac{1}{\zeta_s} \left(1 + \frac{1}{2\zeta_s^2} + \frac{3}{4\zeta_s^4} + \dots \right), \quad |\zeta_s| \ll 1, \quad (\text{B.134})$$

where,

$$\begin{aligned} \sigma = 0, \quad & \mathcal{I}\{\zeta_s\} > 0, \\ \sigma = 1, \quad & \mathcal{I}\{\zeta_s\} = 0, \\ \sigma = 2, \quad & \mathcal{I}\{\zeta_s\} < 0. \end{aligned} \quad (\text{B.135})$$

A set of related integrals arise that are products of u^n with the integrand,

$$\int_{C_L} du \frac{u^n \exp\{-u^2\}}{u - \zeta_s} = \dots, \quad (\text{B.136})$$

which are simply related to the plasma dispersion function $Z(\zeta_s)$. For u^1 , take $u \rightarrow u + \zeta_s$

$$\begin{aligned} & \int_{C_L} du \frac{(u + \zeta_s) \exp\{-(u + \zeta_s)^2\}}{u} \\ &= \int_{C_L} du \left[\exp\{-(u + \zeta_s)^2\} + \frac{\zeta_s \exp\{-(u + \zeta_s)^2\}}{u} \right] \\ &= \sqrt{\pi} + \zeta_s \int_{C_L} du \frac{\exp\{-u^2\}}{u - \zeta_s} \\ &= \sqrt{\pi} [1 + \zeta_s Z(\zeta_s)]. \end{aligned} \quad (\text{B.137})$$

The same procedure follows for u^2 ,

$$\begin{aligned}
& \int_{C_L} du \frac{(u + \zeta_s)^2 \exp\{-(u + \zeta_s)^2\}}{u} \\
&= \int_{C_L} du \exp\{-(u + \zeta_s)^2\} \left[u + 2\zeta_s + \frac{\zeta_s^2}{u} \right] \\
&= -\zeta_s \sqrt{\pi} + 2\zeta_s \sqrt{\pi} + \sqrt{\pi} \zeta_s^2 Z(\zeta_s) \\
&= \sqrt{\pi} \zeta_s [1 + \zeta_s Z(\zeta_s)], \tag{B.138}
\end{aligned}$$

and for u^3 ,

$$\begin{aligned}
& \int_{C_L} du \frac{(u + \zeta_s)^3 \exp\{-(u + \zeta_s)^2\}}{u} \\
&= \int_{C_L} du \exp\{-(u + \zeta_s)^2\} \left[u^2 + \frac{\zeta_s^3}{u} + 3\zeta_s^2 + 3u\zeta_s \right] \\
&= \frac{\sqrt{\pi}}{2} (2\zeta_s^2 + 1) + \sqrt{\pi} \zeta_s^3 Z(\zeta_s) + 3\zeta_s^2 \sqrt{\pi} - 3\sqrt{\pi} \zeta_s^2 \\
&= \frac{\sqrt{\pi}}{2} [1 + 2\zeta_s^2 (1 + \zeta_s Z(\zeta_s))], \tag{B.139}
\end{aligned}$$

and for u^4 ,

$$\begin{aligned}
& \int_{C_L} du \frac{(u + \zeta_s)^4 \exp\{-(u + \zeta_s)^2\}}{u} \\
&= \int_{C_L} du \exp\{-(u + \zeta_s)^2\} \left[u^3 + \frac{\zeta_s^4}{u} + 6u\zeta_s^2 + 4\zeta_s u^2 + 4\zeta_s^3 \right] \\
&= -\frac{\sqrt{\pi}}{2} \zeta_s (2\zeta_s^2 + 3) + \sqrt{\pi} \zeta_s^4 Z(\zeta_s) - 6\sqrt{\pi} \zeta_s^3 + \frac{4\sqrt{\pi} \zeta_s}{2} (2\zeta_s^2 + 1) + 4\zeta_s^3 \sqrt{\pi} \\
&= \frac{\sqrt{\pi}}{2} \zeta_s [1 + 2\zeta_s^2 (1 + \zeta_s Z(\zeta_s))], \tag{B.140}
\end{aligned}$$

and for u^5 ,

$$\begin{aligned}
& \int_{C_L} du \frac{(u + \zeta_s)^5 \exp\{-(u + \zeta_s)^2\}}{u} \\
&= \int_{C_L} du \exp\{-(u + \zeta_s)^2\} \left[u^4 + \frac{\zeta_s^5}{u} + 10\zeta_s^3 u + 10\zeta_s^2 u^2 + 5\zeta_s u^3 + 5\zeta_s^4 \right] \\
&= \frac{\sqrt{\pi}}{4} (4\zeta_s^2 (\zeta_s^2 + 3) + 3) + \sqrt{\pi} \zeta_s^5 Z(\zeta_s) - 10\sqrt{\pi} \zeta_s^4 + 5\sqrt{\pi} \zeta_s^2 (2\zeta_s^2 + 1) \\
&\quad - \frac{5\sqrt{\pi}}{2} \zeta_s^2 (2\zeta_s^2 + 3) + 5\zeta_s^4 \sqrt{\pi} \\
&= \sqrt{\pi} \left[\zeta_s^5 Z(\zeta_s) + \zeta_s^4 - \frac{1}{2} \zeta_s^2 + \frac{3}{4} \right]. \tag{B.141}
\end{aligned}$$

While this procedure is simple manipulation of the integral, this property of the

plasma dispersion function is what permits closure in linear kinetic theory.

B.6 Useful results on the plasma dispersion relation

It is necessary to work out a set of integrals which involve multiples of v_\perp, v_\parallel , the background distribution function and the inverse of $i(k_\parallel v_\parallel - \omega')$ bit where $\omega' = \omega + i\nu_s$. These integrals introduce the plasma distribution function, which appears in the Appendix B.5. Throughout I have used the definition,

$$\alpha_s = n_s^{5/2} \left(\frac{m_s}{2\pi p_s} \right)^{3/2} \quad (\text{B.142})$$

to conserve space. The integrals appear as,

$$2\pi\alpha_s \int_0^\infty dv_\perp v_\perp \int_{-\infty}^\infty dv_\parallel \frac{v_\perp^{n_\perp} v_\parallel^{n_\parallel} \exp\left\{-\frac{m_s n_s}{2p_s}(v_\parallel^2 + v_\perp^2)\right\}}{k_\parallel v_\parallel - \omega'}, \quad (\text{B.143})$$

for n_\perp, n_\parallel specified.

B.6.1 Density integrals

For v_\perp^0, v_\parallel^0 ,

$$\begin{aligned} & 2\pi\alpha_s \int_0^\infty dv_\perp v_\perp \int_{-\infty}^\infty dv_\parallel \frac{\exp\left\{-\frac{m_s n_s}{2p_s}(v_\parallel^2 + v_\perp^2)\right\}}{k_\parallel v_\parallel - \omega'} \\ &= 2\pi\alpha_s \int_0^\infty dv_\perp v_\perp \exp\left\{-\frac{m_s n_s}{2p_s} v_\perp^2\right\} \int_{-\infty}^\infty dv_\parallel \frac{\exp\left\{-\frac{m_s n_s}{2p_s} v_\parallel^2\right\}}{k_\parallel v_\parallel - \omega'} \\ &= 2\pi\alpha_s \frac{k_B T_\perp^s}{m_s} \frac{1}{|k_\parallel|} \int_C du \frac{\exp\{-u^2\}}{u - \zeta_s} \\ &= 2\pi\alpha_s \frac{p_s}{m_s n_s} \frac{1}{|k_\parallel|} \sqrt{\pi} Z(\zeta_s) \\ &= \left(\frac{m_s n_s}{2p_s} \right)^{1/2} \frac{n_s}{|k_\parallel|} Z(\zeta_s). \end{aligned} \quad (\text{B.144})$$

For $v_{\perp}^0, v_{\parallel}^1$,

$$\begin{aligned}
& 2\pi\alpha_s \int_0^\infty dv_{\perp} v_{\perp} \int_{-\infty}^\infty dv_{\parallel} \frac{v_{\parallel} \exp\left\{-\frac{m_s n_s}{2p_s}(v_{\parallel}^2 + v_{\perp}^2)\right\}}{k_{\parallel} v_{\parallel} - \omega'} \\
&= 2\pi\alpha_s \int_0^\infty dv_{\perp} v_{\perp} \exp\left\{-\frac{m_s n_s}{2p_s} v_{\perp}^2\right\} \int_{-\infty}^\infty dv_{\parallel} \frac{v_{\parallel} \exp\left\{-\frac{m_s n_s}{2p_s} v_{\parallel}^2\right\}}{k_{\parallel} v_{\parallel} - \omega'} \\
&= 2\pi\alpha_s \frac{p_s}{m_s n_s} \frac{1}{|k_{\parallel}|} \sqrt{\frac{2p_s}{m_s n_s}} \int_C du \frac{u \exp\{-u^2\}}{u - \zeta_s} \\
&= 2\pi\alpha_s \frac{p_s}{m_s n_s} \frac{1}{|k_{\parallel}|} \sqrt{\frac{2p_s}{m_s n_s}} \sqrt{\pi} [1 + \zeta_s Z(\zeta_s)] \\
&= \frac{n_s}{|k_{\parallel}|} [1 + \zeta_s Z(\zeta_s)]. \tag{B.145}
\end{aligned}$$

For $v_{\perp}^2, v_{\parallel}^0$,

$$\begin{aligned}
& 2\pi\alpha_s \int_0^\infty dv_{\perp} v_{\perp}^3 \int_{-\infty}^\infty dv_{\parallel} \frac{\exp\left\{-\frac{m_s n_s}{2p_s}(v_{\parallel}^2 + v_{\perp}^2)\right\}}{k_{\parallel} v_{\parallel} - \omega'} \\
&= 2\pi\alpha_s \int_0^\infty dv_{\perp} v_{\perp}^3 \exp\left\{-\frac{m_s n_s}{2p_s} v_{\perp}^2\right\} \int_{-\infty}^\infty dv_{\parallel} \frac{\exp\left\{-\frac{m_s n_s}{2p_s} v_{\parallel}^2\right\}}{k_{\parallel} v_{\parallel} - \omega'} \\
&= 2\pi\alpha_s \frac{2(p_s)^2}{(m_s n_s)^2} \frac{1}{|k_{\parallel}|} \int_C du \frac{\exp\{-u^2\}}{u - \zeta_s} \\
&= 2\pi\alpha_s \frac{2(p_s)^2}{(m_s n_s)^2} \frac{1}{|k_{\parallel}|} \sqrt{\pi} Z(\zeta_s) \\
&= \frac{n_s}{|k_{\parallel}|} \left(\frac{2p_s}{m_s n_s}\right)^{1/2} Z(\zeta_s). \tag{B.146}
\end{aligned}$$

For v_\perp^0, v_\parallel^2 ,

$$\begin{aligned}
& 2\pi\alpha_s \int_0^\infty dv_\perp v_\perp \int_{-\infty}^\infty dv_\parallel \frac{v_\parallel^2 \exp\left\{-\frac{m_s n_s}{2p_s}(v_\parallel^2 + v_\perp^2)\right\}}{k_\parallel v_\parallel - \omega'} \\
&= 2\pi\alpha_s \int_0^\infty dv_\perp v_\perp \exp\left\{-\frac{m_s n_s}{2p_s} v_\perp^2\right\} \int_{-\infty}^\infty dv_\parallel \frac{v_\parallel^2 \exp\left\{-\frac{m_s n_s}{2p_s} v_\parallel^2\right\}}{k_\parallel v_\parallel - \omega'} \\
&= 2\pi\alpha_s \frac{p_s}{m_s n_s} \frac{1}{|k_\parallel|} \frac{2p_s}{m_s n_s} \int_C du \frac{u^2 \exp\{-u^2\}}{u - \zeta_s} \\
&= \pi\alpha_s \frac{1}{|k_\parallel|} \left(\frac{2p_s}{m_s n_s}\right)^2 \sqrt{\pi} \zeta_s [1 + \zeta_s Z(\zeta_s)] \\
&= \frac{n_s}{|k_\parallel|} \left(\frac{2p_s}{m_s n_s}\right)^{1/2} \zeta_s [1 + \zeta_s Z(\zeta_s)]. \tag{B.147}
\end{aligned}$$

For v_\perp^0, v_\parallel^0 ,

$$\begin{aligned}
& 2\pi\alpha_s \int_0^\infty dv_\perp v_\perp \int_{-\infty}^\infty dv_\parallel \frac{\exp\left\{-\frac{m_s n_s}{2p_s}(v_\parallel^2 + v_\perp^2)\right\}}{k_\parallel v_\parallel - \omega'} \\
&= 2\pi\alpha_s \int_0^\infty dv_\perp v_\perp \exp\left\{-\frac{m_s n_s}{2p_s} v_\perp^2\right\} \int_{-\infty}^\infty dv_\parallel \frac{\exp\left\{-\frac{m_s n_s}{2p_s} v_\parallel^2\right\}}{k_\parallel v_\parallel - \omega'} \\
&= 2\pi\alpha_s \frac{p_s}{m_s n_s} \frac{1}{|k_\parallel|} \int_C du \frac{\exp\{-u^2\}}{u - \zeta_s} \\
&= 2\pi\alpha_s \frac{p_s}{m_s n_s} \frac{1}{|k_\parallel|} \sqrt{\pi} Z(\zeta_s) \\
&= \left(\frac{m_s n_s}{2p_s}\right)^{1/2} \frac{n_s}{|k_\parallel|} Z(\zeta_s). \tag{B.148}
\end{aligned}$$

B.6.2 Perpendicular pressure integrals

For $v_{\perp}^2, v_{\parallel}^1$,

$$\begin{aligned}
& 2\pi\alpha_s \int_0^\infty dv_{\perp} v_{\perp}^3 \int_{-\infty}^\infty dv_{\parallel} \frac{v_{\parallel} \exp\left\{-\frac{m_s n_s}{2p_s}(v_{\parallel}^2 + v_{\perp}^2)\right\}}{k_{\parallel} v_{\parallel} - \omega'} \\
&= 2\pi\alpha_s \int_0^\infty dv_{\perp} v_{\perp}^3 \exp\left\{-\frac{m_s n_s}{2p_s} v_{\perp}^2\right\} \int_{-\infty}^\infty dv_{\parallel} \frac{v_{\parallel} \exp\left\{-\frac{m_s n_s}{2p_s} v_{\parallel}^2\right\}}{k_{\parallel} v_{\parallel} - \omega'} \\
&= \pi\alpha_s \left(\frac{2p_s}{m_s n_s}\right)^2 \frac{1}{|k_{\parallel}|} \sqrt{\frac{2p_s}{m_s n_s}} \int_C du \frac{u \exp\{-u^2\}}{u - \zeta_s} \\
&= \pi\alpha_s \left(\frac{2p_s}{m_s n_s}\right)^2 \frac{1}{|k_{\parallel}|} \sqrt{\frac{2p_s}{m_s n_s}} \sqrt{\pi} [1 + \zeta_s Z(\zeta_s)] \\
&= \frac{2p_s}{|k_{\parallel}| m_s} [1 + \zeta_s Z(\zeta_s)]. \tag{B.149}
\end{aligned}$$

For $v_{\perp}^4, v_{\parallel}^0$,

$$\begin{aligned}
& 2\pi\alpha_s \int_0^\infty dv_{\perp} v_{\perp}^5 \int_{-\infty}^\infty dv_{\parallel} \frac{\exp\left\{-\frac{m_s n_s}{2p_s}(v_{\parallel}^2 + v_{\perp}^2)\right\}}{k_{\parallel} v_{\parallel} - \omega'} \\
&= 2\pi\alpha_s \int_0^\infty dv_{\perp} v_{\perp}^5 \exp\left\{-\frac{m_s n_s}{2p_s} v_{\perp}^2\right\} \int_{-\infty}^\infty dv_{\parallel} \frac{\exp\left\{-\frac{m_s n_s}{2p_s} v_{\parallel}^2\right\}}{k_{\parallel} v_{\parallel} - \omega'} \\
&= 2\pi\alpha_s \left(\frac{2p_s}{m_s n_s}\right)^3 \frac{1}{|k_{\parallel}|} \int_C du \frac{\exp\{-u^2\}}{u - \zeta_s} \\
&= 2\pi\alpha_s \left(\frac{2p_s}{m_s n_s}\right)^3 \frac{1}{|k_{\parallel}|} \sqrt{\pi} Z(\zeta_s) \\
&= \frac{2n_s}{k_{\parallel}} \left(\frac{2p_s}{m_s n_s}\right)^{3/2} Z(\zeta_s). \tag{B.150}
\end{aligned}$$

For $v_{\perp}^2, v_{\parallel}^2$,

$$\begin{aligned}
& 2\pi\alpha_s \int_0^\infty dv_{\perp} v_{\perp}^3 \int_{-\infty}^\infty dv_{\parallel} \frac{v_{\parallel}^2 \exp\left\{-\frac{m_s n_s}{2p_s} \left(\frac{v_{\parallel}^2}{T_{\parallel}^s} + \frac{v_{\perp}^2}{T_{\perp}^s}\right)\right\}}{k_{\parallel} v_{\parallel} - \omega'} \\
&= 2\pi\alpha_s \int_0^\infty dv_{\perp} v_{\perp}^3 \exp\left\{-\frac{m_s n_s}{2p_s} \frac{v_{\perp}^2}{T_{\perp}^s}\right\} \int_{-\infty}^\infty dv_{\parallel} \frac{v_{\parallel}^2 \exp\left\{-\frac{m_s n_s}{2p_s} \frac{v_{\parallel}^2}{T_{\parallel}^s}\right\}}{k_{\parallel} v_{\parallel} - \omega'} \\
&= 2\pi\alpha_s \left(\frac{2p_s}{m_s n_s}\right)^2 \frac{1}{2|k_{\parallel}|} \frac{2p_s}{m_s n_s} \int_{\mathcal{C}} du \frac{u^2 \exp\{-u^2\}}{u - \zeta_s} \\
&= 2\pi\alpha_s \left(\frac{2p_s}{m_s n_s}\right)^2 \frac{1}{2|k_{\parallel}|} \frac{2p_s}{m_s n_s} \sqrt{\pi} \zeta_s [1 + \zeta_s Z(\zeta_s)] \\
&= \frac{n_s}{k_{\parallel}} \left(\frac{2p_s}{m_s n_s}\right)^{3/2} \zeta_s [1 + \zeta_s Z(\zeta_s)]. \tag{B.151}
\end{aligned}$$

B.6.3 Parallel pressure integrals

For $v_{\perp}^0, v_{\parallel}^3$,

$$\begin{aligned}
& 2\pi\alpha_s \int_0^\infty dv_{\perp} v_{\perp} \int_{-\infty}^\infty dv_{\parallel} \frac{v_{\parallel}^3 \exp\left\{-\frac{m_s n_s}{2p_s} (v_{\parallel}^2 + v_{\perp}^2)\right\}}{k_{\parallel} v_{\parallel} - \omega'} \\
&= 2\pi\alpha_s \int_0^\infty dv_{\perp} v_{\perp} \exp\left\{-\frac{m_s n_s}{2p_s} v_{\perp}^2\right\} \int_{-\infty}^\infty dv_{\parallel} \frac{v_{\parallel}^3 \exp\left\{-\frac{m_s n_s}{2p_s} v_{\parallel}^2\right\}}{k_{\parallel} v_{\parallel} - \omega'} \\
&= 2\pi\alpha_s \frac{p_s}{m_s n_s} \frac{1}{|k_{\parallel}|} \left(\frac{2p_s}{m_s n_s}\right)^{3/2} \int_{\mathcal{C}} du \frac{u^3 \exp\{-u^2\}}{u - \zeta_s} \\
&= 2\pi\alpha_s \frac{p_s}{m_s n_s} \frac{1}{|k_{\parallel}|} \left(\frac{2p_s}{m_s n_s}\right)^{3/2} \frac{\sqrt{\pi}}{2} [1 + 2\zeta_s^2 (1 + \zeta_s Z(\zeta_s))] \\
&= \frac{p_s}{m_s |k_{\parallel}|} [1 + 2\zeta_s^2 (1 + \zeta_s Z(\zeta_s))]. \tag{B.152}
\end{aligned}$$

The v_\perp^2, v_\parallel^2 moment appears in the perpendicular pressure section and the v_\perp^0, v_\parallel^2 appears in the density section. For v_\perp^0, v_\parallel^4 ,

$$\begin{aligned}
& 2\pi\alpha_s \int_0^\infty dv_\perp v_\perp \int_{-\infty}^\infty dv_\parallel \frac{v_\parallel^4 \exp\left\{-\frac{m_s n_s}{2p_s}(v_\parallel^2 + v_\perp^2)\right\}}{k_\parallel v_\parallel - \omega'} \\
&= 2\pi\alpha_s \int_0^\infty dv_\perp v_\perp \exp\left\{-\frac{m_s n_s}{2p_s} v_\perp^2\right\} \int_{-\infty}^\infty dv_\parallel \frac{v_\parallel^4 \exp\left\{-\frac{m_s n_s}{2p_s} v_\parallel^2\right\}}{k_\parallel v_\parallel - \omega'} \\
&= 2\pi\alpha_s \frac{p_s}{m_s n_s} \frac{1}{|k_\parallel|} \left(\frac{2p_s}{m_s n_s}\right)^2 \int_{\mathcal{C}} du \frac{u^4 \exp\{-u^2\}}{u - \zeta_s} \\
&= 2\pi\alpha_s \frac{p_s}{m_s n_s} \frac{1}{|k_\parallel|} \left(\frac{2p_s}{m_s n_s}\right)^2 \frac{\sqrt{\pi}}{2} [\zeta_s^4 Z(\zeta_s) + \zeta_s] \\
&= \frac{n_s}{2|k_\parallel|} \left(\frac{2p_s}{m_s n_s}\right)^{3/2} \zeta_s [1 + 2\zeta_s^2 (1 + \zeta_s Z(\zeta_s))]. \tag{B.153}
\end{aligned}$$

Appendix C

The Chew-Goldberger-Low Equations

The Chew-Goldberger-Low equations are derived in this Appendix. They are first reported in [Chew et al. \[1956\]](#).

C.1 Derivation

Recalling the kinetic equation from Eq. [B.39](#),

$$\left\{ \frac{\partial}{\partial t} + (\hat{b}_i w_{\parallel} + u_i^s) \frac{\partial}{\partial x_i} + \frac{w_{\perp}^2}{2} \frac{\partial \hat{b}_i}{\partial x_i} \frac{\partial}{\partial w_{\parallel}} \right. \\ \left. + \left[\frac{q_s}{m_s} E_{\parallel} - \hat{b}_i \left(\frac{\partial u_i^s}{\partial t} + u_j^s \frac{\partial u_i^s}{\partial x_j} \right) \right] \left(\frac{\partial}{\partial w_{\parallel}} + \frac{w_{\parallel}}{w} \frac{\partial}{\partial w} \right) \right. \\ \left. - \frac{w_{\perp}^2}{2w} \frac{\partial u_i^s}{\partial x_i} \frac{\partial}{\partial w} + \hat{b}_i \hat{b}_j \frac{\partial u_i^s}{\partial x_j} \left[\left(\frac{w_{\perp}^2}{2} - w_{\parallel}^2 \right) \frac{1}{w} \frac{\partial}{\partial w} - w_{\parallel} \frac{\partial}{\partial w_{\parallel}} \right] \right\} f_s = -\nu_s [f_s - F_s] \quad (C.1)$$

to derive the CGL equations we will take the moments $w_{\perp}^2/2$, w_{\parallel}^2 . Let's define the perpendicular and parallel heat fluxes,

$$q_{\perp}^s = m_s \int d^3 w \frac{w_{\perp}^2}{2} w_{\parallel} f_s, \\ q_{\parallel}^s = m_s \int d^3 w w_{\parallel}^3 f_s. \quad (C.2)$$

C.1.1 Perpendicular pressure equation

Beginning with the perpendicular equation first,

$$\begin{aligned}
m_s \int d^3w \frac{w_\perp^2}{2} & \left\{ \underbrace{\frac{\partial}{\partial t}}_a + \underbrace{(\hat{b}_i w_{\parallel} + u_i^s) \frac{\partial}{\partial x_i}}_b + \underbrace{\frac{w_\perp^2}{2} \frac{\partial \hat{b}_i}{\partial x_i} \frac{\partial}{\partial w_{\parallel}}}_c \right. \\
& + \left[\frac{q_s}{m_s} E_{\parallel} - \hat{b}_i \left(\frac{\partial u_i^s}{\partial t} + u_j^s \frac{\partial u_i^s}{\partial x_j} \right) \right] \underbrace{\left(\frac{\partial}{\partial w_{\parallel}} + \frac{w_{\parallel}}{w} \frac{\partial}{\partial w} \right)}_d \\
& - \underbrace{\frac{w_\perp^2}{2w} \frac{\partial u_i^s}{\partial x_i} \frac{\partial}{\partial w}}_e + \hat{b}_i \hat{b}_j \frac{\partial u_i^s}{\partial x_j} \left[\underbrace{\left(\frac{w_\perp^2}{2} - w_{\parallel}^2 \right) \frac{1}{w} \frac{\partial}{\partial w}}_f - \underbrace{w_{\parallel} \frac{\partial}{\partial w_{\parallel}}}_g \right] \right\} f_s \\
& = \underbrace{\nu_s m_s \int d^3w \frac{w_\perp^2}{2} [F_s - f_s]}_h \quad (C.3)
\end{aligned}$$

working these term-by-term, starting with "a",

$$m_s \int d^3w \frac{w_\perp^2}{2} \frac{\partial}{\partial t} f_s = \frac{\partial}{\partial t} p_{\perp}^s \quad (C.4)$$

Since, w_i is the peculiar velocity. For term "b" we have,

$$m_s \int dw^3 \frac{w_\perp^2}{2} (\hat{b}_i w_{\parallel} + u_i^s) \frac{\partial}{\partial x_i} f_s = \hat{b}_i \frac{\partial}{\partial x_i} q_{\perp}^s + u_i \frac{\partial}{\partial x_i} p_{\perp}^s. \quad (C.5)$$

For "c",

$$m_s \int d^3w \left(\frac{w_\perp^2}{2} \right)^2 \frac{\partial \hat{b}_i}{\partial x_i} \frac{\partial}{\partial w_{\parallel}} f_s = -m_s \frac{\partial \hat{b}_i}{\partial x_i} \int d^3w f_s \frac{\partial}{\partial w_{\parallel}} \left(\frac{w_\perp^2}{2} \right)^2 = 2q_{\perp}^s \frac{\partial \hat{b}_i}{\partial x_i} \quad (C.6)$$

where we used integration by parts, using constraints of the distribution function $\lim_{|w_i| \rightarrow \infty} |w_i|^4 f_s = 0$ which we will use throughout. Additionally, $w_{\perp}^2 = w^2 - w_{\parallel}^2$ where we use $w_i^2 = w^2$ interchangably. Term "d",

$$\begin{aligned}
m_s \int d^3w \frac{w_\perp^2}{2} \left(\frac{\partial}{\partial w_{\parallel}} + \frac{w_{\parallel}}{w} \frac{\partial}{\partial w} \right) f_s & = m_s \int d^3w \left(\frac{\partial}{\partial w_{\parallel}} \frac{w_\perp^2}{2} f_s - f_s \frac{\partial}{\partial w_{\parallel}} \frac{w_\perp^2}{2} + \frac{w_\perp^2}{2} \frac{w_{\parallel}}{w} \frac{\partial}{\partial w} f_s \right) \\
& = m_s \int d^3w \left(2w_{\parallel} f_s + w_{\perp}^2 w_{\parallel} \frac{\partial}{\partial w^2} f_s \right) \\
& = m_s \int d^3w \left(2w_{\parallel} f_s + \frac{\partial}{\partial w^2} w_{\perp}^2 w_{\parallel} f_s - f_s \frac{\partial}{\partial w^2} w_{\perp}^2 w_{\parallel} \right) \\
& = m_s \int d^3w \left(2w_{\parallel} f_s - 2w_{\parallel} f_s \right) = 0, \quad (C.7)
\end{aligned}$$

using $dw^2 = 2w dw$. Term "e"

$$\begin{aligned} -m_s \int d^3 w \frac{w_\perp^4}{2w} \frac{\partial u_i^s}{\partial x_i} \frac{\partial}{\partial w} f_s &= -m_s \int d^3 w w_\perp^4 \frac{\partial u_i^s}{\partial x_i} \frac{\partial}{\partial w^2} f_s \\ &= -m_s \frac{\partial u_i^s}{\partial x_i} \int d^3 w \left(\frac{\partial}{\partial w^2} w_\perp^4 f_s - f_s \frac{\partial}{\partial w^2} w_\perp^4 \right) \\ &= 2m_s \frac{\partial u_i^s}{\partial x_i} \int d^3 w f_s w_\perp^2 = 2 \frac{\partial u_i^s}{\partial x_i} p_\perp^s. \end{aligned} \quad (\text{C.8})$$

Term "f",

$$\begin{aligned} m_s \int d^3 w \frac{w_\perp^2}{2} \left(\frac{w_\perp^2}{2} - w_\parallel^2 \right) \frac{1}{w} \frac{\partial}{\partial w} f_s &= m_s \int d^3 w w_\perp^2 \left(\frac{w_\perp^2}{2} - w_\parallel^2 \right) \frac{\partial}{\partial w^2} f_s \\ &= -m_s \int d^3 w f_s \frac{\partial}{\partial w^2} w_\perp^2 \left(\frac{w_\perp^2}{2} - w_\parallel^2 \right) = -m_s \int d^3 w f_s \frac{\partial}{\partial w^2} (w^2 - w_\parallel^2) \left(\frac{(w^2 - w_\parallel^2)}{2} - w_\parallel^2 \right) \\ &= -m_s \int d^3 w f_s \left(\left(\frac{(w^2 - w_\parallel^2)}{2} - w_\parallel^2 \right) + (w^2 - w_\parallel^2) \frac{1}{2} \right) = -m_s \int d^3 w f_s \left(w^2 - 2w_\parallel^2 \right). \end{aligned} \quad (\text{C.9})$$

Term "g",

$$m_s \int d^3 w \frac{w_\perp^2}{2} w_\parallel \frac{\partial}{\partial w_\parallel} f_s = -m_s \int d^3 w f_s \frac{\partial}{\partial w_\parallel} \frac{w^2 - w_\parallel^2}{2} w_\parallel = -m_s \int d^3 w f_s \left(\frac{w^2 - w_\parallel^2}{2} - w_\parallel^2 \right). \quad (\text{C.10})$$

Combining terms "f" and "g",

$$-m_s \int d^3 w f_s \left(w^2 - 2w_\parallel^2 \right) + m_s \int d^3 w f_s \left(\frac{w^2 - w_\parallel^2}{2} - w_\parallel^2 \right) = -m_s \int d^3 w f_s \frac{w_\perp^2}{2} = -p_\perp^s. \quad (\text{C.11})$$

Term "h"

$$\nu_s m_s \int d^3 w \frac{w_\perp^2}{2} [F_s - f_s] = \frac{\nu_s}{3} (p_\parallel^s - p_\perp^s), \quad (\text{C.12})$$

where the over bar denotes the equilibrium. Collecting all of the terms,

$$\frac{d^s}{dt} p_\perp^s + \hat{b}_i \frac{\partial}{\partial x_i} q_\perp^s + 2q_\perp^s \frac{\partial \hat{b}_i}{\partial x_i} + 2 \frac{\partial u_i^s}{\partial x_i} p_\perp^s - \hat{b}_i \hat{b}_j \frac{\partial u_i^s}{\partial x_j} p_\perp^s = \frac{\nu_s}{3} (p_\parallel^s - p_\perp^s), \quad (\text{C.13})$$

where we have used the definition of the convective derivative,

$$\frac{d^s}{dt} = \frac{\partial}{\partial t} + u_i^s \frac{\partial}{\partial x_i} \quad (\text{C.14})$$

Now rewrite the continuity equation (Equation D.26),

$$\begin{aligned} \frac{\partial}{\partial t} n^s + \frac{\partial}{\partial x_i} u_i^s n^s &= \frac{\partial}{\partial t} n^s + n^s \frac{\partial}{\partial x_i} u_i^s + u_i^s \frac{\partial}{\partial x_i} n^s = 0 \\ \Rightarrow \frac{1}{n_s} \frac{d^s}{dt} n_s &= -\partial_i u_i^s. \end{aligned} \quad (\text{C.15})$$

Now we can recall our induction equation (Equation 4.8) with the convective derivative,

$$\frac{d^p}{dt} b_i = b_j \frac{\partial}{\partial x_j} u_i^p - b_i \frac{\partial}{\partial x_j} u_j^p \quad (\text{C.16})$$

Recall that,

$$\frac{d^p}{dt} |b_i| = \hat{b}_i \frac{d^p}{dt} b_i \quad (\text{C.17})$$

from the definition of $\hat{b}_i = b_i/|b_i|$ so that we can write,

$$\frac{1}{|b_i|} \frac{d^p}{dt} |b_i| = \hat{b}_i \hat{b}_j \frac{\partial}{\partial x_j} u_i^p - \frac{\partial}{\partial x_j} u_j^p, \quad (\text{C.18})$$

where we used $\hat{b}_i \hat{b}_i = 1$. Let's return to our equation for the perpendicular pressure and rearrange,

$$\frac{d^p}{dt} p_\perp^s + \hat{b}_i \frac{\partial}{\partial x_i} q_\perp^s + 2q_\perp^s \frac{\partial \hat{b}_i}{\partial x_i} + \frac{\partial u_i^s}{\partial x_i} p_\perp^s + \left(\frac{\partial u_i^s}{\partial x_i} - \hat{b}_i \hat{b}_j \frac{\partial u_i^s}{\partial x_j} \right) p_\perp^s = \frac{\nu_s}{3} (p_\parallel^s - p_\perp^s), \quad (\text{C.19})$$

and if we set $s = p$ our equations for the magnetic field strength and density can be inserted,

$$\frac{d^p}{dt} p_\perp^p + \hat{b}_i \frac{\partial}{\partial x_i} q_\perp^p + 2q_\perp^p \frac{\partial \hat{b}_i}{\partial x_i} - \frac{p_\perp^p}{n_p} \frac{d^p}{dt} n_p - \frac{p_\perp^p}{|b_i|} \frac{d^p}{dt} |b_i| = \frac{\nu_s}{3} (p_\parallel^p - p_\perp^p), \quad (\text{C.20})$$

now if we divide the equation by $n_p |b_i|$ and combine the heat flux terms, the perpendicular CGL equation can be seen after using product rule,

$$n_p |b_i| \frac{d^p}{dt} \frac{p_\perp^p}{n_p |b_i|} = -\frac{\partial}{\partial x_i} q_\perp^p \hat{b}_i - q_\perp^p \frac{\partial \hat{b}_i}{\partial x_i} + \frac{\nu_s}{3} (p_\parallel^p - p_\perp^p). \quad (\text{C.21})$$

C.1.2 Parallel pressure equation

For the parallel pressure equation we consider the moment,

$$\begin{aligned}
& m_s \int d^3w w_{\parallel}^2 \left\{ \underbrace{\frac{\partial}{\partial t}}_a + \underbrace{(\hat{b}_i w_{\parallel} + u_i^s) \frac{\partial}{\partial x_i}}_b + \underbrace{\frac{w_{\perp}^2}{2} \frac{\partial \hat{b}_i}{\partial x_i} \frac{\partial}{\partial w_{\parallel}}}_c \right. \\
& + \left[\frac{q_s}{m_s} E_{\parallel} - \hat{b}_i \left(\frac{\partial u_i^s}{\partial t} + u_j^s \frac{\partial u_i^s}{\partial x_j} \right) \right] \underbrace{\left(\frac{\partial}{\partial w_{\parallel}} + \frac{w_{\parallel}}{w} \frac{\partial}{\partial w} \right)}_d \\
& - \underbrace{\frac{w_{\perp}^2}{2w} \frac{\partial u_i^s}{\partial x_i} \frac{\partial}{\partial w}}_e + \hat{b}_i \hat{b}_j \frac{\partial u_i^s}{\partial x_j} \left[\underbrace{\left(\frac{w_{\perp}^2}{2} - w_{\parallel}^2 \right) \frac{1}{w} \frac{\partial}{\partial w}}_f - \underbrace{w_{\parallel} \frac{\partial}{\partial w_{\parallel}}}_g \right] \right\} f_s \\
& = \underbrace{\nu_s m_s \int d^3w w_{\parallel}^2 [F_s - f_s]}_h. \tag{C.22}
\end{aligned}$$

Starting with term “a”,

$$m_s \int d^3w w_{\parallel}^2 \frac{\partial}{\partial t} f_s = \frac{\partial}{\partial t} p_{\parallel}^s. \tag{C.23}$$

Term “b”

$$m_s \int d^3w w_{\parallel}^2 (\hat{b}_i w_{\parallel} + u_i^s) \frac{\partial}{\partial x_i} f_s = \hat{b}_i \frac{\partial}{\partial x_i} q_{\parallel}^s + u_i^s \frac{\partial}{\partial x_i} p_{\parallel}^s, \tag{C.24}$$

where the definition of the parallel heat flux was introduced at the beginning of this section. Term “c”,

$$\begin{aligned}
& m_s \int d^3w w_{\parallel}^2 \frac{w_{\perp}^2}{2} \frac{\partial \hat{b}_i}{\partial x_i} \frac{\partial}{\partial w_{\parallel}} f_s = -m_s \frac{\partial \hat{b}_i}{\partial x_i} \int d^3w f_s \frac{\partial}{\partial w_{\parallel}} w_{\parallel}^2 \frac{w_{\perp}^2}{2} \\
& = -m_s \frac{\partial \hat{b}_i}{\partial x_i} \int d^3w f_s (w_{\parallel} w_{\perp}^2 - w_{\parallel}^3) = (q_{\parallel} - 2q_{\perp}^s) \frac{\partial \hat{b}_i}{\partial x_i}. \tag{C.25}
\end{aligned}$$

where integration by parts and typical constraints on the distribution functions were used. Term “d”,

$$\begin{aligned}
& m_s \int d^3w w_{\parallel}^2 \left(\frac{\partial}{\partial w_{\parallel}} + \frac{w_{\parallel}}{w} \frac{\partial}{\partial w^2} \right) f_s = -m_s \int d^3w f_s \left(\frac{\partial}{\partial w_{\parallel}} w_{\parallel}^2 + 2 \frac{\partial}{\partial w^2} w_{\parallel}^3 \right) \\
& = -m_s \int d^3w f_s \left(2w_{\parallel} + 2 \frac{\partial}{\partial w^2} \right) = -2m_s \int d^3w f_s \frac{\partial w_{\parallel}}{\partial w^2} \frac{\partial}{\partial w_{\parallel}} w_{\parallel}^3 \\
& = -2m_s \int d^3w f_s w_{\parallel} = 0 \tag{C.26}
\end{aligned}$$

where we used the fact that $\int d^3w w_{\parallel} = 0$ due to the choice of frame. Term "e",

$$\begin{aligned} -m_s \frac{\partial u_i^s}{\partial x_i} \int d^3w w_{\parallel}^2 \frac{(w^2 - w_{\parallel}^2)}{2w} \frac{\partial}{\partial w} f_s &= m_s \frac{\partial u_i^s}{\partial x_i} \int d^3w f_s \frac{\partial}{\partial w^2} (w^2 - w_{\parallel}^2) w_{\parallel}^2 \\ &= m_s \frac{\partial u_i^s}{\partial x_i} \int d^3w f_s \frac{\partial}{\partial w^2} (w^2 - w_{\parallel}^2) w_{\parallel}^2 = m_s \frac{\partial u_i^s}{\partial x_i} \int d^3w f_s \frac{\partial}{\partial w^2} (w^2 - w_{\parallel}^2) w_{\parallel}^2 \\ &= m_s \frac{\partial u_i^s}{\partial x_i} \int d^3w f_s w_{\parallel}^2 = \frac{\partial u_i^s}{\partial x_i} p_{\parallel}^s. \end{aligned} \quad (\text{C.27})$$

Term "f",

$$\begin{aligned} m_s \int d^3w w_{\parallel}^2 \left(\frac{w_{\perp}^2}{2} - w_{\parallel}^2 \right) \frac{1}{w} \frac{\partial}{\partial w} f_s &= 2m_s \int d^3w w_{\parallel}^2 \left(\frac{w_{\perp}^2}{2} - w_{\parallel}^2 \right) \frac{\partial}{\partial w^2} f_s \\ &= -2m_s \int d^3w f_s w_{\parallel}^2 \frac{\partial}{\partial w^2} \left(\frac{w^2 - w_{\parallel}^2}{2} - w_{\parallel}^2 \right) = -m_s \int d^3w f_s w_{\parallel}^2 = -p_{\parallel}^s \end{aligned} \quad (\text{C.28})$$

Term "g",

$$m_s \int d^3w w_{\parallel}^3 \frac{\partial}{\partial w_{\parallel}} f_s = -m_s \int d^3w f_s \frac{\partial}{\partial w_{\parallel}} w_{\parallel}^3 = -3p_{\parallel}^s. \quad (\text{C.29})$$

Term "h",

$$\nu_s m_s \int d^3w w_{\parallel}^2 [F_s - f_s] = p^s - p_{\parallel}^s = \frac{2\nu_s}{3} (p_{\perp}^s - p_{\parallel}^s). \quad (\text{C.30})$$

Collecting all of the terms and combining some of them,

$$\frac{\partial}{\partial t} p_{\parallel}^s + \frac{\partial}{\partial x_i} \hat{b}_i q_{\parallel}^s + u_i^s \frac{\partial}{\partial x_i} p_{\parallel}^s - 2q_{\perp}^s \frac{\partial \hat{b}_i}{\partial x_i} + \frac{\partial u_i^s}{\partial x_i} p_{\parallel}^s + 2p_{\parallel}^s \hat{b}_i \hat{b}_j \frac{\partial u_i^s}{\partial x_j} = \frac{2\nu_s}{3} (p_{\perp}^s - p_{\parallel}^s). \quad (\text{C.31})$$

Now we want to rearrange so we can write the parallel CGL equation. Recalling the induction equation,

$$\frac{1}{|b_i|} \frac{dp}{dt} |b_i| = \hat{b}_i \hat{b}_j \frac{\partial}{\partial x_j} u_i^p - \frac{\partial}{\partial x_j} u_j^p, \quad (\text{C.32})$$

and rearranging the pressure equation,

$$\begin{aligned} \frac{\partial}{\partial t} p_{\parallel}^s + \frac{\partial}{\partial x_i} \hat{b}_i q_{\parallel}^s + u_i^s \frac{\partial}{\partial x_i} p_{\parallel}^s - 2q_{\perp}^s \frac{\partial \hat{b}_i}{\partial x_i} + 3 \frac{\partial u_i^s}{\partial x_i} p_{\parallel}^s \\ + 2p_{\parallel}^s \left(\hat{b}_i \hat{b}_j \frac{\partial u_i^s}{\partial x_j} - \frac{\partial u_i^s}{\partial x_i} \right) = \frac{2\nu_s}{3} (p_{\perp}^s - p_{\parallel}^s), \end{aligned} \quad (\text{C.33})$$

inserting the induction equation,

$$\frac{dp}{dt} p_{\parallel}^p + \frac{\partial}{\partial x_i} \hat{b}_i q_{\parallel}^p - 2q_{\perp}^p \frac{\partial \hat{b}_i}{\partial x_i} + 3 \frac{\partial u_i^p}{\partial x_i} p_{\parallel}^p + 2 \frac{p_{\parallel}^p}{|b_i|} \frac{dp}{dt} |b_i| = \frac{2\nu_p}{3} (p_{\perp}^p - p_{\parallel}^p). \quad (\text{C.34})$$

Recalling the continuity equation,

$$\frac{1}{n_s} \frac{ds}{dt} n_s = - \frac{\partial}{\partial x_i} u_i^s, \quad (\text{C.35})$$

so we can write,

$$\frac{dp}{dt} p_{\parallel}^p + \frac{\partial}{\partial x_i} \hat{b}_i q_{\parallel}^p - 2q_{\perp}^p \frac{\partial \hat{b}_i}{\partial x_i} - 3 \frac{p_{\parallel}^p}{n_p} \frac{dp}{dt} n_s + 2 \frac{p_{\parallel}^p}{|b_i|} \frac{dp}{dt} |b_i| = \frac{2\nu_p}{3} (p_{\perp}^p - p_{\parallel}^p). \quad (\text{C.36})$$

Multiplying by $|b_i|^2/n_p^3$ allows the convective derivatives to be combined, and then multiplying by the inverse,

$$\frac{n_p^3}{|b_i|^2} \frac{dp}{dt} \left(\frac{p_{\parallel}^p |b_i|^2}{n_p^3} \right) = - \frac{\partial}{\partial x_i} \hat{b}_i q_{\parallel}^p + 2q_{\perp}^p \frac{\partial \hat{b}_i}{\partial x_i} + \frac{2\nu_p}{3} (p_{\perp}^p - p_{\parallel}^p). \quad (\text{C.37})$$

Appendix D

Deriving Ohm's Law

We begin by writing the Vlasov equation,

$$\left[\frac{\partial}{\partial t} + v_i \frac{\partial}{\partial x_i} + F_{i,\alpha} \frac{\partial}{\partial v_i} \right] f_\alpha(\mathbf{x}, \mathbf{v}, t) = 0 \quad (\text{D.1})$$

for charged particles subject to an electromagnetic field, we write the Lorentz force per unit mass and Maxwell's equations

$$F_{i,\alpha} = \frac{q_\alpha}{m_\alpha} \left[E_i + \epsilon_{ijk} \frac{v_j B_k}{c} \right] \quad (\text{D.2})$$

$$\frac{\partial}{\partial x_i} E_i = 4\pi \sum_\alpha q_\alpha n_\alpha \quad (\text{D.3})$$

$$\frac{\partial}{\partial x_i} B_i = 0 \quad (\text{D.4})$$

$$\epsilon_{ijk} \frac{\partial}{\partial x_j} E_k = -\frac{1}{c} \frac{\partial}{\partial t} B_i \quad (\text{D.5})$$

$$\epsilon_{ijk} \frac{\partial}{\partial x_j} B_k = \frac{1}{c} \frac{\partial}{\partial t} E_i + \frac{4\pi}{c} \sum_\alpha j_{i,\alpha} \quad (\text{D.6})$$

$$n_\alpha = \int_{\tau_v} d^3 v f_\alpha \quad (\text{D.7})$$

$$n_\alpha j_{i,\alpha} = q_\alpha \int_{\tau_v} d^3 v v_i f_\alpha \quad (\text{D.8})$$

together we have the Vlasov-Maxwell [V-M] system of equations in [cgs] units. The equations are written in modified Einstein notation typical to fluid mechanics, so that the summation of the current density $j_{i,\alpha}$ is vector with latin index i (implied summation) and the explicit sum over species appears with greek index α . The velocity v_i is a phase space variable and independent of space and time, it is the occupation of the state, to be averaged giving the configuration space

velocity $u_{i,\alpha}$. The Lorentz force $F_{i,\alpha}$ depends on the electric E_i and magnetic fields B_i which are functions of space \mathbf{x} and time t . The distribution function $f_\alpha = f_\alpha(\mathbf{x}, \mathbf{v}, t)$ is understood as the probability of particles of species α having phase space coordinates (\mathbf{x}, \mathbf{v}) in the range (d^3x, d^3v) at time t , giving the particle number:

$$N_\alpha = \int_{\tau_x} d^3x \int_{\tau_v} d^3v f_\alpha(\mathbf{x}, \mathbf{v}, t) \quad (\text{D.9})$$

by integrating over the whole volumes in physical τ_x and velocity τ_v space. The equations here are 0th order and the particles describe the electric and magnetic fields via average in a self-consistent manner. Currently our interest is to derive the fluid equations so we introduce these definitions:

$$n_\alpha u_{i,\alpha} = \int_{\tau_v} d^3v v_i f_\alpha \quad (\text{D.10})$$

$$E_{ii}^\alpha = \frac{m_\alpha}{2} \int_{\tau_v} d^3v v_i v_i f_\alpha \quad (\text{D.11})$$

$$P_{ij}^\alpha = m_\alpha \int_{\tau_v} d^3v (v_i - u_{i,\alpha})(v_j - u_{j,\alpha}) f_\alpha \quad (\text{D.12})$$

$$T_{ijj}^\alpha = m_\alpha \int_{\tau_v} d^3v (v_i - u_{i,\alpha})(v_j - u_{j,\alpha})(v_j - u_{j,\alpha}) f_\alpha \quad (\text{D.13})$$

In order, the species α density n_α , the species α configuration space velocity $u_{i,\alpha}$, the species α kinetic energy E_{ii}^α , the species α pressure tensor P_{ij}^α and the species α kinetic energy flux T_{ijj}^α . For completeness these quantities here are integrated over the velocity space τ_v passing to configuration space variables, functions of \mathbf{x} and t .

D.1 Fluid Equations

This section will derive the continuity and momentum which constitute the 0th and 1st orders of the fluid equations. This will be completed from the V-M in an academic manner for clarity and future reference.

D.1.1 Continuity

Taking the 0th moment $\int d^3v$ of the collisionless Boltzmann equation (Eq. D.1) produces the continuity equation:

$$\int_{\tau_v} d^3v \left[\frac{\partial}{\partial t} + v_i \frac{\partial}{\partial x_i} + \frac{F_{i,\alpha}}{m_\alpha} \frac{\partial}{\partial v_i} \right] f_\alpha = 0 \quad (\text{D.14})$$

Now term-by-term the first term can be integrated with the commutation of the derivative and anti-derivative:

$$\int_{\tau_v} d^3v \frac{\partial}{\partial t} f_\alpha = \frac{\partial}{\partial t} \int_{\tau_v} d^3v f_\alpha \quad (\text{D.15})$$

$$= \frac{\partial}{\partial t} n_\alpha \quad (\text{D.16})$$

The second term we use the fact that v_i is a phase space variable so it is independent of x_i and then the commutation of the derivative/anti-derivative to write:

$$\int_{\tau_v} d^3v v_i \frac{\partial}{\partial x_i} f_\alpha = \frac{\partial}{\partial x_i} \int_{\tau_v} d^3v v_i f_\alpha \quad (\text{D.17})$$

$$= \frac{\partial}{\partial x_i} n_\alpha u_{i,\alpha} \quad (\text{D.18})$$

The integral here is the first moment of the velocity field giving the average velocity $u_{i,\alpha} = u_{i,\alpha}(\mathbf{x}, t)$ of the species α product with the density n_α . Continuing with the third term, substituting in the Lorentz force per unit mass (Eq. D.2) for $F_{i,\alpha}/m_\alpha$, passing to the Vlasov equation:

$$\int_{\tau_v} d^3v \frac{q_\alpha}{m_\alpha} \left[E_i + \epsilon_{ijk} \frac{v_j B_k}{c} \right] \frac{\partial}{\partial v_i} f_\alpha \quad (\text{D.19})$$

$$= \frac{q_\alpha}{m_\alpha} \int_{\tau_v} d^3v \frac{\partial}{\partial v_i} E_i f_\alpha + \frac{q_\alpha}{m_\alpha} \int_{\tau_v} d^3v \epsilon_{ijk} \frac{v_j B_k}{c} \frac{\partial}{\partial v_i} f_\alpha \quad (\text{D.20})$$

The first term can be handled with Gauss' Law, noting that the electric field E_i does not depend on velocity,:

$$\frac{q_\alpha}{m_\alpha} \int_{\tau_v} d^3v \frac{\partial}{\partial v_i} E_i f_\alpha = \frac{q_\alpha}{m_\alpha} E_i \int_{\sigma_v} d^2v \hat{v}_i f_\alpha \quad (\text{D.21})$$

We have not commented much about the geometry, but here we have passed from a volume integral d^3v over the volume τ_v to a surface integral d^2v over the surface σ_v , both in velocity phase space. The bounds of the integral are infinite, and so if we consider a physically realizable distribution function, there will be no particles with $\pm\infty$ velocity, hence, the distribution function will go to zero, and the surface integral will be zero as well. So, the above term is zero, with the restriction that the distribution function f_α will go to zero. To make this clear, consider the integral, using Gauss' law to simplify:

$$\int_{\tau_v} d^3v \frac{\partial}{\partial v_i} |v_j|^p f_\alpha = \int_{\sigma_v} d^2v \hat{v}_i |v_j|^p f_\alpha = [|v_j|^p f_\alpha]_{-\infty}^{+\infty} = 0 \quad (\text{D.22})$$

Where $|v_j| = \sqrt{v_j v_j}$ is of order p . Here we assume the distribution function goes to zero quicker than $O(|v_j|^{-p})$. This is not true in general so we make restrictions of order p so that the above equality is true. Last, we note that this will reappear frequently throughout the derivation so we will reference equation D.22 and the surrounding text often. Returning from the digression we demonstrate on the second term involving the magnetic field B_i . It can be shown to be zero, using product rule on the derivative:

$$\frac{q_\alpha}{m_\alpha} \int_{\tau_v} d^3v \epsilon_{ijk} \frac{v_j B_k}{c} \frac{\partial}{\partial v_i} f_\alpha = \frac{q_\alpha}{m_\alpha} \int_{\tau_v} d^3v \left[\epsilon_{ijk} \frac{\partial}{\partial v_i} \frac{v_j B_k}{c} f_\alpha - f_\alpha \epsilon_{ijk} \frac{\partial}{\partial v_i} \frac{v_j B_k}{c} \right] \quad (\text{D.23})$$

The first term is zero due again when we use Gauss' Law, here we restriction on the distribution function that it goes to zero at a rate faster than $O(|v_i|^{-1})$.

Now let's work the second term form above:

$$\begin{aligned} \frac{q_\alpha}{m_\alpha} \int_{\tau_v} d^3v \epsilon_{ijk} \frac{v_j B_k}{c} \frac{\partial}{\partial v_i} f_\alpha &= -\frac{q_\alpha}{m_\alpha} \int_{\tau_v} d^3v f_\alpha \epsilon_{ijk} \frac{\partial}{\partial v_i} \frac{v_j B_k}{c} \\ &= -\frac{q_\alpha}{m_\alpha} \int_{\tau_v} d^3v f_\alpha \epsilon_{ijk} \left[\frac{v_j}{c} \frac{\partial}{\partial v_i} B_k + \frac{B_k}{c} \frac{\partial}{\partial v_i} v_j \right] \end{aligned} \quad (\text{D.24})$$

The first term is zero since the magnetic field only depends on space and time, and the second term is zero since the derivative produces $\frac{\partial}{\partial v_i} v_j = \delta_{ij}$ a kronecker delta δ_{ij} . The kronecker delta δ_{ij} only has a value for $i = j$ and the levi-civita symbol is zero when any of i, j, k are equal, the identity is written: $\delta_{ij} \epsilon_{ijk} = \delta_{ik} \epsilon_{ijk} = \delta_{jk} \epsilon_{ijk} = 0$. We have recovered the continuity equation:

$$\frac{\partial}{\partial t} n_\alpha + \frac{\partial}{\partial x_i} n_\alpha u_{i,\alpha} = 0 \quad (\text{D.26})$$

for species α .

D.1.2 Momentum Equation

To derive the fluid momentum equation we must take the first velocity moment $\int_{\tau_v} d^3v v_j$ of the collisionless Boltzmann equation:

$$\int_{\tau_v} d^3v v_j \left[\frac{\partial}{\partial t} + v_i \frac{\partial}{\partial x_i} + F_{i,\alpha} \frac{\partial}{\partial v_i} \right] f_\alpha = 0 \quad (\text{D.27})$$

The first term can be dealt with the time-independence of the phase velocity, commutation of the derivative/anti-derivative and then the first moment of

velocity field. In that order:

$$\int_{\tau_v} d^3v v_j \frac{\partial}{\partial t} f_\alpha = \int_{\tau_v} d^3v \frac{\partial}{\partial t} v_j f_\alpha \quad (\text{D.28})$$

$$= \frac{\partial}{\partial t} \int_{\tau_v} d^3v v_j f_\alpha \quad (\text{D.29})$$

$$= \frac{\partial}{\partial t} n_\alpha u_{j,\alpha} \quad (\text{D.30})$$

The second term from Eq.D.27 can be considered by first noting the phase velocity v_i does not depend on space and the commutation of the derivative/anti-derivative:

$$\int_{\tau_v} d^3v v_j v_i \frac{\partial}{\partial x_i} f_\alpha = \frac{\partial}{\partial x_i} \int_{\tau_v} d^3v v_j v_i f_\alpha \quad (\text{D.31})$$

Now consider the pressure P_{ij}^α , expanding the terms:

$$P_{ij}^\alpha = \int_{\tau_v} d^3v m_\alpha (v_i - u_{i,\alpha}) (v_j - u_{j,\alpha}) f_\alpha \quad (\text{D.32})$$

$$= \int_{\tau_v} d^3v m_\alpha (v_i v_j - v_i u_{j,\alpha} - u_{i,\alpha} v_j + u_{i,\alpha} u_{j,\alpha}) f_\alpha \quad (\text{D.33})$$

and recognizing that the spatial derivative of the first term here, after dividing by the mass m_α , is the second term in the momentum equation (Eq. D.27), we rewrite the term:

$$\frac{\partial}{\partial x_i} \int_{\tau_v} d^3v v_j v_i f_\alpha = \frac{1}{m_\alpha} \frac{\partial}{\partial x_i} P_{ij}^\alpha + \frac{\partial}{\partial x_i} \int_{\tau_v} d^3v (v_i u_{j,\alpha} + u_{i,\alpha} v_j - u_{i,\alpha} u_{j,\alpha}) f_\alpha \quad (\text{D.34})$$

The integrals, noting that the configuration space velocity $u_{i,\alpha}$ does not depend on the phase space velocity v_i , are simple:

$$\frac{\partial}{\partial x_i} \int_{\tau_v} d^3v v_i u_{j,\alpha} f_\alpha = \frac{\partial}{\partial x_i} u_{j,\alpha} \int_{\tau_v} d^3v v_i f_\alpha = \frac{\partial}{\partial x_i} n_\alpha u_{j,\alpha} u_{i,\alpha} \quad (\text{D.35})$$

$$\frac{\partial}{\partial x_i} \int_{\tau_v} d^3v v_j u_{i,\alpha} f_\alpha = \frac{\partial}{\partial x_i} u_{i,\alpha} \int_{\tau_v} d^3v v_j f_\alpha = \frac{\partial}{\partial x_i} n_\alpha u_{j,\alpha} u_{i,\alpha} \quad (\text{D.36})$$

$$\frac{\partial}{\partial x_i} \int_{\tau_v} d^3v u_{i,\alpha} u_{j,\alpha} f_\alpha = \frac{\partial}{\partial x_i} u_{i,\alpha} u_{j,\alpha} \int_{\tau_v} d^3v f_\alpha = \frac{\partial}{\partial x_i} n_\alpha u_{j,\alpha} u_{i,\alpha} \quad (\text{D.37})$$

After some cancellation yields,

$$\frac{\partial}{\partial x_i} \int_{\tau_v} d^3v v_j v_i f_\alpha = \frac{1}{m_\alpha} \frac{\partial}{\partial x_i} P_{ij}^\alpha + \frac{\partial}{\partial x_i} n_\alpha u_{j,\alpha} u_{i,\alpha} \quad (\text{D.38})$$

We will reuse this method of introducing the pressure to account for the $\int_{\tau_v} d^3v v_j v_i f_\alpha$ term. Now for the last term in Eq. D.27, substituting the Lorentz force per

unit mass in for $F_{i,\alpha}$ appears:

$$\frac{q_\alpha}{m_\alpha} \int_{\tau_v} d^3v v_j \left[E_i + \epsilon_{ilm} \frac{v_l B_m}{c} \right] \frac{\partial}{\partial v_i} f_\alpha \quad (\text{D.39})$$

Starting with the electric field E_i , which is independent of the phase space velocity v_i , term and use product rule to rearrange the terms:

$$\frac{q_\alpha}{m_\alpha} \int_{\tau_v} d^3v v_j E_i \frac{\partial}{\partial v_i} f_\alpha = E_i \frac{q_\alpha}{m_\alpha} \int_{\tau_v} d^3v \left[\frac{\partial}{\partial v_i} f_\alpha v_j - f_\alpha \frac{\partial}{\partial v_i} v_j \right] \quad (\text{D.40})$$

The first term here is simplified with Gauss' Law and the second term produces a kronecker delta:

$$E_i \frac{q_\alpha}{m_\alpha} \int_{\tau_v} d^3v \left[\frac{\partial}{\partial v_i} f_\alpha v_j - f_\alpha \frac{\partial}{\partial v_i} v_j \right] = E_i \frac{q_\alpha}{m_\alpha} \left[\int_{\sigma_v} d^2v \hat{v}_i f_\alpha v_j - \delta_{ij} \int_{\tau_v} d^3v f_\alpha \right] \quad (\text{D.41})$$

The first term is zero for distribution functions we are considering (following Eq. D.22). The remaining integral is simple, concluding:

$$\frac{q_\alpha}{m_\alpha} \int_{\tau_v} d^3v v_j E_i \frac{\partial}{\partial v_i} f_\alpha = -E_i \frac{q_\alpha}{m_\alpha} \delta_{ij} \int_{\tau_v} d^3v f_\alpha = -\frac{q_\alpha}{m_\alpha} E_j n_\alpha \quad (\text{D.42})$$

Now for the magnetic field B_i term from Eq. D.27 with the Lorentz force per unit mass. First rearrange the derivative with product rule:

$$\frac{q_\alpha}{m_\alpha} \int_{\tau_v} d^3v v_j \epsilon_{ilm} \frac{v_l B_m}{c} \frac{\partial}{\partial v_i} f_\alpha = \quad (\text{D.43})$$

$$\frac{q_\alpha}{m_\alpha} \int_{\tau_v} d^3v \left[\frac{\partial}{\partial v_i} v_j \epsilon_{ilm} \frac{v_l B_m}{c} f_\alpha - \epsilon_{ilm} \frac{B_m v_j}{c} f_\alpha \frac{\partial}{\partial v_i} v_l - \epsilon_{ilm} f_\alpha \frac{v_l B_m}{c} \frac{\partial}{\partial v_i} v_j \right] \quad (\text{D.44})$$

The first term is zero for the distribution function we are considering, but now we have advance the restriction to f_α decaying faster than $O(|v_i|^{-2})$ (see Eq. D.22). The second and third term produce kronecker deltas:

$$\frac{q_\alpha}{m_\alpha} \int_{\tau_v} d^3v \left[\frac{\partial}{\partial v_i} v_j \epsilon_{ilm} \frac{v_l B_m}{c} f_\alpha \xrightarrow{0} - \epsilon_{ilm} \frac{B_m v_j}{c} f_\alpha \frac{\partial}{\partial v_i} v_l - \epsilon_{ilm} f_\alpha \frac{v_l B_m}{c} \frac{\partial}{\partial v_i} v_j \right] \quad (\text{D.45})$$

$$= \frac{q_\alpha}{m_\alpha} \int_{\tau_v} d^3v \left[-v_j \epsilon_{ilm} f_\alpha \frac{B_m}{c} \delta_{il} - \epsilon_{ilm} f_\alpha \frac{v_l B_m}{c} \delta_{ij} \right] \quad (\text{D.46})$$

Now the first term is zero due to the identity $\epsilon_{ijk}\delta_{ij} = 0$, but the second term is not, since the index j does not appear in the levi-civita symbol, continuing:

$$\frac{q_\alpha}{m_\alpha} \int_{\tau_v} d^3v \left[-\cancel{v_j \epsilon_{ilm} f_\alpha \frac{B_m}{c} \delta_{il}}^0 - \epsilon_{ilm} f_\alpha \frac{v_l B_m}{c} \delta_{ij} \right] = -\frac{q_\alpha}{m_\alpha} \int_{\tau_v} d^3v \epsilon_{jlm} f_\alpha \frac{v_l B_m}{c} \quad (\text{D.47})$$

The integral is just the first velocity moment:

$$-\frac{q_\alpha}{m_\alpha} \int_{\tau_v} d^3v \epsilon_{jlm} \frac{v_l B_m}{c} f_\alpha = -\frac{q_\alpha}{m_\alpha c} \epsilon_{jlm} B_m \int_{\tau_v} d^3v v_l f_\alpha = -\frac{q_\alpha}{m_\alpha} n_\alpha \epsilon_{jlm} \frac{u_{l,\alpha} B_m}{c} \quad (\text{D.48})$$

Now to write the full momentum equation:

$$\int_{\tau_v} d^3v v_j \left[\frac{\partial}{\partial t} + v_i \frac{\partial}{\partial x_i} + F_{i,\alpha} \frac{\partial}{\partial v_i} \right] f_\alpha \quad (\text{D.49})$$

$$= \frac{\partial}{\partial t} n_\alpha u_{j,\alpha} + \frac{\partial}{\partial x_i} P_{ij}^\alpha + \frac{\partial}{\partial x_i} n_\alpha u_{j,\alpha} u_{i,\alpha} - \frac{q_\alpha n_\alpha}{m_\alpha} \left[E_j + \epsilon_{jlm} \frac{u_{l,\alpha} B_m}{c} \right] \quad (\text{D.50})$$

Re-writing for clarity:

$$\frac{\partial}{\partial t} n_\alpha u_{j,\alpha} + \frac{\partial}{\partial x_i} n_\alpha u_{j,\alpha} u_{i,\alpha} = -\frac{1}{m_\alpha} \frac{\partial}{\partial x_i} P_{ij}^\alpha + \frac{q_\alpha n_\alpha}{m_\alpha} \left[E_j + \epsilon_{jlm} \frac{u_{l,\alpha} B_m}{c} \right] \quad (\text{D.51})$$

D.2 1-Fluid Equations

We have been rigorous thus far, now we will begin employing approximations to simplify the equations. The terms we will introduce are:

1. Mass density: $\rho_m = m_e n_e + m_p n_p$
2. Charge density: $\rho = n_e q_e + n_p q_p$; $q_p = -q_e$
3. Current density: $j_i = u_{i,e} n_e q_e + u_{i,p} n_p q_p$
4. Fluid velocity:

$$u_i = \frac{m_e n_e u_{i,e} + m_p n_p u_{i,p}}{\rho_m}$$

5. Fluid pressure: $P_{ij}^\alpha = P_{ij}^p + P_{ij}^e$

The approximations consist of:

1. Quasi-neutrality: $n_e \approx n_p \Rightarrow n_e = n_p = n$
2. Mass ratio: $1 >> m_e/m_p \approx 0.00108 \Rightarrow \rho_m = n(m_e + m_p) = m_p n$
3. 1-fluid velocity (using the previous two relations):

$$u_i = \frac{m_e n_e u_{i,e} + m_p n_p u_{i,p}}{\rho_m} = \frac{m_p n (u_{i,e}(m_e/m_p) + u_{i,p})}{\rho_m} \approx u_{i,e} \frac{m_e}{m_p} + u_{i,p} \approx u_{i,p}$$

4. Negligible displacement current: $(\Omega^{pc}/\omega_{p,p})^2 << 1$

These approximations are supported by considering length and time scales. First we define characteristic quantities of a plasma:

1. Debye length:

$$\lambda_{D,\alpha} = \left(\frac{k_B T_\alpha}{4\pi n_\alpha q_\alpha^2} \right)^{1/2} \quad (\text{D.52})$$

2. Plasma Frequency:

$$\omega_{p,\alpha} = \left(\frac{4\pi n_\alpha q_\alpha^2}{m_\alpha} \right)^{1/2} \quad (\text{D.53})$$

3. Thermal Speed:

$$v_{th,\alpha} = \left(\frac{k_B T_\alpha}{m_\alpha} \right)^{1/2} = \lambda_{D,\alpha} \omega_{p,\alpha} \quad (\text{D.54})$$

4. Cyclotron Frequency:

$$\Omega^{\alpha c} = \frac{q_\alpha |B_i|}{m_\alpha c} \quad (\text{D.55})$$

5. Alfvén Velocity:

$$u_i^A = \frac{B_i}{\sqrt{4\pi \rho_m}} \quad (\text{D.56})$$

6. Species Inertial Length:

$$d_\alpha = \frac{c}{\omega_{p,\alpha}} = \frac{|u_i^A|}{\omega_{p,\alpha}} \quad (\text{D.57})$$

The Boltzmann constant k_B , speed of light c and the species temperature T_α have been introduced. The definition of the Alfvén velocity here, is defined with

fluid mass density, but we can write it for protons, or electrons, it is not useful to us to make that definition here. The first assumption of quasi-neutrality is the plasma approximation which introduces factors of $1/\lambda_{D,\alpha}^p$ increasing in exponent p , therefore if the length scales we consider are much larger, the approximation is valid. The third assumption of 1-fluid velocity is valid if the frequency range we consider is much larger than the typical speed of the species, say the thermal velocity. Writing these assumptions explicitly:

1. quasi-neutrality: $l \gg \lambda_{D,e}$
3. 1-fluid velocity: $\omega \ll \omega_{p,e}$

The characteristic length scale l and frequency ω are the scales of our system. This is the essence of the magnetohydrodynamic approach: large length-scale and low frequency.

D.2.1 Continuity

Write the continuity equation for the electrons and protons:

$$\frac{\partial}{\partial t} n_e + \frac{\partial}{\partial x_i} n_e u_{i,e} = 0 \quad (\text{D.58})$$

$$\frac{\partial}{\partial t} n_p + \frac{\partial}{\partial x_i} n_p u_{i,p} = 0 \quad (\text{D.59})$$

First, mass continuity, simply multiply by the respective masses and add the two equations:

$$\frac{\partial}{\partial t} (m_p n_p + m_e n_e) + \frac{\partial}{\partial x_i} (m_p n_p u_{i,p} + m_e n_e u_{i,e}) = 0 \quad (\text{D.60})$$

Recognize that we have introduced two variables from the introduction to this section (sec. D.2) to write:

$$\frac{\partial}{\partial t} (m_p n_p + m_e n_e) + \frac{\partial}{\partial x_i} (m_p n_p u_{i,p} + m_e n_e u_{i,e}) = \frac{\partial}{\partial t} \rho_m + \frac{\partial}{\partial x_i} \rho_m u_i = 0 \quad (\text{D.61})$$

Now multiply both equations (eqns. D.58) by respective q_α , substitute in e (as seen in the introduction to section D.2) and add the two equations:

$$\frac{\partial}{\partial t} \left(q_p n_p - q_p n_e \right) + \frac{\partial}{\partial x_i} \left(q_p n_e u_{i,e} - q_p n_e u_{i,e} \right) = 0 \quad (\text{D.62})$$

Recognize we have introduced two quantities from the introduction of section D.2 to write the one-fluid continuity equation:

$$\frac{\partial}{\partial t} \rho + \frac{\partial}{\partial x_i} j_i = 0 \quad (\text{D.63})$$

D.2.2 Combining the momentum equations

Writing the momentum equations (derived in section D.1.2) for protons ($\alpha = p$) and electrons ($\alpha = e$) and multiplying by their respective masses (m_p, m_e):

$$\frac{\partial}{\partial t} m_p n_p u_{j,p} + \frac{\partial}{\partial x_i} m_p n_p u_{j,p} u_{i,p} = -\frac{\partial}{\partial x_i} P_{ij}^p + q_p n_p \left[E_j + \epsilon_{jlm} \frac{u_{l,p} B_m}{c} \right] \quad (\text{D.64})$$

$$\frac{\partial}{\partial t} m_e n_e u_{j,e} + \frac{\partial}{\partial x_i} m_e n_e u_{j,e} u_{i,e} = -\frac{\partial}{\partial x_i} P_{ij}^e + q_e n_e \left[E_j + \epsilon_{jlm} \frac{u_{l,e} B_m}{c} \right] \quad (\text{D.65})$$

Summing the two equations will produce the 1-fluid momentum equation; we will take this term-by-term. Starting with the partial time derivative: multiple by the respective masses, add them, and recognize introduced quantities:

$$\frac{\partial}{\partial t} m_p n_p u_{j,p} + \frac{\partial}{\partial t} m_e n_e u_{j,e} = \frac{\partial}{\partial t} \left(m_p n_p u_{j,p} + m_e n_e u_{j,e} \right) = \frac{\partial}{\partial t} \rho_m u_j \quad (\text{D.66})$$

The non-linear terms: use quasi-neutrality and reciprocate the proton mass:

$$\frac{\partial}{\partial x_i} \left(m_p n_p u_{j,p} u_{i,p} + m_e n_e u_{j,e} u_{i,e} \right) = \frac{\partial}{\partial x_i} m_p n \left(u_{j,p} u_{i,p} + \frac{m_e}{m_p} u_{j,e} u_{i,e} \right) \quad (\text{D.67})$$

In our approximation, the term $\frac{m_e}{m_p} u_{j,e}$ is approximately zero and the flow velocity $u_{j,p} \approx u_i$ so we write:

$$\frac{\partial}{\partial x_i} \left(m_p n_p u_{j,p} u_{i,p} + m_e n_e u_{j,e} u_{i,e} \right) = \frac{\partial}{\partial x_i} \rho_m u_j u_i \quad (\text{D.68})$$

The pressure term can just be summed after we have multiplied by the mass:

$$-\frac{\partial}{\partial x_i} P_{ij}^e - \frac{\partial}{\partial x_i} P_{ij}^p = -\frac{\partial}{\partial x_i} P_{ij} \quad (\text{D.69})$$

Last we can add the Lorentz force terms, summing:

$$q_e n_e \left[E_j + \epsilon_{jlm} \frac{u_{l,e} B_m}{c} \right] + q_p n_p \left[E_j + \epsilon_{jlm} \frac{u_{l,p} B_m}{c} \right] \quad (\text{D.70})$$

$$= E_j \left[q_e n_e + q_p n_p \right] + \epsilon_{jlm} \frac{B_m}{c} \left[q_e n_e u_{l,e} + q_p n_p u_{l,p} \right] \quad (\text{D.71})$$

Recognize, that the first term cancels due to quasi-neutrality and the fact that ($q_p = -q_e$) and second term introduces the current density:

$$E_j \left[q_e n_e + q_p n_p \right] + \epsilon_{jlm} \frac{B_m}{c} \left[q_e n_e u_{l,e} + q_p n_p u_{l,p} \right] = \cancel{E_j \left[n(q_p - q_p) \right]}^0 + \epsilon_{jlm} \frac{j_l B_m}{c} \quad (\text{D.72})$$

Collect all the terms to write the 1-fluid momentum equation:

$$\frac{\partial}{\partial t} \rho_m u_j + \frac{\partial}{\partial x_i} \rho_m u_j u_i = - \frac{\partial}{\partial x_i} P_{ij} + \epsilon_{jlm} \frac{j_l B_m}{c} \quad (\text{D.73})$$

D.2.3 Ohm's Law

First we can work the definition of the current density, by making the quasi-neutrality assumption and writing the charges ($q_p = -q_e$) explicitly:

$$j_i = n_p q_p u_{i,p} + n_e q_e u_{i,e} = n (q_p u_{i,p} + q_e u_{i,e}) = n q_p (u_{i,p} - u_{i,e}) \quad (\text{D.74})$$

Now, rearrange the expression for the electron average velocity, and use the 1-fluid velocity approximation:

$$u_{i,e} = u_{i,p} - \frac{j_i}{n q_p} = u_i - \frac{j_i}{n q_p} \quad (\text{D.75})$$

Obviously these are approximations, but I have used equal signs. We can now write the equations as the average fluid velocity u_i and the current density j_i .

Multiplying by the respective charge ($q_p = -q_e$) and adding the two fluid equations (protons, electrons),

$$\frac{\partial}{\partial t} q_p n_p u_{j,p} + \frac{\partial}{\partial x_i} q_p n_p u_{j,p} u_{i,p} = - \frac{\partial}{\partial x_i} \frac{q_p P_{ij}^p}{m_p} + \frac{q_p^2 n_p}{m_p} \left[E_j + \epsilon_{jlm} \frac{u_{l,p} B_m}{c} \right] \quad (\text{D.76})$$

$$- \frac{\partial}{\partial t} q_p n_e u_{j,e} - \frac{\partial}{\partial x_i} q_p n_e u_{j,e} u_{i,e} = \frac{\partial}{\partial x_i} \frac{q_p P_{ij}^e}{m_e} + \frac{q_p^2 n_e}{m_e} \left[E_j + \epsilon_{jlm} \frac{u_{l,e} B_m}{c} \right] \quad (\text{D.77})$$

allows us to combine them with the Maxwell equations to re-write a simple relation between the magnetic and electric fields. Let's go term-by-term, starting with the the partial time derivative:

$$\frac{\partial}{\partial t} \left(q_p n_p u_{j,p} - q_p n_e u_{j,e} \right) = \frac{\partial}{\partial t} j_j \quad (\text{D.78})$$

Next, the non-linear terms: make the quasi-neutrality assumption and the 1-fluid approximation, then substitute the approximation for the electron velocity (Eq. D.75):

$$\frac{\partial}{\partial x_i} \left(q_p n_p u_{j,p} u_{i,p} - q_p n_e u_{j,e} u_{i,e} \right) = \frac{\partial}{\partial x_i} q_p n \left(u_j u_i - u_{j,e} u_{i,e} \right) \quad (\text{D.79})$$

$$= \frac{\partial}{\partial x_i} q_p n \left[u_j u_i - \left(u_j - \frac{j_j}{n q_p} \right) \left(u_i - \frac{j_i}{n q_p} \right) \right] \quad (\text{D.80})$$

$$= \frac{\partial}{\partial x_i} q_p n \left[u_j u_i - \left(u_j u_i - \frac{u_j j_i}{n q_p} - \frac{j_j u_i}{n q_p} + \frac{j_j j_i}{n^2 q_p^2} \right) \right] \quad (\text{D.81})$$

$$= \frac{\partial}{\partial x_i} q_p n \left(\frac{u_j j_i}{n q_p} + \frac{j_j u_i}{n q_p} - \frac{j_j j_i}{n^2 q_p^2} \right) \quad (\text{D.82})$$

$$= \frac{\partial}{\partial x_i} \left(u_j j_i + j_j u_i - \frac{j_j j_i}{n q_p} \right) \quad (\text{D.83})$$

On to the pressure terms:

$$-\frac{\partial}{\partial x_i} \frac{q_p P_{ij}^p}{m_p} + \frac{\partial}{\partial x_i} \frac{q_p P_{ij}^e}{m_e} = q_p \frac{\partial}{\partial x_i} \left(\frac{P_{ij}^e}{m_e} - \frac{P_{ij}^p}{m_p} \right) \quad (\text{D.84})$$

Last, work the by Lorentz force terms with quasi-neutrality and then the approximation for the electron velocity (Eq. D.75) and 1-fluid velocity:

$$\frac{q_p^2 n_p}{m_p} \left[E_j + \epsilon_{jlm} \frac{u_{l,p} B_m}{c} \right] + \frac{q_p^2 n_e}{m_e} \left[E_j + \epsilon_{jlm} \frac{u_{l,e} B_m}{c} \right] \quad (\text{D.85})$$

$$= q_p^2 n \left[\frac{E_j}{m_p} + \epsilon_{jlm} \frac{u_{l,p} B_m}{m_p c} + \frac{E_j}{m_e} + \epsilon_{jlm} \frac{u_{l,e} B_m}{m_e c} \right] \quad (\text{D.86})$$

$$= q_p^2 n \left[\frac{E_j}{m_p} + \epsilon_{jlm} \frac{u_l B_m}{m_p c} + \frac{E_j}{m_e} + \epsilon_{jlm} \frac{B_m}{m_e c} \left(u_l - \frac{j_l}{n q_p} \right) \right] \quad (\text{D.87})$$

Introduce the reduced mass $\mu = (m_p + m_e)/m_p m_e$ and combine terms:

$$q_p^2 n \left[\frac{E_j}{m_p} + \epsilon_{jlm} \frac{u_l B_m}{m_p c} + \frac{E_j}{m_e} + \epsilon_{jlm} \frac{B_m}{m_e c} \left(u_l - \frac{j_l}{n q_p} \right) \right] \quad (\text{D.88})$$

$$= q_p^2 n \left[\mu E_j + \mu \epsilon_{jlm} \frac{u_l B_m}{c} - \epsilon_{jlm} \frac{B_m j_l}{m_e c n q_p} \right] \quad (\text{D.89})$$

$$= q_p^2 n \mu E_j + \frac{q_p^2 n \mu}{c} \epsilon_{jlm} u_l B_m - \frac{q_p}{m_e c} \epsilon_{jlm} j_l B_m \quad (\text{D.90})$$

Collect all the terms:

$$\frac{\partial}{\partial t} j_j + \frac{\partial}{\partial x_i} \left(u_j j_i + j_j u_i - \frac{j_j j_i}{n q_p} \right) \quad (\text{D.91})$$

$$= q_p \frac{\partial}{\partial x_i} \left(\frac{P_{ij}^e}{m_e} - \frac{P_{ij}^p}{m_p} \right) + q_p^2 n \mu E_j + \frac{2 q_p^2 n \mu}{c} \epsilon_{jlm} u_l B_m - \frac{q_p}{m_e c} \epsilon_{jlm} j_l B_m \quad (\text{D.92})$$

This is the generalized Ohm's law with out the collisional term.

D.2.3.1 Asymptotic Ordering

To compare the relevance of the terms as the scales of interest, we write the Ohm's law in dimensionless quantities, with these characteristic quantities:

$$\boxed{\bar{u}_i = u_i^A; \quad \bar{\omega} = \Omega^{pc}; \quad \bar{l} = u_i^A / \Omega^{pc} = c / \omega_{p,p} = d_p; \quad \bar{n} = n}$$

$$\boxed{\bar{j}_i = \bar{n} u_i^A q_p; \quad \bar{E}_i = m_p u_i^A \Omega^{pc} / q_p; \quad \bar{B} = m_p c \Omega^{pc} / q_p; \quad \bar{P}_{ij}^\alpha = \bar{n} m_\alpha |u_i^A|^2}$$

We have introduced the Alfvèn velocity $u_i^A = B_i / \sqrt{\rho_m}$, the proton cyclotron frequency $\Omega^{pc} = q_p |B_i| / cm_p$, the proton inertial length d_p and finally \bar{n} is the characteristic number density. The algebra is messy, so it will not appear here. The dimensionless equations that we obtain are:

$$\frac{1}{\mu m_p} \frac{\partial}{\partial t} j_j + \frac{1}{\mu m_p} \frac{\partial}{\partial x_i} \left(u_j j_i + j_j u_i - j_j j_i \right) \quad (\text{D.93})$$

$$= \frac{1}{\mu m_p} \frac{\partial}{\partial x_i} \left(P_{ij}^e - P_{ij}^p \right) + E_j + 2 \epsilon_{jlm} u_l B_m - \frac{1}{\mu m_e} \epsilon_{jlm} j_l B_m \quad (\text{D.94})$$

Now we can use Maxwell's system of equations to re-write the time derivative of the current, re-writing them:

$$\frac{\partial}{\partial x_i} E_i = 0 \quad (\text{D.95})$$

$$\frac{\partial}{\partial x_i} B_i = 0 \quad (\text{D.96})$$

$$\epsilon_{ijk} \frac{\partial}{\partial x_j} E_k = -\frac{1}{c} \frac{\partial}{\partial t} B_i \quad (\text{D.97})$$

$$\epsilon_{ijk} \frac{\partial}{\partial x_j} B_k = \frac{1}{c} \frac{\partial}{\partial t} E_i + \frac{4\pi}{c} j_i \quad (\text{D.98})$$

Notice, quasi-neutrality is used in the Gauss' law for the electric field (eqn, D.95) and we have used the fluid current density in Ampere's equation (Eq. D.98). Start by rearranging Ampere's equation (Eq. D.98) for the current density and taking the partial time derivative, also using the linearity of the derivative/anti-derivative:

$$\frac{4\pi}{c} \frac{\partial}{\partial t} j_i = -\frac{1}{c} \frac{\partial^2}{\partial t^2} E_i + \epsilon_{ijk} \frac{\partial}{\partial x_j} \frac{\partial}{\partial t} B_k \quad (\text{D.99})$$

The second term on the RHS can be re-written with Faraday's equation (Eq. D.97), also reciprocate term out front of the partial time derivative of the current density:

$$\frac{\partial}{\partial t} j_i = -\frac{1}{4\pi} \frac{\partial^2}{\partial t^2} E_i - \frac{c^2}{4\pi} \epsilon_{ijk} \frac{\partial}{\partial x_j} \epsilon_{klm} \frac{\partial}{\partial x_l} E_m \quad (\text{D.100})$$

Utilizing the same normalization, as for the Ohm's law we find:

$$\frac{\partial}{\partial t} j_i = -\left(\frac{\Omega^{pc}}{\omega_{p,p}}\right)^2 \left[\frac{\partial^2}{\partial t^2} E_i + \frac{c^2}{|u_i^A|^2} \epsilon_{ijk} \frac{\partial}{\partial x_j} \epsilon_{klm} \frac{\partial}{\partial x_l} E_m \right] \quad (\text{D.101})$$

Distributing the characteristic quantities out front of the square bracket:

$$\frac{\partial}{\partial t} j_i = -\left[\left(\frac{\Omega^{pc}}{\omega_{p,p}}\right)^2 \frac{\partial^2}{\partial t^2} E_i + \epsilon_{ijk} \frac{\partial}{\partial x_j} \epsilon_{klm} \frac{\partial}{\partial x_l} E_m \right] \quad (\text{D.102})$$

Working with the normalization used for Ohm's law, we write:

$$\frac{1}{\mu m_p} \frac{\partial}{\partial t} j_i = -\frac{1}{\mu m_p} \left[\left(\frac{\Omega^{pc}}{\omega_{p,p}}\right)^2 \frac{\partial^2}{\partial t^2} E_i + \left(\frac{\Omega^{pc}}{\omega_{p,p}}\right)^2 \frac{c^2}{|u_i^A|^2} \epsilon_{ijk} \frac{\partial}{\partial x_j} \epsilon_{klm} \frac{\partial}{\partial x_l} E_m \right]^1 \quad (\text{D.103})$$

Noting the definition of the ion inertial length gives one in the second term in the square bracket. Now, combine the equations (re-writing Eq. D.93):

$$-\frac{1}{\mu m_p} \left[\left(\frac{\Omega^{pc}}{\omega_{p,p}} \right)^2 \frac{\partial^2}{\partial t^2} E_j + \epsilon_{jlm} \frac{\partial}{\partial x_l} \epsilon_{mno} \frac{\partial}{\partial x_n} E_o \right] + \frac{1}{\mu m_p} \frac{\partial}{\partial x_i} \left(u_j j_i + j_j u_i - j_j j_i \right) \quad (\text{D.104})$$

$$= \frac{1}{\mu m_p} \frac{\partial}{\partial x_i} \left(P_{ij}^e - P_{ij}^p \right) + E_j + \epsilon_{jlm} u_l B_m - \frac{1}{\mu m_e} \epsilon_{jlm} j_l B_m \quad (\text{D.105})$$

First we can work the double curl of the electric field term, noting the levacivita is a constant tensor, using the identity $\epsilon_{ijk} \epsilon_{klm} = \delta_{il} \delta_{jm} - \delta_{im} \delta_{jl}$ and using Gauss' law for the electric field (Eq. D.95) to recover:

$$\begin{aligned} -\epsilon_{jlm} \frac{\partial}{\partial x_l} \epsilon_{mno} \frac{\partial}{\partial x_n} E_o &= -\frac{\partial}{\partial x_l} \frac{\partial}{\partial x_n} \epsilon_{jlm} \epsilon_{mno} E_o = -\frac{\partial}{\partial x_l} \frac{\partial}{\partial x_n} [\delta_{jn} \delta_{lo} - \delta_{jo} \delta_{ln}] E_o \\ &= -\left[\frac{\partial}{\partial x_l} \frac{\partial}{\partial x_j} \overset{0}{E}_l - \frac{\partial}{\partial x_l} \frac{\partial}{\partial x_l} E_j \right] = \frac{\partial}{\partial x_l} \frac{\partial}{\partial x_l} E_j \end{aligned} \quad (\text{D.106})$$

So that we can write:

$$-\frac{1}{\mu m_p} \left[\left(\frac{\Omega^{pc}}{\omega_{p,p}} \right)^2 \frac{\partial^2}{\partial t^2} E_j - \frac{\partial}{\partial x_l} \frac{\partial}{\partial x_l} E_j \right] + \frac{1}{\mu m_p} \frac{\partial}{\partial x_i} \left(u_j j_i + j_j u_i - j_j j_i \right) \quad (\text{D.107})$$

$$= \frac{1}{\mu m_p} \frac{\partial}{\partial x_i} \left(P_{ij}^e - P_{ij}^p \right) + E_j + \epsilon_{jlm} u_l B_m - \frac{1}{\mu m_e} \epsilon_{jlm} j_l B_m \quad (\text{D.108})$$

In our notation, the frequency ratio out front of the partial time derivative:

$$\left(\frac{\Omega^{pc}}{\omega_{p,p}} \right)^2 = \frac{|B_i|^2}{4\pi n_p c^2} \quad (\text{D.109})$$

So, this term is much smaller than $1/\mu m_p \approx 0.00108$ due to the $c^2 n_p$ in the denominator. Continue by taking $(\Omega^{pc}/\omega_{p,p})^2 \rightarrow 0$ to write:

$$\frac{1}{\mu m_p} \frac{\partial}{\partial x_l} \frac{\partial}{\partial x_l} E_j + \frac{1}{\mu m_p} \frac{\partial}{\partial x_i} \left(u_j j_i + j_j u_i - j_j j_i \right) \quad (\text{D.110})$$

$$= \frac{1}{\mu m_p} \frac{\partial}{\partial x_i} \left(P_{ij}^e - P_{ij}^p \right) + E_j + 2\epsilon_{jlm} u_l B_m - \frac{1}{\mu m_e} \epsilon_{jlm} j_l B_m \quad (\text{D.111})$$

Next we will use the mass ratio ($m_p \gg m_e$) to make the assumption that,

$$\mu = \frac{1}{m_p} + \frac{1}{m_e} \approx \frac{1}{m_e} \quad (\text{D.112})$$

to write:

$$\frac{m_e}{m_p} \frac{\partial}{\partial x_l} \frac{\partial}{\partial x_l} E_j + \frac{m_e}{m_p} \frac{\partial}{\partial x_i} \left(u_j j_i + j_j u_i - j_j j_i \right) \quad (\text{D.113})$$

$$= \frac{m_e}{m_p} \frac{\partial}{\partial x_i} \left(P_{ij}^e - P_{ij}^p \right) + E_j + \epsilon_{jlm} u_l B_m - \epsilon_{jlm} j_l B_m \quad (\text{D.114})$$

At this point we recognize that we have a Helmholtz-like equation for the electric field. At this point, to write the magnetohydrodynamic equations, we must also take the ratio $m_e/m_p \approx 0$. Rearranging a bit and re-writing:

$$E_j = -\epsilon_{jlm} u_l B_m + \epsilon_{jlm} j_l B_m \quad (\text{D.115})$$

We have written the generalized Ohm's law for Hall Magnetohydrodynamics.

Bibliography

- H. Alfvén. Existence of Electromagnetic-Hydrodynamic Waves. *Nature*, 150(3805):405–406, 1942. ISSN 0028-0836. doi: 10.1038/150405d0. [58](#)
- E. Anderson, Z. Bai, C. Bischof, S. Blackford, J. Demmel, J. Dongarra, J. Du Croz, A. Greenbaum, S. Hammarling, A. McKenney, and D. Sorensen. *LAPACK Users' Guide*. Society for Industrial and Applied Mathematics, Philadelphia, PA, third edition, 1999. ISBN 0-89871-447-8 (paperback). [109](#)
- V. Angelopoulos, P. Cruce, A. Drozdov, E. W. Grimes, N. Hatzigeorgiu, D. A. King, D. Larson, J. W. Lewis, J. M. McTiernan, D. A. Roberts, C. L. Russell, T. Hori, Y. Kasahara, A. Kumamoto, A. Matsuoka, Y. Miyashita, Y. Miyoshi, I. Shinohara, M. Teramoto, J. B. Faden, A. J. Halford, M. McCarthy, R. M. Millan, J. G. Sample, D. M. Smith, L. A. Woodger, A. Masson, A. A. Narock, K. Asamura, T. F. Chang, C.-Y. Chiang, Y. Kazama, K. Keika, S. Matsuda, T. Segawa, K. Seki, M. Shoji, S. W. Y. Tam, N. Umemura, B.-J. Wang, S.-Y. Wang, R. Redmon, J. V. Rodriguez, H. J. Singer, J. Vandegriff, S. Abe, M. Nose, A. Shinburi, Y.-M. Tanaka, S. UeNo, L. Andersson, P. Dunn, C. Fowler, J. S. Halekas, T. Hara, Y. Harada, C. O. Lee, R. Lillis, D. L. Mitchell, M. R. Argall, K. Bromund, J. L. Burch, I. J. Cohen, M. Gallay, B. Giles, A. N. Jaynes, O. Le Contel, M. Oka, T. D. Phan, B. M. Walsh, J. Westlake, F. D. Wilder, S. D. Bale, R. Livi, M. Pulupa, P. Whittlesey, A. DeWolfe, B. Harter, E. Lucas, U. Auster, J. W. Bonnell, C. M. Cully, E. Donovan, R. E. Ergun, H. U. Frey, B. Jackel, A. Keiling, H. Korth, J. P. McFadden, Y. Nishimura, F. Plaschke, P. Robert, D. L. Turner, J. M. Weygand, R. M. Candey, R. C. Johnson, T. Kovalick, M. H. Liu, R. E. McGuire, A. Breneman, K. Kersten, and P. Schroeder. The Space Physics Environment Data Analysis System (SPEDAS). *Space Science Reviews*, 215(1):9, 2019. ISSN 0038-6308. doi: 10.1007/s11214-018-0576-4. [141](#)
- Patrick Astfalk and Frank Jenko. On the Quasi-linear Saturation of the Parallel Proton Firehose Instability Using a Full-f Approach. *Journal of Geophysical Research: Space Physics*, 123(9):7153–7166, 2018. ISSN 2169-9380. doi: 10.1029/2017ja025143. [174](#)
- S. D. Bale, J. C. Kasper, G. G. Howes, E. Quataert, C. Salem, and D. Sundkvist. Magnetic Fluctuation Power Near Proton Temperature Anisotropy Instability Thresholds in the Solar Wind. *Physical Review Letters*, 103(21):211101, 2009. ISSN 0031-9007. doi: 10.1103/physrevlett.103.211101. [171](#)
- Aaron Barnes. Collisionless Damping of Hydromagnetic Waves. *Physics of*

Fluids, 9(8):1483, 1966. ISSN 0031-9171. doi: 10.1063/1.1761882. 46, 50, 56, 69, 83, 88, 114, 115, 116, 127, 198

Aaron Barnes and Joseph V Hollweg. Large-amplitude hydromagnetic waves. *Journal of Geophysical Research*, 79(16):2302–2318, 1974. 29

M. Barnes, I. G. Abel, W. Dorland, D. R. Ernst, G. W. Hammett, P. Ricci, B. N. Rogers, A. A. Schekochihin, and T. Tatsuno. Linearized model Fokker–Planck collision operators for gyrokinetic simulations. II. Numerical implementation and tests. *Physics of Plasmas (1994-present)*, 16(7):072107, 2009. ISSN 1070-664X. doi: 10.1063/1.3155085. 113

B. Bavassano and R. Bruno. Evidence of local generation of Alfvénic turbulence in the solar wind. *Journal of Geophysical Research: Space Physics*, 94(A9): 11977–11982, 1989. ISSN 0148-0227. doi: 10.1029/ja094ia09p11977. 88

J. W. Belcher and Leverett Davis. Large-amplitude Alfvén waves in the interplanetary medium, 2. *Journal of Geophysical Research*, 76(16):3534–3563, 1971. ISSN 0148-0227. doi: 10.1029/ja076i016p03534. 83

P. L. Bhatnagar, E. P. Gross, and M. Krook. A Model for Collision Processes in Gases. I. Small Amplitude Processes in Charged and Neutral One-Component Systems. *Physical Review*, 94(3):511–525, 1954. ISSN 0031-899X. doi: 10.1103/physrev.94.511. 45

Trevor A Bowen, Samuel Badman, Petr Hellinger, and Stuart D Bale. Density Fluctuations in the Solar Wind Driven by Alfvén Wave Parametric Decay. *The Astrophysical Journal*, 854(2):L33, 2018. doi: 10.3847/2041-8213/aaabbe. 85

K. J. Bowers, B. J. Albright, L. Yin, B. Bergen, and T. J. T. Kwan. Ultrahigh performance three-dimensional electromagnetic relativistic kinetic plasma simulationa). *Physics of Plasmas*, 15(5):055703, 2008. ISSN 1070-664X. doi: 10.1063/1.2840133. 172

S. I. Braginskii. Transport Phenomena in a Completely Ionized Two-Temperature Plasma. *J. Exptl. Theoret. Phys. (U.S.S.R.)*, 1957. 44, 52, 113

Roberto Bruno and Vincenzo Carbone. The solar wind as a turbulence laboratory. *Living Reviews in Solar Physics*, 10(1):2, 2013. 29, 73, 79, 85, 86, 87

L. F. Burlaga and K. W. Ogilvie. Magnetic and thermal pressures in the solar wind. *Solar Physics*, 15(1):61–71, 1970. ISSN 0038-0938. doi: 10.1007/bf00149472. 83

Benjamin D. G. Chandran, Bo Li, Barrett N. Rogers, Eliot Quataert, and Kai Germaschewski. Perpendicular ion heating by low-frequency Alfvén-wave turbulence in the solar wind. *The Astrophysical Journal*, 720(1):503, 2010. ISSN 0004-637X. doi: 10.1088/0004-637x/720/1/503. [81](#)

C H K Chen. Recent progress in astrophysical plasma turbulence from solar wind observations. *Journal of Plasma Physics*, 2016. doi: 10.1017/s0022377816001124. [12](#), [87](#), [88](#), [89](#), [141](#), [156](#)

G. F. Chew, M. L. Goldberger, and F. E. Low. The Boltzmann equation and the one-fluid hydromagnetic equations in the absence of particle collisions. *Proceedings of the Royal Society of London. Series A. Mathematical and Physical Sciences*, 236(1204):112–118, 1956. ISSN 0080-4630. doi: 10.1098/rspa.1956.0116. [131](#), [132](#), [249](#)

Jr. Coleman, Paul J. Turbulence, Viscosity, and Dissipation in the Solar-Wind Plasma. *The Astrophysical Journal*, 153:371, August 1968. doi: 10.1086/149674. [85](#), [87](#)

F. V. Coroniti and A. Eviatar. Magnetic field reconnection in a collisionless plasma. *Astrophys. J., Suppl. Ser.*, 33:189–210, February 1977. doi: 10.1086/190423. [171](#)

National Research Council, editor. *Space Plasma Physics—The Study of Solar-System Plasmas: Volume 2, Working Papers, Part 1, Solar-System Magnetohydrodynamics*. The National Academies Press, Washington, DC, 1979. doi: 10.17226/12375. URL <https://nap.nationalacademies.org/catalog/12375/space-plasma-physics-the-study-of-solar-system-plasmas-volume>. [198](#)

Steven R Cranmer. Ensemble Simulations of Proton Heating in the Solar Wind via Turbulence and Ion Cyclotron Resonance. *The Astrophysical Journal*, 213(1):16, 2014. ISSN 0067-0049. doi: 10.1088/0067-0049/213/1/16. [79](#)

R C Davidson and Joan M Ogden. Electromagnetic ion cyclotron instability driven by ion energy anisotropy in high-beta plasmas. *Physics of Fluids*, 18(8):1045, 1975. ISSN 0031-9171. doi: 10.1063/1.861253. [174](#), [175](#), [188](#)

Ronald C Davidson. Nonlinear Development of Electromagnetic Instabilities in Anisotropic Plasmas. *Physics of Fluids*, 15(2):317, 1972. ISSN 0031-9171. doi: 10.1063/1.1693910. [174](#), [176](#)

- Peter Debye and Erich Hückel. De la theorie des electrolytes. i. abaissement du point de congelation et phenomenes associes. *Physikalische Zeitschrift*, 24(9): 185–206, 1923. [25](#)
- Paul J. Dellar. Lecture notes for Part 1 of MMathPhys “Kinetic Theory”, 2015. <https://people.maths.ox.ac.uk/dellar/papers/MMPkinetic.pdf>. [9](#), [33](#), [35](#)
- Jr Derby, N F. Modulational instability of finite-amplitude, circularly polarized Alfvén waves. *The Astrophysical Journal*, 224:1013, 1978. ISSN 0004-637X. doi: 10.1086/156451. [85](#)
- Pablo Dmitruk and W. H. Matthaeus. Waves and turbulence in magnetohydrodynamic direct numerical simulations. *Physics of Plasmas*, 16(6):062304, 2009. ISSN 1070-664X. doi: 10.1063/1.3148335. [156](#)
- Walter M. Elsasser. The Hydromagnetic Equations. *Physical Review*, 79(1): 183–183, 1950. ISSN 0031-899X. doi: 10.1103/physrev.79.183. [64](#)
- Bernard S Finn. Laplace and the Speed of Sound. *Isis*, 55(1):7–19, 1964. ISSN 0021-1753. doi: 10.1086/349791. [30](#)
- E. A. Foote and R. M. Kulsrud. Hydromagnetic waves in high beta plasmas. *The Astrophysical Journal*, 233:302–316, October 1979. doi: 10.1086/157391. [59](#), [69](#)
- N. J. Fox, M. C. Velli, S. D. Bale, R. Decker, A. Driesman, R. A. Howard, J. C. Kasper, J. Kinnison, M. Kusterer, D. Lario, M. K. Lockwood, D. J. McComas, N. E. Raouafi, and A. Szabo. The Solar Probe Plus Mission: Humanity’s First Visit to Our Star. *Space Science Reviews*, 204(1-4):7–48, 2016. ISSN 0038-6308. doi: 10.1007/s11214-015-0211-6. [11](#), [76](#)
- S. Peter Gary. *Theory of Space Plasma Microinstabilities*. Cambridge, 1993. [9](#), [10](#), [54](#), [55](#), [57](#), [81](#), [84](#), [112](#), [117](#), [121](#), [130](#), [174](#), [175](#), [203](#)
- S. Peter Gary, Lin Yin, and Dan Winske. Electromagnetic proton cyclotron anisotropy instability: Wave-particle scattering rate. *Geophys. Res. Lett.*, 27 (16):2457–2459, August 2000. doi: 10.1029/2000GL000055. [171](#), [188](#)
- George Gloeckler. In-situ detection of energetic particles. *Heliophysics: Space Storms and Radiation: Causes and Effects*, page 43, 2010. [11](#), [75](#), [76](#)
- P. Goldreich and S. Sridhar. Toward a Theory of Interstellar Turbulence. II. Strong Alfvénic Turbulence. *The Astrophysical Journal*, 438:763, January 1995. doi: 10.1086/175121. [29](#), [68](#), [69](#), [87](#), [139](#), [141](#)

D. B. Graham, Yu. V. Khotyaintsev, M. André, A. Vaivads, A. Divin, J. F. Drake, C. Norgren, O. Le Contel, P.-A. Lindqvist, A. C. Rager, D. J. Gershman, C. T. Russell, J. L. Burch, K.-J. Hwang, and K. Dokgo. Direct observations of anomalous resistivity and diffusion in collisionless plasma. *Nature Communications*, 13(1):2954, 2022. doi: 10.1038/s41467-022-30561-8. [171](#)

E. P. Gross and M. Krook. Model for Collision Processes in Gases: Small-Amplitude Oscillations of Charged Two-Component Systems. *Physical Review*, 102(3):593–604, 1956. ISSN 0031-899X. doi: 10.1103/physrev.102.593. [45](#)

Daniel Grošelj, Christopher H. K. Chen, Alfred Mallet, Ravi Samtaney, Kai Schneider, and Frank Jenko. Kinetic Turbulence in Astrophysical Plasmas: Waves and/or Structures? *Physical Review X*, 9(3):031037, 2019. doi: 10.1103/physrevx.9.031037. [156](#)

Fan Guo, Hui Li, William Daughton, and Yi-Hsin Liu. Formation of Hard Power Laws in the Energetic Particle Spectra Resulting from Relativistic Magnetic Reconnection. *Physical Review Letters*, 113(15):155005, 2014. ISSN 0031-9007. doi: 10.1103/physrevlett.113.155005. [173](#)

D. A. Gurnett and L. A. Frank. Ion acoustic waves in the solar wind. *Journal of Geophysical Research: Space Physics*, 83(A1):58–74, 1978. ISSN 0148-0227. doi: 10.1029/ja083ia01p00058. [85](#)

S Hamasaki. Relaxation of anisotropic collisionless plasma. *Physics of Fluids*, 16(1):145, 1973. ISSN 0031-9171. doi: 10.1063/1.1694161. [174](#), [187](#)

Gregory W. Hammett and Francis W. Perkins. Fluid moment models for Landau damping with application to the ion-temperature-gradient instability. *Physical Review Letters*, 64(25):3019–3022, 1990. ISSN 0031-9007. doi: 10.1103/physrevlett.64.3019. [52](#)

R.E. Hartle and P.A. Sturrock. Two-Fluid Model of the Solar Wind. *The Astrophysical Journal*, 1968. [79](#)

Jiansen He, Eckart Marsch, Chuanyi Tu, Shuo Yao, and Hui Tian. Possible evidence of Alfvén-cyclotron waves in the angle distribution of magnetic helicity of solar wind turbulence. *The Astrophysical Journal*, 731(2):85, 2011. ISSN 0004-637X. doi: 10.1088/0004-637x/731/2/85. [12](#), [80](#)

Jiansen He, Chuanyi Tu, Eckart Marsch, Christopher H K Chen, Linghua Wang, Zhongtian Pei, Lei Zhang, Chadi S Salem, and Stuart D Bale. Proton heating in solar wind compressible turbulence with collisions between

counter-propagating waves. *The Astrophysical Journal*, 813(2):L30, 2015a. doi: 10.1088/2041-8205/813/2/l30. [89](#)

Jiansen He, Linghua Wang, Chuanyi Tu, Eckart Marsch, and Qiugang Zong. Evidence of Landau and cyclotron resonance between protons and kinetic waves in solar wind turbulence. *The Astrophysical Journal*, 800(2):L31, 2015b. doi: 10.1088/2041-8205/800/2/l31. [171](#)

P. Helander, M. Strumik, and A. A. Schekochihin. Constraints on dynamo action in plasmas. *J. Plasma Phys.*, 82(6):905820601, 2016. ISSN 0022-3778. doi: 10.1017/s0022377816000982. [171](#)

Petr Hellinger, Pavel Trávníček, Justin C. Kasper, and Alan J. Lazarus. Solar wind proton temperature anisotropy: Linear theory and WIND/SWE observations. *Geophysical Research Letters*, 33(9), 2006. ISSN 1944-8007. doi: 10.1029/2006gl025925. [12](#), [18](#), [81](#), [82](#), [145](#), [146](#)

Timothy S Horbury, Miriam Forman, and Sean Oughton. Anisotropic Scaling of Magnetohydrodynamic Turbulence. *Physical Review Letters*, 101(17):175005, 2008. ISSN 0031-9007. doi: 10.1103/physrevlett.101.175005. [87](#)

G G Howes, S D Bale, K G Klein, C H K Chen, C S Salem, and J M TenBarge. The slow-mode nature of compressible wave power in solar wind turbulence. *The Astrophysical Journal Letters*, 2011. doi: 10.1088/2041-8205/753/1/l19. [84](#)

Gregory G Howes, Steven C Cowley, William Dorland, Gregory W Hammett, Eliot Quataert, and Alexander A Schekochihin. Astrophysical Gyrokinetics: Basic Equations and Linear Theory. *The Astrophysical Journal*, 651(1):590–614, 2006. ISSN 0004-637X. doi: 10.1086/506172. [10](#), [58](#), [59](#), [111](#)

S Y Huang and F Sahraoui. Testing of the Taylor Frozen-in-flow Hypothesis at Electron Scales in the Solar Wind Turbulence. *The Astrophysical Journal*, 876(2):138, 2019. doi: 10.3847/1538-4357/ab17d3. [152](#)

J. D. Huba. Nrl (naval research laboratory) plasma formulary. revised. Technical report, NAVAL RESEARCH LAB WASHINGTON DC, 1987. [149](#)

P. Hunana, D. Laveder, T. Passot, P. L. Sulem, and D. Borgogno. Reduction of compressibility and parallel transfer by Landau damping in turbulent magnetized plasmas. *The Astrophysical Journal*, 743(2):128, 2011. ISSN 0004-637X. doi: 10.1088/0004-637x/743/2/128. [156](#)

P. Hunana, A. Tenerani, G. P. Zank, M. L. Goldstein, G. M. Webb, E. Khomenko, M. Collados, P. S. Cally, L. Adhikari, and M. Velli. An

introductory guide to fluid models with anisotropic temperatures. Part 2. Kinetic theory, Padé approximants and Landau fluid closures. *Journal of Plasma Physics*, 85(6):205850603, 2019a. ISSN 0022-3778. doi: 10.1017/s0022377819000850. [132](#)

P. Hunana, A. Tenerani, G. P. Zank, M. L. Goldstein, G. M. Webb, E. Khomenko, M. Collados, P. S. Cally, L. Adhikari, and M. Velli. An introductory guide to fluid models with anisotropic temperatures. Part 2. Kinetic theory, Padé approximants and Landau fluid closures. *Journal of Plasma Physics*, 85(6):205850603, 2019b. ISSN 0022-3778. doi: 10.1017/s0022377819000850. [45](#), [46](#), [48](#), [49](#), [98](#)

P Hunana, T Passot, E Khomenko, D Martinez-Gomez, M Collados, A Tenerani, G P Zank, Y Maneva, M L Goldstein, and G M Webb. Generalized fluid models of the Braginskii type. *arXiv*, 2022. [111](#)

P. S. Iroshnikov. Turbulence of a Conducting Fluid in a Strong Magnetic Field. *Soviet Astronomy - AJ*, 7:566, February 1964. [68](#)

J D Jackson. Longitudinal plasma oscillations. *Journal of Nuclear Energy. Part C, Plasma Physics, Accelerators, Thermonuclear Research*, 1(4):171, 1960. ISSN 0368-3281. doi: 10.1088/0368-3281/1/4/301. [50](#)

May-Britt Kallenrode. *Space physics: an introduction to plasmas and particles in the heliosphere and magnetospheres*. Springer Science & Business Media, 2004. [77](#)

J. C. Kasper, A. J. Lazarus, J. T. Steinberg, K. W. Ogilvie, and A. Szabo. Physics-based tests to identify the accuracy of solar wind ion measurements: A case study with the Wind Faraday Cups. *Journal of Geophysical Research: Space Physics (1978–2012)*, 111(A3), 2006. ISSN 2156-2202. doi: 10.1029/2005ja011442. [94](#), [144](#), [146](#)

Justin C. Kasper, Alan J. Lazarus, and S. Peter Gary. Wind/SWE observations of firehose constraint on solar wind proton temperature anisotropy. *Geophysical Research Letters*, 29(17):20–1–20–4, 2002. ISSN 1944-8007. doi: 10.1029/2002gl015128. [144](#)

P. J. Kellogg and T. S. Horbury. Rapid density fluctuations in the solar wind. *Annales Geophysicae*, 23(12):3765–3773, 2005. doi: 10.5194/angeo-23-3765-2005. [84](#)

Paul J. Kellogg. Fluctuations and Ion Isotropy in the Solar Wind. *Astrophys. J.*, 528(1):480–485, January 2000. doi: 10.1086/308147. [171](#)

Maurice G. Kendall and Alan Stuart. *The Advanced Theory of Statistics. Vol.1: Distribution theory*. Macmillan, New York, 1977. 160

Andrej Nikolaevich Kolmogorov. On degeneration (decay) of isotropic turbulence in an incompressible viscous liquid. In *Dokl. Akad. Nauk SSSR*, volume 31, pages 538–540, 1941a. 67

Andrej Nikolaevich Kolmogorov. Equations of turbulent motion in an incompressible fluid. In *Dokl. Akad. Nauk SSSR*, volume 30, pages 299–303, 1941b. 67

Andrey Nikolaevich Kolmogorov. Dissipation of energy in the locally isotropic turbulence. In *Dokl. Akad. Nauk SSSR A*, volume 32, pages 16–18, 1941c. 67

Robert H Kraichnan. Inertial-Range Spectrum of Hydromagnetic Turbulence. *Physics of Fluids*, 8(7):1385, 1965. ISSN 0031-9171. doi: 10.1063/1.1761412. 68

Nicholas A Krall and Alvin W Trivelpiece. *Principles of plasma physics*, volume 41. American Association of Physics Teachers, 1973. 9, 25, 26, 27, 33, 54, 100, 225

M. Kruskal and C. Oberman. On the stability of plasma in static equilibrium. *Journal of Nuclear Energy* (1954), 7(3-4):278, 1958. ISSN 0891-3919. doi: 10.1016/0891-3919(58)90119-0. 45, 49

R.M. Kulsrud. *MHD description of plasma*. North-Holland Publishing Company, 1983. 45, 46, 47, 48, 49, 96, 100

M. W. Kunz, J. Squire, A. A. Schekochihin, and E. Quataert. Self-sustaining sound in collisionless, high- β plasma. *J. Plasma Phys.*, 86(6):905860603, November 2020. doi: 10.1017/S0022377820001312. 171

Matthew W. Kunz, Alexander A. Schekochihin, and James M. Stone. Firehose and Mirror Instabilities in a Collisionless Shearing Plasma. *Phys. Rev. Lett.*, 112(20):205003, May 2014. doi: 10.1103/PhysRevLett.112.205003. 171

Matthew W. Kunz, James M. Stone, and Eliot Quataert. Magnetorotational Turbulence and Dynamo in a Collisionless Plasma. *Phys. Rev. Lett.*, 117(23):235101, December 2016. doi: 10.1103/PhysRevLett.117.235101. 171

LD Landau. 61—on the vibrations of the electronic plasma. *The Collected Papers of LD Landau*, pages 445–460, 1965. 46, 53

Lev Davidovich Landau. On the vibrations of the electronic plasma. *Uspekhi Fizicheskikh Nauk*, 93(3):527–540, 1967. 50

Lev Davidovich Landau and Evgenii Mikhailovich Lifshitz. *Statistical Physics: Volume 5*, volume 5. Elsevier, 2013. [144](#)

R. P. Lepping, M. H. Acuña, L. F. Burlaga, W. M. Farrell, J. A. Slavin, K. H. Schatten, F. Mariani, N. F. Ness, F. M. Neubauer, Y. C. Whang, J. B. Byrnes, R. S. Kennon, P. V. Panetta, J. Scheifele, and E. M. Worley. The WIND magnetic field investigation. *Space Science Reviews*, 71(1-4):207–229, 1995. ISSN 0038-6308. doi: 10.1007/bf00751330. [91](#)

R. P. Lin, K. A. Anderson, S. Ashford, C. Carlson, D. Curtis, R. Ergun, D. Larson, J. McFadden, M. McCarthy, G. K. Parks, H. Rème, J. M. Bosqued, J. Coutelier, F. Cotin, C. D'Uston, K. P. Wenzel, T. R. Sanderson, J. Henrion, J. C. Ronnet, and G. Paschmann. A three-dimensional plasma and energetic particle investigation for the wind spacecraft. *Space Science Reviews*, 71(1-4):125–153, 1995a. ISSN 0038-6308. doi: 10.1007/bf00751328. [91](#)

R. P. Lin, K. A. Anderson, S. Ashford, C. Carlson, D. Curtis, R. Ergun, D. Larson, J. McFadden, M. McCarthy, G. K. Parks, H. Rème, J. M. Bosqued, J. Coutelier, F. Cotin, C. D'Uston, K. P. Wenzel, T. R. Sanderson, J. Henrion, J. C. Ronnet, and G. Paschmann. A three-dimensional plasma and energetic particle investigation for the wind spacecraft. *Space Science Reviews*, 71(1-4):125–153, 1995b. ISSN 0038-6308. doi: 10.1007/bf00751328. [141](#)

Yoram Lithwick and Peter Goldreich. Compressible Magnetohydrodynamic Turbulence in Interstellar Plasmas. *The Astrophysical Journal*, 562(1):279–296, November 2001. doi: 10.1086/323470. [69](#)

J. S. Marron and M. P. Wand. Exact Mean Integrated Squared Error. *The Annals of Statistics*, 20(2):712–736, 1992. ISSN 0090-5364. doi: 10.1214/aos/1176348653. [159](#)

E. Marsch and H. Goldstein. The effects of Coulomb collisions on solar wind ion velocity distributions. *Journal of Geophysical Research: Space Physics*, 88(A12):9933–9940, 1983. ISSN 0148-0227. doi: 10.1029/ja088ia12p09933. [79](#)

Eckart Marsch. Kinetic Physics of the Solar Corona and Solar Wind. *Living Reviews in Solar Physics*, 3(1):1, 2006. ISSN 2367-3648. doi: 10.12942/lrsp-2006-1. [74](#), [79](#), [81](#), [171](#)

Lorenzo Matteini, Simone Landi, Petr Hellinger, Filippo Pantellini, Milan Maksimovic, Marco Velli, Bruce E. Goldstein, and Eckart Marsch. Evolution of the solar wind proton temperature anisotropy from 0.3 to 2.5 AU. *Geophysical*

Research Letters, 34(20), 2007. ISSN 1944-8007. doi: 10.1029/2007gl030920.

82

William H. Matthaeus and Melvyn L. Goldstein. Measurement of the rugged invariants of magnetohydrodynamic turbulence in the solar wind. *Journal of Geophysical Research: Space Physics*, 87(A8):6011–6028, 1982. ISSN 0148-0227. doi: 10.1029/ja087ia08p06011. 29, 153

D. J. McComas, B. L. Barraclough, J. T. Gosling, C. M. Hammond, J. L. Phillips, M. Neugebauer, A. Balogh, and R. J. Forsyth. Structures in the polar solar wind: Plasma and field observations from Ulysses. *Journal of Geophysical Research: Space Physics*, 100(A10):19893–19902, 1995. ISSN 0148-0227. doi: 10.1029/95ja01634. 83

D. J. McComas, H. A. Elliott, N. A. Schwadron, J. T. Gosling, R. M. Skoug, and B. E. Goldstein. The three-dimensional solar wind around solar maximum. *Geophysical Research Letters*, 30(10):n/a–n/a, 2003. ISSN 1944-8007. doi: 10.1029/2003gl017136. 11, 74

D. B. Melrose. *Instabilities in Space and Laboratory Plasmas*. Cambridge University Press, 1986. doi: 10.1017/cbo9780511564123.012. 56, 81, 178

Romain Meyrand, Anjor Kanekar, William Dorland, and Alexander A. Schekochihin. Fluidization of collisionless plasma turbulence. *PNAS*, 116(4):1185–1194, January 2019. doi: 10.1073/pnas.1813913116. 30, 171

D. Montgomery, M. R. Brown, and W. H. Matthaeus. Density fluctuation spectra in magnetohydrodynamic turbulence. *Journal of Geophysical Research: Space Physics*, 92(A1):282–284, 1987. ISSN 0148-0227. doi: 10.1029/ja092ia01p00282. 69

J. J. More, B. S. Garbow, and K. E. Hillstrom. User guide for minpack-1. [in fortran]. Technical report, Argonne National Lab., IL (USA), 8 1980. URL <https://www.osti.gov/biblio/6997568>. 107

Dmitry Moseev and Mirko Salewski. Bi-Maxwellian, slowing-down, and ring velocity distributions of fast ions in magnetized plasmas. *Physics of Plasmas*, 26(2):020901, 2019. ISSN 1070-664X. doi: 10.1063/1.5085429. 175

Yasuhide Narita and Eckart Marsch. Kinetic slow mode in the solar wind and its possible role in turbulence dissipation and ion heating. *The Astrophysical Journal*, 805(1):24, 2015. doi: 10.1088/0004-637x/805/1/24. 199

Isaac Newton. *The Principia: mathematical principles of natural philosophy*. University of California Press, 1687. 30

- Nilan Norris. The standard errors of the geometric and harmonic means and their application to index numbers. *Ann. Stat.*, 11(4):445–448, 1940. [160](#)
- K. W. Ogilvie, D. J. Chornay, R. J. Fritzenreiter, F. Hunsaker, J. Keller, J. Lobell, G. Miller, J. D. Scudder, E. C. Sittler, R. B. Torbert, D. Bodet, G. Needell, A. J. Lazarus, J. T. Steinberg, J. H. Tappan, A. Mavretic, and E. Gergin. SWE, a comprehensive plasma instrument for the WIND spacecraft. *Space Science Reviews*, 71(1-4):55–77, 1995. ISSN 0038-6308. doi: 10.1007/bf00751326. [94](#), [144](#)
- Hideo Okuda. Nonphysical noises and instabilities in plasma simulation due to a spatial grid. *Journal of Computational Physics*, 10(3):475–486, 1972. ISSN 0021-9991. doi: 10.1016/0021-9991(72)90048-4. [173](#)
- K. T. Osman, W. H. Matthaeus, A. Greco, and S. Servidio. Evidence for Inhomogeneous Heating in the Solar Wind. *The Astrophysical Journal Letters*, 727(1):L11, 2011. ISSN 2041-8205. doi: 10.1088/2041-8205/727/1/l11. [81](#)
- S. Oughton, W. H. Matthaeus, M. Wan, and K. T. Osman. Anisotropy in solar wind plasma turbulence. *Philosophical Transactions of the Royal Society A: Mathematical, Physical and Engineering Sciences*, 373(2041):20140152, 2015. ISSN 1364-503X. doi: 10.1098/rsta.2014.0152. [141](#)
- Mathew J. Owens and Robert J. Forsyth. The Heliospheric Magnetic Field. *Living Reviews in Solar Physics*, 10(1):5, 2013. ISSN 2367-3648. doi: 10.12942/lrsp-2013-5. [11](#), [77](#), [78](#)
- E. N. Parker. Dynamics of the Interplanetary Gas and Magnetic Fields. *The Astrophysical Journal*, 128:664, November 1958. doi: 10.1086/146579. [10](#), [71](#), [72](#), [73](#), [76](#)
- M. J. D. Powell. An efficient method for finding the minimum of a function of several variables without calculating derivatives. *The Computer Journal*, 7(2):155–162, 1964. ISSN 0010-4620. doi: 10.1093/comjnl/7.2.155. [107](#)
- François Rincon, Francesco Califano, Alexander A. Schekochihin, and Francesco Valentini. Turbulent dynamo in a collisionless plasma. *PNAS*, 113(15):3950–3953, April 2016. doi: 10.1073/pnas.1525194113. [171](#)
- M N Rosenbluth and N Rostoker. Theoretical Structure of Plasma Equations. *Physics of Fluids*, 2(1):23, 1959. ISSN 0031-9171. doi: 10.1063/1.1724387. [45](#), [48](#)
- A. A. Schekochihin and S. C. Cowley. Turbulence, magnetic fields, and plasma physics in clusters of galaxies. *Phys. Plasmas*, 13(5):056501–056501, May 2006. doi: 10.1063/1.2179053. [32](#), [171](#)

- A. A. Schekochihin, S. C. Cowley, W. Dorland, G. W. Hammett, G. G. Howes, E. Quataert, and T. Tatsuno. Astrophysical gyrokinetics: kinetic and fluid turbulent cascades in magnetized weakly collisional plasmas. *The Astrophysical Journal Supplement Series*, 182(1):310, 2009. ISSN 0067-0049. doi: 10.1088/0067-0049/182/1/310. [29](#), [69](#), [111](#), [113](#)
- A. A. Schekochihin, J. T. Parker, E. G. Highcock, P. J. Dellar, W. Dorland, and G. W. Hammett. Phase mixing versus nonlinear advection in drift-kinetic plasma turbulence. *J. Plasma Phys.*, 82(2):905820212, April 2016. doi: 10.1017/S0022377816000374. [27](#), [171](#)
- S. Servidio, F. Valentini, D. Perrone, A. Greco, F. Califano, W. H. Matthaeus, and P. Veltri. A kinetic model of plasma turbulence. *Journal of Plasma Physics*, 81(1):325810107, 2015. ISSN 0022-3778. doi: 10.1017/s0022377814000841. [82](#)
- Prateek Sharma, Gregory W Hammett, and Eliot Quataert. Transition from Collisionless to Collisional Magnetorotational Instability. *The Astrophysical Journal*, 596(2):1121–1130, 2003. ISSN 0004-637X. doi: 10.1086/378234. [49](#), [102](#)
- Charles W Smith, Philip A Isenberg, William H Matthaeus, and John D Richardson. Turbulent Heating of the Solar Wind by Newborn Interstellar Pickup Protons. *The Astrophysical Journal*, 638(1):508–517, 2006. ISSN 0004-637X. doi: 10.1086/498671. [11](#), [78](#), [79](#)
- P B Snyder, G W Hammett, and W Dorland. Landau fluid models of collisionless magnetohydrodynamics. *Physics of Plasmas*, 4(11):3974–3985, 1997. ISSN 1070-664X. doi: 10.1063/1.872517. [45](#), [48](#), [49](#)
- Lyman Spitzer. *Physics of fully ionized gases*. Courier Corporation, 2006. [149](#)
- Lyman Spitzer and Richard Härm. Transport Phenomena in a Completely Ionized Gas. *Physical Review*, 89(5):977–981, 1953. ISSN 0031-899X. doi: 10.1103/physrev.89.977. [43](#), [44](#)
- J. Squire, M. W. Kunz, E. Quataert, and A. A. Schekochihin. Kinetic Simulations of the Interruption of Large-Amplitude Shear-Alfvén Waves in a High- β Plasma. *Phys. Rev. Lett.*, 119(15):155101, October 2017. doi: 10.1103/PhysRevLett.119.155101. [171](#)
- J Squire, A A Schekochihin, and E Quataert. Amplitude limits and nonlinear damping of shear-Alfvén waves in high-beta low-collisionality plasmas. *New Journal of Physics*, 19(5):055005, 2017a. ISSN 1367-2630. doi: 10.1088/1367-2630/aa6bb1. [82](#)

- J. Squire, A. A. Schekochihin, E. Quataert, and M. W. Kunz. Magneto-immutable turbulence in weakly collisional plasmas. *Journal of Plasma Physics*, 85(1):905850114, 2019. ISSN 0022-3778. doi: 10.1017/s0022377819000114. [132](#)
- Jonathan Squire, Eliot Quataert, and Matthew Walter Kunz. Pressure-anisotropy-induced nonlinearities in the kinetic magnetorotational instability. *J. Plasma Phys.*, 83(6), 2017b. [171](#)
- Joshua E Stawarz, Charles W Smith, Bernard J Vasquez, Miriam A Forman, and Benjamin T MacBride. The turbulent cascade and proton heating in the solar wind at 1 AU. *The Astrophysical Journal*, 697(2):1119–1127, 2009. ISSN 0004-637X. doi: 10.1088/0004-637x/697/2/1119. [29](#)
- Thomas H Stix. *Waves in plasmas*. Springer Science & Business Media, 1992. [50](#), [53](#), [54](#), [59](#), [203](#)
- Peter Stubbe. Landau damping of sound in a rarefied neutral gas. *Physics of Fluids*, 6(9):3164–3174, 1994. ISSN 1070-6631. doi: 10.1063/1.868093. [113](#)
- Tao Tang. The Hermite Spectral Method for Gaussian-Type Functions. *SIAM Journal on Scientific Computing*, 14(3):594–606, 1993. ISSN 1064-8275. doi: 10.1137/0914038. [181](#)
- G I Taylor. The Spectrum of Turbulence. *Proceedings of the Royal Society of London. Series A - Mathematical and Physical Sciences*, 164(919):476–490, 1938. ISSN 0080-4630. doi: 10.1098/rspa.1938.0032. [152](#)
- Lewi Tonks and Irving Langmuir. Oscillations in Ionized Gases. *Physical Review*, 33(2):195–210, 1929. ISSN 0031-899X. doi: 10.1103/physrev.33.195. [24](#), [54](#)
- C. Y. Tu and E. Marsch. MHD structures, waves and turbulence in the solar wind: Observations and theories. *Space Science Reviews*, 73(1-2):1–210, 1995. ISSN 0038-6308. doi: 10.1007/bf00748891. [29](#), [83](#), [85](#)
- C. -Y. Tu and E. Marsch. On the nature of compressive fluctuations in the solar wind. *Journal of Geophysical Research: Space Physics*, 99(A11):21481–21509, 1994. ISSN 0148-0227. doi: 10.1029/94ja00843. [83](#)
- C.-Y. Tu and E. Marsch. Anisotropy regulation and plateau formation through pitch angle diffusion of solar wind protons in resonance with cyclotron waves. *Journal of Geophysical Research: Space Physics (1978–2012)*, 107(A9):SSH 7–SSH 7–8, 2002. ISSN 2156-2202. doi: 10.1029/2001ja000150. [171](#)

- Daniel Verscharen, Benjamin D G Chandran, Kristopher G Klein, and Eliot Quataert. Collisionless isotropization of the solar-wind protons by compressive fluctuations and plasma instabilities. *The Astrophysical Journal*, 831(2):128, 2016. doi: 10.3847/0004-637x/831/2/128. [82](#), [171](#)
- Daniel Verscharen, Christopher H K Chen, and Robert T Wicks. On Kinetic Slow Modes, Fluid Slow Modes, and Pressure-balanced Structures in the Solar Wind. *The Astrophysical Journal*, 840(2):106, 2017. doi: 10.3847/1538-4357/aa6a56. [84](#), [112](#)
- Daniel Verscharen, Kristopher G Klein, and Bennett A Maruca. The multi-scale nature of the solar wind. *arXiv*, 2019. doi: 10.1101/s41116-019-0021-0. [9](#), [10](#), [12](#), [13](#), [28](#), [61](#), [84](#), [86](#), [90](#), [91](#), [92](#), [93](#), [150](#)
- A A Vlasov. The vibrational properties of an electron gas. *Soviet Physics Uspekhi*, 10(6):721–733, 1968. ISSN 0038-5670. doi: 10.1070/pu1968v010n06abeh003709. [24](#)
- Shuo Yao, J S He, C Y Tu, L H Wang, and E Marsch. Small-scale pressure-balanced structures driven by oblique slow mode waves measured in the solar wind. *The Astrophysical Journal*, 774(1):59, 2013. ISSN 0004-637X. doi: 10.1088/0004-637x/774/1/59. [84](#)
- Peter H. Yoon. Kinetic instabilities in the solar wind driven by temperature anisotropies. *Reviews of Modern Plasma Physics*, 1(1):4, 2017. doi: 10.1007/s41614-017-0006-1. [10](#), [59](#), [62](#), [82](#), [171](#), [174](#), [186](#), [191](#)
- G. P. Zank, W. H. Matthaeus, and C. W. Smith. Evolution of turbulent magnetic fluctuation power with heliospheric distance. *Journal of Geophysical Research*, 101(A8):17093–17108, August 1996. doi: 10.1029/96JA01275. [29](#), [85](#)